

**Corrosion Assessment and Mechanisms of Materials in Pre-hydrolysis and
Hydrothermal Liquefaction Biorefining Systems**

by

Minkang Liu

A thesis submitted in partial fulfillment of the requirements for the degree of

Doctor of Philosophy

in

Materials Engineering

Department of Chemical and Materials Engineering

University of Alberta

© Minkang Liu, 2022

Abstract

Advanced biomass conversion technologies, including hot dilute acidic pre-hydrolysis and hydrothermal liquefaction, have been developed for the generation of renewable bioenergy products and biochemicals from existing biomass resources and biowastes. However, the deployment of the technologies is hindered because of significant corrosion and materials technology gaps in terms of cost-effective construction and safe operation of biorefining reactors. This study intends to address the corrosion challenges and support the development of materials selection guidelines for the successful commercialization of the two technologies.

Hot dilute acidic pre-hydrolysis biorefining technology is a pretreatment method used for direct conversion of raw biomass into fermentable and enzymatic intermediates in dilute acid (such as H_2SO_4 and H_2SO_3) at 100 - 200 °C. Little information on corrosion is available for determining materials performance in such environments. This study finds that Fe-based steels (SS316L and DSS 2205) suffer active corrosion, and their corrosion rates increase with increasing temperature, service time, and addition of corrodants (Cl^- , S^{2-} , and organic acid), while Alloy C-276 exhibits acceptable resistance. More importantly, it is found that increasing Cr content even up to 22.5 wt.% cannot provide satisfactory protection since the formed Cr-enriched oxides are thermodynamically unstable and experience chemical dissolution. Increasing Mo content in alloys, on the other hand, could significantly improve corrosion resistance due to the formation of stable Mo-enriched oxide layer which demonstrates the promising resistance to hot dilute acid and the corrodants released. This novel finding is completely different from previous studies about the effect of Mo on corrosion.

Hydrothermal liquefaction is a thermochemical technology to convert wet biomass and biowaste to bio-oils and biochemicals in pressurized water at 250 - 370 °C and pressure up to 25 MPa. In this study, the effects of temperature, pressure and flow rate have been well investigated using high temperature autoclaves and environmental loops. It is found that increasing temperature up to 365 °C remarkably enhances the corrosion of P91 steel, and there is a transition temperature (around 310 °C) for SS310, above which its corrosion rate decreases with further increase in temperature. Increasing pressure and flow rate leads to a noticeable increase in the corrosion rate of P91 steel. Different from P91, the corrosion rate of SS310 only slightly increases with pressure, and decreases with an increase in flow rate due to the formation of an inner Cr-enriched oxide layer and suppressed nodular oxidation.

Homogenous catalysts (such as K_2CO_3) are commonly used to achieve optimum carbon conversion efficiency. This study finds that the addition of 0.5 M K_2CO_3 results in a significant increase in the corrosion rates of P91 and SS310, and remarkably changes the microstructure of surface scales. At 310 °C, the presence of chloride and sulfide ions does not trigger pitting, but can cause an increase in corrosion rates due to the formation of less protective oxide layers. The presence of acetic acid further accelerates the corrosion. The corrosion mechanism in catalytic HTL environments has thus been proposed based on the testing results and thermodynamic simulations.

In the non-catalytic and catalytic HTL environments, thermodynamic calculations indicate that major alloying elements (Fe, Cr, Ni and Mo) could experience general oxidation or active corrosion, depending on temperature and pH. Under the HTL conversion conditions, overall ranking in terms of increasing corrosion resistance is:

P91 << SS316L < SS310 < Alloy C-276 < Alloy 625

Increasing Cr and Mo contents in alloys should improve their resistance to the environmental attack. Increasing Ni content has a negligible effect in non-catalytic HTL environment, but can improve the corrosion performance in the catalytic environments. Post-mortem characterizations further reveal the roles of alloying elements in the corrosion layers and advance the mechanistic understanding of their impact on corrosion. Stress corrosion cracking is another concern when evaluating suitable alloys. Uniaxial constant strain and U-bending techniques were adopted to evaluate SCC susceptibility of SS316L and SS310 in a catalytic HTL environment at 365 °C. Preliminary results show that increasing strain deformation enhances the corrosion. However, the SCC risk of the tested steels, even under 3.3% deformation, is much lower than expected. More assessments are still needed to confirm the above findings and determine the SCC risk of welded construction steels and alloys.

Preface

This thesis is an original work completed by Minkang Liu under the supervisions of Dr. Jing-Li Luo and Dr. Yimin Zeng. It contains seven chapters:

Chapter 1 is the introduction of research background on hot dilute acidic pre-hydrolysis and hydrothermal liquefaction systems, including an overview of the conversion technologies, corrosion types in different biorefining environments, preliminary materials screening processes, and existing materials knowledge gaps. Dr. Yimin Zeng and Dr. Jing-Li Luo provided valuable comments and revisions. Minkang Liu carried out the literature review, analyzed the data and prepared the manuscript.

Chapter 2 summarizes the testing methodologies used in this study, including testing sample preparation, autoclave testing procedures, and subsequent corrosion rate assessments and corrosion product examinations.

Chapter 3 has been submitted to *Corrosion Science* as Minkang Liu, Yimin Zeng, Jing-Li Luo, Corrosion of Candidate Constructional Alloys under Hot Dilute Acidic Pre-Hydrolysis Biorefining Conditions: Influence of Temperature, Alloying Elements and Corrodants. Dr. Yimin Zeng and Dr. Jing-Li Luo provided useful guidance and revised the manuscript. Minkang Liu was responsible for conceptualization and thermodynamic calculation, designing and conducting all the experiments, data analyzing and curating, and manuscript writing.

Chapter 4 has been published as Minkang Liu, Yimin Zeng, Jing-Li Luo, Influence of Major Operating Parameters (Temperature, Pressure and Flow Rate) on the Corrosion of Candidate Alloys for the Construction of Hydrothermal Liquefaction Biorefining Reactors, *Energy & Fuels*, 36-6 (2022), 3134-3153. Dr. Yimin Zeng and Dr. Jing-Li Luo provided preliminary conceptualization, insightful comments, valuable discussions and comments. Minkang Liu conducted thermodynamic calculations, carried out all the experiments, analyzed data and results, and wrote the manuscript.

Chapter 5 has been published as Minkang Liu, Yimin Zeng, Jing-Li Luo, Impacts of catalyst, inorganic and organic corrodants on corrosion under batch-mode catalytic biomass hydrothermal liquefaction conversion, *Corrosion Science*, Volume 204, 2022, 110409. Dr. Yimin Zeng and Dr.

Jing-Li Luo provided valuable comments, discussions and revisions. Minkang Liu designed and carried out experiments, analyzed data and results, and wrote the manuscript.

Chapter 6 has been submitted to *Corrosion Science* as “Roles of Major Alloying Elements in Steels and Alloys on Corrosion under Biomass Hydrothermal Liquefaction (HTL) Conversion”. Dr. Yimin Zeng and Dr. Jing-Li Luo provided valuable comments, discussions and revision. Minkang Liu was responsible for conceptualizing, designing and conducting all the experiments, data collecting, data analyzing, and manuscript writing.

Chapter 7 covers the preliminary testing results of stress corrosion cracking of two candidate stainless steels in catalytic HTL environments containing inorganic and organic corrodants. Dr. Yimin Zeng and Dr. Jing-Li Luo provided valuable suggestions, comments, discussions and revision. Minkang Liu designed and conducted all the experiments, collected and analyzed data, and wrote the manuscript.

Chapter 8 includes the summary of the main conclusions of the thesis work and the future prospects of the research.

Acknowledgements

First and foremost, I would like to express my deep gratitude to my supervisors, Dr. Jing-Li Luo and Dr. Yimin Zeng, for their continuous support, encouragement, patience and invaluable advice. Their constant critical feedbacks helped me in every step along this journey and inspired me to become a researcher and further pursue my career in this field.

My deep appreciation goes to my supervisory committee member, Dr. Hyun-Joong Chung for his thoughtful suggestions and assistance during my research progress.

I would like to thank my group members at University of Alberta, Dr. Kaiyang Li, Dr. Chen Shen, Dr. Chong Sun, Dr. Subiao Liu, Dr. Yaqian Zhang, Dr. Jiankuan Li, Dr. Shuo Shuang, Dr. Tengfei Li, and Dr. Xianzong Wang for their great collaboration and help during my research in lab. I would also like to thank my colleagues in CanmetMATERIALS, Dr. Jian Li, Mrs. Pei Liu, Dr. Babak Shalchi, Mrs. Renata Zavadil, Mrs. Catherine Bibby, Mr. Jie Liang, Mrs. Jennifer Collier, Mrs. Magdalene Matchim, Mr. Chao Shi, Mr. Maciej Podlesny, Dr. Xin Pang, Dr. Xue Han, Dr. Nicholas Senior, Dr. Taylor Martino, and Mr. Elliott Asare.

I would like to acknowledge the funding support from Canadian NRCan OERD Clean Energy and Forest Innovation programs, and Natural Sciences and Engineering Research Council of Canada (NSERC) Discovery Grant (GRPIN-2016-05494).

My special thanks go to my family, for raising me with unconditional love and help, and for encouraging me to go through this tough but meaningful journey.

Table of Contents

Abstract.....	ii
Preface.....	v
Acknowledgements.....	vii
List of Tables	xii
List of Figures.....	xiii
List of Symbols.....	xix
List of Abbreviations	xx
Chapter 1. Introduction	1
1.1 Overview of biomass resources.....	1
1.2. Biomass conversion technologies studied in this thesis.....	2
1.2.1. Overview of biomass conversion technologies	2
1.2.2. Two innovative biorefining reactors investigated in this study.....	3
1.2.2.1. Hot dilute acidic pre-hydrolysis technology	3
1.2.2.2. Hydrothermal liquefaction technology	4
1.3. Materials knowledge gaps in the construction of two biorefining reactors	7
1.3.1. Corrosion challenges under hot dilute sulfuric acidic pre-hydrolysis biorefining processes.....	7
1.3.2. Corrosion challenge under HTL conversion processes	9
1.4. Candidate alloys for the construction of pre-hydrolysis and HTL reactors	12
1.5. Objectives and contents of the thesis	16
Chapter 2. Methodologies.....	18
2.1. Testing sample preparation	18
2.2. Testing methodology and procedure under different testing conditions.....	19
2.3. Corrosion rate assessments.....	19
2.4. Corrosion products characterization.....	21
Chapter 3. Corrosion of Candidate Constructional Alloys under Hot Dilute Acidic Pre-Hydrolysis Biorefining Conditions: Influence of Temperature, Alloying Elements and Corrodants.....	22
3.1. Introduction	22
3.2. Experimental Procedure	26
3.2.1. Testing sample preparation.....	26

3.2.2. Test methodology and procedures	27
3.2.3. Corrosion rate assessment	28
3.2.4. Corrosion products characterization	29
3.3. Main Results.....	30
3.3.1. Influence of temperature and operating time.....	30
3.3.2. Effect of alloying elements on corrosion.....	37
3.3.2.1. Effect of alloying element Cr.....	37
3.3.2.2. Effect of alloying element Mo	41
3.3.3. Effect of inorganic corrodants and biomass	45
3.4. Discussion	56
3.5. Conclusions	63
Chapter 4. Influence of Major Operating Parameters (Temperature, Pressure and Flow Rate) on the Corrosion of Candidate Alloys for the Construction of Hydrothermal Liquefaction Biorefining Reactors	64
4.1. Introduction	65
4.2. Experimental procedure	70
4.2.1. Testing sample preparation.....	70
4.2.2. Testing methodology and procedure	70
4.2.3. Corrosion rate assessments.....	73
4.2.4. Corrosion products characterization.....	75
4.3. Main Results.....	76
4.3.1. Effect of operating temperature on corrosion.....	76
4.3.2. Effect of flow rate on corrosion.....	84
4.3.3 Effect of operating pressure on corrosion.....	90
4.4. Discussion	95
4.4.1. Influence of temperature on corrosion in HTL water.....	95
4.4.2. Influence of flow rate on corrosion in HTL water.....	98
4.4.3. Influence of operating pressure on corrosion in HTL water	100
4.5. Conclusions	101
Chapter 5. Impacts of Catalyst, Inorganic and Organic Corrodants on Corrosion under Batch- mode Catalytic Biomass Hydrothermal Liquefaction Conversion	103
5.1. Introduction	104

5.2. Experimental Procedure	107
5.2.1. Test Sample Preparation	107
5.2.2. Autoclave testing methodology and procedure	108
5.2.3. Corrosion rate assessment	110
5.2.4. Corrosion products characterization	111
5.3. Main Results.....	112
5.3.1. Effect of alkaline catalyst on corrosion	112
5.3.2. Influence of inorganic corrodants on corrosion.....	121
5.3.3. Impact of organic acid on corrosion	127
5.4. Discussion	133
5.5. Conclusions	140
Chapter 6. Roles of Major Alloying Elements in Steels and Alloys on Corrosion under Biomass Hydrothermal Liquefaction (HTL) Conversion.....	142
6.1. Introduction	143
6.2. Thermodynamic simulation.....	145
6.3. Experimental testing procedure.....	147
6.3.1. Preparation of testing samples	147
6.3.2. Autoclave testing methodology and procedure	148
6.3.3. Corrosion rate assessment	150
6.3.4. Corrosion product characterization	151
6.4. Results and Discussion.....	152
6.4.1. Pourbaix diagrams of major alloying elements under catalytic HTL conversion conditions.....	152
6.4.2. Influence of major alloying elements on corrosion processes under the HTL conversion.....	155
6.4.2.1. Effects of alloying elements on corrosion kinetics	155
6.4.3. Influence of alloying elements on the corrosion layers formed in HTL environments	161
6.4.3.1. Roles of Cr and Ni in corrosion layers grown on Fe-based steels	161
6.4.3.2. Roles of Ni and Mo in corrosion layers formed on the alloys with medium Cr content.....	169
6.4.3.3. Roles of Ni and Mo in corrosion layers formed on high Cr content alloys	173
6.4.3.4. Role of Mo in Ni-based alloys	178

6.5. Conclusions	179
Chapter 7. Stress Corrosion Cracking Susceptibility of Candidate Reactor Alloys under Catalytic Hydrothermal Liquefaction Conditions	181
7.1. Introduction	181
7.2. Experimental	183
7.2.1. SCC testing specimen preparation.....	183
7.2.2. Autoclave test matrix and methodologies	188
7.2.3. Post-Morten Characterization of tested samples	189
7.3. Main Results and Discussion	189
7.3.1. Microstructure and mechanical properties of tested steels.....	189
7.3.2. SCC susceptibility under simulated catalytic HTL conversion.....	192
7.4. Conclusions	198
Chapter 8. Summary and Future Prospects.....	199
8.1. Summary	199
8.2. Future prospects	201
Bibliography	203

List of Tables

Table 1-1. Relative cost ratio of different types of steels and alloys.....	11
Table 3-1. Normalized bulk chemical composition of SS316L, DSS 2205, and Alloy C-276. ...	26
Table 3-2. Testing conditions of static autoclave test.....	27
Table 3-3. Gibbs energy of Fe, Cr, Ni and Mo oxides and sulfates formation with water and sulfuric acid at 100 and 200 °C, respectively [282-284].	60
Table 4-1. Normalized bulk chemical composition of SS310 and P91 steels.	70
Table 4-2. Test matrix conducted to investigate the influence of temperature, pressure and flow rate on the corrosion of SS310 and P91 steels in hot pressurized HTL water.....	73
Table 4-3. The estimated Gibbs energy of major alloy elements formation present in the two steels at three HTL temperatures.	95
Table 4-4. Estimated diffusion rates of Cr, Fe, Ni and O ions in Cr ₂ O ₃ at HTL operating temperatures based on database in references [352-357].	98
Table 4-5. Estimated diffusion rates of Fe and O ions in Fe ₃ O ₄ at HTL operating temperatures based on database in references [358-360].	98
Table 5-1. The chemical compositions of SS310 and P91 steels used in this study.....	107
Table 5-2. Tests conducted to investigate the effects of alkaline catalyst, inorganic corrodants, and organic acid on the corrosion of candidate reactor steels.	109
Table 5-3. Oxide and hydroxide formation reactions possibly occurred on the two steels in catalytic HTL environments and estimated Gibbs free energy at 310 °C.	134
Table 6-1. Normalized bulk chemical composition of steels and alloys used in this study.	148
Table 6-2. Test matrix conducted to identify the impacts of alloying elements under simulated non-catalytic and catalytic HTL conversion conditions.	149
Table 7-1. The bulk chemical composition of tested austenitic stainless steels used in this study.	184

List of Figures

Fig. 1-1. Schematic of hot dilute acidic pre-hydrolysis treatment of lignocellulosic feedstocks at mill plants.....	4
Fig. 1-2. Schematic of hydrothermal liquefaction (HTL) of wet biomass/biowaste feedstocks using pressurized subcritical water.	5
Fig. 1-3. (a) Comparison of the operating temperature and pressure ranges of water used in HTL reactors with those in nuclear reactors; (b) The properties of subcritical water applied in a typical HTL reactor. Note that the above figures were drawn based on the information provided in references [127, 152-154]. Fig. 1-3 (b) was reproduced with permission from [154].	10
Fig. 3-1. Schematic of hot dilute acidic pre-hydrolysis treatment of lignocellulosic feedstocks.	23
Fig. 3-2. (a) Schematic of autoclave setup used for this study; and (b) Photographic image of opened static autoclave with a PTFE linear, holder and testing samples.	28
Fig. 3-3. Photographic images of alloy coupons taken before and after the exposure to 0.05 M H ₂ SO ₄ at pre-hydrolysis biorefining temperatures for different exposure durations.....	30
Fig. 3-4. Top-view SEM images of SS316L steel samples after corroded in 0.05 M H ₂ SO ₄ at 100 °C, 150 °C and 200 °C, respectively.....	31
Fig. 3-5. Cross-sectional SEM view of SS316L steel and corresponding elemental mapping of Cr, Fe, O, and S after the exposure to 0.05 M H ₂ SO ₄ at 100 °C, 150 °C and 200 °C, respectively.	33
Fig. 3-6. XRD spectra collected on SS316L steel samples after the exposure to 0.05 M H ₂ SO ₄ at different biorefining temperatures.	34
Fig. 3-7. Top and cross-sectional SEM views and corresponding EDS results of Zr702 after the exposure to 0.05 M H ₂ SO ₄ along with three tested alloys at 200 °C.....	35
Fig. 3-8. Cross-sectional SEM views of corroded SS316L steel after the exposure to 0.05 M H ₂ SO ₄ at 200 °C for 14 and 42 days, respectively.....	36
Fig. 3-9. XRD spectra collected on SS316L steel sample after the exposure to 0.05 M H ₂ SO ₄ at 200 °C for 42 days.	36
Fig. 3-10. Variation of the average corrosion rates (mm/y) of SS316L with temperature and exposure time in 0.05 M H ₂ SO ₄	37
Fig. 3-11. Top-view SEM images of DSS 2205 samples after the exposure to 0.05 M H ₂ SO ₄ at 100 °C, 150 °C and 200 °C for 14 days, respectively.....	38
Fig. 3-12. Cross-sectional SEM views and corresponding elemental mapping of DSS 2205 steel after the exposure to in 0.05 M H ₂ SO ₄ at different temperatures for 14 days.	39
Fig. 3-13. XRD spectra collected on DSS 2205 steel samples after the exposure to 0.05 M H ₂ SO ₄ at 100 °C, 150 °C and 200 °C, respectively.....	40
Fig. 3-14. Comparison of the average corrosion rates (mm/y) of SS316L and DSS 2205 steels in 0.05 M H ₂ SO ₄ at pre-hydrolysis operating temperatures for different exposure durations.	41
Fig. 3-15. Top-view SEM images of Alloy C-276 samples after corroded in 0.05 M H ₂ SO ₄ at different pre-hydrolysis operating temperatures for 14 days, respectively.....	42

Fig. 3-16. Cross-sectional SEM view of Alloy C-276 after the exposure to 0.05 M H ₂ SO ₄ at 200 °C for 14 days.	42
Fig. 3-17. Cross-sectional high-resolution TEM images and corresponding elemental mapping of Alloy C-276 samples after corroded in 0.05 M H ₂ SO ₄ at 100 °C and 200 °C for 14 days, respectively.	44
Fig. 3-18. Cross-sectional high-resolution TEM images and corresponding elemental mapping results of Zr702 after the exposure to 0.05 M H ₂ SO ₄ along with other tested alloys at 200 °C... ..	44
Fig. 3-19. Comparison of the average corrosion rates (mm/y) of SS316L and Alloy C-276 in 0.05 M H ₂ SO ₄ at the temperature range of 100-200 °C for different exposure time.	45
Fig. 3-20. Photographic images of testing coupons taken before and after the exposure to different testing solutions at 200 °C for 14 days.	46
Fig. 3-21. Top-view SEM images of SS316L steel samples after corroded in (a) 0.05 M H ₂ SO ₄ + 700 ppm Cl ⁻ + 500 ppm S ²⁻ ; and (b) 0.05 M H ₂ SO ₄ + 25 wt.% biomass at 200 °C for 14 days, respectively.	47
Fig. 3-22. Cross-sectional SEM views of SS316L steel and corresponding elemental mappings of Cr, Fe, O, and S after corroded in (a) 0.05 M H ₂ SO ₄ + 700 ppm Cl ⁻ + 500 ppm S ²⁻ ; and (b) 0.05 M H ₂ SO ₄ + 25 wt.% biomass at 200 °C for 14 days, respectively.	48
Fig. 3-23. XRD spectra collected on SS316L steel samples after the exposure to 0.05 M H ₂ SO ₄ with inorganic corrodants and softwood at 200 °C, respectively.	49
Fig. 3-24. Top-view SEM images of DSS 2205 samples after corroded in (a) 0.05 M H ₂ SO ₄ + 700 ppm Cl ⁻ + 500 ppm S ²⁻ ; and (b) 0.05 M H ₂ SO ₄ + 25 wt.% biomass at 200 °C for 14 days, respectively.	50
Fig. 3-25. Cross-sectional SEM view of DSS 2205 steel and corresponding elemental mapping of Cr, Fe, O, and S after corroded in (a) 0.05 M H ₂ SO ₄ + 700 ppm Cl ⁻ + 500 ppm S ²⁻ ; and (b) 0.05 M H ₂ SO ₄ + 25 wt.% biomass at 200 °C for 14 days, respectively.	51
Fig. 3-26. XRD spectra collected on DSS 2205 steel samples after the exposure to 0.05 M H ₂ SO ₄ with inorganic corrodants and softwood at 200 °C, respectively.	52
Fig. 3-27. SEM top-view images of Alloy C-276 samples after corroded in (a) 0.05 M H ₂ SO ₄ + 700 ppm Cl ⁻ + 500 ppm S ²⁻ ; and (b) 0.05 M H ₂ SO ₄ + 25 wt.% biomass at 200 °C for 14 days, respectively.	53
Fig. 3-28. Cross-sectional high-resolution TEM images and corresponding elemental mapping of Alloy C-276 samples after corroded in 0.05 M H ₂ SO ₄ with addition of inorganic corrodants and softwood at 200 °C for 14 days, respectively.	53
Fig. 3-29. Comparison of the average corrosion rates (mm/y) of (a) SS316L, (b) DSS 2205, and (c) Alloy C-276 in three different biorefining solutions at 200 °C after 14 days' exposure, respectively.	55
Fig. 3-30. Established Pourbaix diagrams at 100 °C: (a) Fe-0.05 M H ₂ SO ₄ system, and (b) Ni-0.05 M H ₂ SO ₄ system.	58
Fig. 3-31. Established Pourbaix diagrams of Cr-0.05 M H ₂ SO ₄ system at (a) 100, and (b) 200 °C, respectively.	58
Fig. 3-32. Established Pourbaix diagrams of Mo-0.05 M H ₂ SO ₄ system at (a) 100, and (b) 200 °C, respectively.	59

Fig. 4-1. (a) Comparison of the operating temperature and pressure ranges of water used in HTL reactors with those in nuclear reactors; (b) The properties of subcritical water applied in a typical HTL reactor. Note that the above figures were drawn based on the information provided in references [127, 152-154]. Fig. 4-1(b) was reproduced with permission from [154]. Copyright 2008 Royal Society of Chemistry.	67
Fig. 4-2. Schematic of (a) static autoclaves and (b) water loop facilities used in this study.	72
Fig. 4-3. Photographic images of SS310 and P91 steels (20 mm long × 10 mm wide × 2 mm thick) before and after the exposure to hot water at different HTL operating temperatures.	76
Fig. 4-4. Top-view and cross-sectional SEM views of (a) SS310 and (b) P91 steels corroded in HTL water at different operating temperatures.	78
Fig. 4-5. XRD spectra collected on P91 steel samples after the exposures to HTL water at different HTL operating temperatures.	79
Fig. 4-6. High resolution TEM cross-sectional images and corresponding elemental mapping on SS310 after the exposure to HTL water at different temperatures: (a) 250 °C; (b) 310 °C; and (c) 365 °C.	80
Fig. 4-7. XPS depth profiling spectra collected on a SS310 sample after the exposure to 250 °C ultrapure water: (a) O 1s, (b) Fe 2p _{3/2} , and (c) Cr 2p _{3/2} region.	81
Fig. 4-8. XPS depth profiling XPS spectra collected on a SS310 sample after the exposure to 365 °C ultrapure water: (a) O 1s, (b) Fe 2p _{3/2} , and (c) Cr 2p _{3/2} region.	81
Fig. 4-9. Variation of average corrosion rate of SS310 steel with HTL operating temperature. Note that the corrosion rates were evaluated based on direct weight gain and weight loss measurements as described in the experimental section.	83
Fig. 4-10. Variation of average corrosion rate of P91 steel with HTL operating temperature. Note that the corrosion rates were assessed based on direct weight gain and weight loss measurements as described in the experimental section.	83
Fig. 4-11. Photographic images of SS310 and P91 steels (20 mm long × 10 mm wide × 2 mm thick) showing surface appearance before and after corrosion in 310 °C HTL water at different flow rates.	84
Fig. 4-12. Top and cross-sectional SEM images of SS310 and P91 after the exposure to 310 °C loop water at the flow rate of 1.1 m/s.	85
Fig. 4-13. Comparison of XRD spectra collected on P91 steel samples after the exposures to 310 °C at the flow rates of 0 and 1.1 m/s, respectively.	86
Fig. 4-14. Cross-sectional SEM image and corresponding EDS elemental mapping on P91 steel after the exposure to 310 °C water at the flow rate of 1.1 m/s.	86
Fig. 4-15. TEM cross-sectional images and corresponding EDS elemental mapping on SS310 after the exposure to 310 °C water with the flow rate of 1.1 m/s.	87
Fig. 4-16. XPS core level spectra collected on a SS310 sample after corroded in 1.1 m/s flowing water at 310 °C: (a) O 1s, (b) Fe 2p _{3/2} , and (c) Cr 2p _{3/2} region.	88
Fig. 4-17. Variation of the corrosion rates of SS310 steel with flow rate in HTL water at 310 °C.	89
Fig. 4-18. Variation of corrosion rates of P91 steel with flow rate in HTL water at 310 °C.	89

Fig. 4-19. Photographic images of SS310 and P91 steels (20 mm long × 10 mm wide × 2 mm thick) before and after the exposure to 310 °C hot water at the flow rate of 1.1 m/s and different HTL operating pressures.	90
Fig. 4-20. Top-view SEM images of SS310 and P91 after the exposure to 310 °C loop water at the flow rate of 1.1 m/s and 25 MPa.	91
Fig. 4-21. Cross-sectional SEM image and corresponding EDS elemental mapping on P91 steel after the exposure to 310 °C water at the flow rate of 1.1 m/s and 25 MPa.	91
Fig. 4-22. Comparison of XRD spectra collected on P91 steel samples after the exposures to 310 °C with flow rate of 1.1 m/s at different pressures.	92
Fig. 4-23. TEM Cross-sectional images and corresponding EDS elemental mapping on SS310 after the exposure to 25 MPa water at 310 °C.	93
Fig. 4-24. XPS core level spectra collected on a SS310 sample after corroded under 25 MPa in 1.1 m/s flowing water at 310 °C: (a) O 1s, (b) Fe 2p _{3/2} , and (c) Cr 2p _{3/2} region.	93
Fig. 4-25. Variation of the corrosion rates of SS310 with HTL operating pressure in 310 °C water with the flow rate of 1.1 m/s.	94
Fig. 4-26. Variation of the corrosion rates of P91 steel with HTL operating pressure in 310 °C water with the flow rate of 1.1 m/s.	94
Fig. 4-27. Schematic of ion distribution and contents near a steel surface under flowing conditions in this study.	100

Fig. 5-1. (a) Schematic of autoclave setup used in this study, and (b) A top-view of Alloy C-276 autoclave with an Alloy 625 liner and sample holder used for the designed tests.	109
Fig. 5-2. Photographic images of SS310 and P91 steels before and after the exposure to ultrapure water and 0.5 M K ₂ CO ₃ at 310 °C for 10 days, respectively.	113
Fig. 5-3. Top and cross-sectional SEM images of (a) P91 and (b) SS310 steels after the exposures to ultrapure water and 0.5 M K ₂ CO ₃ at 310 °C for 10 days, respectively.	115
Fig. 5-4. XRD spectra collected on P91 steel samples after the exposures to ultrapure water and 0.5 M K ₂ CO ₃ at 310 °C for 10 days, respectively.	116
Fig. 5-5. Cross-sectional Black-field (BF) and corresponding EDS elemental mapping images of SS310 after exposed to (a) ultrapure water; and (b) 0.5 M K ₂ CO ₃ at 310 °C for 10 days, respectively.	117
Fig. 5-6. BF image and corresponding selected area diffraction (SAD) patterns of cross-sectional SS310 samples after the exposure to 310 °C (a) ultrapure water and (b) 0.5 M K ₂ CO ₃ for 10 days.	119
Fig. 5-7. Estimated average corrosion rates of (a) SS310 and (b) P91 steel in ultrapure water and 0.5 M K ₂ CO ₃ at 310 °C for 10 days, respectively. Note that the corrosion rates presented here were assessed based on both direct mass change and weight loss measurements for comparison.	121
Fig. 5-8. Photographic images of SS310 and P91 steels before and after the exposures to 0.5 M K ₂ CO ₃ and 0.5 M K ₂ CO ₃ + 3,500 ppm Cl ⁻ + 2,500 ppm S ²⁻ at 310 °C, respectively.	122
Fig. 5-9. Top and cross-sectional SEM images of (a) P91 and (b) SS310 steels after corroded in 0.5 M K ₂ CO ₃ + 3,500 ppm Cl ⁻ + 2,500 ppm S ²⁻ at 310 °C for 10 days, respectively.	123

Fig. 5-10. XRD spectra collected on P91 steel samples after the exposures to 0.5 M K ₂ CO ₃ and 0.5 M K ₂ CO ₃ + 3,500 ppm Cl ⁻ + 2,500 ppm S ²⁻ at 310 °C for 10 days, respectively.....	124
Fig. 5-11. Black-field (BF) image and corresponding EDS elemental mapping images of SS310 after exposed to 0.5 M K ₂ CO ₃ + 3,500 ppm Cl ⁻ + 2,500 ppm S ²⁻ at 310 °C for 10 days.....	125
Fig. 5-12. Estimated average corrosion rates of (a) SS310 and (b) P91 steel in 0.5 M K ₂ CO ₃ and 0.5 M K ₂ CO ₃ + 3,500 ppm Cl ⁻ + 2,500 ppm S ²⁻ at 310 °C for 10 days, respectively.	126
Fig. 5-13. Photographic images of SS310 and P91 steels before and after the exposure to 0.5 M K ₂ CO ₃ + 3,500 ppm Cl ⁻ + 2,500 ppm S ²⁻ with and without the addition of acetic acid at 310 °C for 10 days, respectively.	127
Fig. 5-14. Top and cross-sectional SEM images of (a) P91 and (b) SS310 steels after corroded in 0.5 M K ₂ CO ₃ + 3,500 ppm Cl ⁻ + 2,500 ppm S ²⁻ containing 5 wt.% and 10 wt.% acetic acid at 310 °C for 10 days, respectively.	129
Fig. 5-15. XRD spectrum collected on P91 steel after the exposures to 0.5 M K ₂ CO ₃ + 3500 ppm Cl ⁻ + 2500 ppm S ²⁻ with and without 10 wt.% acetic acid at 310 °C for 10 days.	130
Fig. 5-16. HAADF and BF images with corresponding EDS elemental mapping images of SS310 after exposed to 0.5 M K ₂ CO ₃ + 3,500 ppm Cl ⁻ + 2,500 ppm S ²⁻ + 10 wt.% acetic acid at 310 °C for 10 days.....	131
Fig. 5-17. Estimated average corrosion rates of (a) SS310 and (b) P91 steels in 0.5 M K ₂ CO ₃ + 3,500 ppm Cl ⁻ + 2,500 ppm S ²⁻ with and without acetic acid at 310 °C for 10 days, respectively.	132
Fig. 5-18. Constructed Pourbaix diagram of Fe-H ₂ O system at 310 °C. Note that the diagram is also applicable for the 0.5 M K ₂ CO ₃ solution with inorganic/organic corrodants.....	137
Fig. 5-19. Constructed Pourbaix diagram of Cr-H ₂ O system at 310 °C. Note that the diagram is also applicable for the 0.5 M K ₂ CO ₃ solution with inorganic/organic corrodants.....	137

Fig. 6-1. (a) Schematic of the static autoclave setup used in this study; (b) Top-view photograph of the Alloy C-276 autoclave with an Alloy 625 liner, testing samples and sample holder.....	150
Fig. 6-2. Established Pourbaix diagrams of major alloying elements and H ₂ O system at the temperature range of 250 - 365 °C.....	155
Fig. 6-3. Photographic images of five candidate alloys before and after the exposures to three HTL conversion environments at 310 °C for 10 days, respectively.	156
Fig. 6-4. Comparison of the average corrosion rates of Fe-based steels and Ni-based alloys with different alloying element contents in non-catalytic and catalytic HTL environments at 310 °C.	161
Fig. 6-5. SEM top-views of (a) P91, (b) SS16L and (c) SS16 samples after corroded in non-catalytic and catalytic HTL environments 310 °C.....	163
Fig. 6-6. XRD spectra collected on P91 samples after corroded in non-catalytic and catalytic HTL environments at 310 °C, respectively.	164
Fig. 6-7. SEM cross-sectional images and corresponding EDS elemental mappings of P91 samples after corroded in different HTL environments at 310 °C.	166
Fig. 6-8. TEM Black-field (BF) and HAADF images with corresponding EDS elemental mapping collected on SS316L and SS310 samples after the exposures to (a) ultrapure water; (b)	

0.5 M K ₂ CO ₃ ; and (c) 0.5 M K ₂ CO ₃ + 3500 ppm Cl ⁻ + 2500 ppm S ²⁻ + 5 wt.% acetic acid at 310 °C for 10 days, respectively.	169
Fig. 6-9. SEM top-view images of Alloy C-276 after corroded in ultrapure water, 0.5 M K ₂ CO ₃ , and 0.5 M K ₂ CO ₃ + 3500 ppm Cl ⁻ + 2500 ppm S ²⁻ + 5 wt.% acetic acid at 310 °C for 10 days, respectively.	172
Fig. 6-10. Black-field (BF) images and corresponding EDS elemental mapping on Alloy C-276 after exposed in (a) ultrapure water; (b) 0.5 M K ₂ CO ₃ ; and (c) 0.5 M K ₂ CO ₃ + 3500 ppm Cl ⁻ + 2500 ppm S ²⁻ + 5 wt.% acetic acid at 310 °C for 10 days, respectively.	173
Fig. 6-11. SEM top-view images of Alloy 625 after corroded in ultrapure water, 0.5 M K ₂ CO ₃ , and 0.5 M K ₂ CO ₃ + 3500 ppm Cl ⁻ + 2500 ppm S ²⁻ + 5 wt.% acetic acid at 310 °C for 10 days, respectively.	176
Fig. 6-12. Black-field (BF) and HADDF images with corresponding EDS elemental mappings on Alloy 625 after exposed in (a) ultrapure water; (b) 0.5 M K ₂ CO ₃ ; and (c) 0.5 M K ₂ CO ₃ + 3500 ppm Cl ⁻ + 2500 ppm S ²⁻ + 5 wt.% acetic acid at 310 °C for 10 days, respectively.	177
Fig. 6-13. BF image of Alloy 625 exposed in 0.5 M K ₂ CO ₃ solution and selected area diffraction (SAD) obtained from different oxide layers.	178
Fig. 7-1. Schematic of the dimensions of cylindrical tensile specimens used in this study (units in mm).	184
Fig. 7-2. Schematic of a custom-made loading frame used in this study.	185
Fig. 7-3. A photographic image of loading stressing frame and testing specimens before accommodated into a static autoclave.	185
Fig. 7-4. A photographic image showing how to in-situ measure the applied strain level of a tensile specimen with application of an optical extensometer.	187
Fig. 7-5. The dimensions of a U-bending sample used in this study.	187
Fig. 7-6. Schematic of (a) loading process and (b) the photographic images of U-bending samples.	188
Fig. 7-7. Optical images of the microstructures of SS310 and SS316L steels used in this study.	190
Fig. 7-8. Normalized Stress-strain curves of SS310 at different temperatures.	191
Fig. 7-9. Normalized Stress-strain curves of SS316L at different temperatures.	192
Fig. 7-10. Photographic images of U-bending and uniaxial tensile specimens after tested in 0.5 M K ₂ CO ₃ + 3500 ppm Cl ⁻ + 2500 ppm S ²⁻ + 10 wt.% acetic acid at 365 °C.	193
Fig. 7-11. SEM top-view images of SS316L after the exposure to 0.5 M K ₂ CO ₃ + 3500 ppm Cl ⁻ + 2500 ppm S ²⁻ + 10 wt.% acetic acid under different strain loading levels at 365 °C.	194
Fig. 7-12. SEM top-view images of SS310 after the exposure to 0.5 M K ₂ CO ₃ + 3500 ppm Cl ⁻ + 2500 ppm S ²⁻ + 10 wt.% acetic acid under different strain loading levels at 365 °C.	195
Fig. 7-13. Cross-sectional SEM images of SS316L samples after the autoclave exposure.	196
Fig. 7-14. Cross-sectional SEM images of SS310 samples after the autoclave exposure.	196

List of Symbols

ΔE	Activation energy
a	Activity
A	Area
A'	Arrhenius constant
d	Density of alloy
D	Diffusion coefficient
Δm	Direct mass change
E_T	Electrochemical potential at temperature T
S_T^θ	Entropy
F	Faraday constant
R	Gas constant
ΔG_T^θ	Gibbs free energy
C_p	Heat capacity
η	Molar mass ratio
n	Number of electrons
E_T^θ	Standard electrochemical potential
ε	Strain level
T	Temperature
t	Time

List of Abbreviations

BF	Bright field
CHTL	Catalytic hydrothermal liquefaction
DSS	Duplex stainless steel
EDS	Energy-dispersive X-ray spectroscopy
EDTA	Ethylenediaminetetraacetic acid
FIB	Focused ion beam
GHG	Greenhouse gas
HAADF	High-angle annular dark-field
HMF	Hydroxymethylfurfural
HTL	Hydrothermal liquefaction
IGSCC	Intergranular stress corrosion cracking
PTFE	Polytetrafluoroethylene
SAD	Selected area diffraction
SCC	Stress corrosion cracking
SCWG	Supercritical water gasification
SEM	Scanning electron microscopy
SS	Stainless steel
TEM	Transmission electron microscopy
XPS	X-ray photoelectron spectroscopy
XRD	X-ray diffraction

Chapter 1. Introduction

1.1 Overview of biomass resources

Due to serious concerns over the rapid growth in global population and greenhouse gas (GHG) emissions, there is a continuously increasing interest in substituting non-renewable fossil fuels with renewable and sustainable alternatives for energy and chemicals production [1]. Considerable investments and efforts have been spent on transforming current energy plants to a more environmental and ecological-friendly system. Renewable energy sources, such as forest and agricultural biomass materials, animal manures, and engineered microalgae, are abundant in nature and much more environmentally safe than fossil fuel resources, and hold the key potential to partially and even completely replace fossil fuel-based energy resources for future clean energy production [2-7]. Up to date, there are three generations of biofuels, defined on the basis of their sources of raw biomass and harvesting procedures. The first generation of biofuels includes ethanol and biodiesel, which are made from food sources, such as sugarcane, barley, and corn. Their major drawback is that the application of edible biomass feedstocks inevitably introduces negative impact on biodiversity and competition for foods. Therefore, the feasibility of first generation biofuels is quite debatable, and intensive efforts have been applied for utilizing non-food materials as the feedstocks. The second generation of biofuels is usually converted from wood, organic waste, food waste and specific biomass crops, which are constantly replenished in nature. The obvious advantages are: (1) some of the biowaste feedstocks do not need to be cultivated; and (2) the wood and crops have shorter harvest timelines compared to the biomass used for the first generation. However, it is still arguable as a less cost-efficient process since the second generation of biomass requires a chain of pre-treatment processes to recover the fermentable sugar before subsequent biorefining processes. Due to the limitations of the first and second generations, a different source of biofuel feedstock, named microalgae, has been explored in recent years. Microalgae biomass has high growth rates and can contribute to a considerable amount of global CO₂ reduction from the atmosphere [8]. Moreover, microalgae can produce many available biomolecules, such as vitamins, carbohydrates, lipids, and proteins. Although some studies stated that the biofuel generated from microalgae is less stable and its conversion requires higher energy input compared to the first and second generations, it seems that the advantages of microalgae still surpass the drawbacks, and it thus becomes one of the most cost-efficient and environmental-friendly biomass feedstocks. According to my comprehensive literature review, the second and

third generation of biomass feedstocks are widely used in the biorefining industry to meet our daily energy demands.

1.2. Biomass conversion technologies studied in this thesis

1.2.1. Overview of biomass conversion technologies

Biorefining technology involves the integrated processing of these renewable feedstocks to marketable biofuels, biochemicals and biomaterials [9-13]. In order to achieve optimum conversion efficiency, a number of studies have been conducted to develop different types of conversion methods, including biochemical (such as anaerobic digestion and fermentation) and thermochemical (including hydrothermal liquefaction, gasification, pyrolysis, torrefaction and combustion) technologies. Among them, fermentation and anaerobic digestion are usually employed in the environments with moisture content of 40 - 90 % and pH range of 3 - 8 at temperature < 60 °C [14, 15]. Bioethanol is the main product generated by these biochemical processes. Compared to the slow biochemical conversion methods, thermochemical biorefining can convert raw biomass streams to desired bioproducts in a much quicker and more efficient way. According to their application capacity, hydrothermal liquefaction, gasification, and pyrolysis are seen as the most promising technologies that have attracted particular attention [16-19]. Pyrolysis conversion is an oxygen-deprived thermochemical decomposition process at elevated temperatures [20]. Depending on conversion conditions, pyrolysis processes can be classified into three categories: slow pyrolysis (slow heating rates for a long time, temperatures < 300 °C), moderate pyrolysis (temperatures between 300 to 500°C) and fast pyrolysis (temperatures > 500 °C for a short duration) [19, 21, 22]. To obtain the maximum yield of bio-oil as the desired product, moderate temperature, short gas residence time and high heating rates are usually recommended at industrial plants. Up to date, pyrolysis is the only industrially realized technology for the conversion of biomass into crude bio-oils [23, 24]. Gasification is another promising technology for the conversion of biomass to gaseous products (mostly H₂ and CO) using gasifying agents of air/oxygen, steam, supercritical water, or flue gases at the temperature range of 500 - 1400 °C [25-29]. The choice of the type of gasifying agent is coherently determined by the properties of desired product gas [30]. Similar to pyrolysis conversion, the gasification involves a costive pretreatment process to dry the feedstock down to a moisture content of < 10 - 20% before

being fed into an air, oxygen, or steam gasifier. Compared to these, supercritical water gasification (SCWG) is a relatively new technology that can produce hydrogen-enriched gaseous products directly from wet biomass [29, 31]. According to literature reviews, gasification technology has been successfully applied at industrial scale, and more than 100 gasification plants/projects are either operated or under development around the world.

1.2.2. Two innovative biorefining reactors investigated in this study

Based on the demands of Canadian bioenergy industry, this study focuses on the materials performance under the following two specific biorefining conditions: hot dilute acidic pre-hydrolysis and hydrothermal liquefaction.

1.2.2.1. Hot dilute acidic pre-hydrolysis technology

Many obstacles are involved in the hydrolysis conversion of lignocellulosic biomass to reach optimal performance with acceptable costs, mainly due to the recalcitrance of biomass. The native properties of lignocellulosic biomass feedstock introduce challenges to the efficiency of pre-hydrolysis because of their rigid internal structure, high degree of polymerization and low assessable surface area of hemicellulose/cellulose, and strong fiber strength within the biomass structure [32-34]. It is thus required to overcome the biomass recalcitrance, i.e., to disrupt the biomass structure and make the cellulose/hemicellulose accessible to the enzymes in the subsequent hydrolysis processes. Pre-hydrolysis technology has thus been developed with the application of different catalysts and solutions for the direct conversion of biomass feedstocks to fermentable sugars and other enzymatic intermediates for further treatment [4, 34-42]. Based on the pH value of the solution used, the pre-hydrolysis method can be classified as an acidic, neutral or alkaline pre-hydrolysis process. Although no pretreatment method is able to achieve a 100% conversion of biomass into fermentable sugars, the addition of hot dilute sulfuric acid has been demonstrated to be the most efficient and economical method for attacking the lignocellulosic structure [43-51]. Pioneer studies have shown that more than 75% of cellulose and hemicellulose in raw lignocellulose feedstocks can be transformed into fermentable sugars at elevated temperatures [48, 52-58]. Fig. 1-1 schematically presents the proposed hot dilute acidic pre-hydrolysis biorefining process. The optimum acidic pre-hydrolysis operating conditions have not yet been well defined even though considerable efforts have been devoted. However, it is generally

accepted that dilute sulfuric acid (0.05 - 0.1 M) can serve as an effective medium to achieve a desired conversion efficiency at the temperature range of 90 - 200 °C [43,-47, 49, 51, 59-63]. Despite the promising application potential of the hot dilute sulfuric acid biorefining, materials technology barriers remarkably retard the deployment of this technology in the forest sector. One of the most difficult challenges is the corrosion of reactor because of the use of dilute sulfuric acid at elevated temperatures. Detailed background information is provided in the next section. Moreover, the hydrolysates obtained for the hot acidic pretreatment may contain unwanted by-products, such as acetic acid (generated from the acetyl groups linked to the hemicellulose structure), furfural and hydroxymethylfurfural (5-HMF) [64]. These organic products are aggressive to reactor alloys and toxic to microorganisms. Their concentrations in the hydrolysate need to be well controlled to facilitate the fermentation process and minimize the corrosion attack to the reactor [65]. Furthermore, other by-products (such as furfural) are known to be lethal to human beings, i.e., only 65 mg/kg median lethal dose [66]. The toxicity and carcinogenicity of 5-HMF is also known and have been validated through in vitro tests [67, 68].

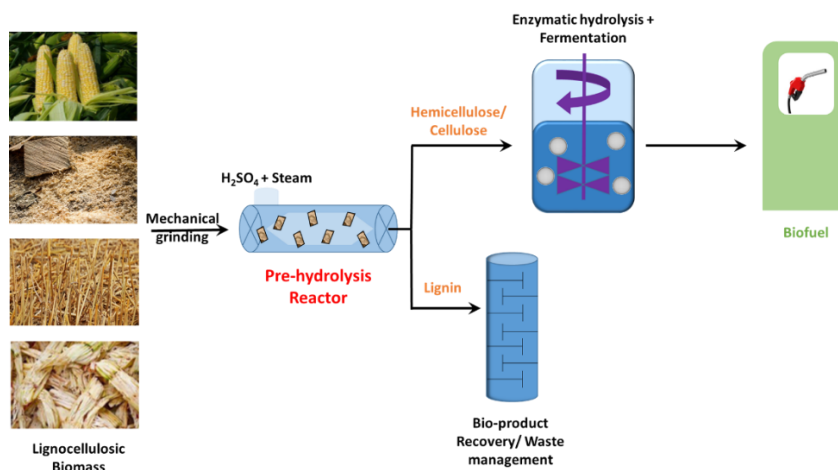


Fig. 1-1. Schematic of hot dilute acidic pre-hydrolysis treatment of lignocellulosic feedstocks at mill plants.

1.2.2.2. Hydrothermal liquefaction technology

The primary chemical components of lignocellulosic biomass, agricultural residuals and forestry wastes are cellulose, hemicellulose, and lignin, as well as considerable amounts of moisture. As mentioned above, a costly dewatering and drying treatment is needed prior to the utilization of

these feedstocks for the pyrolysis and gasification conversion. The limitation of these thermochemical technologies and high moisture content in biowastes and third generation feedstocks have promoted the development of an advanced biorefining technology named as hydrothermal liquefaction (HTL). As schematically shown in Fig. 1-2, HTL is also a thermochemical process in which hot pressurized water is used as a reaction medium to convert various wet biomass streams, particularly microalgae and bio-wastes streams, to valuable bio-oils and biochemicals. Compared with other thermochemical technologies, HTL has three major advantages: (1) it can operate without costly pre-drying and/or mechanical grinding; (2) the process is versatile and environmentally friendly because of the use of pressurized water as the reaction medium; and (3) the produced bio-crude oils have better quality (such as lower oxygen, less corrosivity and higher heating value) compared to pyrolysis oils [69-72]. Note that HTL is a quite complicated process involving a series of complicated reactions (such as hydrolysis, depolymerization, dehydrogenation, deoxygenation, cracking/fragmentation, water-reforming, and gasification) to produce bio-oil along with water-soluble products (WSP), biochar, and non-condensable gases.

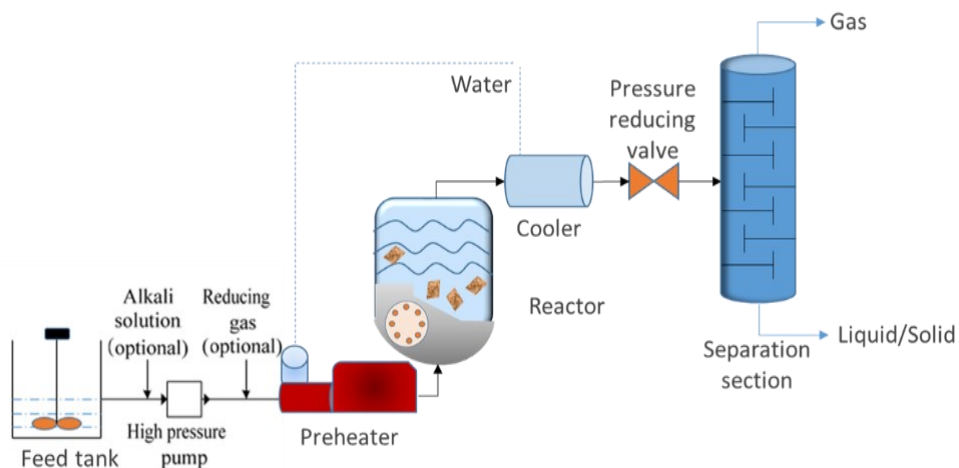


Fig. 1-2. Schematic of hydrothermal liquefaction (HTL) of wet biomass/biowaste feedstocks using pressurized subcritical water.

Hydrothermal liquefaction of biomass has been widely investigated in batch or continuous modes. Several operating parameters, including temperature, pressure, retention time, the addition of

catalysts, and water-to-biomass ratio are recognized as the key factors that control the yields and characteristics of HTL products. In a typical HTL process, subcritical water is used as the primary reactant to transform wet biomass or biowaste feedstocks into crude bio-oils in the temperature range of 250 - 370 °C and pressure from saturated vapor pressure to 25 MPa [73-77]. Increasing the temperature can result in enhanced conversion efficiency and bio-oil yields. However, above a critical temperature, further increase in temperature leads to a decrease in the oil yields accompanied by a higher yield of solid residues (i.e., biochar) due to the condensation and re-polymerization of the reaction intermediates. A similar trend is observed for the effect of retention time on the bio-oil yield, which can be attributed to the competitive reactions of hydrolytic degradation and condensation/re-polymerization for an extended length of reaction time. Increasing pressure can enhance the solubility of organic compounds in biomass feedstocks and consequently increase the carbon conversion efficiency.

Except for temperature, pressure and residence time, the introduction of catalyst in the HTL of biomass can significantly enhance the liquefaction efficiency and consequently improve bio-oil yield and quality. Different types of homogeneous and heterogeneous catalysts have been evaluated under hydrothermal liquefaction processes, and it has been found that alkali catalysts (such as K_2CO_3 , Na_2CO_3 , NaOH, K_2CO_3 , KOH and LiOH) can effectively increase the bio-oil yields [76-89]. Among them, it is generally accepted that the addition of 0.5 - 1.0 M K_2CO_3 can result in the highest conversion efficiency in HTL processes [90-94]. For example, previous studies found that the yield of bio-oil after the introduction of 0.5 M K_2CO_3 would be increased by up to about 3 times higher than that without the addition of catalysts [79, 93- 95].

The HTL conversion efficiency is also coherently related to the operation mode applied. Most laboratory and pilot-scale HTL studies are performed in batch-mode reactors, while continuous flow operations are more desirable for industrial-scale applications of HTL to promote the energy utilization efficiency and improve the economic feasibility of the process [83, 96]. One of challenges to use a continuous flow reactor is the limitation on biomass particles size and solid concentration of the feedstock to enable continuous pumping and avoid possible clogging problems for the pump and conversion reactor.

Although HTL technology is conceptually simple and economically favorable in comparison with other existing thermochemical methods, industrial-scale HTL plants are still unavailable

worldwide because of economic concerns and technical impediments, such as relatively high capital investment, ultra-high pressure pumps, and the lack of applicable materials technology solutions for the cost-effective construction and long-term safe operation of HTL reactors. As described above, the reactor alloys are exposed to hot pressurized aqueous environments with the presence of catalysts, inorganic and organic corrodants (such as Cl^- , S^{2-} and organic acids) released during the conversion.

1.3. Materials knowledge gaps in the construction of two biorefining reactors

To meet urgent industrial needs, this study intends to address corrosion and materials technology challenges under the above two specific biorefining conditions, and partially support the development of innovative cost-effective materials technology solutions for the commercialization of the biorefining technologies in international and Canadian forest sectors. As described above, the conversion reactors at hot dilute acidic pre-hydrolysis and HTL plants are required to be operated in harsh environments, thus facing the challenges of selecting suitable constructional alloys for cost-effective construction and long-term safe operation. According to my comprehensive literature review, very limited information is available to describe the corrosion performance of commercial Fe-based steels and Ni-alloys in these two specific biorefining processes. In fact, this study is the first one ever to address the corrosion challenges in the catalytic HTL conversion processes.

1.3.1. Corrosion challenges under hot dilute sulfuric acidic pre-hydrolysis biorefining processes

Numerous studies have been conducted to assess the corrosion performance in sulfuric acid solutions at ambient temperatures [97-100]. Corrosion processes in these environments are governed by electrochemical reactions, especially in dilute sulfuric acid. Depending on temperature and its concentration, sulfuric acid can interact with steels and alloys to form oxides/sulfates, accompanied by the cathodic reduction of protons. For example, austenitic stainless steels (SS304, SS316, etc.) experienced passivity in H_2SO_4 above 93% concentration, but will suffer active-passive transition at temperature above 40 °C [101]. A similar trend has also

been observed when decreasing the acid concentration (< 2.5 M), where it will gradually change to a more reducing environment, making the formed surface scales much less protective to metals. For the hot dilute acidic pre-hydrolysis biorefining in the temperature range of 100 - 200 °C, corrosion database and knowledge of commonly used stainless steels and alloys are really scarce. Previous studies investigated the corrosion of Fe-based steels and Ni-based alloys in dilute sulfuric acids only at temperature < 100 °C, and found that austenitic stainless steels exhibited high corrosion rates up to 5 mm/year [98-100, 102], while NiCrMo alloys, such as Alloy 825 and Alloy C-276, showed much lower corrosion rates (< 0.5 mm/year). With an increase in temperature up to 200 °C, the second dissociation constant of sulfuric acid will be remarkably increased, thus making the acid more aggressive to these alloys [103, 104]. Unfortunately, very few efforts have been made to investigate the corrosion performance of NiCrMo alloys in dilute sulfuric acids in the temperature range of 100 - 200 °C. Moreover, inorganic and organic matter will be released from biomass during the conversion, leading to a further concern in the corrosion performance of constructional steels and alloys. Chloride and sulfide ions are the most common inorganic corrodants present in lignocellulosic biomass with concentration between 200 and 3,000 ppm, and between 75 and 2,500 ppm, respectively [105-107]. Mixed effects regarding the corrosivity of dilute acids with these notorious pit-initiating anions at elevated temperatures will further complicate the screening of construction materials [102, 108]. Furthermore, organic compounds (such as polysaccharides, furfural, acetic acid, etc.) generated during the conversion can affect the corrosion processes as well [109-112], where acetic acid will be up to 10-19 wt.% in liquid phase depending on the types of biomass feedstocks used [113, 114]. Previous studies indicated that the presence of acetic acid and Cl^- anions at 180 °C would remarkably damage the integrity of surface oxide scale formed on 13Cr steels [115]. Under the pre-hydrolysis condition, the influence of organic corrodants released from the conversion still remains as a puzzle since no study has been conducted in this field.

Except for the impacts of environmental parameters, the roles of major alloying elements (especially Mo and Cr) in commercial steels and alloys on corrosion in the hot dilute acidic solution are also required to be clarified. Alloying elements Fe and Ni are unlikely to support the formation of protective surface scales on the alloys in such aggressive environments since Fe and Ni oxides are much less stable when comparing to Cr and Mo oxides based on thermodynamic predictions

at elevated temperatures. A recent study revealed that surface Cr oxide layers could not protect Cr-bearing steels from condensed acidic phase (pH = 2) at temperature > 100 °C [108]. About the effect of Mo, considerable studies have also been conducted at temperatures < 100 °C [116-120]. It has generally been concluded that increasing Mo content in an alloy would improve its resistance to acidic solutions. However, the role of Mo in acidic corrosion is still far from clear [121, 122]. For instance, Sugimoto et al. proposed that increasing Mo content might lead to the formation of a better protective oxide film since Mo⁶⁺ cations could be dissolved in Cr oxyhydroxide network [123], while other groups showed that the addition of Mo could facilitate the formation of MoO(OH)₂ or MoO₄²⁻ at some weak location to suppress localized active dissolution [124-126].

In general, little information is available to determine the corrosion modes and extents of candidate construction alloys in hot dilute sulfuric acid pre-hydrolysis environments, making the selection of suitable alloys of construction difficult.

1.3.2. Corrosion challenge under HTL conversion processes

As mentioned above, subcritical water at temperature close to supercritical point (373.9 °C) and pressure up to 25 MPa is used for the HTL conversion of wet biomass and biowastes because of its unique dissociation constant, density and dielectric constant, as indicated in Fig. 1-3. The distinct difference in dielectric constant at 250 - 370 °C can lead to a remarkable change in the chemical dissolution of oxide layers formed on HTL reactor alloys [127-129], causing the concern of the effect of temperature on corrosion. Most previous studies have focused on the influence of temperature on corrosion of stainless steels and Ni-based alloys at temperature ≤ 315 °C or > 500 °C [130-138]. Some reported results are even controversial, and very limited research investigated the alloy performance at the temperature range of 315-370 °C [139-141], which is the typical temperature range for the HTL conversion. Moreover, very limited information is available to identify the influence of pressure and flow rate on corrosion. In fact, increasing pressure can enhance the conversion efficiency of biomass [142], but may also result in an increase in water conductivity and dissociation constant to enhance the chemical dissolution of surface oxide scales formed on Fe-based steels and Ni-based alloys [143-145]. Furthermore, the flow rate at continuous pilot HTL plants is about 0.5 - 2.0 m/s to achieve the homogeneity of the feeding slurry and

mitigate clogging in high-pressure pumps and conversion reactors [91, 146-150]. This leads to another concern of flow-accelerated corrosion (FAC) in the selection of suitable constructional alloys, especially for low-alloyed steels (such as carbon steels and ferrite/martensite steels) [151]. According to the literature review, very few works have been performed to identify the impact of FAC on corrosion in pressurized subcritical water in the temperature range of 250 - 370 °C.

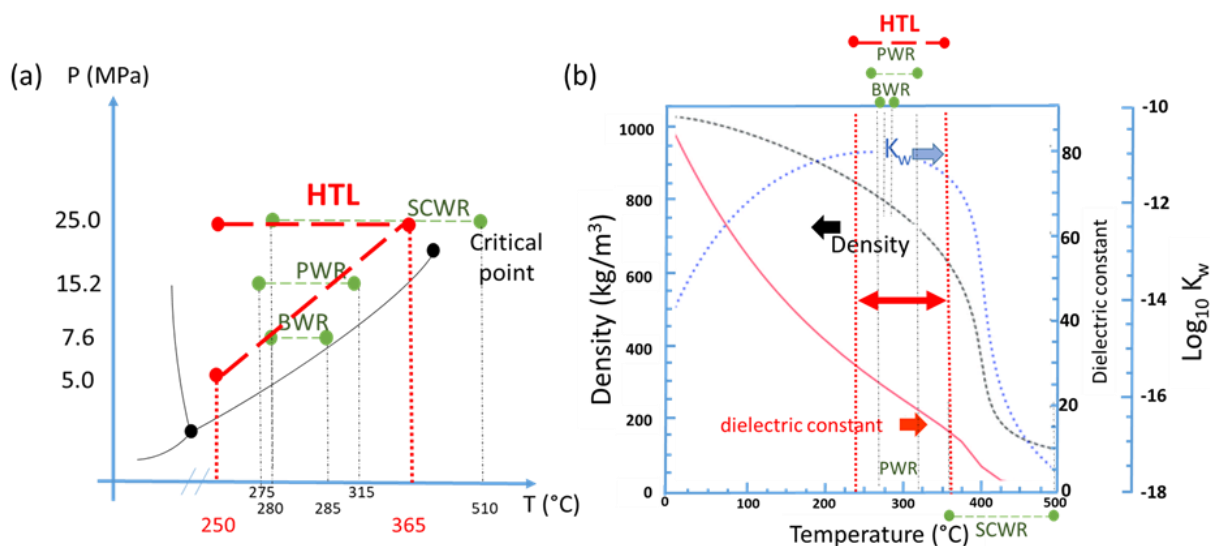


Fig. 1-3. (a) Comparison of the operating temperature and pressure ranges of water used in HTL reactors with those in nuclear reactors; (b) The properties of subcritical water applied in a typical HTL reactor. Note that the above figures were drawn based on the information provided in references [127, 152-154]. Fig. 1-3 (b) was reproduced with permission from [154].

During the HTL conversion, the HTL reactor alloys also suffer the attack from the catalysts, the inorganic and organic corrodants released from biomass feedstocks (such as Cl^- , S^{2-} and organic acids). These unique operating characteristics make previous corrosion knowledge and experience accumulated at high temperature nuclear and chemical plants inapplicable for constructing HTL reactors [127, 152, 153]. The application of homogenous alkali catalysts can significantly increase the pH value of HTL conversion environments. Former studies found that increasing pH value from 7 to 13 in aqueous solutions at temperature > 100 °C resulted in a noticeable increase in the dissolution of surface oxide scales formed on austenitic stainless steels, since the protective metal oxides would be transformed into the hydroxides with higher solubility [52, 155-158].

Meanwhile, inorganic (particularly Cl^- and S^{2-}) and organic corrodants (such as organic acids and other by-products) shall be generated during the HTL conversion of wet feedstocks, especially biowastes (such as black liquor), possibly accelerating the corrosion of reactor alloys and even introducing unwanted structural damage after short-term service [159-164]. Several studies have shown that both Cl^- and S^{2-} are notorious agents to facilitate pitting and enhance the stress corrosion cracking risk of Fe-based steels and Ni-based alloys in high temperature aqueous solutions [165-170]. The presence of organic acids (such as formic, acetic and butyric acids) in hot water may accelerate the chemical dissolution of oxide scales formed on stainless steels at temperatures > 120 °C [91, 171-174].

Except for the above operating parameters, the influence of alloying elements on corrosion is also a critical issue in the cost-effective selection of suitable alloys for the construction and development of novel alloys for bioenergy industry. Due to the complicated nature of HTL environments, it is still unclear which alloying element could contribute to the formation of protective scales on Fe-based steels and Ni-based alloys. For instance, the chemical dissolution of Fe, Cr, Ni and Mo oxides and other compounds is coherently related to the environmental pH and temperature [175]. Very limited studies have been conducted to identify their performance in high temperature aqueous solutions at pH 7-13 and temperature range from 320 to 370 °C. Moreover, as stated above, capacity investment is a key economic factor affecting the deployment of HTL technology at industrial scale. As indicated in Table 1-1, the application of Ni-based alloys will result in a noticeably higher cost of construction when comparing to that of stainless steels.

Table 1-1. Relative cost ratio of different types of steels and alloys obtained from suppliers.

Types	Relative Cost Ratio based on the assumption of the cost of SS304L = 1.0
SS310	2.75
SS316L	1.25
Alloy C-276	5.75
Alloy 625	7.40

Besides the general corrosion, stress corrosion cracking (SCC) is also a critical concern in the selection of suitable steels and alloys of construction. As mentioned above, the HTL conversion

can occur at pressure up to 25 MPa, which inevitably introduces high stress applied to the reactor wall [176, 177]. The presence of aggressive catalyst, Cl^- , S^{2-} , and organic acids may enhance the SCC risks. In fact, several studies have shown that the SCC of austenitic stainless steels (such as SS304, SS310, and SS316L) could occur in aqueous solution with chloride content > 150 ppm under the loading close to their yield strengths at temperature > 70 °C [178-183]. Moreover, in basic solutions, the presence of sulfides possibly results in higher SCC susceptibility of austenitic stainless steels at elevated temperatures [184, 185]. For nickel-based alloys, intergranular cracking may occur in aqueous solutions with the presence of Cl^- at temperature close to the supercritical water point (373.9 °C) [186-189]. Unfortunately, most of the available information is insufficient to determine whether candidate constructional alloys would experience SCC cracking under the HTL conditions.

1.4. Candidate alloys for the construction of pre-hydrolysis and HTL reactors

To address corrosion and materials knowledge gaps on the construction of hot dilute acidic pre-hydrolysis and HTL reactors, it is necessary to appropriately pre-select candidates for intensive corrosion assessments based on public database. There are different types of commercial alloys which have been successfully applied in various industries. A general overview of the alloy types, compositions, mechanical behaviors, and corrosion performance of Fe-based, Ni-based, titanium, and zirconium alloys has been made to provide profound background information on the pre-selection of alloys in this study:

Stainless steels

Stainless steels are iron-based alloys that contain a minimum of 12% Cr to prevent the formation of rust and achieve their stainless characteristics through the formation of an adherent and compact Cr-enriched oxide film in unpolluted atmospheres. The steels have acceptable corrosion resistance and good mechanical properties in harsh environments, as well as decent weldability for construction of chemical, nuclear and thermal power reactors. Other alloying elements (such as Ni, Mn, Mo, and Si) are added to achieve particular characteristics for industrial applications. For example, the addition of Mn would increase toughness, strength and hardenability [190]. Compared with high Cr-bearing austenitic stainless steels, duplex stainless steels have improved

corrosion resistance to localized corrosion and mechanical properties at temperature < 400 °C, which can be attributed to their unique dual-phase austenite and ferrite matrix [191]. For instance, duplex stainless steel type 2205 exhibited promising performance in acidic environments at oil and refining industries, and is a more cost-effective candidate when comparing with Cr-bearing austenitic stainless steels [192, 193].

For hot dilute acidic pre-hydrolysis biorefining, the reactor of a pilot-scale plant was constructed with SS316 based on the literature review [194]. However, corrosion performance of the reactor has not yet been released to the public. Moreover, austenitic stainless steels have been widely used in paper and pulp plants in which hot acids with pH of 1.5 - 2 are applied at 125 - 145 °C [195]. Furthermore, the reported results about the corrosion performance of austenitic stainless steels in hot acidic environments are controversial [196-199]. For instance, continuous digesters at sulfite pulp mills are still made of SS316L even though austenitic stainless steels generally exhibit unacceptable high corrosion rates in hot acidic conditions. In addition, duplex stainless steels have been employed in the biorefining industry. For example, DSS2101, 2205 and 2507 are applied for the harsh biomass conversion environments during biodiesel production [200].

For advanced HTL technology, the knowledge and experience accumulated in high temperature aqueous systems, such as light-water nuclear reactors (LWR) at temperature < 320 °C and supercritical water nuclear reactors at temperature > 500 °C indicate that several austenitic stainless steels (such as SS316L, SS310 and SS347) may be suitable candidates for subsequent study [133-138]. As described above, little information is available to identify the corrosion performance of these steels in complicated HTL environments that contain not only hot pressurized water, but also catalyst, inorganic and organic corrodants [52, 155-158, 165-170].

Ferritic/Martensitic Steels

Ferritic martensitic (F/M) steels have Cr content between 9 and 12 wt.% in the substrate and exhibit suitable creep and oxidation resistance and low susceptibility to stress corrosion cracking (SCC) in high temperature environments [201, 202]. In this family, P91 is a well-known low-alloyed steel and widely used for the fabrication of boiler tubes at temperature up to 620 °C because of its high resistance to stress corrosion cracking and excellent thermal properties, such as high resistance to thermal fatigue and high thermal conductivity [203, 204]. Given its low cost and promising high

temperature performance, P91 is therefore selected in this study to determine whether it is applicable to the construction of HTL reactors.

Nickel-based alloys

Ni can easily alloy with most of the metal elements, such as Cr, Fe, Mo and Cu. The addition of nickel to other metals can alter the properties of the resulting alloys with desired characteristics such as improved corrosion or oxidation resistance, increased high-temperature creep performance, and lower thermal expansion coefficients. Depending on heat treatment processes, a two-phase equilibrium microstructure is usually generated in Ni-based alloys, consisting of gamma (γ) and gamma-prime (γ') which is largely responsible for high temperature mechanical properties of the alloys [205]. Besides Fe-based stainless steels, Ni-based alloys are also utilized in weak acidic environment at temperature < 100 °C [122, 156, 199, 206-208]. Several studies have indicated that Ni-based alloys generally exhibit better corrosion resistance than austenitic stainless steels in the weak acid solutions [98-100, 116-120, 209, 210]. For instance, the corrosion rate of Alloy C-276 was found to be less than 0.5 mm/year in 1 M H₂SO₄ at temperature < 100 °C. Thus, Alloy C-276 is chosen as a representative in this study to identify the corrosion performance of Ni-based alloys and explore the role of alloying element Mo in corrosion under hot dilute pre-hydrolysis biorefining condition.

Under HTL conversion conditions, Ni-based alloys should also be promising candidates alloys due to the decent performance in high temperature environments with Cl⁻ and S²⁻ [211-213]. Alloy C-276 with 16 wt.% Mo is one of the most well-established alloys with many successful application cases in high temperature environments [214, 215]. For example, the alloy only experienced a very small weight change when exposed to supercritical water containing 0.5 M NaOH at 400 °C and 25 MPa for 50 hours [215]. Alloy 625 is another well-recognized high-temperature alloy used in harsh environments [216-220]. For instance, it only exhibited minimal corrosion rate of 4.4 um/year when exposed to supercritical water at 527.5 °C up to 200 hours [220]. Therefore, the corrosion behaviors of the two alloys were examined in this study under representative HTL conversion conditions.

Titanium alloys

Titanium alloys are classified into different classes, including alpha/near alpha titanium alloy, characterized by the use of alpha stabilizers (such as aluminum or oxygen), alpha and beta titanium alloy, and beta/near beta titanium alloy, characterized by the use of beta-stage stabilizers [221]. Titanium alloys are commonly used in extractive metallurgy environments where they are the primary materials of choice for use in autoclave liners and internal components during high-pressure acid leaching (HPAL) of nickel laterite ores at 250 °C and 5 MPa with sulfuric acid concentration of 30 -100 g/L [222]. Because of their high cost, however, they are not considered for constructing industrial-scale hot dilute pre-hydrolysis biorefining reactors in this study.

Zirconium alloys

Nuclear grade zirconium alloys are widely utilized for the fabrication of nuclear reactor core at existing nuclear power plants due to the good mechanical properties and excellent corrosion resistance at elevated temperatures [223]. They are also used for the construction of body implants because of their unique biocompatible characteristic [175]. Non-reactor grade zirconium alloys (such as Zr702 and 705) are also used for the construction of process facilities containing high concentrations of sulfuric acid at temperatures above 100 °C [224]. From the corrosion perspective, the non-reactor grade zirconium alloys might be pre-selected for further examination of their application potential in the construction of hot dilute acidic pre-hydrolysis and HTL reactors. From an economic consideration, however, they were not pre-selected as suitable candidates in this study due to the high capital cost. Note that Zr702 is used as a reference material in the following hot dilute acidic pre-hydrolysis testing to support the characterization of surface scales formed on tested alloys.

In general, many Fe-based steels (SS310, SS316L, DSS 2205 and P91) and several Ni-based alloys (Alloy C-276 and Alloy 625) are the most commonly used commercial alloys in harsh environments due to their reasonable cost, applicable weldability, good corrosion performance and acceptable mechanical properties at elevated temperatures. Therefore, they were pre-selected in this study for corrosion and stress corrosion cracking assessments under hot dilute pre-hydrolysis and HTL conditions, respectively.

1.5. Objectives and contents of the thesis

The main objectives of this thesis are presented as follows:

- Evaluate the corrosion performance and mechanisms of candidate constructional alloys under the hot dilute acidic pre-hydrolysis and HTL conversion conditions to fill significant knowledge gaps on material selection and support the deployment of two biorefining technologies at bioenergy sectors;
- Improve the fundamental understanding of how inorganic and organic corrodants released during the biomass conversion affect corrosion to help further optimization of the two biorefining processes from materials technology perspective;
- Advance the understanding of the roles of major alloying elements (Fe, Cr, Ni, and Mo) on corrosion in aqueous solutions at elevated temperatures to provide an innovative direction towards the production of novel alloys and biorefinery equipment with superior performances but low cost.

To achieve these objectives, the following investigations were completed. Firstly, in hot dilute acidic pre-hydrolysis biorefining, the effects of temperature, service time and biomass on the corrosion of stainless steels (SS316L and DSS 2205) and nickel-based alloy (Alloy C-276) were studied. The roles of alloying elements were identified, and the corresponding corrosion mechanisms were proposed. Detailed information is presented in Chapter 3.

Secondly, for HTL conversion, the influences of operating temperature, pressure and flow rate on the corrosion of two candidate constructional steels, Cr-bearing SS310 and low-Cr P91 steels, were assessed using high temperature autoclaves and an environmental loop facility under typical HTL conversion conditions. The obtained results are included in Chapter 4.

Moreover, the impacts of alkaline catalyst, inorganic corrodants (Cl^- and S^{2-}), and organic acids on corrosion in catalytic HTL biorefining processes were thoroughly evaluated and compared. Detailed information can be found in Chapter 5.

Furthermore, to clarify the effects of alloying elements (Fe, Cr, Ni and Mo) on corrosion in non-catalytic and catalytic HTL conversion environments, thermodynamic simulations were performed to predict their corrosion modes. The corrosion kinetics of five alloys with different chemical

compositions were also investigated under representative HTL conversion conditions. The results and discussions are provided in Chapter 6.

Finally, based on corrosion testing results, two austenitic stainless steels (SS316L and SS310) were selected for preliminary SCC susceptibility evaluation using constant-strain and U-bending methodologies under catalytic HTL conversion conditions. Detailed information is shown in Chapter 7.

Chapter 8 is a general summary of studies and recommendations of future work.

Chapter 2. Methodologies

2.1. Testing sample preparation

In this work, rectangular coupons (20 mm long × 10 mm wide × 2 mm thick) were machined from commercial P91 tube, SS310, SS316L, DSS 2205, Alloy 625, and Alloy C-276 plates. Their bulk compositions and processing conditions are listed in each corresponding chapter, according to mill test certificates (MTC) provided by suppliers. A small hole with 2 mm radius was drilled into each coupon near the top to facilitate mounting on a home-made sample holder. Before each test under pre-hydrolysis and hydrothermal conditions, four freshly prepared coupons of one alloy were used to ensure the accuracy and precision of results reported. All the test coupons were well polished with a series of SiC papers up to 600 grit in deionized water to completely remove potential contaminations and defects introduced during machining, cleaned with ethanol in an ultrasonic bath for at least 10 minutes followed by ultrapure water, and finally dried using pressurized air. Subsequently, a sample ID was stamped on each prepared coupon near its top edge. Optical microscopy inspection was also conducted to ensure that the surface finish of each prepared coupon met the corrosion testing requirements. Prior to each corrosion test, the prepared coupons were weighed using a Mettler Toledo micro-balance with the precision of 1 µg and dimensioned using a digital caliper with the precision of 10 µm.

Before the SCC test, cylinder and U-bending samples of SS310 and SS316L were prepared. Note that all cylinder samples were machined with the tensile axis along the rolling direction of the plates and were threaded in both ends with a round gauge section for subsequently fitting into a custom-made loading frame, shown in Chapter 7. The cylinder and U-bending samples were also well polished with SiC papers up to 600 grit in deionized water to completely remove possible contaminations, cleaned in ethanol and ultrapure water, and finally dried using pressurized air. Note that the loading frame was made of Alloy 33 and the washers and nuts were fabricated with Alloy C-276, to ensure adequate stiffness and strength of the loading frame during the tests.

2.2. Testing methodology and procedure under different testing conditions

For tests performed under pre-hydrolysis conditions, a 6.7 L static autoclave made of Alloy C-276 with PTFE liner was used. The methodology described in ASTM G31 was adopted to conduct immersion testing and the test solution was prepared through the dilution of reagent grade 98% H₂SO₄ with deionized water [251]. Inorganic corrodants and softwoods were also added to simulate the pre-hydrolysis conversion conditions. The prepared test coupons were hung on a custom-made Zr702 holder using pre-oxidized Zr702 wires, and then accommodated inside the PTFE linear. After that, the linear was filled with 3-liter 0.05 M H₂SO₄, sealed and purged with N₂ for about one hour to produce a deaerated environment. For the test performed under hydrothermal conditions, the Alloy C-276 autoclave with an Alloy 625 liner was used. Supercritical-loop facility was also used to simulate high pressure and high flow rate conditions, as seen in Chapter 4. The prepared coupons were hung on the Alloy 625 holder using pre-oxidized Ni-Cr wires (80% Ni and 20% Cr, oxidized at 400 °C for 12 hours) to avoid galvanic effect between the coupons and holder. After accommodating the testing samples/holder and testing solution, the autoclave was also sealed and purged with N₂ for about an hour to produce a deaerated environment.

After leak test, the autoclave was heated to the designated temperature with a well-controlled heating rate to avoid overshooting. The time when temperature once reached the target was recorded as the starting time and the tests were to proceed for 10, 14 or 42 days, respectively. Temperature and pressure were routinely monitored and recorded to avoid any unexpected autoclave leakage or thermal fluctuations. After reaching the planned duration, the autoclave was powered off and cooled down in air. At room temperature, the samples were moved out, rinsed with distilled water, dried with pressurized air, photographed, and re-weighed using the Mettler Toledo micro-balance.

2.3. Corrosion rate assessments

Two techniques were used to evaluate the corrosion rates of the samples under pre-hydrolysis and hydrothermal testing conditions. The first one was to directly measure the mass change of a steel coupon before and after an exposure. This method is usually used to assess high temperature

oxidation kinetics of an alloy based on the assumption that surface oxidation of the alloy would be the dominant reaction during the high temperature exposure and that the formed corrosion products would be compact without localized nodular oxidation and/or spallation. The corrosion rate ($\mu\text{m}/\text{year}$) can be estimated by [225]:

$$\text{Corr. Rate} = \frac{\eta \cdot 8.76 \times 10^7 \cdot \Delta m}{dAt} \quad (2-1)$$

where Δm (g) is the direct mass change of a coupon before and after an exposure; d (g/cm^3) is the steel density; η is the molar mass ratio of consumed alloying elements to oxygen in formed corrosion products; A (cm^2) is the average surface area of the coupon; and t (h) is the testing duration. The average corrosion rate of an alloy after a test was obtained from the four parallel corroded coupons based on ASTM G16 [226].

The second technique was to measure the weight loss of a coupon after each test, involving two main steps: (a) completely removing the formed corrosion products on the coupon based on ASTM-G1 standard [227]; and (b) weighing the mass change of the coupon before the testing and after descaling [228, 229]. Descaling processes can be successfully achieved via immersing the coupons in specific chemical solutions, which do not corrode the steel substrates, but can effectively remove the formed corrosion layers through accelerated chemical dissolution reactions. In this study, the descaling of austenitic stainless steels was done by immersing the corroded coupons in 90 °C solution A (2 wt.% citric acid + 5 wt.% dibasic ammonium citrate + 0.5 wt.% disodium EDTA) for 30 min and 90 °C solution B (4 wt.% potassium permanganate + 5 wt.% caustic soda) for 30 min, followed by a 15 min of ultrasonic cleaning in ethanol. The coupons were then immersed in 90 °C solution A again for next 30 min and weighed. The above process was applied repeatedly until the weight of a coupon reached a constant value, as described in references [230, 231]. The descaling of P91 steel was carried out by immersing corroded coupons in a solution of 500 ml HCl + 3.5 g hexamethylene tetraamine + 500 ml ultrapure water at room temperature for 10 min. Cotton swab and soft copper brush were used to gently remove any remaining corrosion products after the immersion. The average corrosion rate of a coupon ($\mu\text{m}/\text{year}$) was then calculated by [232]:

$$\text{Corr. Rate} = \frac{8.76 \times 10^7 \cdot \Delta m}{dAt} \quad (2-2)$$

where Δm (g) is the mass loss of a coupon by measuring the difference in mass before exposure and after the descaling; d (g/cm^3) is the steel density; A (cm^2) is the surface area of the coupon; and t (h) is the exposure duration. The average corrosion rate of an alloy after a test was obtained from three parallel corroded and descaled coupons based on ASTM G16 [226]. Depending on the testing conditions, different corrosion rate assessment methods were used and detailed in each corresponding chapter.

2.4. Corrosion products characterization

In this study, the coupon with the direct mass change value closest to the average value in a given replicate set after a test was selected for subsequent corrosion products characterization. Optical images were taken to firstly check surface morphology of the corroded coupons. The coupons were then examined using a FEI Nova NanoSEM 650 scanning electron microscope (SEM) system operated at 20 keV and equipped with an Oxford energy dispersive X-ray spectroscopy (EDS) system to identify corrosion modes (such as active corrosion, general oxidation, and/or pitting etc.) and roughly characterize the chemical properties of formed corrosion products. For relatively thick corrosion layers, their phase compositions were determined by X-ray diffraction (XRD) technique with a Co $K\alpha$ X-ray source operated at 40 kV and 150 mA instead. Diamond saw cutting or FEI Helios NanoLab™ DualBeam™ Focus Ion Beam (FIB) microscope was applied for producing cross-sectional views of the corroded samples, depending on the corrosion product layers' thickness. Before the FIB operation, a thin platinum (Pt) layer was deposited on the coupons in vacuum to protect the formed surface scale. After the FIB operation, the cross-sectional samples were thinned and collected using *in-situ* lift-out technique for following TEM examinations. The TEM characterizations, including Bright field (BF) imaging, High-angle annular dark-field (HAADF) imaging and EDS element mapping were conducted using a Tecnai Osiris™ scanning transmission electron microscope (STEM) equipped with super X-field emission gun (FEG) and X-ray detection system operated at 200 kV. Besides that, XPS spectra were also collected on the selected samples by PHI Quantera II Scanning XPS Microprobe operated at 15 kV with take-off angle of 45° . Ar ion sputtering with ion beam of 1 kV voltage and 1 mA current was carried out at a step size of 0.8 eV for depth profiling. The collected spectra were deconvoluted and analyzed using commercial XPSPEAK 4.1 software.

Chapter 3. Corrosion of Candidate Constructional Alloys under Hot Dilute Acidic Pre-Hydrolysis Biorefining Conditions: Influence of Temperature, Alloying Elements and Corrodants

In the previous chapter, I have briefly introduced the basic autoclave testing procedures, corrosion rate assessment and post-mortem microscopic characterization methods. In this chapter, I carried out six autoclave tests under different pre-hydrolysis conditions to examine the corrosion performance of SS316L, DSS 2205 and Alloy C-276. It was found that austenitic stainless steels underwent active corrosion while Alloy C-276 showed adequate performance, likely due to the formation of oxide layers with completely different chemistry found on its surface. Moreover, the influences of temperature, test duration, inorganic corrodants and softwoods were also studied and the impact on corrosion rates and formed oxide layers was discussed in detail.

Abstract

Hot dilute acidic pre-hydrolysis is used to convert lignocellulosic biomass to sugar and other intermediates in 0.05 M H₂SO₄ at elevated temperatures (100-200 °C). This study investigated the corrosion of three constructional candidates (SS316L, DSS 2205, and Alloy C-276) using autoclave methodology and advanced characterization techniques. Under simulated biorefining conditions, SS316L and DSS 2205 experienced active corrosion while Alloy C-276 exhibited excellent performance because of the formation of a protective Mo-enriched oxide layer. Increasing temperature and the addition of inorganic/organic corrodants only had marginal effects on the corrosion of Alloy C-276, but noticeably enhanced the corrosion of SS316L and DSS 2205.

Keywords: Sulfuric acid; Acid corrosion; Weight loss; SEM; TEM; Stainless steel; Alloy

3.1. Introduction

Some parts of the background information have been included in Chapter 1.

Over the past decades, intensive efforts have been devoted to developing innovative biorefining technologies for the generation of renewable biomass-based chemicals and energy products, which

can be used as reliable and sustainable energy alternatives to partially and even completely replace depleting fossil fuel resources and clean our existing living environment [233, 234]. Generally, biomass resources are organic materials originating from agricultural, forest, animal manures, industrial wastes, and engineered microalgae [235, 236]. Among them, lignocellulosic biomass exhibits outstanding the advantage of being low carbon footprint, environmental friendly and sustainable [237-239]. Nevertheless, this category of biomass feedstocks is usually composed of rigid cellulose-hemicellulose-lignin structure, which cannot be easily broken down into enzymes-accessible cellulose compounds using conventional grinding methods [240]. Advanced pre-treatment methods, such as biochemical, thermochemical, and/or biological pathways, are thus needed to decompose the structure and increase the accessibility of hydrolytic enzymes for the fermentation of glucose/sugar and the formation of bioethanol products [4, 34, 38-42]. Among the proposed pre-treatment pathways, hot dilute acidic pre-hydrolysis, as schematically shown in Fig. 3-1, has been developed as a promising method to achieve the optimum yield of fermentable sugars [47, 48, 50, 51]. Pioneer research has demonstrated that most cellulose and hemicellulose (>75%) in raw lignocellulosic feedstocks can be converted to fermentable sugars in dilute acidic solutions at elevated temperatures [48, 52-56]. Although the optimum pre-hydrolysis operating conditions have not yet been well defined by forest industry, it is generally concluded that dilute sulfuric acid (0.05 - 0.1 M) can serve as an effective medium to achieve desired conversion efficiency at the temperature range of 90 - 200 °C [43-46, 47, 49, 51].

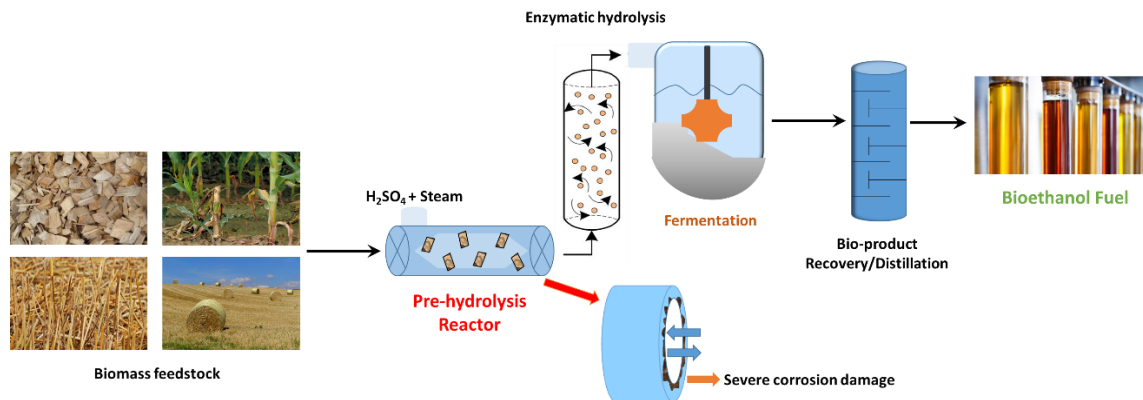


Fig. 3-1. Schematic of hot dilute acidic pre-hydrolysis treatment of lignocellulosic feedstocks.

Despite the above promising achievements, the deployment of the pre-hydrolysis technology in paper and pulp mill plants has been significantly hindered due to the fact that the corrosion

knowledge of steels and alloys in hot dilute sulfuric acid is really scarce, making the cost-effective selection of alloys for construction difficult. Most previous studies focused on the corrosion of Fe-based steels and Ni-based alloys in dilute sulfuric acids (0.05 - 2 M) at temperature ≤ 100 °C, and found that NiCrMo alloys (such as Alloy 825 and Alloy C-276) exhibited much better corrosion resistance (< 0.5 mm/year) than austenitic stainless steels (SS316 and SS304L, etc.) [98-100]. At room temperature, Alloy C-276, instead of SS304 and SS316, has been recommended for the service in dilute sulfuric acid (< 1 M) [97]. However, few research has been conducted to identify the corrosion of steels and alloys in the dilute acid at temperature >100 °C. Surprisingly, the continuous digesters at sulfite pulp mills are still made of SS316L and operated in the sulfuric acid (pH = 1.5 - 2) at elevated temperatures (125 - 145 °C) with a tolerant corrosion rate ≤ 1.2 mm/year [195, 241, 242]. Moreover, a pilot-scale hot dilute acidic pre-hydrolysis biorefining reactor has been made of SS316 [194], while the related corrosion performance of the reactor has not yet been released to the public. Clearly, it is necessary to determine whether Fe-based stainless steels are suitable for the construction of hot dilute acidic pre-hydrolysis reactors for long-term safe operation.

During the pre-hydrolysis conversion processes, the roles of two major alloying elements (Mo and Cr) in steels and alloys on corrosion are also required to be clarified. Our recent study indicated that the formed surface Cr oxide layers could not effectively protect Cr-bearing steels from dilute acid (a mixture of H_2SO_4 , HNO_3 , HCl , and H_2CO_3) attack (pH = 2) at temperature > 100 °C [108]. About the effect of Mo, considerable studies have also been conducted at temperature < 100 °C [116-120]. For example, Lloyd *et al.* [209, 210] investigated the performance of Ni-Cr-Mo alloys in 0.1 M H_2SO_4 + 1 M NaCl at temperature ≤ 85 °C, and found that the accumulation of Mo in the outer oxide regions could effectively mitigate the acid attack. Up to today, it has been generally accepted that increasing Mo content in steel can improve the resistance to acidic solutions. However, the role of Mo in corrosion process is still far from clear [121, 122]. For instance, Sugimoto *et al.* proposed that the addition of Mo might help the formation of a protective oxide film in which Mo^{6+} ions would be dissolved in chromium oxyhydroxide network [123], while other studies implied that the addition of Mo could also facilitate the formation of $\text{MoO}(\text{OH})_2$ or MoO_4^{2-} to suppress localized active dissolution of the formed oxide layer [124-126]. Except for temperature and alloying elements, limited information on corrosion is available to describe the

impacts of inorganic and organic matters released from biomass during the conversion [76]. The most common inorganic corrodants that are present in lignocellulosic biomass include chloride and sulfide ions, which can facilitate localized corrosion and stress corrosion cracking in hot dilute sulfuric acid [243-246]. The concentrations of Cl^- and S^{2-} in most lignocellulose biomass resources in North America are around 200 -3000 ppm and 75 -2500 ppm, respectively [105-107]. A previous study indicated that the addition of 0.017 M Cl^- to 1 M sulfuric acid at 94 °C led to a noticeable increase in the corrosion rate of SS316L [102]. However, Li *et al.* found that the presence of 0.005 M Cl^- in the mixture of dilute sulfuric acid, nitric acid, hydrochloric acid, and carbonic acid solution (pH ~ 2) did not result in pitting at temperature ≤ 150 °C [108]. Therefore, it is unclear whether the presence of these trace amounts of Cl^- and S^{2-} can cause severe corrosion damage (especially pitting) in the pre-hydrolysis conversion processes. Moreover, organic compounds (such as polysaccharides, furfural, and acetic acid (HAc)) produced during the conversion may affect corrosion as well [109-112]. For example, the content of acetic acid is about 10 - 19 wt.% in liquid phase after the hot acidic pre-hydrolysis conversion, depending on the type of biomass feedstocks used [113, 114]. Previous studies reported that in acetic acid (0.01 and 0.065 M, respectively) with 20,000 ppm Cl^- at 180 °C, localized corrosion occurred on 13Cr, 13Cr-1Mo and 13Cr-2Mo steels via the processes of destroying the integrity of surface oxide scale and increasing the solubility of iron oxides [115]. On the contrary, furfural compounds and their derivatives generated during the conversion may act as corrosion inhibitors, as indicated by previous studies [247, 248]. These compounds have heterocyclic and aromatic cores along with heterogeneous atoms such as oxygen, nitrogen and sulfur, which can interact with metals to increase their surface hydrophobicity [247-250]. According to my literature review, the influence of inorganic and organic corrodants released from conversion remains a puzzle.

Therefore, this study investigated the corrosion of three representative alloys SS316L, DSS 2205, and Alloy C-276 in deaerated 0.05 M H_2SO_4 with/without the addition of inorganic corrodants and raw biomass at elevated temperatures. SS316L was selected because of its wide application in the paper and pulp industry, as described above [195]. Duplex stainless steel 2205 has exhibited promising performance in acidic environments at oil and refining industries, and is a more cost-competitive candidate compared to Cr-bearing austenitic stainless steels [192, 193]. As mentioned above, Alloy C-276 generally shows excellent performance in weak acidic solutions [122, 156, 199, 206-208]. This study is anticipated to advance the mechanistic understanding of how steels

and alloys corrode in hot dilute acidic pre-hydrolysis environments and support the development of materials technology solutions for the biorefinery construction.

3.2. Experimental Procedure

3.2.1. Testing sample preparation

Rectangular coupons (20 mm long × 10 mm wide × 2 mm thick) were machined from commercial SS316L, DSS 2205, and Alloy C-276 plates, and their bulk compositions are listed in Table 3-1 based on the associated mill test certificates (MTC) provided by suppliers. SS316L plate was made via annealing at 1038 °C and subsequently quenching in water, while C-276 plate was produced through solution annealing at 1148 °C for 30 minutes before subsequent water quenching. DSS 2205 was fabricated with solution annealed at 1065 °C and then quenched in water. A small hole with 2 mm radius was drilled into each coupon near the top to facilitate mounting on a home-made sample holder. For each test, four freshly prepared coupons of each alloy were used to ensure the accuracy and precision of the results reported. All the test coupons were well grinding with a series of SiC papers up to 600 grit in deionized water to completely remove potential contaminations and defects introduced during machining, cleaned with ethanol in an ultrasonic bath for at least 10 minutes and then with ultrapure water afterwards, and finally dried using pressurized air. After that, a specimen ID was stamped on each prepared coupon near its top edge. Optical microscopy inspection was also conducted to ensure that the surface finish of each prepared coupon meet corrosion testing requirements. Prior to a corrosion test, the prepared coupons were weighed using a Mettler Toledo micro-balance with the precision of 1 µg and dimensioned using a digital caliper with the precision of 10 µm.

Table 3-1. Normalized bulk chemical composition of SS316L, DSS 2205, and Alloy C-276.

	Composition (wt.%)							
	Cr	Mo	Mn	Ni	Fe	C	Si	P
SS316L	16.60	2.00	1.20	10.0	balance	0.02	0.30	0.02
DSS 2205	22.50	3.03	1.17	5.61	balance	0.02	0.42	0.03

Alloy C-276	15.90	15.50	0.40	58.80	5.70	0.01	0.02	0.01
--------------------	-------	-------	------	-------	------	------	------	------

3.2.2. Test methodology and procedures

Table 3-2 summarizes the test matrix conducted in a 6.7 L static autoclave made of Alloy C-276 to identify the influence of temperature, duration, and inorganic/organic corrodants on corrosion. The methodology described in ASTM G31 was adopted to conduct immersion testing in the autoclave as shown schematically in Fig. 3-2(a) [251]. The test solution (0.05 M H₂SO₄) used for tests #1-4 was prepared through the dilution of reagent grade 98% H₂SO₄ with deionized water. In test #5, 700 ppm KCl and 500 ppm Na₂S were also added to the prepared 0.05 M H₂SO₄ to simulate the pre-hydrolysis conversion conditions with the presence of inorganic corrodants. Note that sulfide would likely being oxidized into other sulfur species during the test, given the low pH value of solution. In test #6, 25 wt.% of softwoods that mainly composed of 55% cellulose, 11% hemicellulose, and 26% lignin, were added into 0.05 M H₂SO₄ and well mixed before testing to clarify the influence of corrosive organic compounds released during the conversion.

The prepared test coupons were hung on a custom-made Zr702 holder using pre-oxidized Zr702 wires, and then accommodated inside a PTFE linear (see Fig. 3-2(b)). After that, the linear was filled with 3L 0.05 M H₂SO₄, sealed and purged with N₂ for about one hour to produce a deaerated environment. After leak test, the autoclave was heated up to test temperature with a well-controlled heating rate to avoid overshooting. The time when temperature once reached the target was recorded and the tests were to proceed for 14 and 42 days, respectively. Once reaching the planned duration, the autoclave was powered off and cooled down in air. At room temperature, the samples were moved out, rinsed with distilled water, dried with pressurized air, photographed, and re-weighed using the Mettler Toledo micro-balance.

Table 3-2. Testing conditions of static autoclave test.

Objective	Test	Conditions
Influence of temperature	#1	In 0.05 M H ₂ SO ₄ at 100 °C for 14 days
	#2	In 0.05 M H ₂ SO ₄ at 150 °C for 14 days
	#3	In 0.05 M H ₂ SO ₄ at 200 °C for 14 days

Effect of exposure time	#4	In 0.05 M H ₂ SO ₄ at 200 °C for 42 days
Impact of inorganic/organic corrodants	#5	In 0.05 M H ₂ SO ₄ + 700 ppm Cl ⁻ + 500 ppm S ²⁻ at 200 °C for 14 days
	#6	In 0.05 M H ₂ SO ₄ + 25 wt.% biomass at 200 °C for 14 days

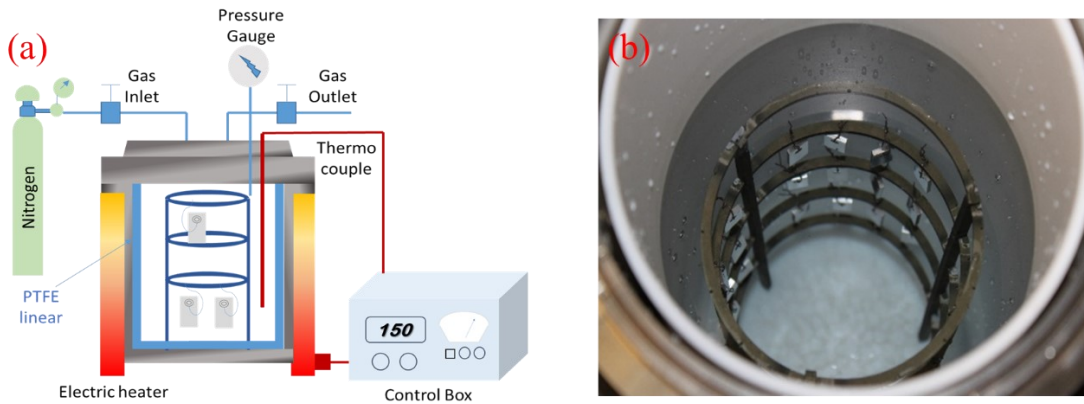


Fig. 3-2. (a) Schematic of autoclave setup used for this study; and (b) Photographic image of opened static autoclave with a PTFE linear, holder and testing samples.

3.2.3. Corrosion rate assessment

In this study, all the testing samples experienced negative weight change after each corrosion test. Therefore, weight loss measurements, instead of direct weight change, were adopted as a more accurate and consistent metric to assess and rank the corrosion rates of candidate alloys. Based on ASTM G1 standard and previous studies [228, 252], the weight loss measurements include two major steps: (a) completely removing formed corrosion products from a corroded coupon; (b) weighing the mass difference of the coupon before autoclave testing and after descaling. Descaling can be achieved by immersing the coupons in a specific chemical solution which does not corrode the coupon substrates, but can effectively remove the formed corrosion products through enhanced chemical dissolution reactions. In this study, the descaling of three candidate alloys was achieved by immersing the corroded coupons in 90 °C solution A (2 wt.% citric acid + 5 wt.% dibasic ammonium citrate + 0.5 wt.% disodium EDTA) for 30 mins and 90 °C solution B (4 wt.%

potassium permanganate + 5 wt.% caustic soda) for 30 mins, followed by a 15 mins of ultrasonic cleaning in ethanol. After rinsing with water and drying with pressurized air, the coupons were then immersed in 90 °C solution A again for 30 mins and weighed. The above immersion treatment process was applied repeatedly until the weight of the coupon reached a constant value as described in the reference [230]. The corrosion rate of the coupon (mm/year) was then estimated by [232]:

$$Corr.Rate = \frac{8.76 \times 10^4 \cdot \Delta m}{dAt} \quad (3-1)$$

where Δm (g) is the mass loss of a coupon before exposure and after descaling, d (g/cm^3) is the steel density, A (cm^2) is surface area of the coupon, and t (h) is the exposure duration. In this study, the average corrosion rate of the steel after a test was obtained from three parallel corroded and de-scaled coupons based on ASTM G16 [253].

3.2.4. Corrosion products characterization

In this study, the coupon with the direct mass change value closest to the average value in a given replicate set after a corrosion test was selected for subsequent corrosion product characterization. Optical images were firstly taken to check surface morphology of corroded coupons. The coupons were then examined using a FEI Nova NanoSEM 650 scanning electron microscope (SEM) system operated at 20 keV and equipped with an Oxford energy dispersive X-ray spectroscopy (EDS) system including 127 eV resolution detector to identify corrosion modes (active corrosion, general oxidation, and/or pitting) and the chemical properties of formed corrosion products. As the corrosion products formed on SS316L and DSS 2205 were quite thick, their phase compositions were thus determined using X-ray diffraction (XRD) technique with a $\text{Co K}\alpha$ X-ray source which operated at 40 kV and 150 mA. The cross-sectional views of stainless steels were produced by using a low-speed diamond saw cutting machine running at the speed of 125 rpm, followed by cold mounting. Different from them, the corrosion products formed on Alloy C-276 were relatively thin and a FEI Helios NanoLab™ DualBeam™ FIB microscope was applied for producing cross-sectional views of the area from the corrosion products to metal substrate. Before FIB operation, a thin layer of Pt coating was plated on the coupons to protect the formed surface scale. After FIB operation, the cross-sectional samples were thinned and collected using in-situ lift-out technique

for further TEM examination. The TEM characterizations, including high-angle annular dark-field (HAADF) imaging, element mapping and corresponding EDS analyses, were conducted by Tecnai Osiris™ scanning/transmission electron microscope (S/TEM) equipped with super X-field emission gun (FEG) and X-ray detection system operated at 200 kV.

3.3. Main Results

3.3.1. Influence of temperature and operating time

The photographic images of alloy coupons before and after exposure to 0.05 M H₂SO₄ at 100, 150, and 200 °C are shown in Fig. 3-3, respectively. Before the tests, the freshly prepared steel coupons exhibited neat surfaces with shining metal luster. After the exposure at 100 °C, the surface color of SS316L, DSS 2205, and Alloy C-276 were brown, of which the darkest surface was presented on SS316L. No pitting or other type of localized corrosion was found. With increasing temperature, black corrosion products were grown on both SS316L and DSS 2205 while the corroded Alloy C-276 showed greenish appearance. At 200 °C, spalling also occurred on SS316L. These observations suggest that the stainless steels would have less resistance to the hot dilute acid attack comparing to the Ni-alloy and corresponding corrosion damage might be remarkably enhanced with temperature. In addition, extending exposure time at 200 °C possibly advanced corrosion of the three alloys.

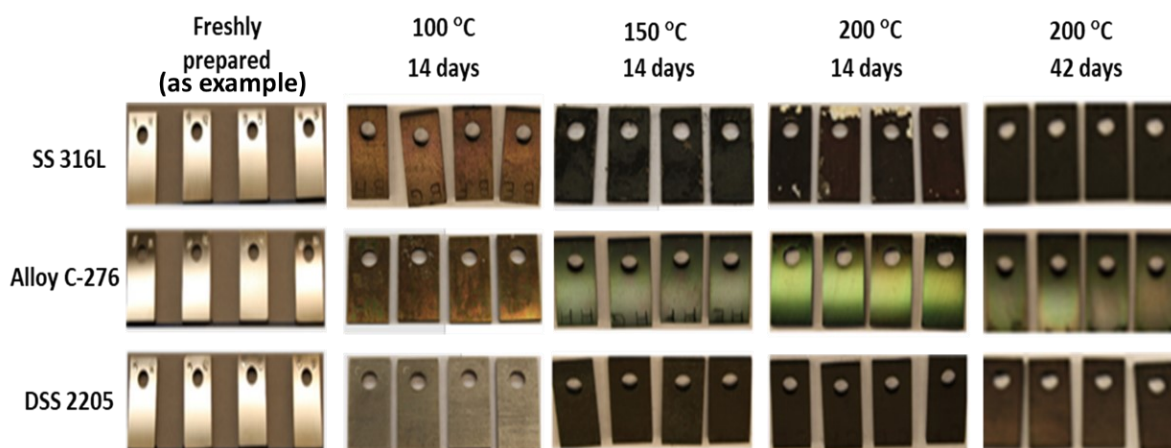


Fig. 3-3. Photographic images of alloy coupons taken before and after the exposure to 0.05 M H₂SO₄ at pre-hydrolysis biorefining temperatures for different exposure durations.

As shown in Fig. 3-4, relatively thick corrosion layers were formed on the surface of SS316L after all the three tests since abrasion marks were barely visible. Randomly distributed large deposit particles, which were possibly formed during the autoclave cooling-down, were observed on the formed surface scales. Localized nodular oxidation was likely to firstly increase with temperature but subsequently decrease at temperature $> 150\text{ }^{\circ}\text{C}$. Moreover, a cracking line was visible within the corrosion layer formed at $150\text{ }^{\circ}\text{C}$.

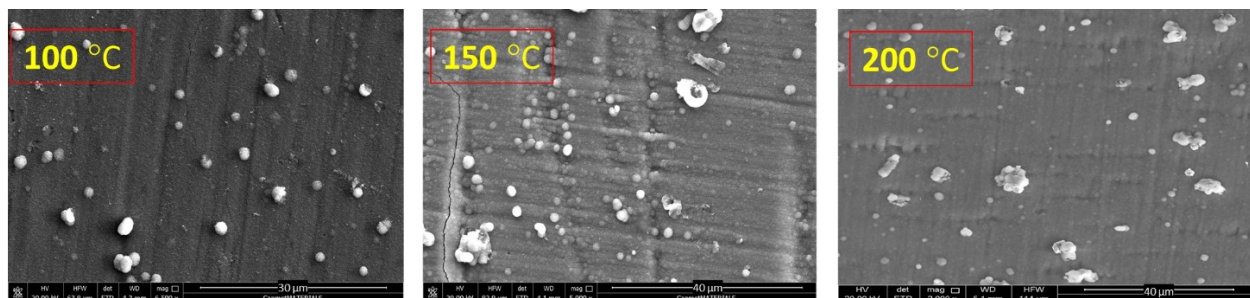


Fig. 3-4. Top-view SEM images of SS316L steel samples after corroding in $0.05\text{ M H}_2\text{SO}_4$ at $100\text{ }^{\circ}\text{C}$, $150\text{ }^{\circ}\text{C}$ and $200\text{ }^{\circ}\text{C}$, respectively.

To further reveal the properties of the corrosion layers formed at different temperatures, the cross-sections of the corroded samples were produced using standard diamond saw cutting method, and the corresponding SEM/EDS results are shown in Fig. 3-5. The corrosion layer formed at $100\text{ }^{\circ}\text{C}$ was relatively fragile by the presence of micro-pores. At higher temperatures, micro-cracks were formed within the surface scales and also penetrated down to the steel substrate. At the three testing temperatures, EDS mapping results indicate that the formed corrosion layers are mainly composed of elements Cr, O and S, implying that the layers might be composed of Cr_2O_3 , $\text{Cr}_2(\text{SO}_4)_3$ and/or CrSO_4 . Moreover, the average thickness of the corrosion layer noticeably increased with temperature, from approximately $35\text{ }\mu\text{m}$ at $100\text{ }^{\circ}\text{C}$ to about $120\text{ }\mu\text{m}$ at $200\text{ }^{\circ}\text{C}$, suggesting that the formed corrosion product could not effectively protect the steel from the hot dilute acid attack and the micro-cracks might act as small “windows” to facilitate the diffusion of aggressive anions to the steel substrate. This result also implied that the influence of temperature on the formation of corrosion layers might be more noticeable than that on the chemical dissolution of the layers. In addition, the XRD spectra were collected on the corroded SS316L samples, and the results are shown in Fig. 3-6. Due to the weak signal and wider peaks, it can be concluded that only a small

fraction of the corrosion products is crystalline and the majority is amorphous/nanocrystalline. Note that the major peaks of Cr_2O_3 could be found near 33.6° , 36.2° , 41.8° , 54.9° , 63.4° , 65.1° ; the main peaks of NiCr_2O_4 would be at around 46.2° , 57.6° , 74.8° , 75.5° ; and the peaks of $\text{Cr}_2(\text{SO}_4)_3$ would be near 43.2° , 46.3° , 57.1° , 57.9° , 63.7° . It is worth noticing that peaks at certain locations are shown as broad peaks or not shown, probably due to the limited occurrence of crystallization in selected orientations and limited amount of them in the oxide layer. At the pre-hydrolysis refining temperatures, the corrosion layers formed on the steels were mainly consist of Cr_2O_3 along with small amounts of $\text{Cr}_2(\text{SO}_4)_3$. Based on the observations in Figs. 3-4 and 3-5, the peaks of NiCr_2O_4 and FeSO_4 on the spectra were likely from the corrosion particles deposited on the steel during autoclave cooling-down. Note that the peak of $\text{Cr}_2(\text{SO}_4)_3$ at 46.3° degree partially overlapped with that of NiCr_2O_4 .

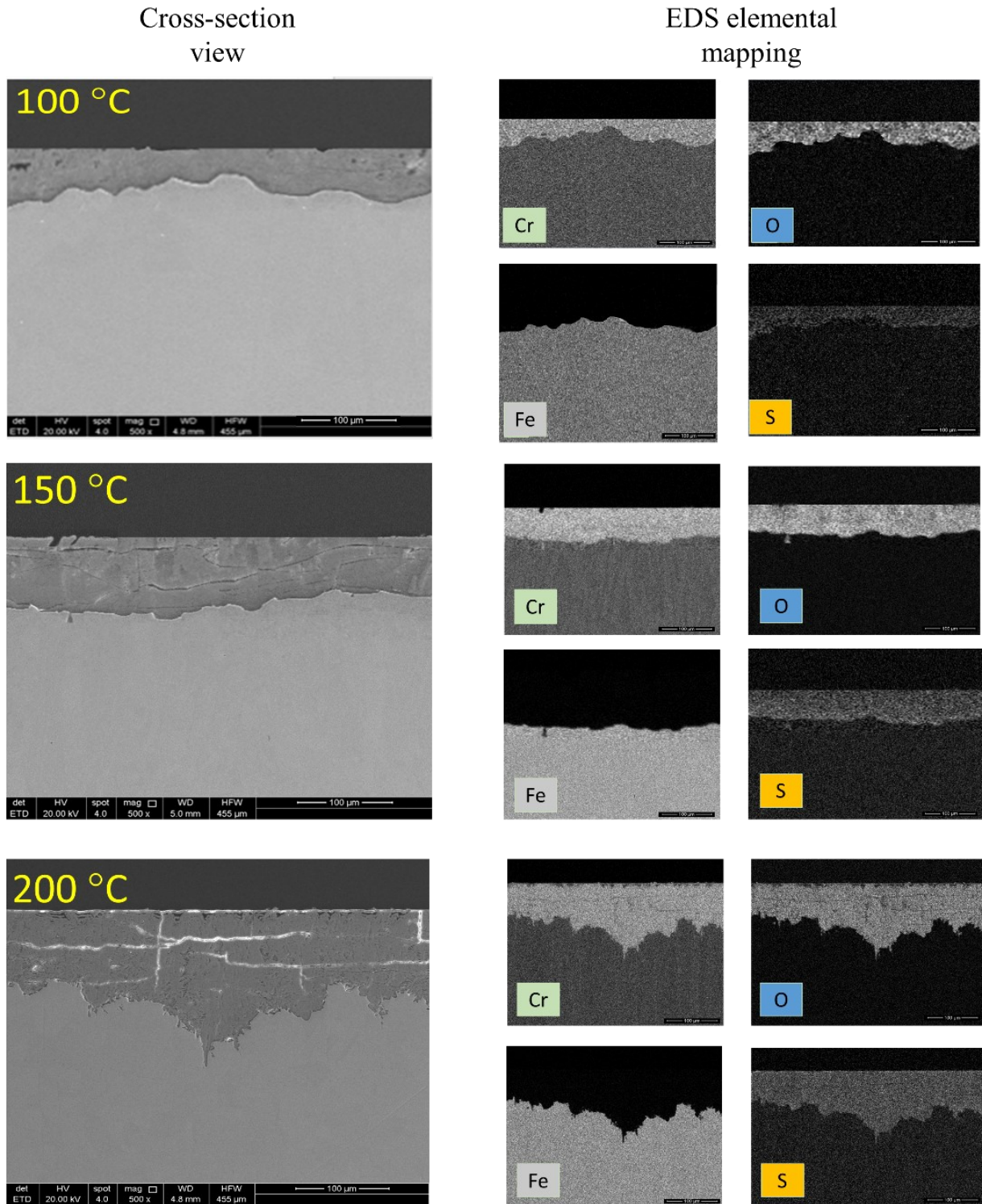


Fig. 3-5. Cross-sectional SEM view of SS316L steel and corresponding elemental mapping of Cr, Fe, O, and S after the exposure to 0.05 M H₂SO₄ at 100 °C, 150 °C and 200 °C, respectively.

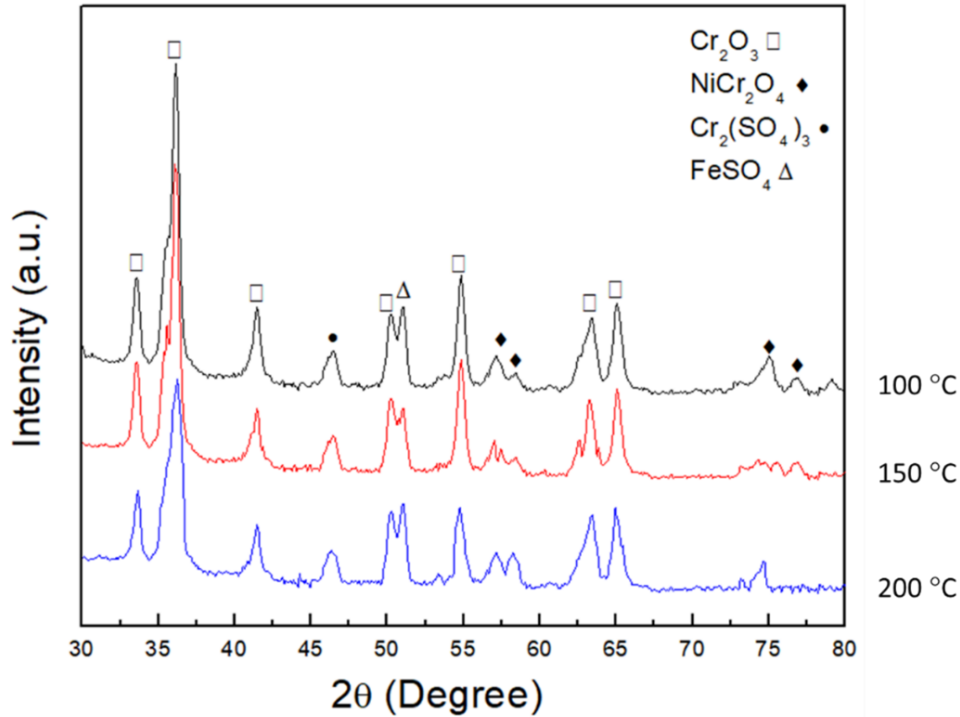


Fig. 3-6. XRD spectrum collected on SS316L steel samples after the exposure to 0.05 M H₂SO₄ at different biorefining temperatures.

To determine whether the continuous corrosion layer on the steel was formed during the corrosion exposure or from the deposition of dissolvable corrosion products during autoclave cooling-down, Zr702 coupons were also prepared and tested with SS316L samples in the autoclave at 200 °C, and the results are shown in Fig. 3-7. Only about 2 μm thick Cr oxide layer was present on Zr702 after the test, indicating that most of the corrosion layers shown in Fig. 3-5 should be formed during the exposure to the dilute sulfuric acid. Therefore, increasing biorefining temperature resulted in a noticeable increase in the corrosion of the steel in 0.05 M H₂SO₄ since the formed corrosion layer was non-protective with the presence of micro-pores and even cracks.

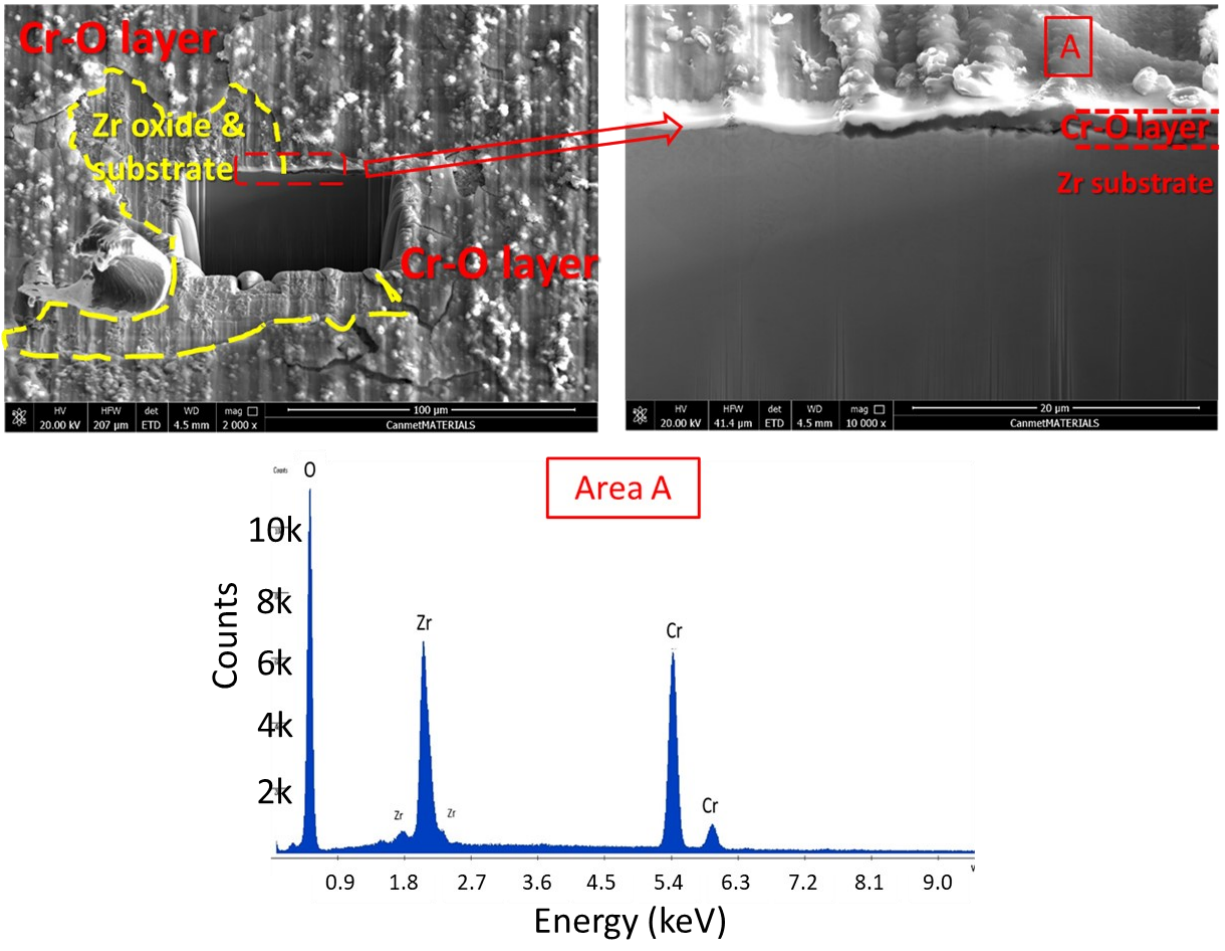


Fig. 3-7. Top and cross-sectional SEM views and corresponding EDS results of Zr702 after the exposure to 0.05 M H₂SO₄ along with three tested alloys at 200 °C.

In order to examine the long-term corrosion performance of the steels in the dilute acid, the steel samples were also tested at 200 °C for 42 days. Following that, FIB/SEM techniques were employed to produce cross-sectional views of the corroded samples, and the results are shown in Fig. 3-8. Note that only part of the formed corrosion layer after the 14 days' exposure is shown there due to the FIB operating limitation on thick corrosion layers. Extending exposure time advanced the formation of micro-cracks. Surprisingly, the average thickness of the corrosion layer decreased with time, suggesting that the chemical dissolution of the formed corrosion products might become dominant after the long-term exposure at 200 °C. XRD characterization results (see Fig. 3-9) indicated that the corrosion products formed after long-term exposure were still mainly

composed of Cr_2O_3 along with some $\text{Cr}_2(\text{SO}_4)_3$. In comparison with the results in Fig. 3-6, extending time also likely resulted in continuous deposition of NiCr_2O_4 particles and the complete disappearance of FeSO_4 as the peaks of FeSO_4 were not detected in Fig. 3-9.

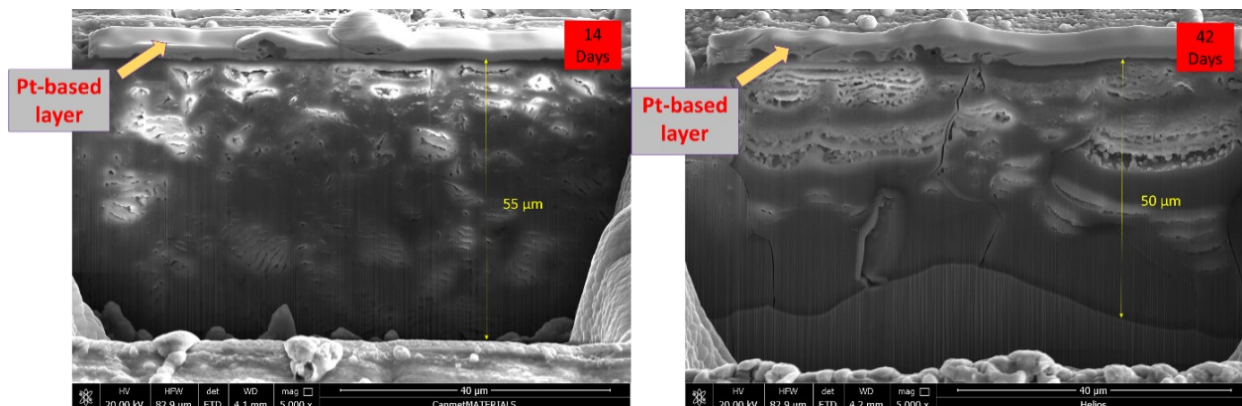


Fig. 3-8. Cross-sectional SEM views of corroded SS316L steel after the exposure to 0.05 M H_2SO_4 at 200 °C for 14 and 42 days, respectively.

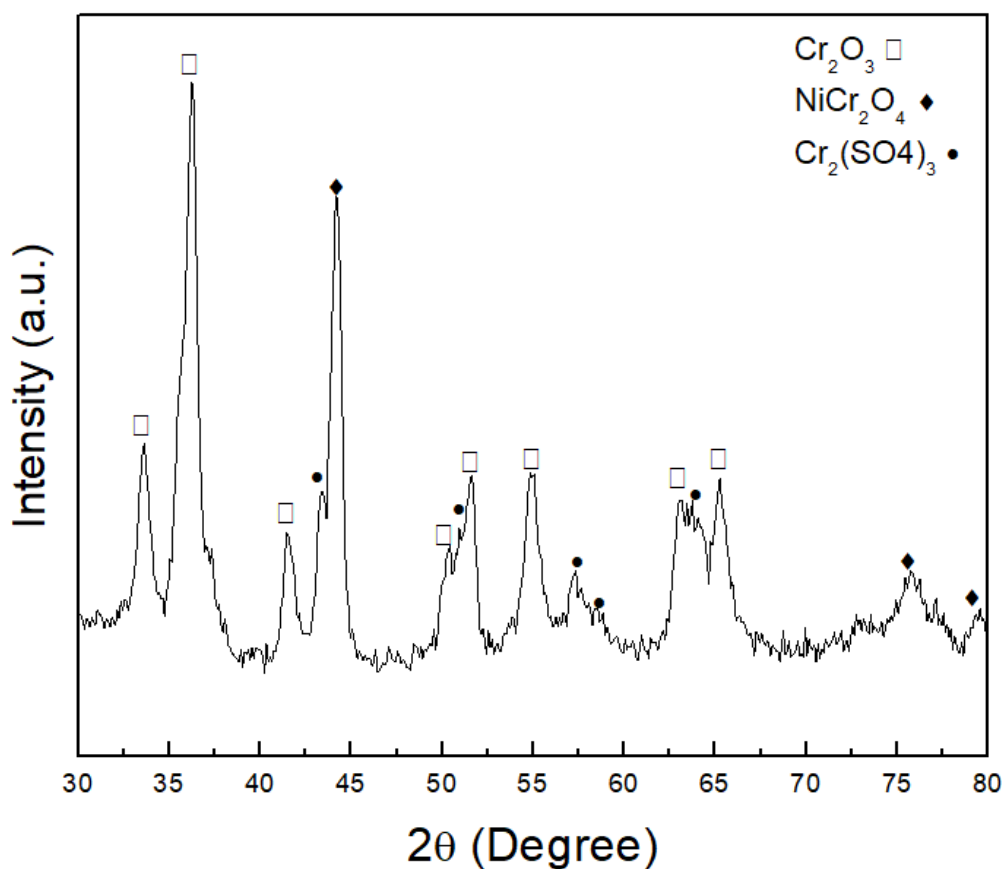


Fig. 3-9. XRD spectra collected on SS316L steel sample after the exposure to 0.05 M H_2SO_4 at 200 °C for 42 days.

The variations of the average corrosion rates of SS316L with temperature and time in 0.05M H₂SO₄ are shown in Fig. 3-10. Under the pre-hydrolysis biorefining conditions, the corrosion rate of the steel was considerably high (> 1 mm/year), and increased with temperature. A sharp increase in the corrosion rate occurred when temperature increases from 150 °C to 200 °C. At 200 °C, extending exposure time also led to a noticeable increase in the corrosion rate. This could be attributed to the influence of exposure time on the chemical dissolution of corrosion layers as implied in Fig. 3-8. The corrosion rate results further confirmed that the corrosion layers formed on the steel could not effectively protect the steel in the hot dilute acidic solution and possibly lost most of their resistance to the biorefining environment at temperature >150 °C.

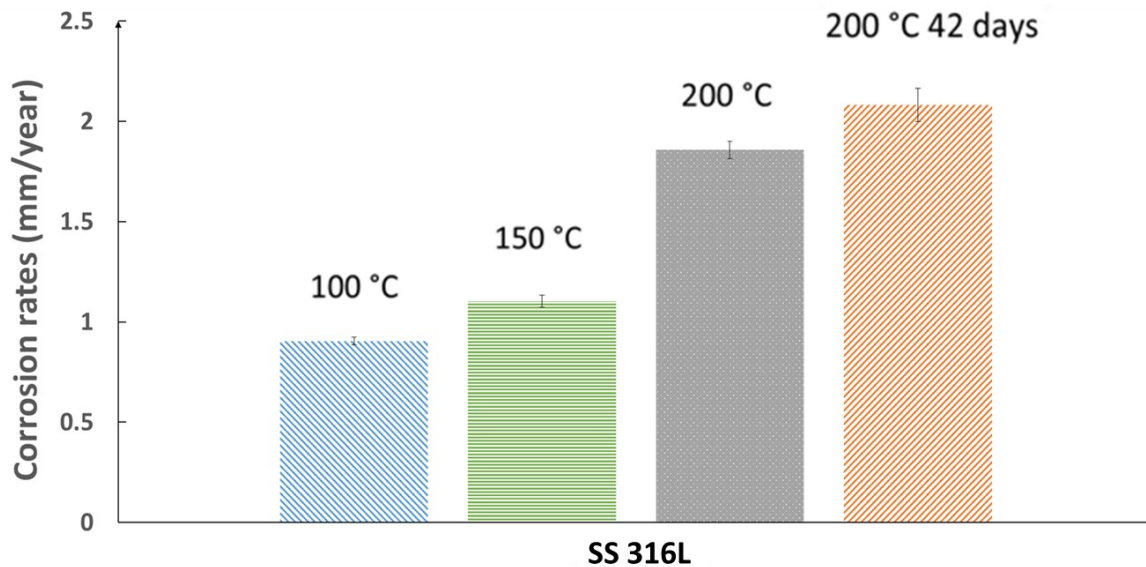


Fig. 3-10. Variation of the average corrosion rates (mm/y) of SS316L with temperature and exposure time in 0.05 M H₂SO₄.

3.3.2. Effect of alloying elements on corrosion

3.3.2.1. Effect of alloying element Cr

To clarify the effect of Cr content in steels on corrosion in the hot dilute acidic solution, DSS 2205 with 22.5% Cr was also tested with SS316L under the same conditions. Note that the Mo content in DSS 2205 is slightly higher than that in SS316L (see Table 3-1). Based on the top-view SEM images (see Fig. 3-11), the corrosion layer formed on DSS 2205 at the three testing temperatures was still relatively thick because the mechanically polishing marks were barely visible. Moreover,

both nodular and deposition particles were formed on the corrosion layers and their intensities increased with temperature. Interestingly, no pit or crack was found on the corroded DSS 2205 samples after all the three exposures.

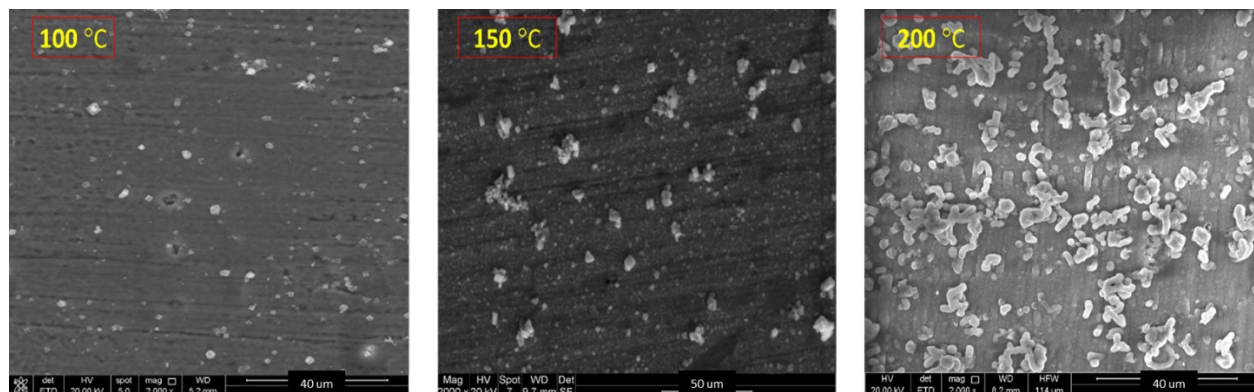


Fig. 3-11. Top-view SEM images of DSS 2205 samples after the exposure to 0.05 M H_2SO_4 at 100 °C, 150 °C and 200 °C for 14 days, respectively.

To reveal the nature of corrosion products formed, the cross-sections of the corroded DSS 2205 samples were also produced using the conventional diamond saw cutting method, and the corresponding SEM/EDS mapping results are shown in Fig. 3-12. The average thickness of corrosion layer formed on DSS 2205 was consistently thinner than that grown on SS316L, and initially increased with temperature, i.e., from approximately 28 μm at 100 °C to about 50 μm at 150 °C. Different from that of SS316L steel, however, further increasing temperature did not lead to a noticeable increase in the layer thickness. Moreover, micro-cracks were also found within the corrosion layers, and became more noticeable at higher temperature. Based on the results shown on Fig. 3-5 and 3-12, increasing Cr content in the stainless steels was likely to improve the corrosion resistance to the hot dilute sulfuric acid, but could not provide satisfactory protection to the steel from the engineering application point of view. In addition, EDS mapping results indicated that the corrosion layers formed on DSS 2205 were also composed of elements Cr, O and S, similar to those grown on SS316L. XRD characterizations (see Fig. 3-13) reveal that the corrosion layers formed on DSS 2205 would be also mainly composed of Cr_2O_3 and $Cr_2(SO_4)_3$, similar to those present on SS316L. The weak signal and wider peaks again indicate that only a small fraction of the corrosion products was crystalline and the majority was amorphous structure. As shown in the figure, the peaks of deposited $NiCr_2O_4$ particles were also detected on the corroded

DSS 2205 samples. Furthermore, it also seems that content of $\text{Cr}_2(\text{SO}_4)_3$ in the formed corrosion layer would increase with temperature. Note that the intensity mismatch of NiCr_2O_4 between the obtained XRD spectra and the standard one was due to the existence of amorphous/nanocrystalline structure and/or accumulated stress within the corrosion products.

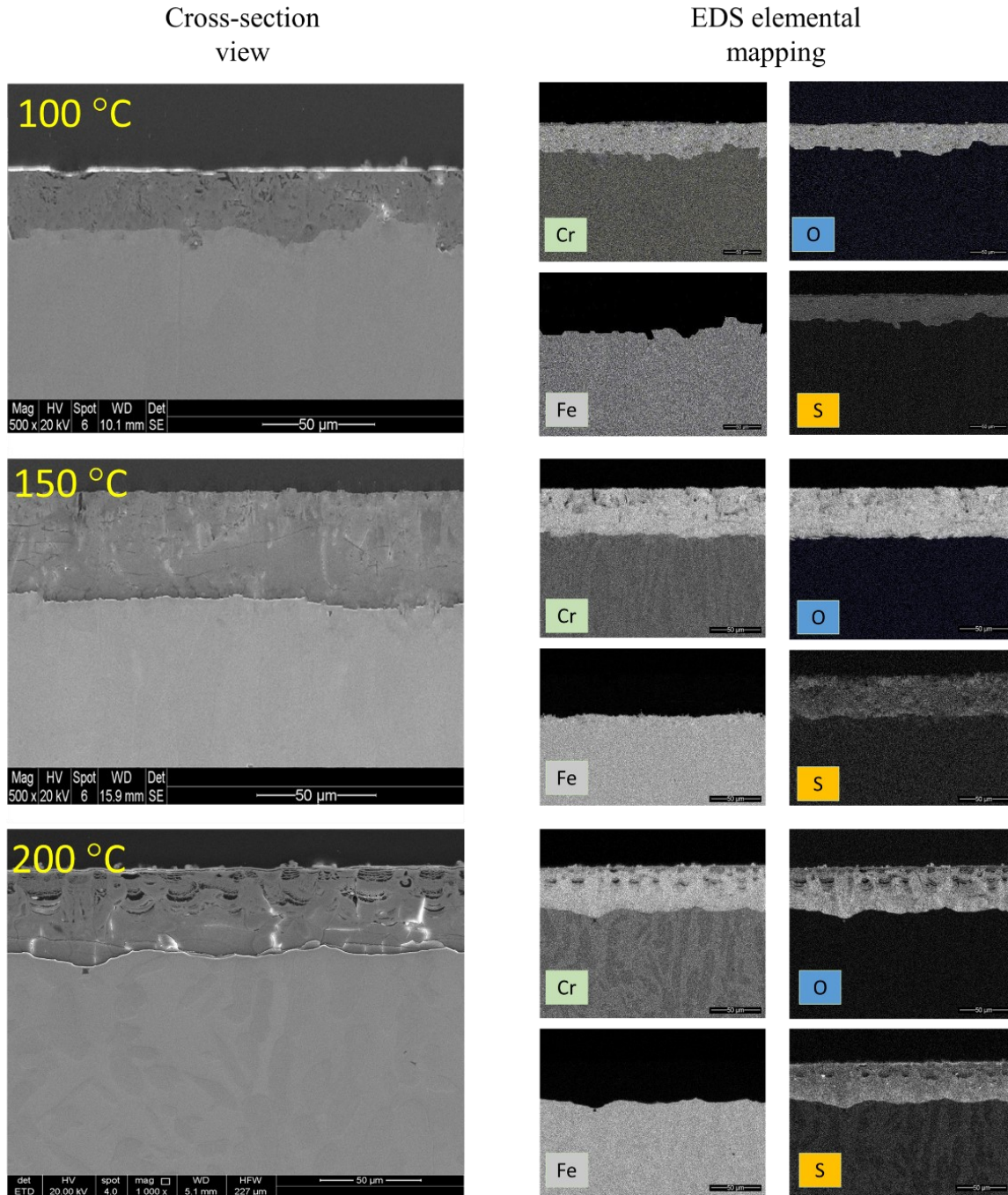


Fig. 3-12. Cross-sectional SEM views and corresponding elemental mapping of DSS 2205 steel after the exposure to in 0.05 M H_2SO_4 at different temperatures for 14 days.

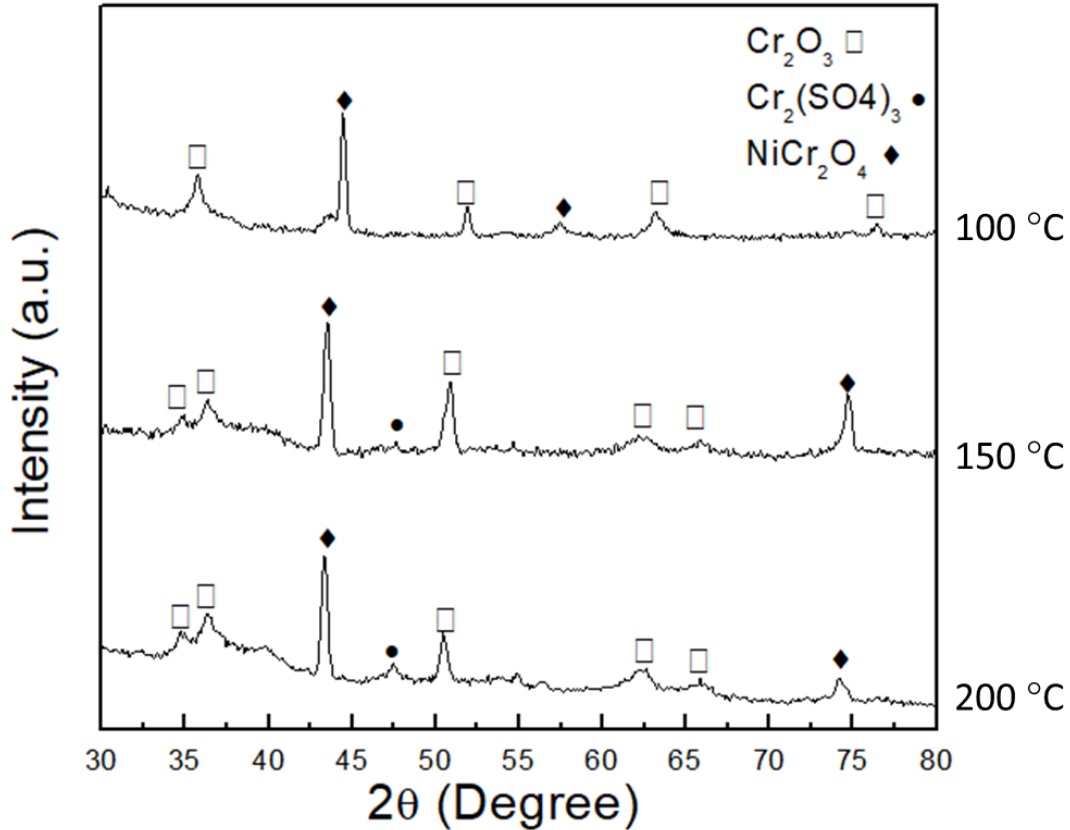


Fig. 3-13. XRD spectra collected on DSS 2205 steel samples after the exposure to 0.05 M H₂SO₄ at 100 °C, 150 °C and 200 °C, respectively.

The average corrosion rates of DSS 2205 in the hot dilute sulfuric acid were evaluated based on weight loss measurements as described above, and the results are presented in Fig. 3-14. The corrosion rate of the steel increased with temperature, and a remarkable increase in the rate occurred when increasing temperature from 100 to 150 °C, consistent with the SEM cross sectional results (see Fig. 3-12). These results further indicate that the formed continuous Cr oxide layer would become less protective to the Cr-bearing steel from the hot dilute acid attack at temperature ≥ 150 °C. Moreover, at the temperature range of 100 -200 °C, the corrosion rate of DSS 2205 was consistently lower than that of SS316L, confirming that increasing Cr content in stainless steels could partially improve their performance in the hot dilute sulfuric acid. However, such improvement is still insufficient to reach the target of long-term safe operation, since the corrosion rate of the duplex steel could be up to 1.25 mm/year at 200 °C and increase with exposure time

under the pre-hydrolysis conversion, exceeding the acceptable corrosion rates (1.0 mm/year) of similar batch reactors used in paper and pulp industries [254].

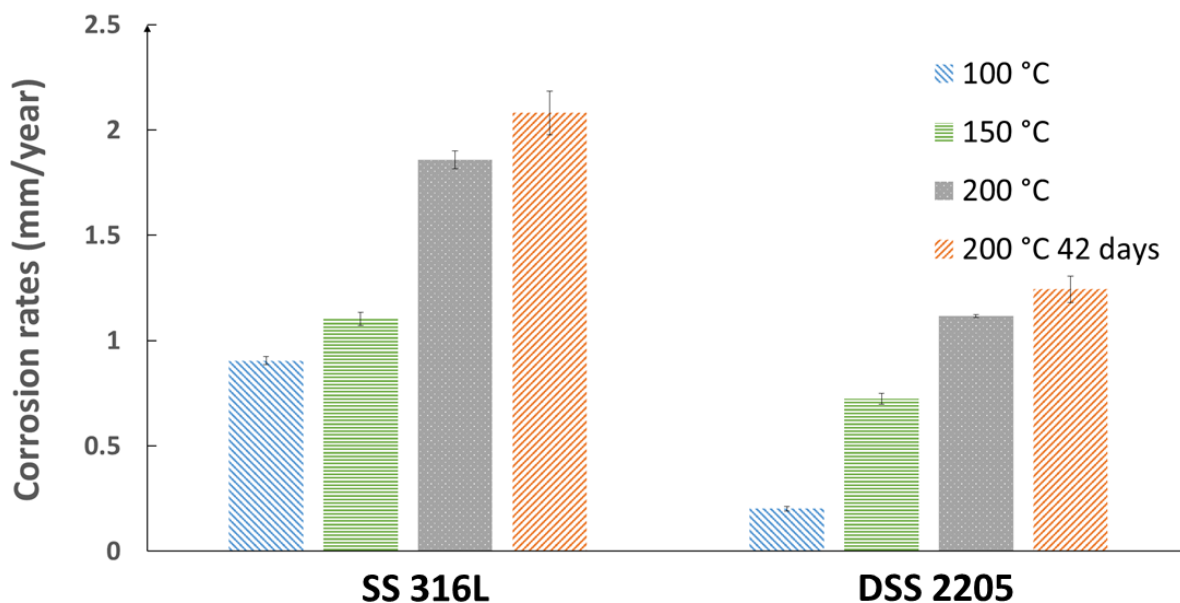


Fig. 3-14. Comparison of the average corrosion rates (mm/y) of SS316L and DSS 2205 steels in 0.05 M H₂SO₄ at pre-hydrolysis operating temperatures for different exposure durations.

3.3.2.2. Effect of alloying element Mo

As described above, Mo is another critical alloying element that can affect corrosion performance of Fe-based stainless steels and Ni-based alloys in the hot dilute sulfuric acid. To identify its effect, Alloy C-276 samples with 15.5 wt.% Mo were prepared and tested with two steel coupons in the same environment. Note that the Cr content in Alloy C-276 is slightly lower than that in SS316L. As shown in Fig. 3-15, the corrosion layers formed on Alloy C-276 were much thinner than those grown on SS316L and DSS 2505 since the grinding lines formed during sample preparation were still clearly visible after the exposures. Different from the two stainless steels, nodular oxidation did not occur on the Ni-based alloy. However, the deposited corrosion particles were still observed and their density likely increased with temperature, similar to that occurred on the two Fe-based steels. Moreover, no crack was found within the corrosion layer formed on the alloy. Furthermore, the cross-sectional image of Alloy C-276 after the exposure to 0.05 M H₂SO₄ at 200 °C for 14 day is presented in Fig. 3-16. Compared with the two stainless steels, a much more uniform, compact

and continuous surface oxide scale was formed on the alloy and its average thickness was significantly thinner ($< 2 \mu\text{m}$) than those grown on the two Fe-based steels.

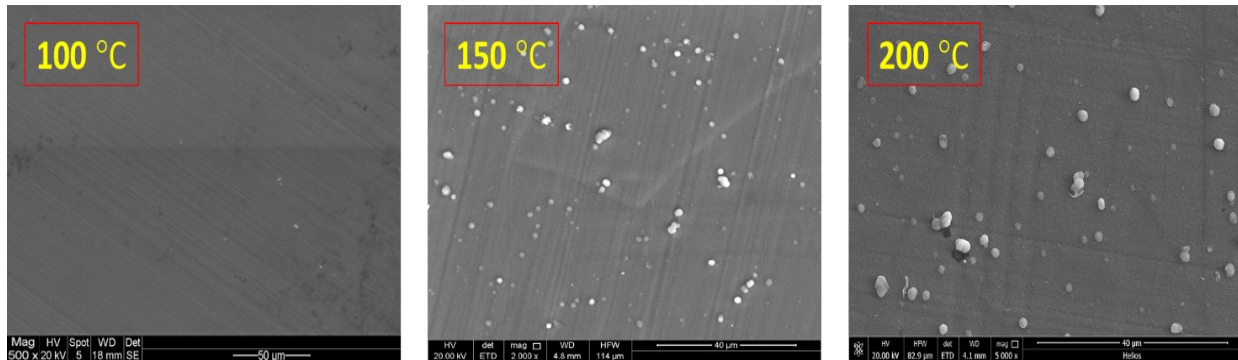


Fig. 3-15. Top-view SEM images of Alloy C-276 samples after corroding in 0.05 M H_2SO_4 at different pre-hydrolysis operating temperatures for 14 days, respectively.

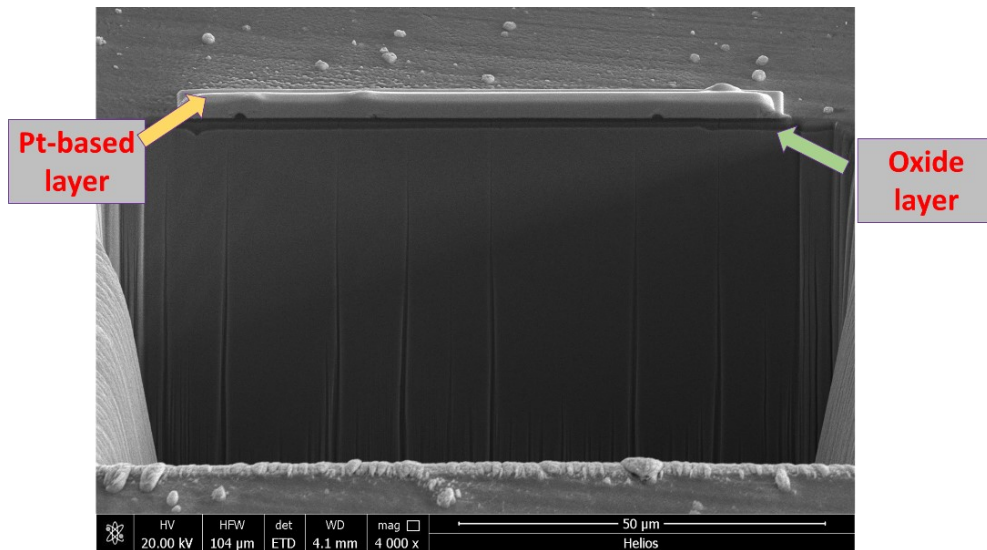


Fig. 3-16. Cross-sectional SEM view of Alloy C-276 after the exposure to 0.05 M H_2SO_4 at 200 °C for 14 days.

To further clarify the role of Mo in the formed surface oxide scales on Alloy C-276, TEM characterizations were conducted on the cross-sectional area of tested specimens, and the results are shown in Fig. 3-17. At the testing temperatures, the formed surface scales on the alloy were consisted of three different layers, including outer Cr oxide, middle Mo oxide/sulfate, and inner Mo/Cr oxide/sulfate layers. Both Fe and Ni elements were not found within the formed surface scales. However, the outer Cr oxide layer on Alloy C-276 was actually formed from the re-

deposition of dissolved Cr cations during the autoclave cooling-down, since only Zr oxides, instead of Cr oxides (see Fig. 3-18), could be naturally grown on Zr702 during the exposure to the hot dilute sulfuric acid. Note that Zr702 is composed of 99.2 wt.% of (Zr+Hf) with Hf content $\leq 4.5\%$, and the Cr content in the alloy is less than 0.2 % based on the chemical composition certificate provided by the supplier. Therefore, in the dilute sulfuric acid in the temperature range of 100-200 °C, the surface scale grown on the alloy was actually double-layer structure, i.e., composed of outer Mo oxide/sulfate and inner Mo/Cr oxide/sulfate layers. At 200 °C, a third layer, which was enriched in Mo sulfate and Cr cations, was present just above the substrate, suggesting that increasing temperature would enhance the outward diffusion of cations and inward diffusion of sulfate anions and the presence of more Mo sulfate might suppress Cr oxidation at the interface of oxide and substrate. Moreover, the thickness of the formed surface scale increased with temperature, from about 500 nm at 100 °C to ~950 nm to 200 °C, both of which were significantly thinner than those formed on the stainless steels, further confirming that the addition of Mo into the steels and alloys would remarkably protect them from dilute sulfuric acid attack at elevated temperatures. In addition, the selected area diffraction (SAD) patterns were collected on the formed oxide layers at different temperatures, the results indicated that the outer Mo oxide and inner Mo/Cr oxide layers both had amorphous structure.

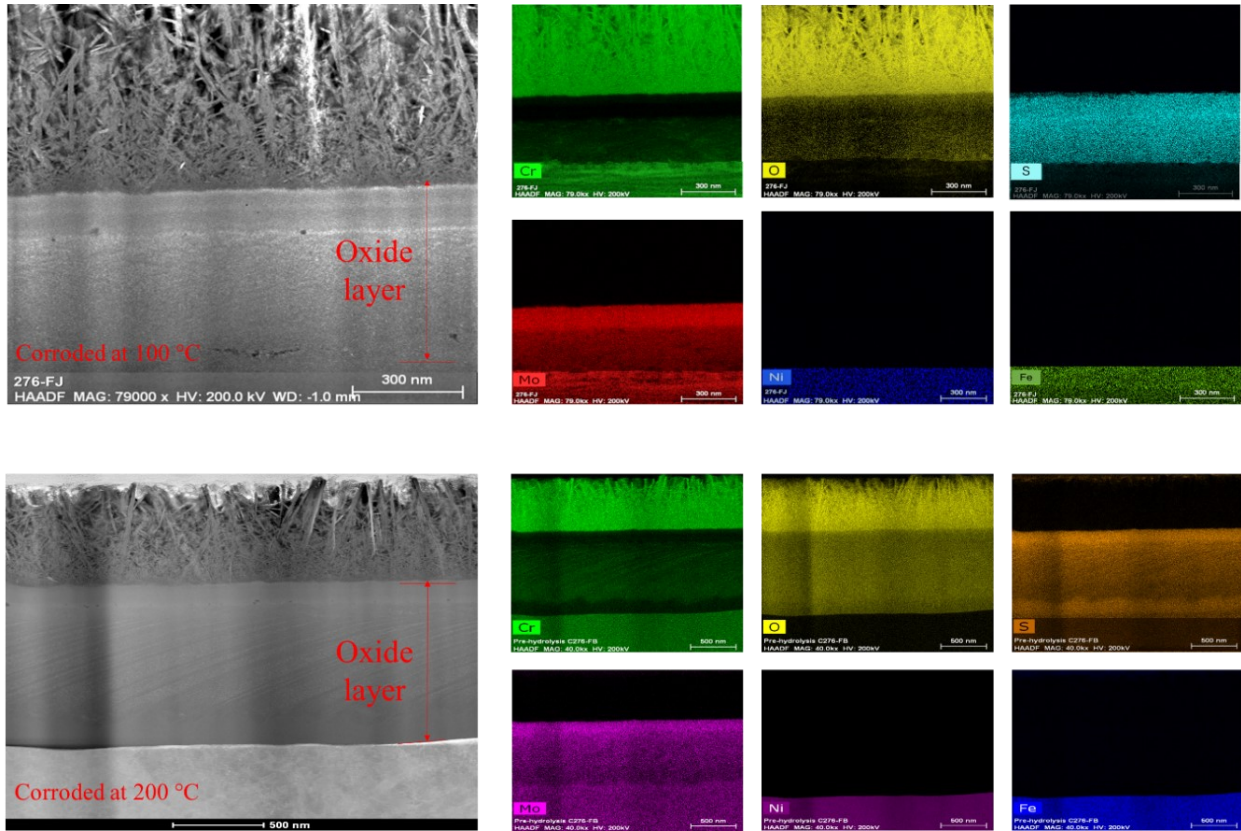


Fig. 3-17. Cross-sectional high-resolution TEM images and corresponding elemental mapping of Alloy C-276 samples after corroded in 0.05 M H₂SO₄ at 100 °C and 200 °C for 14 days, respectively.

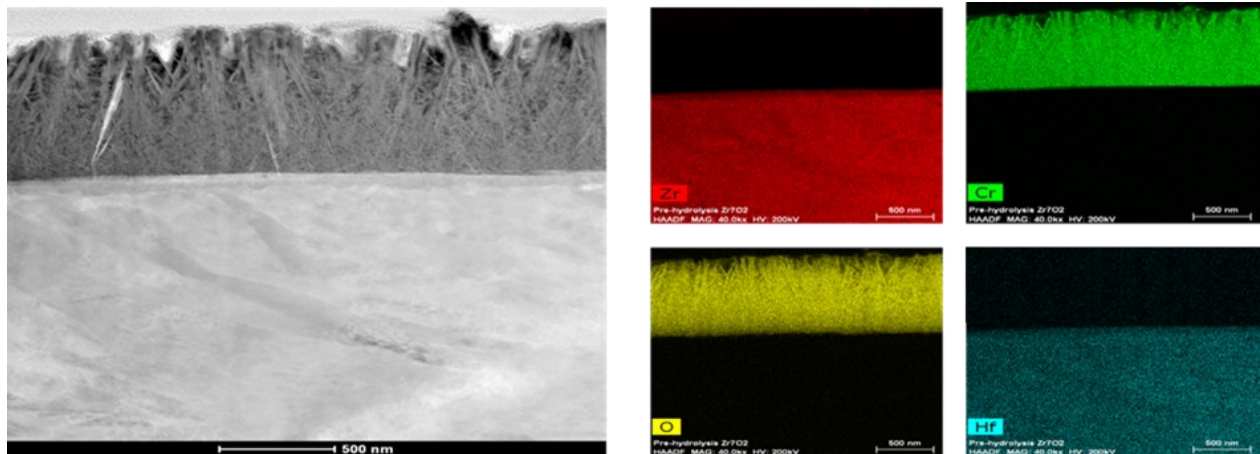


Fig. 3-18. Cross-sectional high-resolution TEM images and corresponding elemental mapping results of Zr7O₂ after the exposure to 0.05 M H₂SO₄ along with other tested alloys at 200 °C.

The variation of the average corrosion rates of Alloy C-276 with temperature and time in 0.05 M H₂SO₄ is shown in Fig. 3-19. The corrosion rate of the alloy only slightly increased with temperature and exposure time, and the maximum rate (0.04 mm/year) occurred at 200 °C after 42 days of exposure, significantly lower than those of the two Fe-based steels. The results in Figs. 3-16, 17 and 19 clearly demonstrate that the addition of element Mo into the steels and alloys could remarkably enhance their resistance to the dilute sulfuric acid at the temperature range of 100-200 °C. Detailed discussion about the role of Mo on corrosion is presented in the Discussion section.

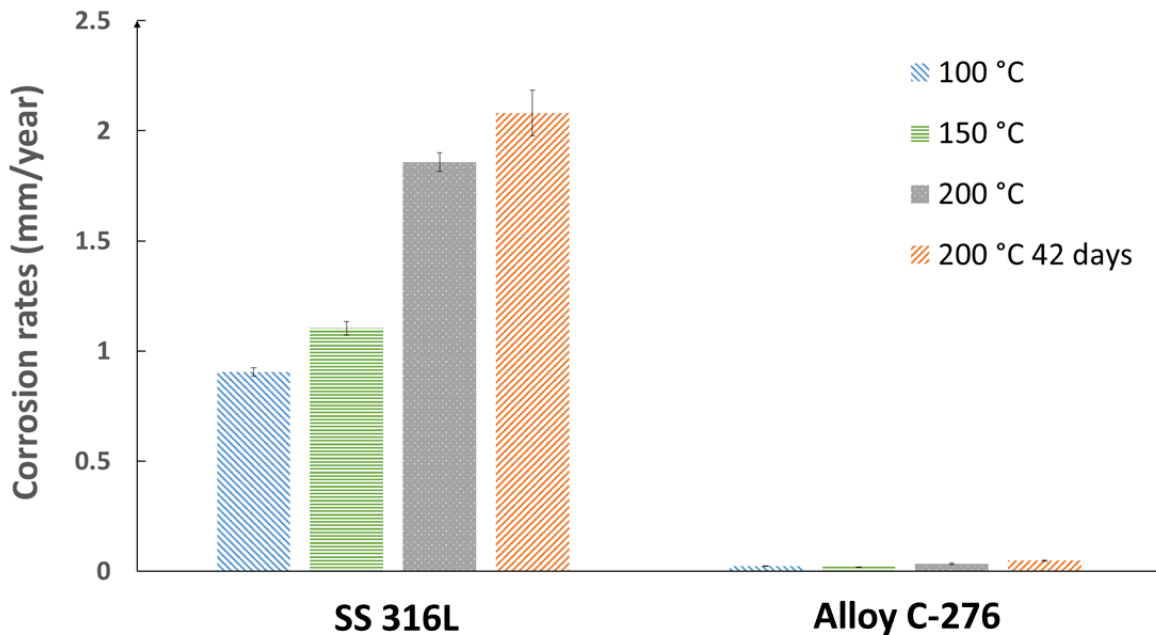


Fig. 3-19. Comparison of the average corrosion rates (mm/y) of SS316L and Alloy C-276 in 0.05 M H₂SO₄ at the temperature range of 100-200 °C for different exposure duration.

3.3.3. Effect of inorganic corrodants and biomass

The photographic images of alloy coupons before and after exposure to 0.05 M H₂SO₄ + 700 ppm Cl⁻ + 500 ppm S²⁻ and 0.05 M H₂SO₄ + 25 wt.% biomass at 200 °C are shown in Fig. 3-20, respectively. Because of the acidic environment created by sulfuric acid solution, sulfide would likely be oxidized and form thiosulfate or other compounds. After the exposure to 0.05 M H₂SO₄ with inorganic corrodants at 200 °C, the surface appearances of SS316L and DSS 2205 were similar to that in 0.05 M H₂SO₄ only. Different from the two stainless steels, Alloy C-276 exhibited

more brownish appearance after tested in inorganic corrodants-containing solution compared to those in the dilute acid only. With the addition of inorganic corrodants into the hot dilute acid, SS316L and DSS 2205 still experienced more severe corrosion damage than Alloy C-276. However, the presence of oxidized sulfur/sulfate contents did not trigger pitting corrosion on the three alloys. Interestingly, the addition of raw wood biomass into 0.05 M H₂SO₄ resulted in darker surface on all three alloys, implying that either the formed corrosion products might become thicker or biorefining by-products might be deposited on the alloy surfaces during the exposure.

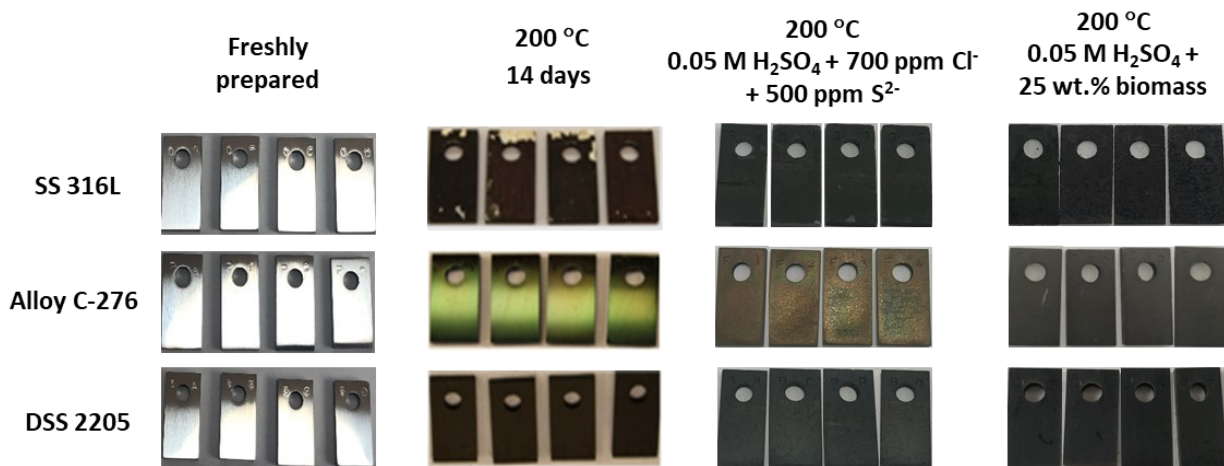


Fig. 3-20. Photographic images of testing coupons taken before and after the exposure to different testing solutions at 200 °C for 14 days.

To further clarify the influence of inorganic and organic compounds on corrosion in the hot dilute sulfuric acid, SEM/EDS/XRD/TEM techniques were employed to examine the alloy samples after the exposures. For SS316L, the top- and cross-sectional SEM images (see Fig. 3-21 and 3-22) indicated that the presence of several hundred ppm of inorganic corrodants (S²⁻ and Cl⁻) or the introduction of softwood in the hot dilute sulfuric acid enhanced nodular oxidation and micro-crack formation compared to that indicated in Fig. 3-4 at 200 °C. As shown in Fig 22, the presence of 700 ppm Cl⁻ and 500 ppm S²⁻ made the formed surface scale more porous with higher density of micro-cracks and enhanced localized oxide dissolution along the cracks down to the substrate compared to that presented in Fig. 3-5(c) at 200 °C, but the average thickness of the formed corrosion layer was close to that grown in 0.05 M H₂SO₄ at 200 °C. Interestingly, EDS mapping results showed that sulfur was not only present within the corrosion layer, but also accumulated on the steel. This implied that the enhanced nodular oxidation might be associated with the formed sulfur-contained oxides (such as Cr₂(SO₄)₃). The mapping results also showed that the formed

corrosion layer was mainly composed of Cr, O and S, similar to that in 0.05 M H₂SO₄. In the biomass-containing environment, severe localized attack was found and localized oxide dissolution along the cracks was obviously developed within the steel. The introduction of biomass also led to the formation of much thinner corrosion layer than those formed in 0.05 M H₂SO₄ and in inorganic corrodants containing solutions (see Fig 5 and 22), implying that the presence of biomass might either remarkably accelerate the chemical dissolution of corrosion layer or suppress the hot dilute acidic attack. The EDS mapping results indicated that the formed corrosion scale was mainly consisted of Cr, O and S. The S content within the corrosion layer was possibly higher than those grown in 0.05 M H₂SO₄ or inorganic corrodants-contained solution. In addition, XRD characterizations (see Fig. 3-23) showed the corrosion layers formed under the two testing conditions were mainly composed of Cr₂O₃ and Cr₂(SO₄)₃, similar to those exposed to 0.05 M H₂SO₄ only. The peaks of nickel-chromium spinel oxide and iron sulfate were also found. They were possibly collected from the deposition particles on the steel during autoclave cooling-down.

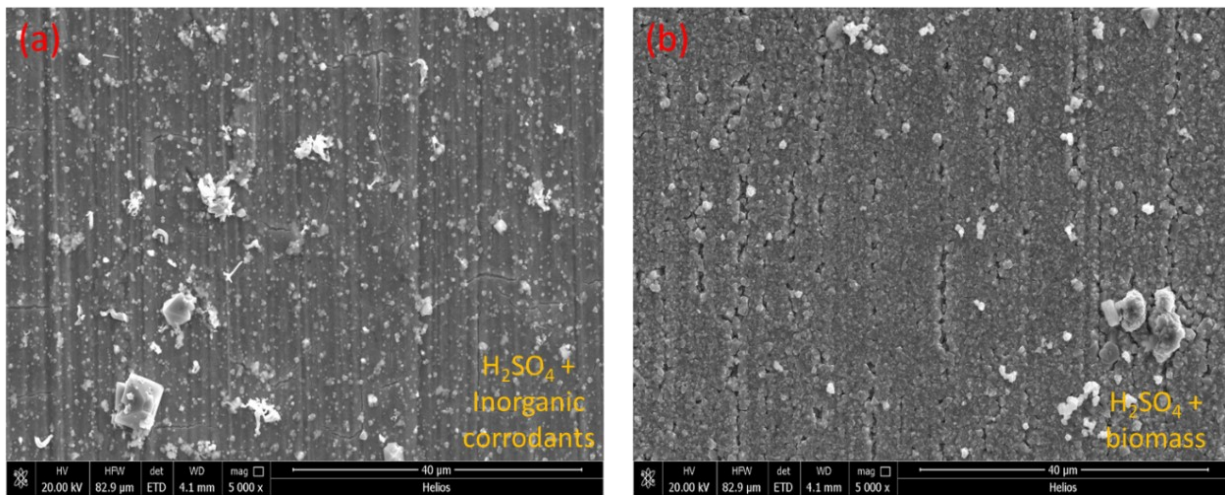


Fig. 3-21. Top-view SEM images of SS316L steel samples after corroded in (a) 0.05 M H₂SO₄ + 700 ppm Cl⁻ + 500 ppm S²⁻; and (b) 0.05 M H₂SO₄ + 25 wt.% biomass at 200 °C for 14 days, respectively.

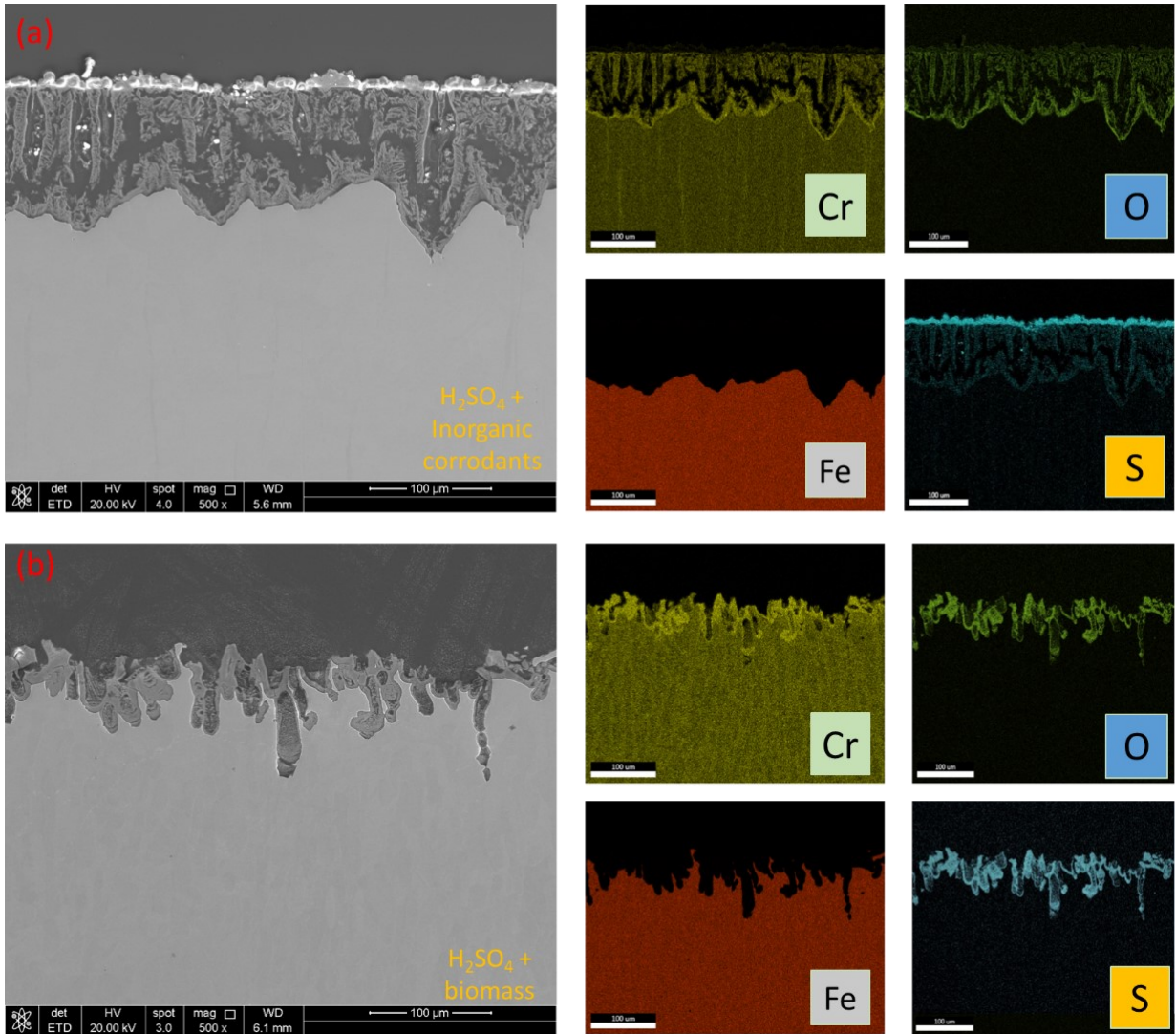


Fig. 3-22. Cross-sectional SEM views of SS316L steel and corresponding elemental mappings of Cr, Fe, O, and S after corroding in (a) 0.05 M H_2SO_4 + 700 ppm Cl^- + 500 ppm S^{2-} ; and (b) 0.05 M H_2SO_4 + 25 wt.% biomass at 200 °C for 14 days, respectively.

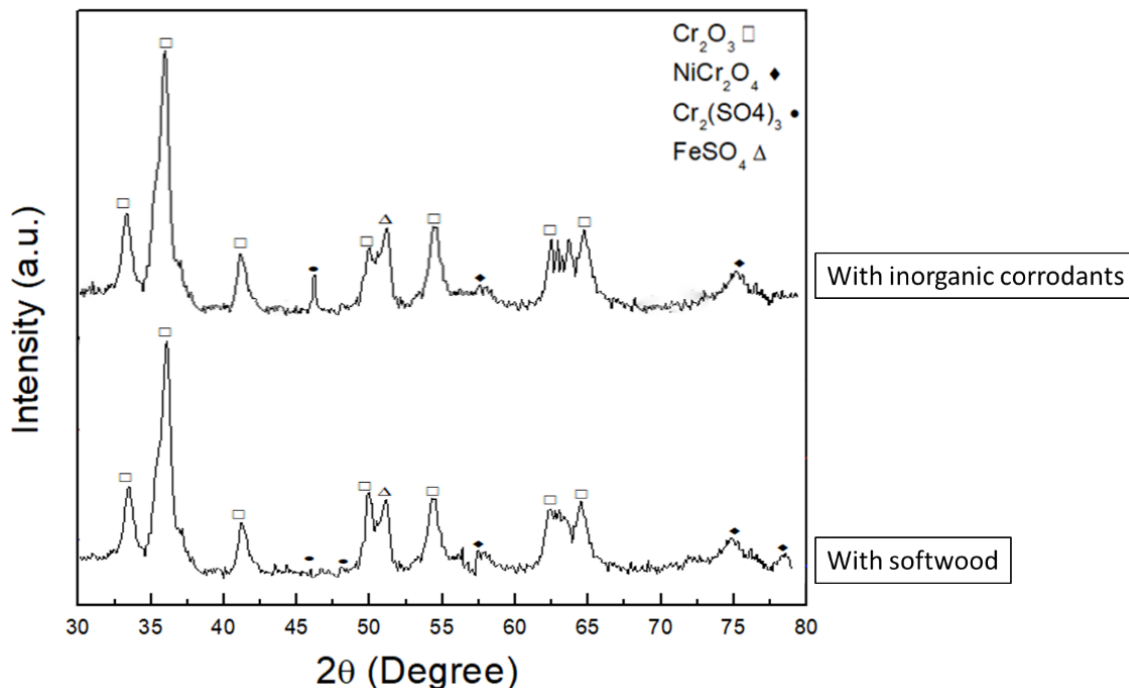


Fig. 3-23. XRD spectra collected on SS316L steel samples after the exposure to 0.05 M H₂SO₄ with inorganic corrodants and softwood at 200 °C, respectively.

Figs. 3-24 and 3-25 show the microscopic structure of the corrosion layers formed on Cr-bearing DSS 2205 steel after the exposures to the two biorefining conditions. Compared to that grown in 0.05 M H₂SO₄ at 200 °C (see Figs. 3-11 and 3-12), localized nodular oxidation was promoted, and general corrosion was enhanced with the presence of inorganic corrodants, since the formed layer was noticeably thicker. Compared with SS316L, the influence of S²⁻ and Cl⁻ on the micro-crack formation was less severe on DSS 2205. In the biomass-containing environment, the introduction of softwood was likely to facilitate the formation of microcracks, which act as “windows” for the migration of aggressive ions down to the substrate. Interestingly, the corrosion layer formed on DSS 2205 in the biomass-containing solution was noticeably thinner and less uniform than those grown in 0.05 M H₂SO₄ and inorganic corrodants-containing solutions, similar to that of SS316L. In addition, EDS mapping and XRD characterization results (see Figs. 3-25 and 3-26) revealed that the corrosion layer formed on the steel in inorganic corrodants or biomass-containing solutions was mainly composed of Cr₂O₃ and Cr₂(SO₄)₃, similar to that exposed to 0.05 M H₂SO₄. Nickel-chromium spinel oxide peaks were also found and likely attributed to the deposit particles on the surface. The results implied that the addition of inorganic corrodants or softwood remarkably

changed the oxide layer thickness and morphology, but only had marginal effect on the phase composition of the layer. Based on the results shown in Figs. 3-22 and 3-24, increasing Cr content in the steels would, to some degree, improve their resistance to the two biorefining environments.

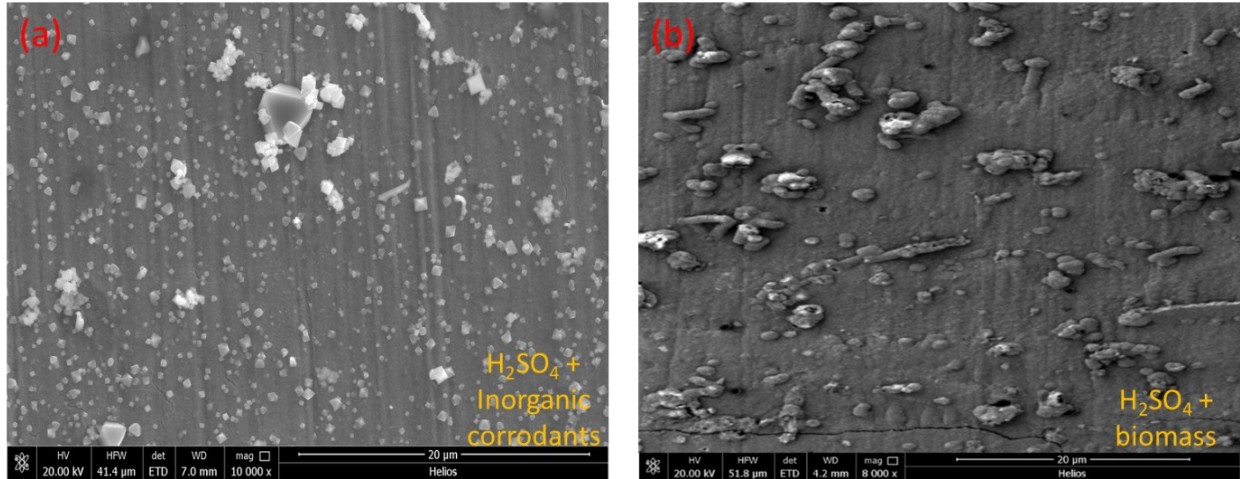


Fig. 3-24. Top-view SEM images of DSS 2205 samples after corroding in (a) 0.05 M $H_2SO_4 + 700$ ppm $Cl^- + 500$ ppm S^{2-} ; and (b) 0.05 M $H_2SO_4 + 25$ wt.% biomass at 200 °C for 14 days, respectively.

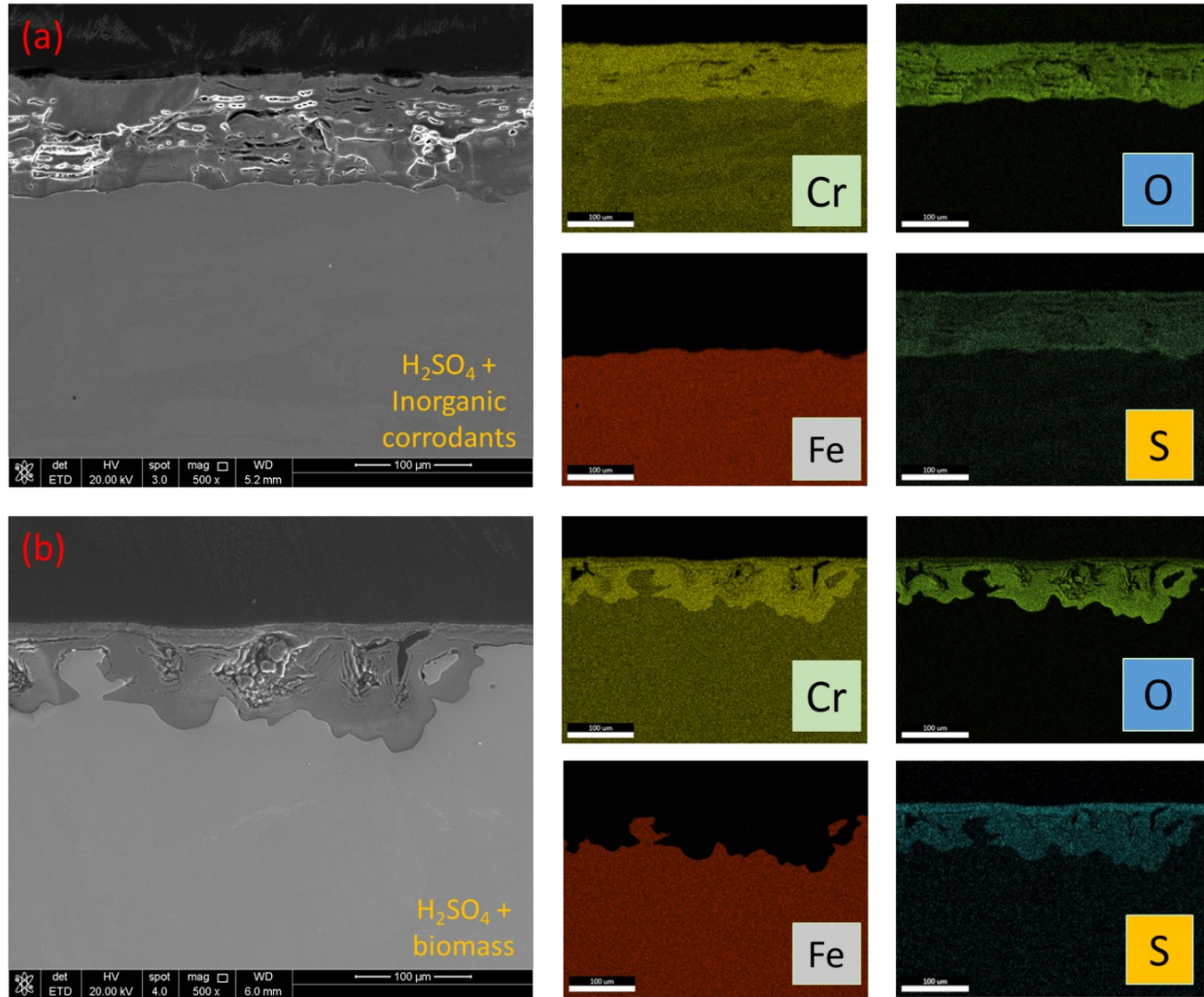


Fig. 3-25. Cross-sectional SEM view of DSS 2205 steel and corresponding elemental mapping of Cr, Fe, O, and S after corroding in (a) 0.05 M H₂SO₄ + 700 ppm Cl⁻ + 500 ppm S²⁻; and (b) 0.05 M H₂SO₄ + 25 wt.% biomass at 200 °C for 14 days, respectively.

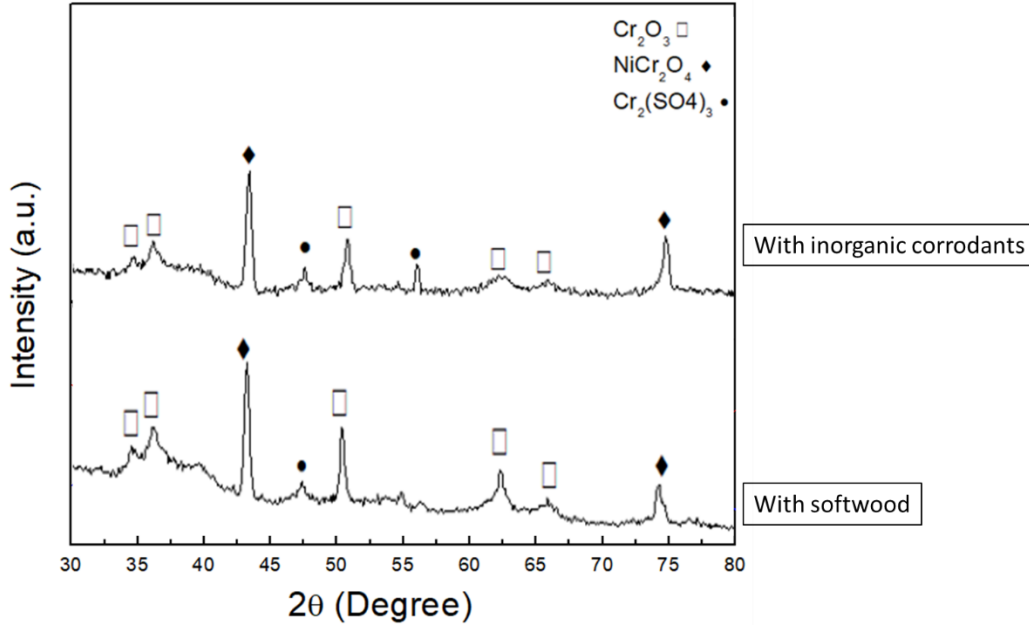


Fig. 3-26. XRD spectra collected on DSS 2205 steel samples after the exposure to 0.05 M H₂SO₄ with inorganic corrodants and softwood at 200 °C, respectively.

For Mo-bearing Alloy C-276, the top-view SEM images (see Fig. 3-27) indicated that the presence of several hundred ppm of inorganic corrodants (S²⁻ and Cl⁻) in the hot acid solution promoted the formation of needle-shaped oxides compared to that shown in Fig. 3-15. Moreover, the existence of softwood in the acid seemed to enhance nodular oxides formation on the alloy. As the oxide layers on the alloy were quite thin, FIB/TEM techniques were applied for their examination, and the results are shown in Fig. 3-28. With the addition of inorganic corrodants or softwood into the 0.05 M H₂SO₄, the formed surface scale was consisted of only a uniform and compact Mo-enriched oxide layer with small amounts of sulfates and Cr cations. Note that the outer Cr oxides were produced from the re-deposition of dissolved corrosion products during the autoclave cooling-down as demonstrated in Fig. 3-18. In the inorganic corrodant-containing solution, the average thickness of surface scale was around 900 nm, close to that formed in 0.05 M H₂SO₄, indicating that the presence of several hundred ppm of inorganic corrodants (S²⁻ and Cl⁻) would not apparently damage the protectiveness of Mo-enriched oxide layer formed on the alloy. Moreover, little amount of Cr was present in the layer comparing to that shown in Fig. 3-17, suggesting that the existence of aggressive S²⁻ and Cl⁻ ions might, more or less, enhance the selective dissolution of Cr cations into the hot acid solution. In the biomass-containing solution, the average thickness of

the formed layer was around 280 nm, thinner than those formed in 0.05 M H₂SO₄ and inorganic corrodants-containing solutions. In addition, elemental S was detected in the Mo-enriched oxides formed under the two biorefining conditions, similar to that grown in 0.05 M H₂SO₄ alone.

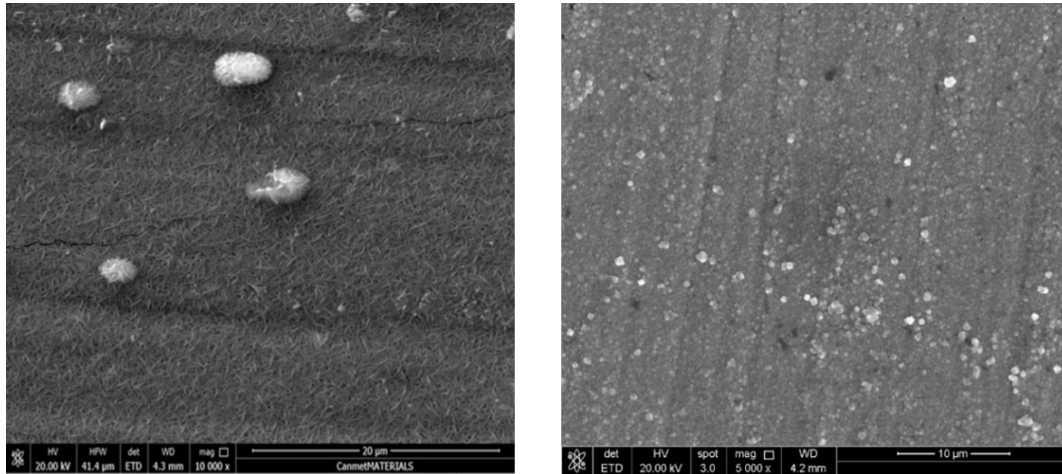


Fig. 3-27. SEM top-view images of Alloy C-276 samples after corroding in (a) 0.05 M H₂SO₄ + 700 ppm Cl⁻ + 500 ppm S²⁻; and (b) 0.05 M H₂SO₄ + 25 wt.% biomass at 200 °C for 14 days, respectively.

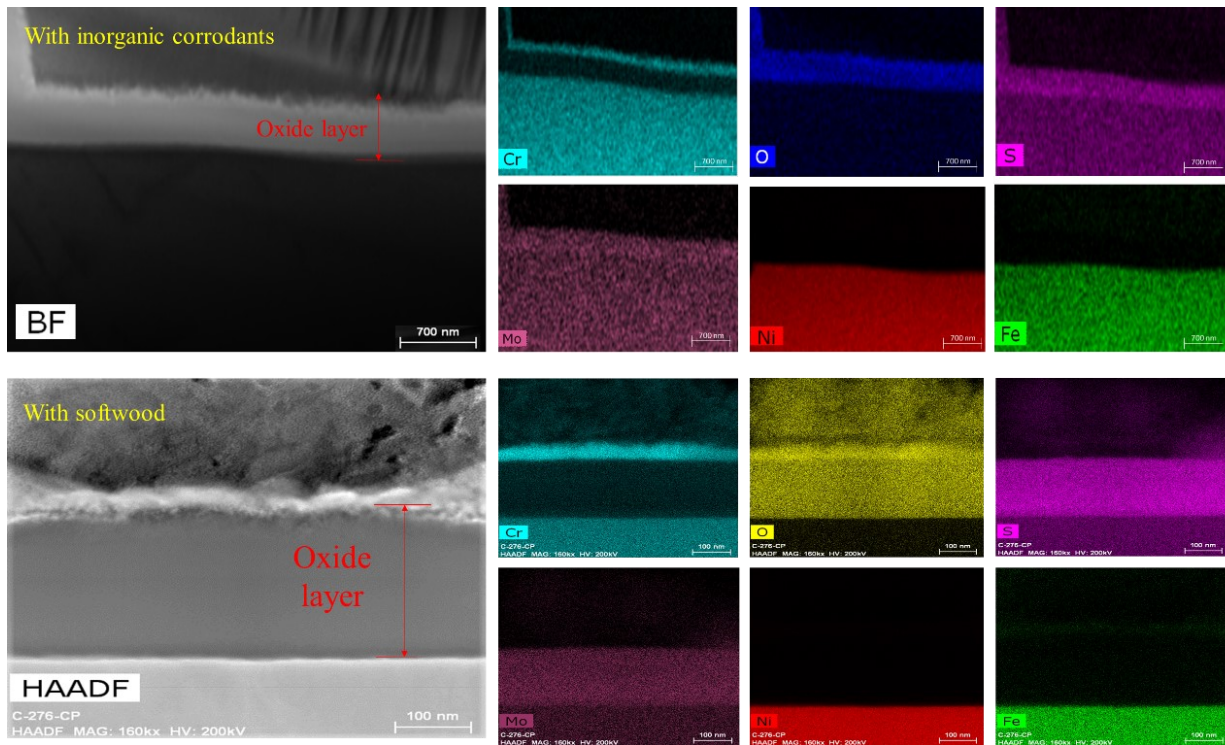


Fig. 3-28. Cross-sectional high-resolution TEM images and corresponding elemental mapping of Alloy C-276 samples after corroding in 0.05 M H₂SO₄ with addition of inorganic corrodants and softwood at 200 °C for 14 days, respectively.

The effects of inorganic and organic corrodants on the average corrosion rates of the three alloys are shown in Fig. 3-29. For SS316L, its corrosion rate was increased with the addition of S^{2-} and Cl^- ions, consistent with the cross-sectional characterization results, i.e., the presence of these inorganic corrodants led to the formation of more porous oxide scales along with micro-cracks penetrating down to the substrate (see Figs. 3-5 and 3-22). The addition of 25% softwood into 0.05 M H_2SO_4 , on the other hand, did not result in a noticeable increase in the corrosion rate. As described above, the introduction of biomass led to the formation of thinner corrosion layers compared to those formed in 0.05 M H_2SO_4 and inorganic corrodant-containing solutions. Thus, it was possible that the presence of softwood and its organic by-products might suppress the general corrosion of the steel. Another possibility is that the consumption of sulfuric acid for the conversion of softwood might change the solution chemistry, making it less aggressive to Cr_2O_3 and $Cr_2(SO_4)_3$. Nevertheless, the influence of softwood on localized corrosion could not be ignored as shown in Fig. 3-22.

The influence of inorganic corrodants on the corrosion rates of Cr-bearing DSS 2205 steel was similar to those on SS316L. Different from SS316L, the addition of 25% softwood led to a slight increase in the corrosion rate of DSS 2205. This may be mainly attributed to the observation that the presence of softwood could enhance the formation of micro-cracks within the surface layer and consequently enhance the migration of aggressive ions from solution to the substrate (see Fig. 3-25). However, it should be mentioned that the corrosion rate of DSS 2205 was consistently lower than that of SS316L under three different biorefining conditions at 200 °C, suggesting that increasing Cr content in the steels could improve their corrosion performance under the pre-hydrolysis biorefining conditions. For Mo-bearing Alloy C-276, the addition of inorganic and organic corrodants only had marginal impacts on its corrosion rate. Different from DSS 2205, the introduction of softwood led to a slight decrease in the corrosion rate of Alloy C-276. Based on the results in Figs. 3-28 and 3-29, it was possible that the presence of softwood might suppress general oxide formation and chemical dissolution. In the three testing environments, Alloy C-276 exhibited the best performance and would be the most promising candidate of construction from the corrosion point of view.

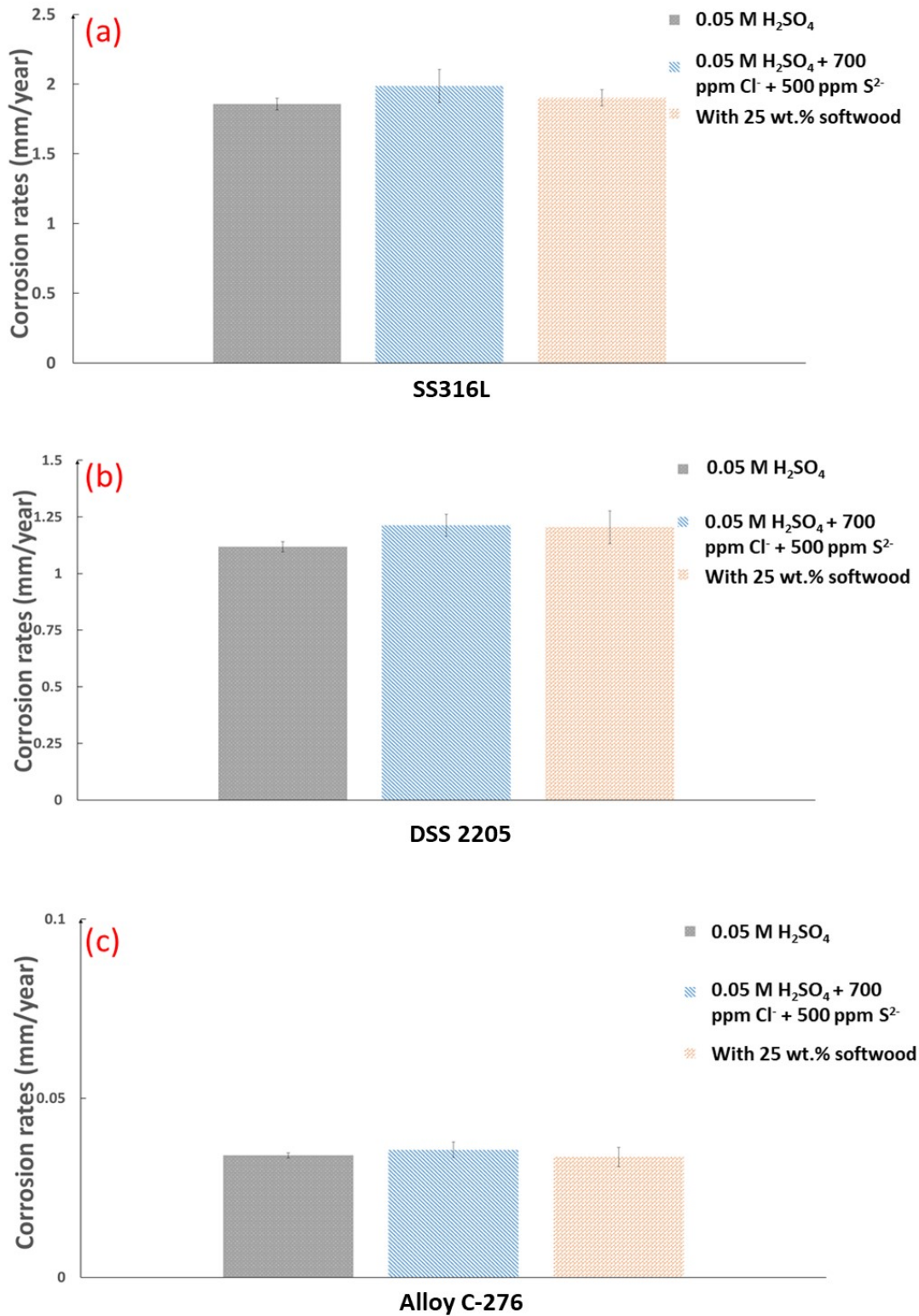


Fig. 3-29. Comparison of the average corrosion rates (mm/y) of (a) SS316L, (b) DSS 2205, and (c) Alloy C-276 in three different biorefining solutions at 200 °C after 14 days' exposure, respectively.

3.4. Discussion

In the pre-hydrolysis biorefining environments, the Nernst equation of an electrochemical reaction ($aA + mH^+ + ne^- = bB + cH_2O$) occurred on the tested alloys can be calculated by [255, 256]

$$E_T = E_T^0 - 2.303 * \frac{mRT}{nF} * pH - 2.303 * \frac{RT}{nF} * \lg\left(\frac{a_B^b}{a_A^a}\right) \quad (3-2)$$

where E_T^0 and E_T stand for the standard electrochemical potential and electrochemical potential at temperature T , respectively; R is the gas constant; a_A or a_B is the overall activity of species A or B. Note that the dissolved concentrations of ions in the equation could be assumed to be 10^{-6} mol/L and the activities of solid to be unity [255, 257, 258]. At a designated pre-hydrolysis operating temperature, the standard electrochemical potential (E_T^θ) of the reaction ($aA + mH^+ + ne^- = bB + cH_2O$) is calculated by:

$$E_T^\theta = -\frac{\Delta G_T^\theta}{nF} \quad (3-3)$$

where ΔG_T^θ is the Gibbs free energy of the reaction at the designated temperature (J), F is the Faraday constant (96485 C/mol), and n is the number of electrons transferred in the reaction (mol). The Gibbs free energy can be calculated by:

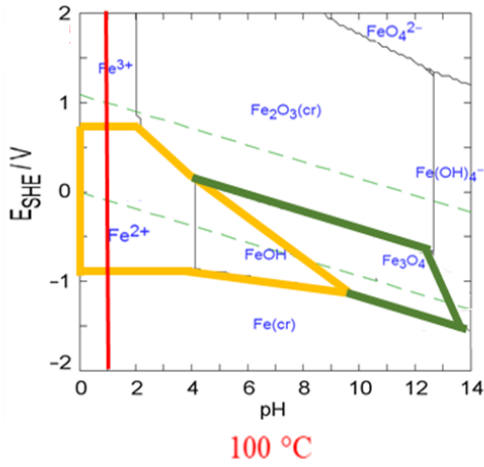
$$\Delta G_T^\theta = \Delta G_{298}^\theta - (T - 298)S_{298}^\theta + \int_{298}^T C_p dT - T \int_{298}^T C_p \frac{dT}{T} + \int_{P_v}^P V dP \quad (3-4)$$

where ΔG_{298}^θ stands for the Gibbs free energy of formation of the species at room temperature; S_{298}^θ represents for the entropy at room temperature, C_p is the heat capacity for the specie; $\int_{P_v}^P V dP$ is related to the pressure term and determined to be negligible in this study. At a hot dilute pre-hydrolysis operating temperature, the Pourbaix diagram of a major alloying element (Cr, Ni, Fe or Mo) could thus be constructed based on pre-existing databases provided in the references [255, 256, 259-263] and the following assumptions:

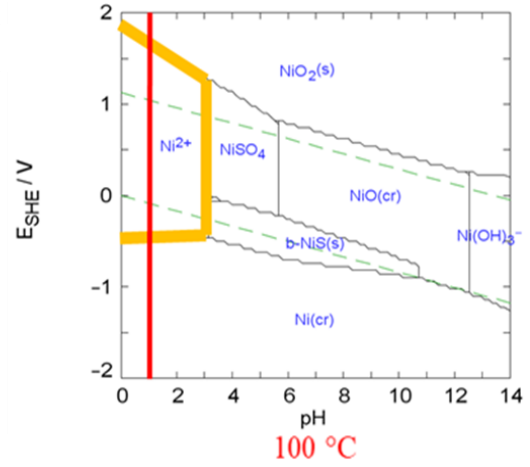
- (1) The effect of pressure on thermodynamic properties of an aqueous specie or solid in dilute sulfuric acid was neglected since the properties would be much more sensitive to operating temperature;

- (2) Due to the lack of experimental data, the activity coefficient of a solid or aqueous species at elevated temperatures could be assumed to be unity, similar to those used in former studies [257, 264, 265];
- (3) The reaction solution could be treated as an ideal dilute solution with limited concentration of cations and anions, making the activity of a solute very close to its concentration in solution.

As shown in Fig. 3-30, the calculated Pourbaix diagrams predict that alloying elements Fe and Ni could not form stable oxides in 0.05 M H₂SO₄ even at 100 °C and would suffer active corrosion under the biorefining conditions. Compared with Fe and Ni, Cr is generally recognized as a corrosion-resistant alloying element in many harsh environments [266-268]. As implied in Fig. 3-31, however, Cr would also experience active corrosion instead of passivation in the dilute acidic pre-hydrolysis environments at the temperature range of 100 - 200 °C. This is consistent with the above testing results of SS316L and DSS 2205, i.e., increasing Cr content in the steels even up to 22.5% still could not provide sufficient resistance to the hot dilute sulfuric acid attack. Different from the above alloying elements, Mo would undergo either passivation to form MoO₂ or active corrosion to generate dissolvable Mo³⁺ ions during the pre-hydrolysis conversion processes (see Fig. 3-32). Note that former studies indicated that stable MoO₂ instead of MoO₃ should be formed on Ni-Cr-Fe-Mo alloys in the spontaneous passivation region when exposed to acidic solutions [269, 270]. Moreover, increasing temperature is likely to push the passivation region to higher pH area, possibly making the element Mo suffer active corrosion in 0.05 M H₂SO₄ at 200 °C. However, this is different from the results shown in Figs. 3-17 and 3-19, suggesting that the corrosion of Mo-bearing Alloy C-276 would be dominated by the formation and chemical dissolution rates of oxides formed on the alloy.

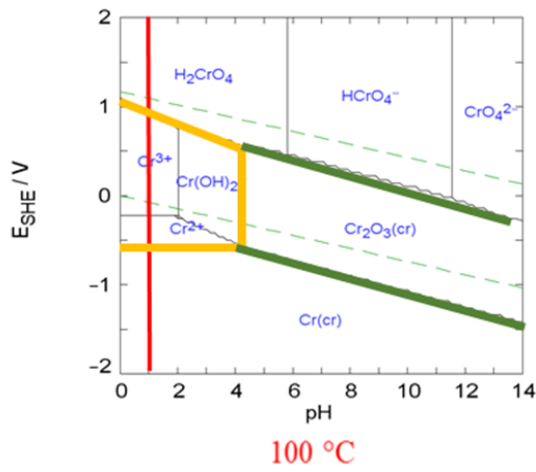


(a)

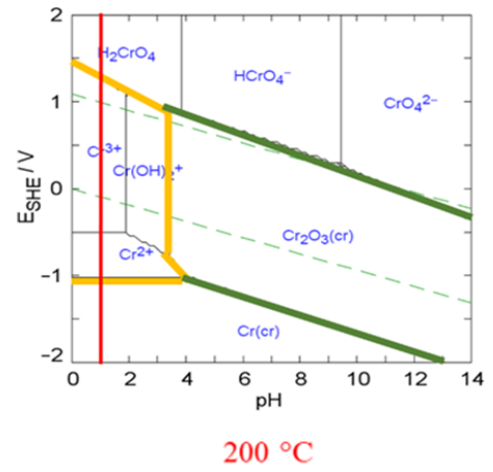


(b)

Fig. 3-30. Established Pourbaix diagrams at 100 °C: (a) Fe-0.05 M H₂SO₄ system, and (b) Ni-0.05 M H₂SO₄ system.



(a)



(b)

Fig. 3-31. Established Pourbaix diagrams of Cr-0.05 M H₂SO₄ system at (a) 100, and (b) 200 °C, respectively.

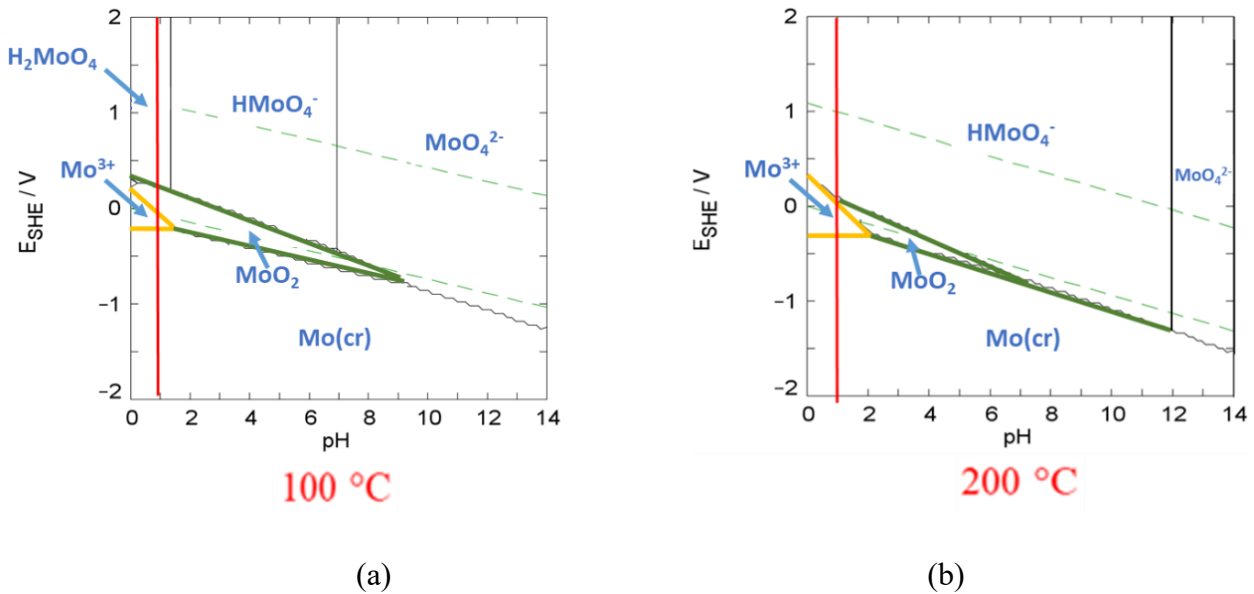


Fig. 3-32. Established Pourbaix diagrams of Mo-0.05 M H₂SO₄ system at (a) 100, and (b) 200 °C, respectively.

According to the above thermodynamic simulations, it is very likely that the corrosion process of the three tested alloys in the hot dilute acid would be dominated by the formation and dissolution rates of corrosion layers formed on their surface. As predicted in Table 3-3, the corrosion layers formed on SS316L, Cr-bearing DSS 2205 and Mo-bearing Alloy C-276 would likely be composed of Cr/Fe oxides/sulfates, Cr oxides/sulfates, and Cr/Mo oxides/sulfates, respectively. Note that except Ni, other major alloy elements Fe, Cr and Mo in the tested alloys could spontaneously react with the solution to form oxides and sulfates. However, as shown in Figs. 3-5 and 3-6, the corrosion layer on SS316L was mainly consist of Cr₂O₃ along with small amounts of Cr₂(SO₄)₃. This could be attributed to the difference between the chemical dissolution rates of Cr₂O₃ and Fe₃O₄. In the hot dilute sulfuric acid, the dissolution rates of iron oxides have been found to be remarkably higher than that of Cr₂O₃ [271-273], and increase with temperature based on previous studies [274, 275], making the formed iron oxides readily dissolve into 0.05M H₂SO₄ at the temperature range of 100 -200 °C and resulting in only chromium oxides/sulfates left on SS316L. This could also lead to the corrosion rate of DSS 2205 being noticeably lower than that of SS316L in the hot dilute sulfuric acid, as shown in Fig. 3-14, since the surface scales formed on Cr-bearing DSS 2205 should consist of Cr-enriched oxides/sulfates as indicated in previous studies in high temperature aqueous solutions [276, 277].

Different from the two stainless steels, Mo-enriched oxides/sulfates were present on Alloy C-276 after the exposures to the hot dilute acid (see Fig. 3-17). Although the dissolution rate of Mo oxides in dilute sulfuric acid is not available based on our literature review, it would be expected to be much lower than that of Cr₂O₃ based on the previous studies [208, 209, 278] and the observations in Fig. 3-17. Once a thin Mo-enriched oxide layer is formed on the alloys, the further growth of the oxide layer will depend on the inward diffusion of oxygen ions and outward diffusion of Mo/Cr cations within the layer. As implied in former studies [279, 280], the diffusion rate of Cr in Mo oxide would be quite low. Thus, the above two factors could result in a surface scale on Alloy C-276 composed of outer Mo oxide and inner Mo/Cr oxide layers, consequently making the alloy exhibit lower corrosion rate compared to that of stainless steels, as shown in Fig. 3-19.

Table 3-3. Gibbs energy of Fe, Cr, Ni and Mo oxides and sulfates formation with water and sulfuric acid at 100 and 200 °C, respectively [281, 282, 283].

Reaction	100 °C (kJ/mol)	200 °C (kJ/mol)
$2Fe + 3H_2O = Fe_2O_3 + 3H_2$	-45.035	-63.767
$2Fe + 3H_2SO_4 = Fe_2(SO_4)_3 + 3H_2$	-206.535	-219.634
$2Cr + 3H_2O = Cr_2O_3 + 3H_2$	-357.327	-376.379
$2Cr + 3H_2SO_4 = Cr_2(SO_4)_3 + 3H_2$	-517.656	-527.740
$Ni + H_2O = NiO + H_2$	20.639	14.703
$Ni + H_2SO_4 = NiSO_4 + H_2$	-75.482	-78.695
$Mo + 2H_2O = MoO_2 + 2H_2$	-67.749	-79.692
$Mo + 3H_2SO_4 = Mo(SO_4)_3 + 3H_2$	-342.848	-354.219

As shown in Figs. 3-14 and 3-19, increasing temperature from 100 °C to 200 °C led to an increase in the corrosion rates of the tested alloys, particularly SS316L and DSS 2205. Numerous studies have demonstrated that increasing temperature can enhance the oxidation of alloying elements at the interface between oxide and substrate and advance the diffusion of cations and anions within an oxide layer [125, 283]. Besides oxide formation rate, previous studies showed that increasing

temperature could also accelerate the chemical dissolution rates of iron oxides in dilute acids [275, 284, 285], consequently making the environment more aggressive. Moreover, as shown in Figs. 3-5 and 3-12, increasing temperature could enhance the formation of micro-cracks within the corrosion layers grown on SS316L and DSS 2205, possibly introducing accelerated localized dissolution of oxides/sulfates along the cracks. The results in Fig. 19 imply that the influence of temperature on the dissolution of Mo oxide would be less noticeable. Furthermore, as shown in Fig. 3-14, the variation of the corrosion rates of SS316L and DSS 2205 with temperature would likely follow Arrhenius law:

$$Corr. = A' * e^{\frac{-\Delta E}{RT}} \quad (3-5)$$

where Corr. (mm/year) is the corrosion rate at a testing temperature T(K), A' is the Arrhenius constant, ΔE (kJ/mol) is the activation energy, and R ($8.314 \text{ J}\cdot\text{K}^{-1}\cdot\text{mol}^{-1}$) is the gas constant. Thus, the Arrhenius constants and activation energy of the two steels in the hot dilute sulfuric acid were estimated by

$$\text{For SS316L,} \quad Corr. = 23.72 \cdot \exp(-10.31/RT) \quad (3-6)$$

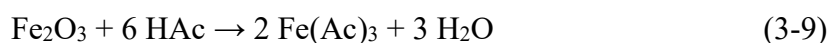
$$\text{For DSS 2205,} \quad Corr. = 807.26 \cdot \exp(-25.42/RT) \quad (3-7)$$

In addition, extending exposure time also led to an increase in the corrosion rates of the tested alloys in the hot dilute sulfuric acid as shown in Figs. 3-14 and 3-19, which could be because extending time might facilitate the micro-crack formation within thick corrosion layers formed on SS316L and DSS 2205, and thus make the oxide more readily dissolved in the hot dilute acid as suggested in Fig. 3-8. For Alloy C-276, the effect of exposure time should be marginal (see Fig. 3-19) and it is likely that extending time might aid further growth of surface oxide scale instead of accelerating oxide dissolution.

As indicated in Fig. 3-29, the presence of inorganic corrodants and softwood in the biorefining environments only had marginal effects on the average corrosion rates of the three alloys at 200 °C. Based on the results in Figs. 3-17 and 3-28, the Mo-enriched oxide layer formed on Alloy C-276 would have sufficient resistance to the attack of Cl^- , S^{2-} and organic acids and then effectively protect the alloy in the pre-hydrolysis biorefining processes. However, the influence of inorganic and organic corrodants on localized corrosion of SS316L and DSS 2205 could not be ignored as

shown in Figs. 3-22 and 3-25. Although their bulk concentrations were only several hundred ppm in the biorefining environments, both Cl^- and S^{2-} could locally accumulate along the micro-cracks that were present in the corrosion layers as they have much higher migration rates into the cracks to balance ion charge than SO_4^{2-} and OH^- [244, 286-289]. Once accumulated, Cl^- ions would likely displace sulfates/oxides, form soluble metal-anion complexes and subsequently remove the local oxides, consequently facilitating the formation and penetration of micro-cracks down to the metal substrates. Meanwhile, the accumulated S^{2-} could react with metal cations on the crack walls to form sulfates and further damage the oxide integrity along the cracks as indicated in previous studies [290-292].

In the softwood-containing environments, organic compounds and acids would be generated during the exposures as mentioned above [109, 110, 111, 112]. Given their lower dissociation constant compared to dilute sulfuric acid [293, 294], the produced organic acids could not change the environmental pH remarkably and would unlikely accelerate general corrosion. At the micro-cracks, they could accumulate and then promote the general/localized dissolution of sulfates/oxides within the micro-cracks and facilitate the crack penetration as shown in Figs. 3-22 and 3-25. For example, acetic acid (HAc), which is about 10 - 19 wt.% in liquid phase after the hot acidic pre-hydrolysis conversion [113, 114], might interact with metal or metal sulfates/oxides to form dissolvable metal-complexes [295], for instance:



In addition, as shown in Figs. 3-22 and 3-25, the corrosion layers formed on SS316L and DSS 2205 in softwood-containing solution were noticeably thinner than those grown in 0.05 M H_2SO_4 with and without inorganic corrodants at 200 °C. One possibility is that the furfural and other heterocyclic compounds produced during the pre-hydrolysis conversion might reduce the accessibility of H^+ , S^{2-} , Cl^- and other detrimental anions to the oxide layer, helping to maintain the oxide layer integrity.

3.5. Conclusions

This study investigated the roles of alloying elements, operating temperature, inorganic and organic corrodants on the corrosion of SS316L, DSS 2205 and Alloy C-276 in dilute sulfuric acid pre-hydrolysis conversion at the temperature range of 100 - 200 °C, and the following conclusions are made:

- (1) SS316L suffered active corrosion in the biorefining environments. Increasing Cr content in stainless steels even up to 22.5 wt.% could, to some extent, mitigate corrosion damage, but was not sufficient to protect the steels from the hot dilute acid attack. In 0.05 M H₂SO₄, the corrosion rates of SS316L and DSS 2205 increased with operating temperature and exposure time. The corrosion layers formed on the two steels were composed of Cr-enriched oxides and sulfates.
- (2) Different from Cr, increasing Mo content in alloys could significantly improve corrosion resistance due to the formation of a continuous, compact and stable surface scale consisted of outer Mo oxide and inner Mo/Cr oxides along with small amount of Mo sulfates. In 0.05 M H₂SO₄, increasing temperature and exposure time only led to a slight increase in the corrosion rate of Alloy C-276.
- (3) The inorganic and organic corrodants (Cl⁻, S²⁻, and organic acids), which could have released from the biomass feedstocks during the conversion, only had marginal effect on the corrosion of Alloy C-276, but they could noticeably enhance the localized corrosion of SS316L and DSS 2205 under the biorefining conditions.

Chapter 4. Influence of Major Operating Parameters (Temperature, Pressure and Flow Rate) on the Corrosion of Candidate Alloys for the Construction of Hydrothermal Liquefaction Biorefining Reactors

In the previous chapter, the effect of testing temperature, duration, inorganic corrodants and biomass on the corrosion performance of SS316L, DSS 2205 and Alloy C-276 was studied in pre-hydrolysis conversion conditions. In fact, the intermediate products from pre-hydrolysis conversion could be further refined into final bioproducts through hydrothermal liquefaction. In this chapter, two representative steels, SS310 and P91 steel were selected as candidate materials in order to study the influence of HTL operating parameters on their corrosion performance. I have carried out autoclave tests and high temperature high pressure loop tests, and found that under all testing conditions, the corrosion rates and formed oxide layer on SS310 and P91 were significantly different attributed to their distinct Cr content in base metal. This study has also found that the corrosion rates of P91 steel increase with operating temperature, while there exists a transition temperature for SS310, above which its corrosion rate decreases with increasing temperature. The influence of operating pressure and flow rate was also discussed in detail.

Abstract

Hydrothermal liquefaction (HTL) is a promising thermochemical technology to convert wet biomass and biowastes into marketable biooils and biochemicals in an environmental-friendly manner. However, industrial deployment of this technology has been significantly hindered due to very limited materials and corrosion knowledge for the selection of appropriate alloys for the construction and long-term safe operation of HTL reactors. This study investigated the influence of operating temperature, pressure and flow rate on the corrosion modes and extents of two candidate constructional steels (SS310 and P91) using high-temperature static autoclaves and environmental loop facilities under representative HTL conversion conditions, followed by post-mortem XRD, XPS, SEM/EDS, FIB and TEM characterizations of formed corrosion products. The two steels experienced general and/or nodular oxidation in hot HTL water at 250-365 °C. Increasing temperature and flow rate resulted in a noticeable increase in the corrosion rate of P91. For SS310, there is critical temperature point (around 310 °C) above which its corrosion rate

decreases with temperature. Increasing flow rate suppressed the nodular oxidation of SS310 and consequently led to a decrease in the corrosion rate. Increasing pressure from 9.8 to 25 MPa promoted the oxide formation on SS310 while cause an increased dissolution rate of the corrosion layer grown on P91 steel at 310 °C. In the simulated HTL conversion environments, the corrosion layer on P91 was mainly composed of magnetite (Fe_3O_4) and chromite ($\text{Fe}_{3-x}\text{Cr}_x\text{O}_4$) while a compact and protective inner Cr-enriched layer was formed on SS310 along with presence of other cations. Related corrosion mechanisms were also discussed and proposed.

Keywords: Hydrothermal liquefaction; Stainless steel; SEM; XPS; TEM; General oxidation

4.1. Introduction

Some parts of the literature review have been covered in Chapter 1.

The depletion of fossil fuel sources and deterioration in global climate triggered by the fossil fuel combustion have motivated intensive worldwide efforts towards the replacement of these non-renewable fuels with significant reduction in greenhouse gas emissions [89, 296]. Compared with the fossil resources, most forest and agricultural biomass materials are renewable, much less toxic and abundant in nature [2-7]. Over the past several decades, innovative biochemical and thermochemical technologies (such as anaerobic digestion, fermentation, hydrothermal liquefaction, gasification, pyrolysis, and torrefaction) have been developed to convert different categories of raw biomass feedstocks, such as wood, agricultural residues, engineered microalgae and industrial/municipal biowastes, into marketable energy alternatives, which can partially and even completely replace the fossil fuel derivatives [9-13, 297]. Among these proposed conversion technologies, hydrothermal liquefaction (HTL), which was originally developed for the liquefaction of wood chips into heavy oils using hot water and alkali catalysts [69-72], has attracted particular industrial attention because of its two important advantages: (a) directly feeding wet biomass and biowaste feedstocks without costly dewatering and/or drying pre-treatment processes; and (b) producing the bio-oils with better properties (such as lower oxygen contents and higher heating value) compared to the crude oils generated from pyrolysis processes [298]. In a HTL process, subcritical water is used as the primary reactant to transform wet biomass or biowaste

streams into crude bio-oils and/or bio-chemicals at the temperature range of 250 - 370 °C and pressure up to 25 MPa [73-77].

The HTL is conceptually simple and economically favorable in comparison with other existing thermochemical methods. Despite that HTL technology has been well established at laboratory and pilot scales, industrial-scale HTL plant has not yet been deployed due to the economic concern and technical impediments, such as relatively high capital investment and the lack of materials technology solutions for the cost-effective construction and long-term safe operation of conversion reactors which are required to be operated in hot pressurized aqueous environments containing basic catalysts, inorganic and organic corrodants (such as Cl^- , S^{2-} and organic acids). The materials knowledge and experience accumulated at high temperature nuclear plants, such as boiling water reactor (BWR) [299, 300], pressurized water reactor (PWR) [301-303], and next generation supercritical water reactor (SCWR) [230, 304] may help the pre-selection of candidate alloys for the construction of HTL reactors. Nevertheless, as schematically indicated in Fig. 4-1(a), the temperature and pressure of subcritical water used in HTL reactors are quite different from those in the nuclear plants [127, 152-154]. In fact, the water applied for the HTL reactor has its unique dissociation constant, density and dielectric constant (see Fig. 4-1(b)), possibly introducing the uncertainty of how steels and alloys corrode under the HTL conversion processes. For instance, the sharp drop of dielectric constant of water from 250 °C to 370 °C can lead to a remarkable change in the chemical dissolution of surface oxide layers formed on HTL reactor alloys [127-129]. Moreover, there are specific requirements on the wall thickness and lifetime of a HTL reactor, quite different from those in the nuclear reactors in which neutron economy and irradiation-assisted corrosion damages are key concerns [305, 306].

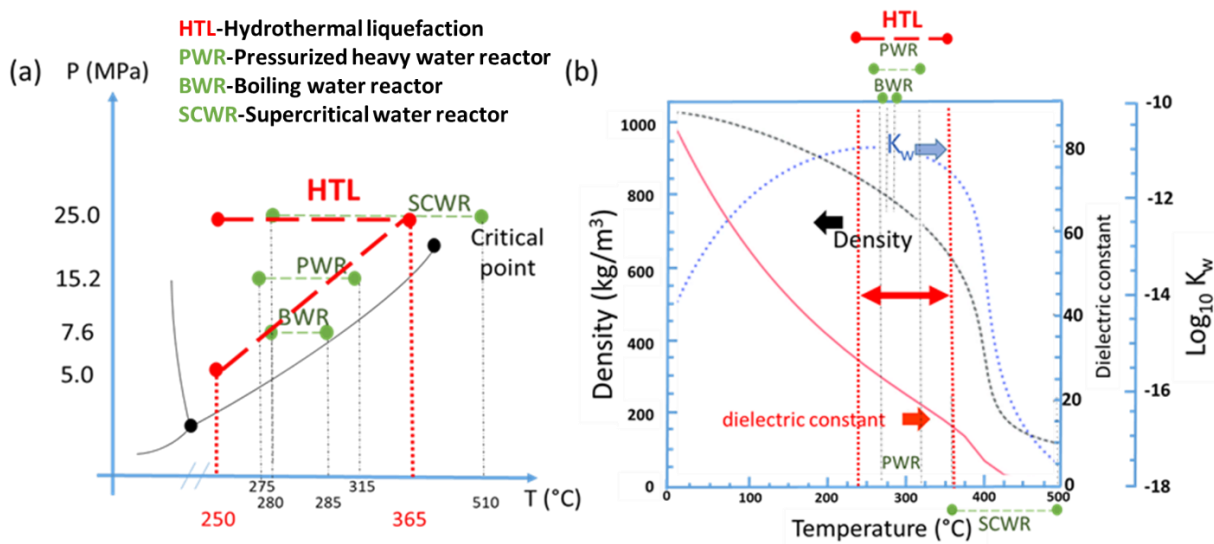


Fig. 4-1. (a) Comparison of the operating temperature and pressure ranges of water used in HTL reactors with those in nuclear reactors; (b) The properties of subcritical water applied in a typical HTL reactor. Note that the above figures were drawn based on the information provided in references [127, 152-154]. Fig. 4-1(b) was reproduced with permission from [154]. Copyright 2008 Royal Society of Chemistry.

In order to develop appropriate materials technology solutions for the construction of HTL plants, it is critical to identify the influence of critical operating parameters (temperature, pressure and flow rate) on corrosion. In subcritical water, the influence of temperature on corrosion has been intensively studied at temperature ≤ 315 °C [130-132]. Unfortunately, some reported results are controversial, and very limited works investigate the alloy performance at temperature > 320 °C [139-141]. For example, previous studies found that the corrosion rate of SS 304 steel linearly increased with temperature in subcritical water [140], while other investigations indicated that at the temperature range of 300 - 350 °C, the corrosion rate of the steel continuously decreased with an increase in temperature [141]. As a matter of fact, the related HTL corrosion mechanisms at temperature > 300 °C are still unclear [140, 141, 307]. Moreover, for high Cr-bearing austenitic stainless steels (such as SS310 and SS347), considerable efforts have been employed to identify their corrosion performance at temperature < 320 °C for the application at light water reactor plants and at temperature > 500 °C for the development of the supercritical water nuclear reactor [133-138, 308-310]. Several studies showed that the corrosion kinetics of the two steels are likely

following parabolic law within the testing temperature ranges [133, 136]. Furthermore, ferritic martensitic (FM) steels with the Cr content of 9-12 wt.%, which exhibit suitable creep, oxidation resistance and low susceptibility to stress corrosion cracking (SCC) in high temperature environments, may be applicable for the construction of HTL reactors because of their much lower cost compared to austenitic stainless steels and Ni-based alloys [201, 202]. However, little information is available to describe their performance in subcritical water under representative HTL operating conditions.

As mentioned above, the water used in HTL is required to be pressurized up to 25 MPa to promote the solubility of organic compounds in biomass feedstocks and consequently increase carbon conversion efficiency [73-77]. In supercritical water, previous studies indicated that increasing pressure could promote the clusters of H₂O molecules and make the steam with density close to that of liquid phase, likely accelerating the oxidation of stainless steels and enhancing their stress corrosion cracking (SCC) risk [311-313]. For instance, in 700 °C H₂O environment, increasing pressure from 10 to 30 MPa could result in a remarkable increase in the weight loss of SS347 and 20Cr-25Ni alloys [314]. In subcritical water, however, few studies have been carried out to clarify the influence of pressure on corrosion. In fact, increasing pressure can result in an increase in water conductivity and dissociation constant, consequently enhancing the chemical dissolution of surface oxide scales formed on Fe-based steels and Ni-based alloys [143-145]. For instance, increasing pressure from 10 MPa to 15 MPa at 310 °C could lead to the conductivity of pure water increased by nearly one order of magnitude, i.e., from approximately 10⁻⁶ to 10⁻⁵ Ω⁻¹cm⁻¹ [315]. Such a sharp increase in water conductivity might damage the integrity of surface oxide scales formed on austenitic stainless steels [128, 315-317]. For example, one study showed that increasing pressure from 12.9 to 15 MPa in 0.1 ppm H₂SO₄ solution at 330 °C resulted in an enhanced dissolution of oxides formed on SS316L and subsequently triggered the formation of intergranular cracks [318]. Clearly, it is necessary to investigate the effect of operating pressure on corrosion under the HTL conditions for the development of the suitable materials technology solutions of construction.

Furthermore, HTL biorefining can be operated in either batch or continuous mode. The latter is more desirable for industrial-scale applications due to the advantage of its high energy utilization efficiency and economic feasibility. In the continuous HTL mode, the optimum flow rates have

not yet been well defined due to the existence of unwanted clogging problems occur in high pressure pumps and conversion reactors at pilot-scale platforms. However, based on the pilot-scale results, the suitable flow rate is likely to be in the range of 0.5 - 2.0 m/s to ensure the homogeneity of the feeding slurry and effectively prevent potential clogging issues [91, 146-150]. Moreover, the continuously stirred tank reactor (CSTR) has been developed to solve the clogging issue using impeller/magnetic stir bar to assist rotation from about 100 to 600 rpm, consequently introducing linear flow movement at the rate of less than 1 m/s above reactor surface [71, 319]. From the corrosion perspective, flow-accelerated corrosion (FAC) is a concern on the selection of suitable construction alloys, especially for low-alloyed steels (such as P91 steel), for the construction of continuous HTL plants. During FAC, normally protective oxide layers on steels exhibit high dissolution rates in the fluids with high flow rates, making the oxide layer becoming thinner and less protective. At nuclear reactor plants, the FAC of carbon steels and low-alloyed steels has been well documented [320-322]. For low-alloyed steels, increasing flow rate can enhance the dissolution of surface iron oxides on the steels [151]. But increasing Cr content in the steels may suppress FAC-induced damage [323]. For the steels with Cr contents >12%, the FAC is unlikely to be a serious issue in water at temperature < 250 °C [324, 325]. However, little information is available to determine the influence of flow rate on corrosion in highly pressurized hot subcritical water at temperature > 250 °C.

Therefore, this study investigated the influence of temperature, pressure and flow rate on the corrosion of two candidate constructional steels (P91 and SS310) under simulated HTL conversion conditions. P91 is a well-known low-alloyed ferritic-martensitic steel and widely used for boiler tube fabrication at temperature up to 620 °C because of its high resistance to stress corrosion cracking and favorable thermal properties, such as high resistance to thermal fatigue and high thermal conductivity [203, 204]. SS310 is a Cr-bearing austenitic stainless steel and exhibits excellent corrosion performance in subcritical water at temperature < 290 °C and supercritical water at temperature \geq 500 °C [304, 326-331]. This study is anticipated to advance the fundamental understanding of how steels corrode in hot pressurized subcritical water and partially support the development of materials technology solutions for the cost-effective construction and long-term safe operation of industrial-scale HTL plants.

4.2. Experimental procedure

4.2.1. Testing sample preparation

Rectangular coupons (20 mm long × 10 mm wide × 2 mm thick) were machined from a commercial P91 cylinder and SS310 plate, respectively. The normalized bulk compositions are listed in Table 4-1 based on the associated mill test certificate (MTC) provided by suppliers. SS310 plate was made via annealing at 1050 °C and subsequently quenching in water, while P91 cylinder was fabricated through annealing at ~1000 °C, cooling down to 200 °C, and then tempering at 760 °C. A small hole with 2 mm radius was drilled into each coupon near the top to facilitate mounting on a custom-made coupon holder made of Alloy 625. For each test, four freshly prepared coupons of a steel were used to ensure the accuracy and precision of results reported. All the test coupons were well grinded with a series of SiC papers down to 600 grit in deionized water to completely remove potential contaminations and defects possibly introduced during machining, rinsed with ethanol in an ultrasonic bath for at least 10 minutes, cleaned with ultrapure water, and dried using pressurized air. After that, a sample ID was stamped on each prepared coupon near its top edge. Optical microscopy inspection was conducted to determine whether the surface finish of each coupon meet standard high temperature corrosion testing requirements. Prior to a corrosion test, the prepared coupons were weighed using a Mettler Toledo microbalance with the precision of 1 µg and dimensioned using a digital caliper with the precision of 10 µm.

Table 4-1. Normalized bulk chemical composition of SS310 and P91 steels.

Steel Types	Composition (wt. %)							
	Cr	Ni	Mn	C	Mo	Si	N	Fe
SS310	24.20	21.80	1.60	0.02	/	0.20	0.10	Bal.
P91	8.36	0.07	0.47	0.11	0.90	0.33	/	Bal.

4.2.2. Testing methodology and procedure

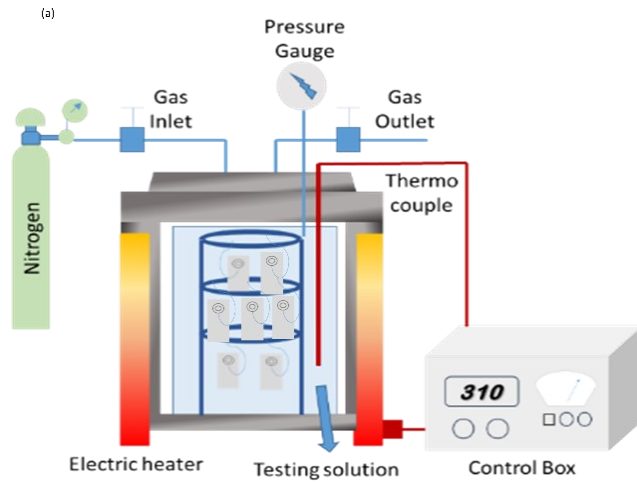
Table 4-2 summarizes the test matrix conducted in static autoclaves and high temperature water loop testing facilities (see Fig. 4-2) for identifying the influence of temperature, pressure and flow rate. Ideally, the static autoclave tests should be conducted using pressurized water at the

temperatures of interest. However, the temperature/pressure combination cannot be attained using pure water alone since the static autoclave without associated high pressure pump can only be pressurized up to the maximum steam pressure at a desired testing temperature. For example, pure water can only provide 9.87 MPa vapor pressure at 310 °C, but can achieve 25 MPa at 310 °C in a supercritical water loop facility with an associated high-pressure pump. Thus, a supercritical water autoclave loop (see Fig. 4-2(b)), which can be operated at temperature ≤ 500 °C and pressure up to 25 MPa, was used to investigate the effects of pressures and flow rates.

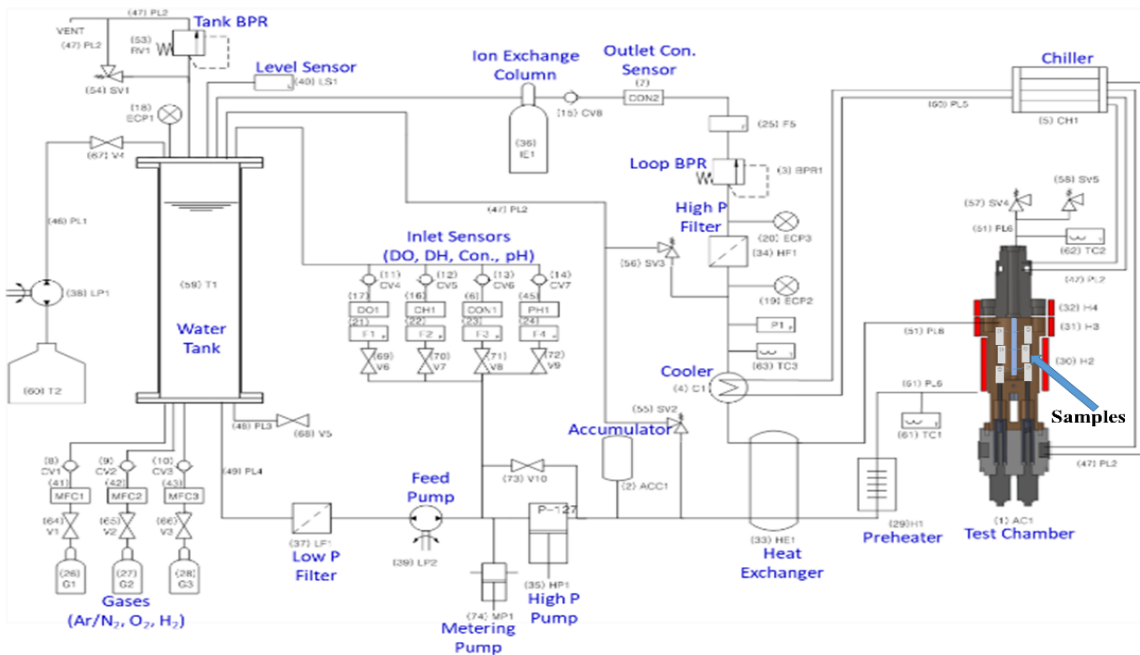
As schematically shown in Fig. 4-2(a), Tests #1 and 2 were carried out in an Alloy C-276 autoclave with an Alloy 625 liner inside, while Test #3 was done in an Alloy 625 autoclave due to the safety concern of autoclaves. The prepared coupons were hung on the Alloy 625 holder using pre-oxidized Ni-Cr wires (80% Ni and 20% Cr, oxidized at 400 °C for 12 hours) to avoid potential galvanic effect between the coupons and holder. After accommodating the testing samples/holder and deaerated ultrapure water, the autoclave was sealed and purged with N₂ for about an hour to produce a deaerated environment. After successful leak test, the autoclave was heated up to the designated temperature, with a decrease in heating rate (from ~ 6 °C/min to ~ 3 °C/min) to avoid overshooting when approaching the target temperature. The time once temperature reached the target value was recorded as starting time and the tests proceeded for 10 days. Temperature and pressure were routinely monitored and recorded to avoid any unexpected autoclave leakage or thermal fluctuations. Once reaching the target duration, the autoclave was powered off and cooled down in air. At room temperature, the testing samples were removed, rinsed with distilled water, dried with pressurized air, and finally reweighed using the Mettler Toledo microbalance.

For the Tests # 4-7, the freshly prepared coupons were hung on another holder also made of Alloy 625 inside the loop autoclave using the pre-oxidized Ni-Cr wires. The tests were conducted in deionized water with continuous N₂ purging. Four freshly prepared coupons of a steel were also suspended on the holder and then inserted into the autoclave chamber. After leak test, deionized water was continuously cycled inside the loop at room temperature and ambient pressure for about 30 minutes. Following that, a high-pressure pump was applied for pressurizing the water to the target pressure. Once the targeted pressure was stable, the loop water was heated up to the designated temperature. The flow rate was adjusted accordingly to the target value for simulating those occurred in continuous HTL reactors. After reaching the exposure duration, the heater was

switched off and the autoclave was cooled down in air. At room temperature, the steel samples were collected for subsequent characterizations, same as those tested in the static autoclaves.



(a) Static autoclave setup



(b) High-temperature high-pressure water loop

Fig. 4-2. Schematic of (a) static autoclaves and (b) water loop facilities used in this study.

Table 4-2. Test matrix conducted to investigate the influence of temperature, pressure and flow rate on the corrosion of SS310 and P91 steels in hot pressurized HTL water.

Targets	Test #	Conditions
Influence of temperature	#1	in the static Alloy C-276 autoclave containing deaerated ultrapure water at 250 °C for 10 days
	#2	in the static Alloy C-276 autoclave containing deaerated ultrapure water at 310 °C for 10 days
	#3	in the static Alloy 625 autoclave containing deaerated ultrapure water at 365 °C for 10 days
Effect of flow rates	#4	in water loop containing deaerated water with flow rate of 0.6 m/s at 310 °C and saturated vapor pressure for 10 days
	#5	in water loop containing deaerated water with flow rate of 1.1 m/s at 310 °C and saturated vapor pressure for 10 days
Impact of pressure	#6	in water loop containing deaerated water with flow rate of 1.1 m/s at 310 °C and 15 MPa for 10 days
	#7	in water loop containing deaerated water with flow rate of 1.1 m/s at 310 °C and 25 MPa for 10 days

4.2.3. Corrosion rate assessments

Two techniques were used to evaluate the corrosion rates of the steels in the hot pressurized HTL water. The first was to directly measure the mass change of a steel coupon before and after a corrosion exposure. This method is a usually used to assess high temperature oxidation kinetics of an alloy based on the assumption that surface oxidation of the alloy would be the dominant reaction during the high temperature exposure and the formed corrosion products would be compact without localized nodular oxidation and/or spallation. The corrosion rate ($\mu\text{m}/\text{year}$) can be estimated by [225]:

$$\text{Corr. Rate} = \frac{\eta \cdot 8.76 \times 10^7 \cdot \Delta m}{dAt} \quad (4-1)$$

where Δm (g) is the direct mass change of a coupon before and after an exposure; d (g/cm^3) is the steel density; η is the molar mass ratio of consumed alloying elements to oxygen in formed corrosion products, and was about 2.2 for SS310 and 2.3 for P91 steel, respectively [230]; A (cm^2) is the average surface area of the coupon; and t (h) is the testing duration. Note that the molar mass ratio used in the equation was based on the assumption that Cr and Fe oxides were the major components in oxide layer formed on SS310 and P91, respectively. The average corrosion rate of a steel after a test was obtained from the four parallel corroded coupons based on ASTM G16 [226].

The second was to measure the weight loss of a coupon after a hot pressurized HTL water test, involving two main steps: (a) completely removing the formed corrosion products on the coupon based on ASTM-G1 standard [227]; and (b) weighing the mass difference of the coupon before the testing and after descaling [228, 229]. Descaling processes can be successfully achieved via immersing the coupons in specific chemical solutions, which do not corrode the steel substrates, but can effectively remove the formed corrosion layers through accelerated chemical dissolution reactions. In this study, the descaling of SS310 was done by immersing the corroded coupons in 90 °C solution A (2 wt.% citric acid + 5 wt.% dibasic ammonium citrate + 0.5 wt.% disodium EDTA) for 30 min and 90 °C solution B (4 wt.% potassium permanganate + 5 wt.% caustic soda) for 30 min, followed by a 15 min of ultrasonic cleaning in ethanol. The coupons were then immersed in 90 °C solution A again for next 30 min and weighed. The above process was applied repeatedly until the weight of a coupon reached a constant value as described in references [230, 231]. The descaling of P91 steel was carried out by immersing corroded coupons in the solution of 500 ml HCl + 3.5 g hexamethylene tetraamine + 500 ml ultrapure water at room temperature for 10 min. Cotton swab and soft copper brush was used to gently remove any remaining corrosion products after the immersion. The average corrosion rate of a coupon ($\mu\text{m}/\text{year}$) was then calculated by [232]:

$$\text{Corr. Rate} = \frac{8.76 \times 10^7 \cdot \Delta m}{dAt} \quad (4-2)$$

where Δm (g) is the mass loss of a coupon before an exposure and after the descaling; d (g/cm^3) is the steel density; A (cm^2) is the surface area of the coupon; and t (h) is the exposure duration. The

average corrosion rate of a steel after a test was obtained from three parallel corroded and descaled coupons based on ASTM G16 [226].

4.2.4. Corrosion products characterization

In this study, the coupon with the direct mass change value closest to the average value in a given replicate set after a HTL exposure was selected for subsequent corrosion product characterization. Optical images were taken firstly to primarily check surface morphology of corroded coupons. The coupons were then examined using a FEI Nova NanoSEM 650 scanning electron microscope (SEM) system operated at 20 KeV and equipped with an Oxford energy dispersive X-ray spectroscopy (EDS) system to identify corrosion modes (such as active corrosion, general oxidation, and/or pitting etc.) and roughly characterize the chemical properties of formed corrosion products. As the corrosion products formed on P91 steel were considerably thick, their phase compositions were determined using X-ray diffraction (XRD) technique with a Co K α X-ray source operated at 40 kV and 150 mA. Diamond saw cutting method was also used to examine the cross-sectional area of corroded P91 steel samples. Compared with the corrosion layer formed on P91, that formed on SS310 samples were quite thin and consequently a FEI Helios NanoLab™ DualBeam™ Focus Ion Beam (FIB) microscope was applied for producing cross-sectional view of the area from the top surface of a corrosion layer to metal substrate. Before the FIB operation, a thin platinum (Pt) layer was deposited on the coupons in vacuum to protect the formed surface scale. After the FIB operation, the cross-sectional samples were thinned and collected using in-situ lift-out technique for following TEM examinations. The TEM characterizations, including Bright field (BF) imaging, High-angle annular dark-field (HAADF) imaging and EDS element mapping, were conducted using a Tecnai Osiris™ scanning transmission electron microscope (STEM) equipped with super X-field emission gun (FEG) and X-ray detection system operated at 200 kV. Besides, XPS spectra were also collected on corroded SS310 samples using PHI Quantera II Scanning XPS Microprobe operated at 15 kV with take-off angle of 45°. Ar ion sputtering with ion beam of 1 kV voltage and 1 mA current was carried out at a step size of 0.8 eV for depth profiling purpose. The collected spectra were deconvoluted and analyzed using commercial XPSPEAK 4.1 software.

4.3. Main Results

4.3.1. Effect of operating temperature on corrosion

The photographic images of SS310 and P91 coupons before and after Tests #1-3 in hot ultrapure water are shown in Fig. 4-3. Before the tests, the surfaces of freshly prepared coupons were neat with shining metal luster. After the exposures, the coupon exhibited different color, indicating the formation of corrosion products with different thickness. For SS310, spalling did occur after Test#1. After Test #2, corrosion product deposition happened based on the variation of appearance. Interestingly, after Test #3 in 365 °C ultrapure water, uniform and compact surface oxide scales were formed on the steel. For P91 steel, the surface was much darker than that of SS310 after all the tests, implying the formation of thicker corrosion products. In addition, no pit was found on the two steels after all three tests.

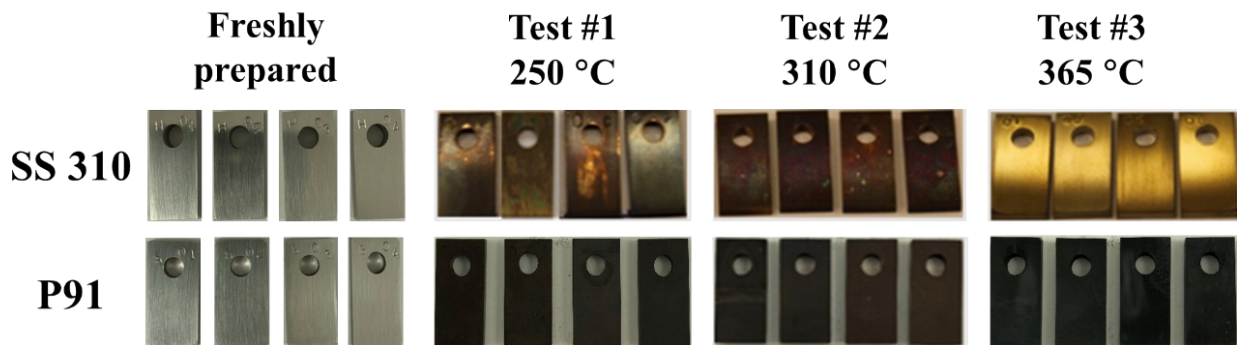
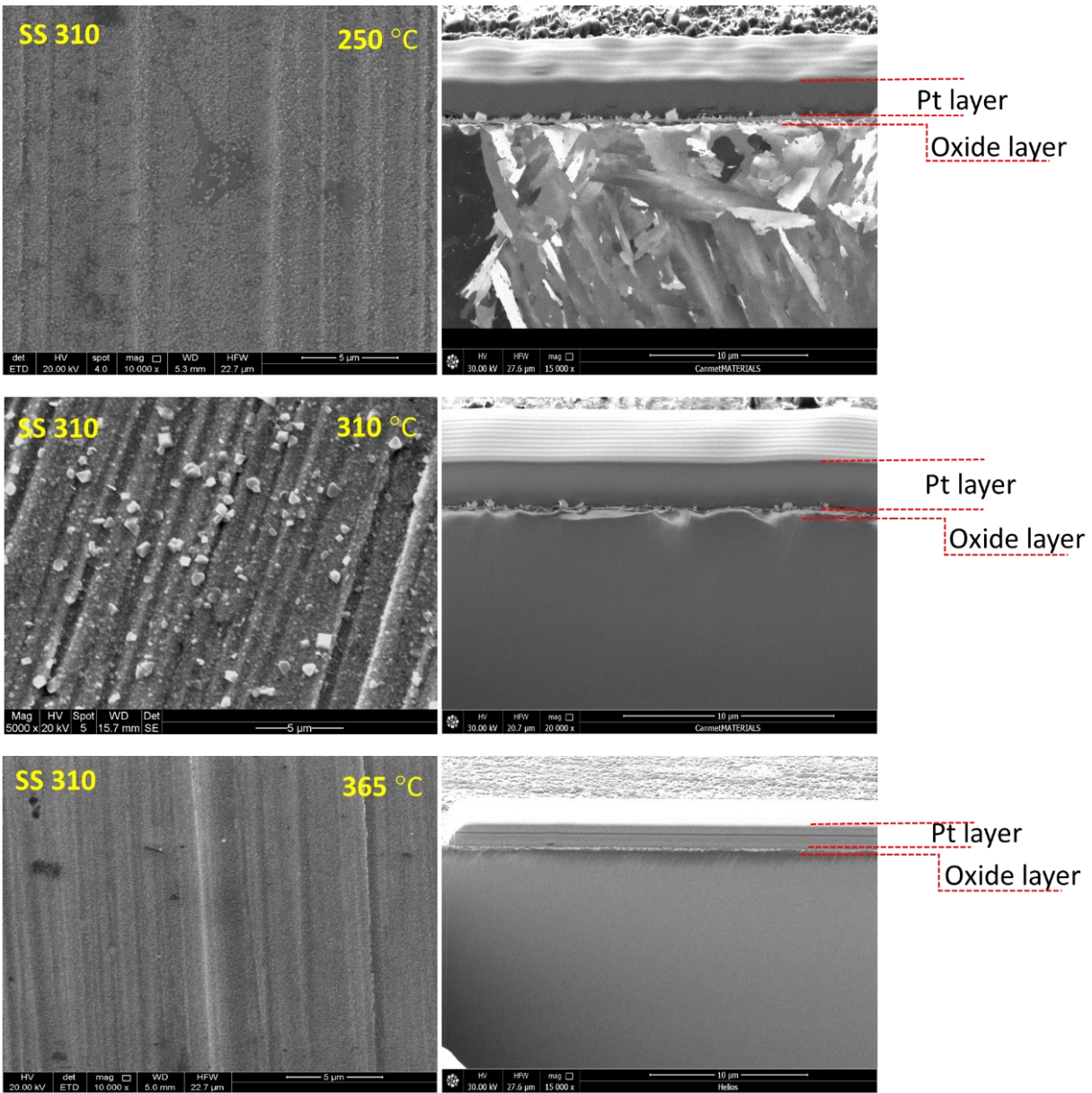


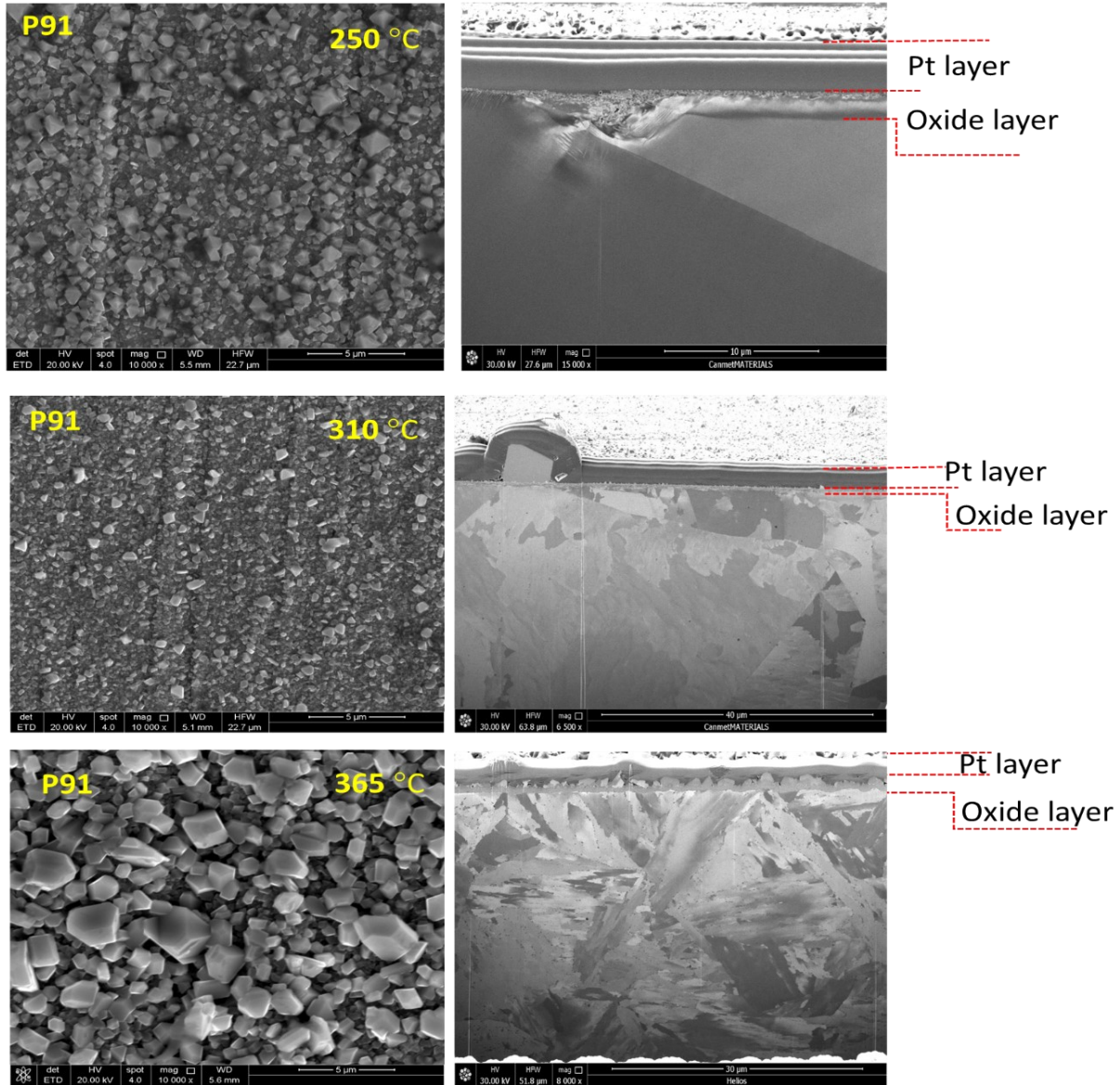
Fig. 4-3. Photographic images of SS310 and P91 steels (20 mm long \times 10 mm wide \times 2 mm thick) before and after the exposure to hot water at different HTL operating temperatures.

Fig. 4-4 shows the SEM top and cross-sectional views of SS310 and P91 steels after the exposure to the HTL water at different temperatures. As shown on the top-view images, the surface scales formed on SS310 were quite thin since the mechanically polishing lines were clearly visible after the tests. Moreover, tiny nodular oxides were likely to be grown on the steel at temperature \leq 310 °C. At 365 °C, however, the nodular oxides became almost negligible. Furthermore, corrosion deposits were also found on the steel after the exposure at temperature \leq 310 °C. These cross-sectional images further confirm that the formation of nodular and deposit particles would occur at temperature \leq 310 °C. For P91 steel, the top-view images implied that the formed surface scale

was likely to be much thicker than that on SS310 at a testing temperature (see Fig. 4-4). Compared to SS310 steel, much larger oxide particles were grown on P91, especially after the exposure at 365 °C. Based on the cross-sectional images, the average thickness of surface scales formed on P91 was about 3 - 4 μm, and increased with temperature up to 365 °C. Meanwhile, nodular oxidation and deposition of large corrosion product particles on P91 steel also became noticeable at a higher temperature.



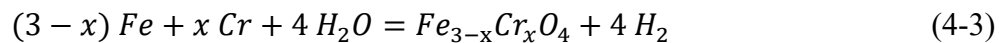
(a) Top and cross-sectional views of corroded SS310 samples



(b) Top and cross-sectional views of corroded P91 samples

Fig. 4-4. Top-view and cross-sectional SEM views of (a) SS310 and (b) P91 steels corroded in HTL water at different operating temperatures.

As the surface scales formed on P91 steel were thick, XRD technique was employed and the collected spectra are shown in Fig. 4-5. At 250 °C, the formed corrosion layer was mainly composed of magnetite (Fe_3O_4) and chromite ($Fe_{3-x}Cr_xO_4$). The chromite might be formed through



Note that the peaks of ferrite phase were collected from the steel substrate. Increasing temperature from 250 °C to 365 °C did not result in the noticeable change of the phase compositions of the formed corrosion layers, suggesting that the oxidation formation and growth reactions would not change with temperature in the HTL water during the HTL conversion.

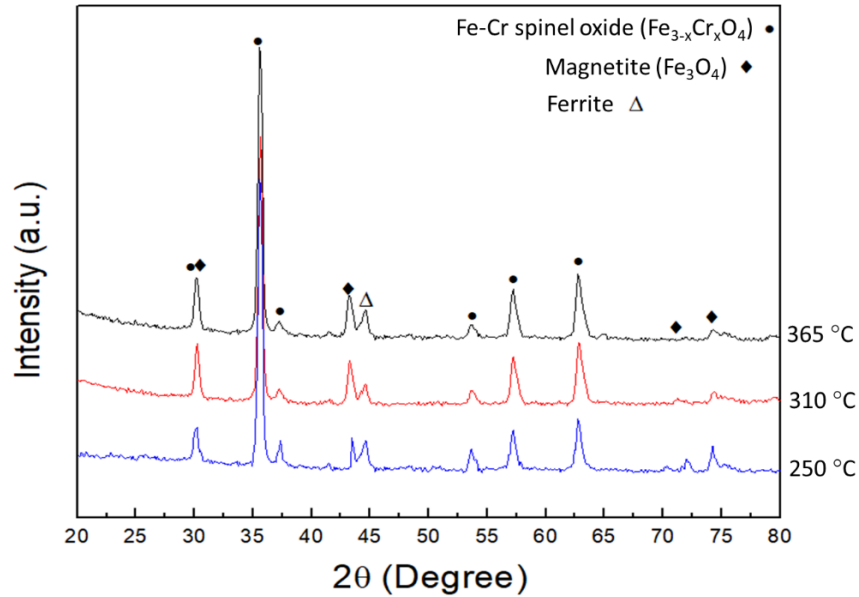


Fig. 4-5. XRD spectra collected on P91 steel samples after the exposures to HTL water at different HTL operating temperatures.

As mentioned above, FIB/TEM techniques were applied for characterizing the properties of thin oxide scales formed on SS310 steel samples, and the results are shown in Fig. 4-6. At temperature ≤ 310 °C, both nodular and/or deposition particles were randomly formed. These nodular particles were mainly composed of Fe oxides while the deposited particles consisted of Fe and Ni oxides. Note that an Alloy 625 (with 64 wt.% Ni) liner or autoclave was used to contain testing specimens and hot water during the exposures. Below the particles, a continuous thin and compact Cr-enriched oxide layer was formed. Note that after the exposure to 310 °C water, the accumulation of alloying element Ni was observed at the interface of oxide layer/metal. Interestingly, only a single Cr-enriched oxide layer with trace amount of Fe cations was formed at 365 °C. Moreover, the average thickness (~ 25 nm) of surface oxide layer on the steel at 365 °C was noticeably thinner than that formed at temperature ≤ 310 °C (~ 60 nm), suggesting that there should be a transition

temperature between 310 - 365 °C above which the oxide formation and chemical dissolution would be changed. The selected area diffraction (SAD) patterns collected on the Cr-enriched oxide layers at different temperatures were halo ring patterns, indicated that the layers would have amorphous structure.

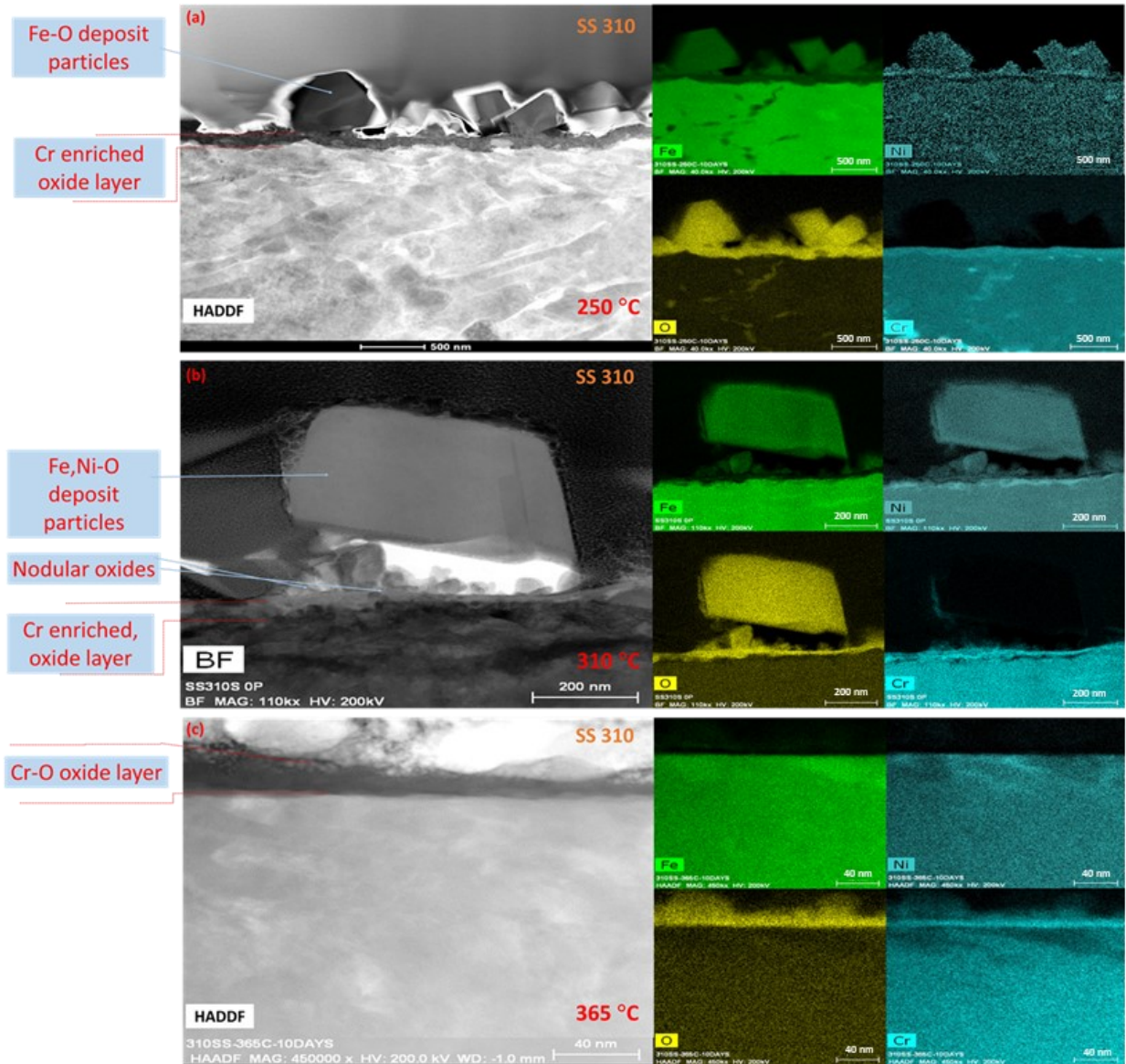


Fig. 4-6. High resolution TEM cross-sectional images and corresponding elemental mapping on SS310 after the exposure to HTL water at different temperatures: (a) 250 °C; (b) 310 °C; and (c) 365 °C.

To identify the chemical state of major elements (Cr, Fe and O) in the surface scales on SS310 steel, XPS characterizations were conducted, and the results are shown in Figs. 4-7 and 4-8, respectively. After corroding in 250 °C water, the formed nodular/deposited particles were composed of iron oxide and hydroxides, consistent with the TEM characterizations. Underneath that, the continuous Cr oxide layer were mainly composed of Cr_2O_3 and $\text{Cr}(\text{OH})_3$ accompanied with small amounts of $\text{Fe}^{3+}/\text{Fe}^{2+}$ cations. At 365 °C, the XPS spectra confirm the disappearance of nodular oxidation and showed that the formed continuous oxide scale was also mainly composed of Cr_2O_3 and $\text{Cr}(\text{OH})_3$ with the presence of $\text{Fe}^{3+}/\text{Fe}^{2+}$ cations. It is worth noticing that Ar ion bombardment may cause the chemical states of cations and anions changed during depth profiling.

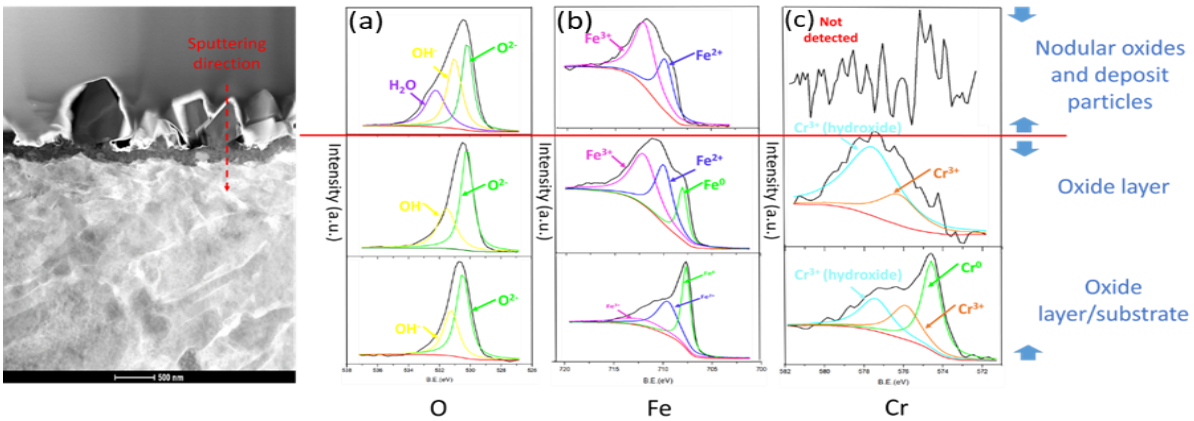


Fig. 4-7. XPS depth profiling spectra collected on a SS310 sample after the exposure to 250 °C ultrapure water: (a) O 1s, (b) Fe 2p_{3/2}, and (c) Cr 2p_{3/2} region.

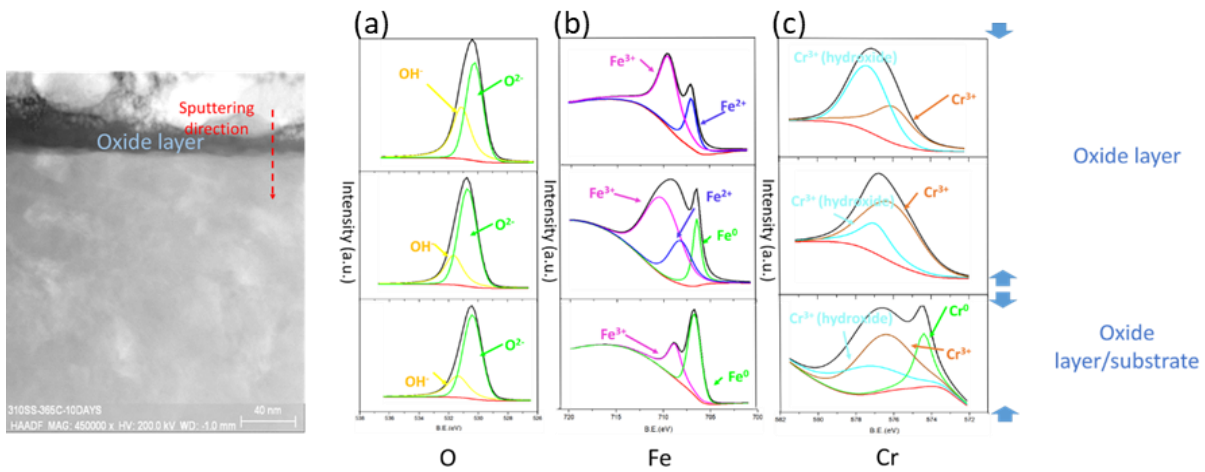


Fig. 4-8. XPS depth profiling XPS spectra collected on a SS310 sample after the exposure to 365 °C ultrapure water: (a) O 1s, (b) Fe 2p_{3/2}, and (c) Cr 2p_{3/2} region.

As described above, the average corrosion rates of the two steels were evaluated based on both equation (4-1) and (4-2), and results are shown in Figs. 4-9 and 4-10, respectively. Note that scales on the vertical axis in Fig. 4-10 is much larger than that in Fig. 4-9. At a desired testing temperature, the corrosion rate of a steel obtained from direct mass change measurements was consistently lower than that from weight loss method. This may be attributed to the following factors:

- (1) As shown in Figs. 4-4 and 4-6, nodular oxidation and/or deposition occurred on the steels when exposed to high temperature HTL water, introducing the inaccuracy of using the direct mass change method for corrosion rate assessment;
- (2) As indicated in Figs. 4-5 and 4-7, the formed surface scales on the two steels were not just composed of Fe_2O_3 and/or Cr_2O_3 , resulting in less accurate estimation of the molar mass ratio (η) values in equation (4-1);
- (3) The chemical dissolution of formed oxide scales cannot be ignored. As shown in Fig. 4-5, the corrosion products formed on P91 steel were composed of magnetite which chemical dissolubility would increase with temperature in the HTL water based on previous studies [332, 333]. For SS310 steel, the formed hydroxides (see Fig. 4-8) would exhibit higher solubility than Cr oxides in the hot HTL water [334, 335].

Therefore, weight loss measurement can be considered as a more accurate method on the corrosion rate assessments comparing to direct weight change measurements from the engineering application point of view, and therefore applied for determining the corrosion rates of the two steels in this study.

As shown in Fig. 4-9, the average corrosion rate of SS310 steel did not consistently increase with temperature, and its maximum value occurred at 310 °C. Based on the results in Figs. 4-6 and 4-9, it was very likely that the transition point on the surface oxide formation and dissolution could be around ~310 °C or just slightly higher. This transition could originate from the variation of water chemistry (such as dielectric constant and dissociation constant) with temperature as indicated in Fig. 4-1 and the properties of formed surface scales on the steels after exposure, as shown in Figs. 4-6, 4-7 and 4-8. Different from SS310, the average corrosion rate of P91 steel continuously increase with temperature, consistent with the cross-sectional SEM observations (see Fig. 4-4). At a HTL operating temperature, the corrosion rate of P91 steel was much higher than that of SS310, which could be mainly attributed to the difference of the chemical composition

between SS310 and P91 that consequently led to the formation of different surface scales on the two steels.

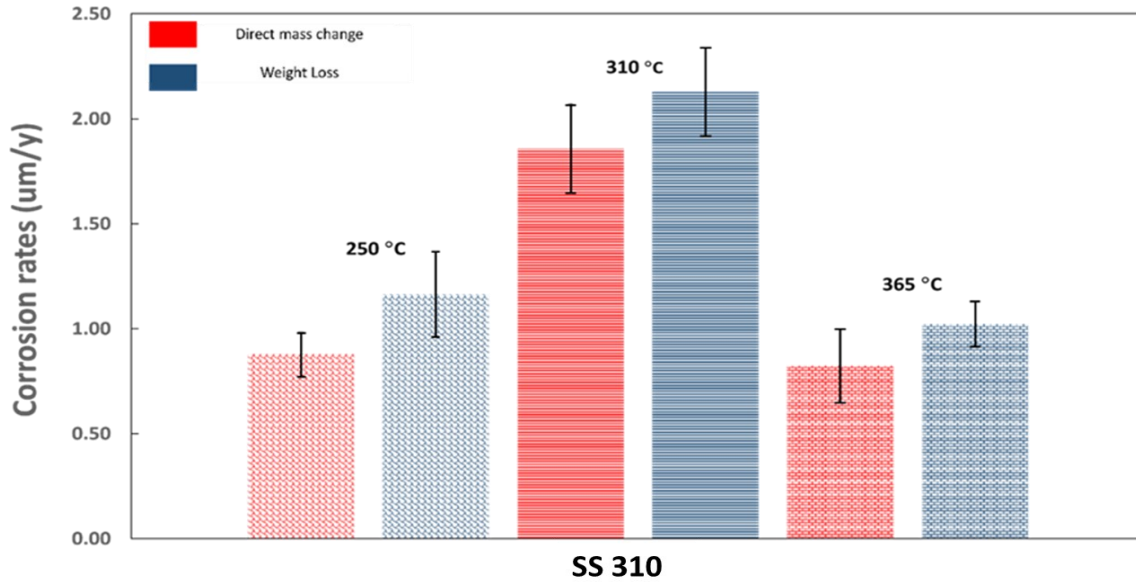


Fig. 4-9. Variation of average corrosion rate of SS310 steel with HTL operating temperature. Note that the corrosion rates were evaluated based on direct weight gain and weight loss measurements as described in the experimental section.

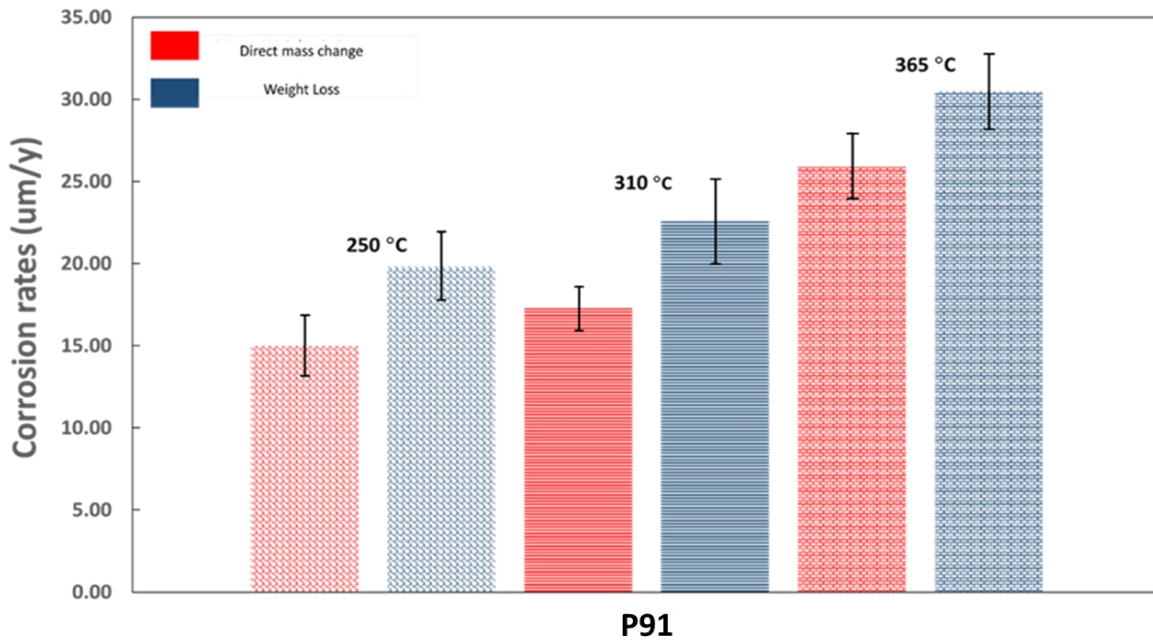


Fig. 4-10. Variation of average corrosion rate of P91 steel with HTL operating temperature. Note that the corrosion rates were assessed based on direct weight gain and weight loss measurements as described in the experimental section.

4.3.2. Effect of flow rate on corrosion

Fig. 4-11 shows the photographic images of SS310 and P91 coupons after high temperature loop tests in 310 °C water at different flow rates. Compared to the results in the static condition at the same temperature (Test #2), the surface of SS310 tested in the water with flow rate of 1.1 m/s did not exhibit apparent change at 310 °C, implying the formation of similar surface scale. However, P91 steels became slightly darker, suggesting the formation of thicker surface scales in the flowing water. Nodular oxidation or corrosion product deposition also likely occurred on SS310 steel, similar to that under the static condition.

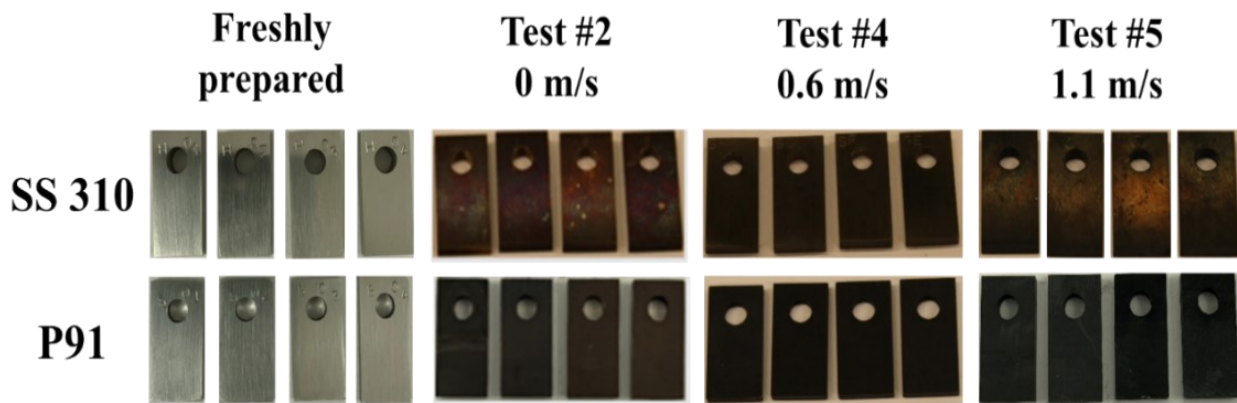
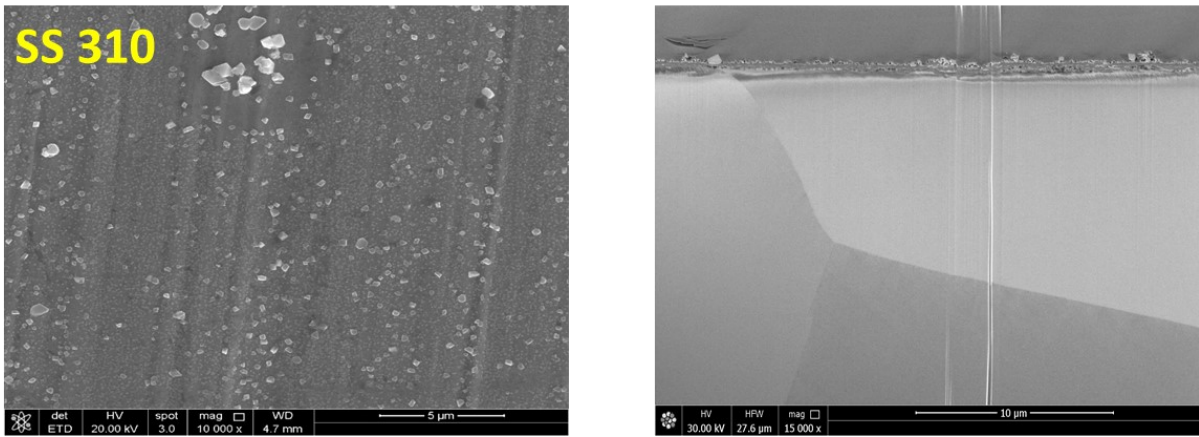


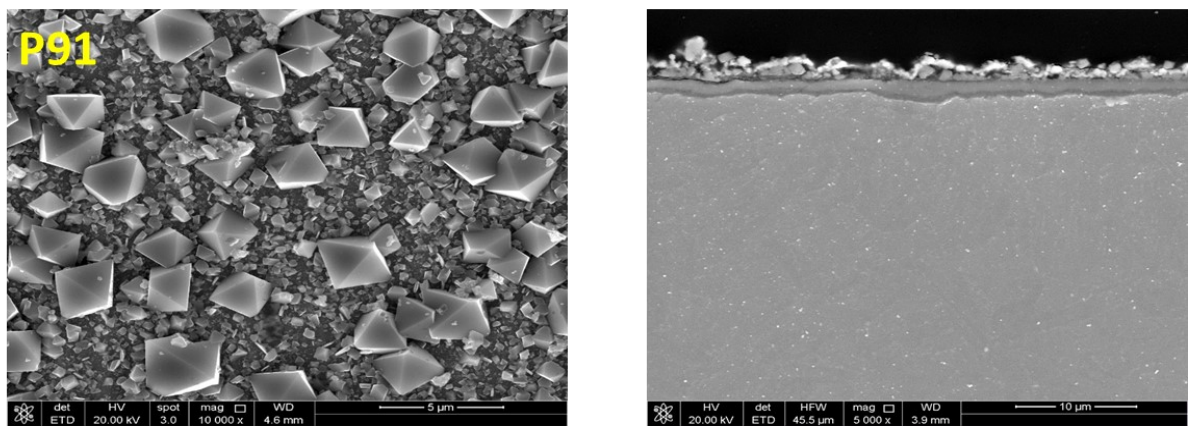
Fig. 4-11. Photographic images of SS310 and P91 steels (20 mm long × 10 mm wide × 2 mm thick) showing surface appearance before and after corrosion in 310 °C HTL water at different flow rates.

The top and cross-sectional SEM images of the two steels are shown in Fig. 4-12. As the corrosion scales formed on SS310 were quite thin, FIB cutting and subsequent cross-sectional SEM characterization were conducted. Different from that, the corrosion products found on P91 steel would be expected to be thick and diamond saw cutting method was thus applied before performing cross-sectional SEM examinations. Compared with the observations in Fig. 4-4(a), increasing flow rate to 1.1 m/s at 310 °C likely suppressed localized nodular oxidation and the deposition of corrosive particles, and resulted in a decrease in oxide layer thickness found on SS310. The surface layer formed on SS310 remained relatively uniform and compact. Different from SS310, increasing in flow rate to 1.1 m/s led to the formation of larger oxides/deposit particles

and thicker corrosion layer on P91 steel when comparing to those formed under static condition (see Fig. 4-4(b)).



(a) Top and cross-sectional views of a corroded SS310 sample



(b) Top and cross-sectional views of a corroded P91 steel sample

Fig. 4-12. Top and cross-sectional SEM images of SS310 and P91 after the exposure to 310 °C loop water at the flow rate of 1.1 m/s.

For P91 steel samples after corroding in 310 °C water with the flow rate of 1.1 m/s, XRD spectra (see Fig. 4-13) collected on the tested sample showed that the formed corrosion layer was mainly composed of magnetite (Fe_3O_4) and chromite ($\text{Fe}_{3-x}\text{Cr}_x\text{O}_4$), similar to that grown under static conditions (see Fig. 4-5). These results implied that increasing in flow rate from static to 1.1 m/s did not result in a noticeable change of the chemistry of formed corrosion layers, suggesting that the oxide formation reactions would not vary with flow rate during the conversion processes. To

identify the microstructure of corrosion layer formed, EDS mapping was also performed on the cross-sectional area of the corroded sample, and the results are shown in Fig 3-14. The formed corrosion layer consists of two sub-layers, including outer porous Fe oxides and inner relatively compact and uniform Fe/Cr oxides. As implied in Fig. 4(b) and 12(b), increasing flow rate might accelerate the dissolution of outer Fe oxides into the water and/or reduce the deposition of dissolvable corrosion particles from the hot water during the cooling down of loop facility.

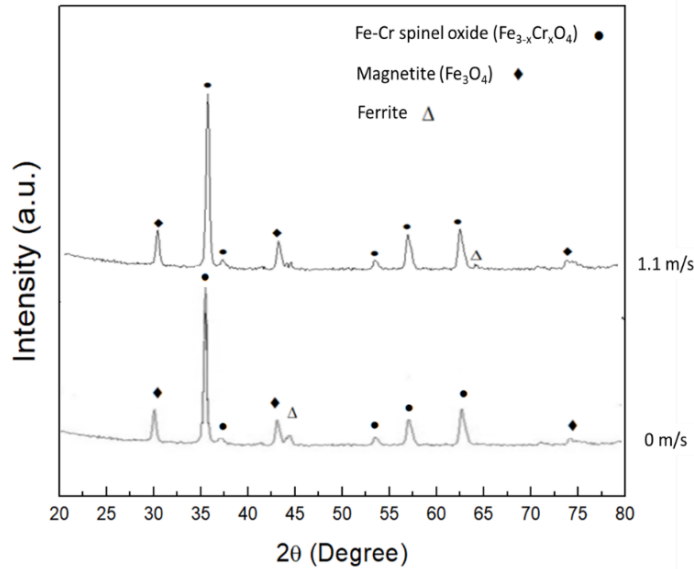


Fig. 4-13. Comparison of XRD spectra collected on P91 steel samples after the exposures to 310 °C at the flow rates of 0 and 1.1 m/s, respectively.

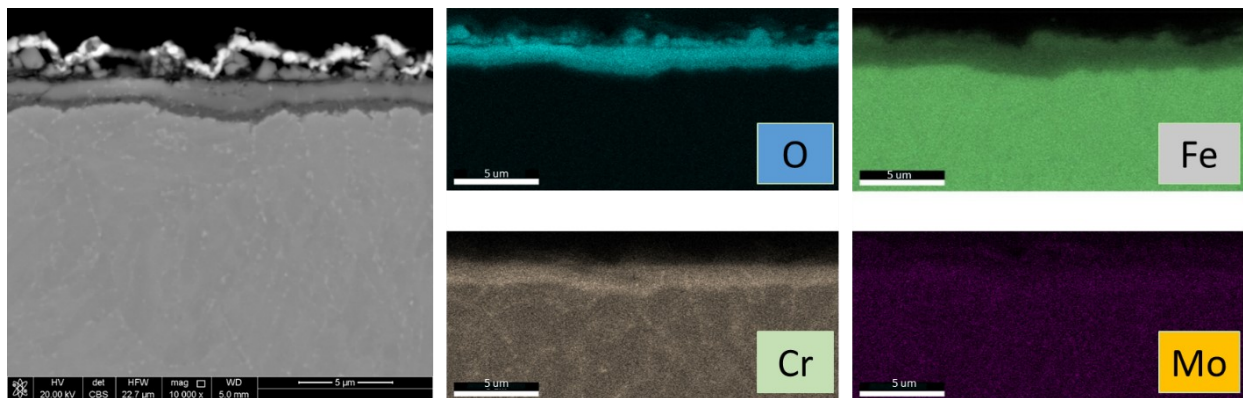


Fig. 4-14. Cross-sectional SEM image and corresponding EDS elemental mapping on P91 steel after the exposure to 310 °C water at the flow rate of 1.1 m/s.

As the oxide layer formed on Cr-bearing SS310 would be quite thin even at the flow rate of 1.1 m/s, FIB and TEM techniques were employed to identify the nature of the layer and the results are shown in Fig. 4-15. Similar to that grown in static condition (see Fig. 4-5), the formed layer was also mainly composed of Cr-enriched oxides and alloying element Ni accumulated at the layer/metal interface. Different from the static condition, the deposition of (Fe, Ni)-O particles was remarkably suppressed in the loop and the nodules were mainly consist of Cr oxides. To further clarify the effect of flow rate, XPS characterizations were conducted on the corroded SS310 and the results are presented in Fig. 4-16. The formed Cr-enriched oxide layer is primarily composed of Cr_2O_3 and $\text{Cr}(\text{OH})_3$ with $\text{Fe}^{3+}/\text{Fe}^{2+}$ cations, similar to those grown under the static conditions (see Fig. 4-8). These implied that the flow rate would only have marginal effect on general oxidation of the steel in the hot HTL water.

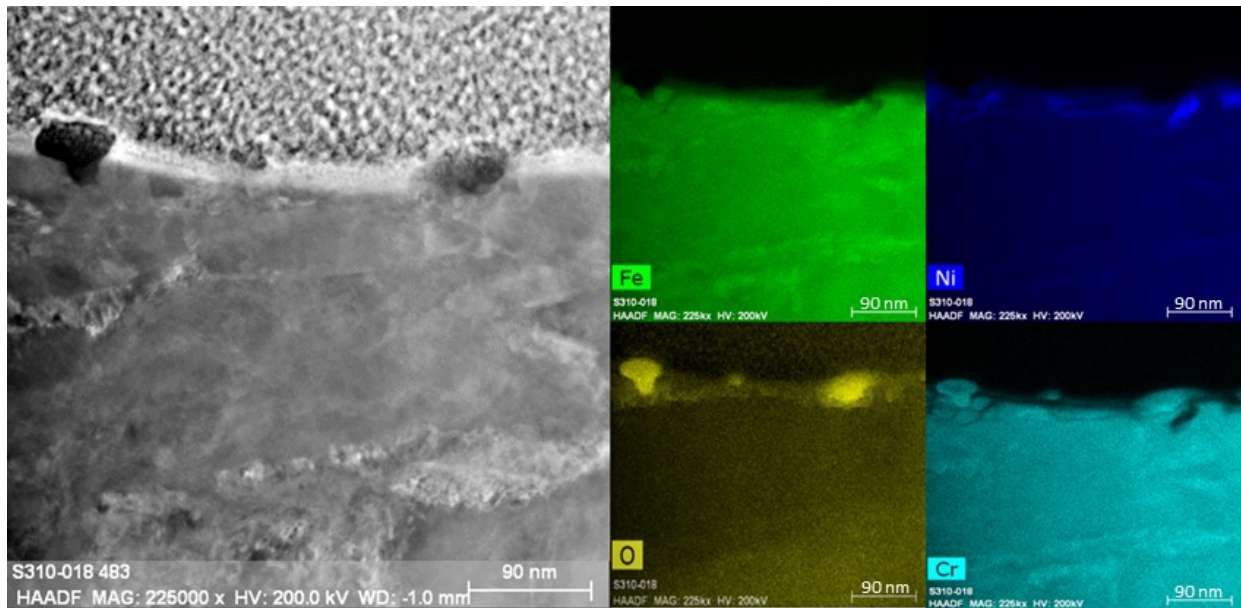


Fig. 4-15. TEM cross-sectional images and corresponding EDS elemental mapping on SS310 after the exposure to 310 °C water with the flow rate of 1.1 m/s.

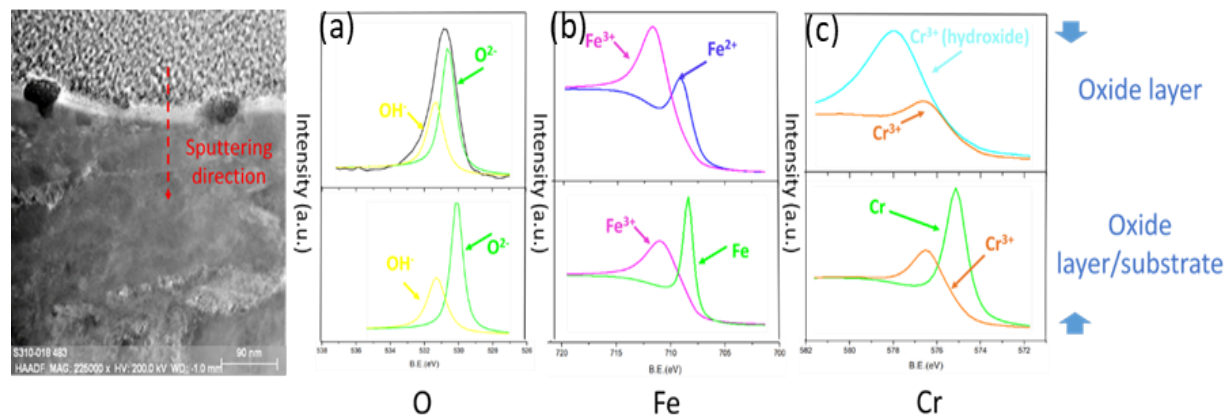


Fig. 4-16. XPS core level spectra collected on a SS310 sample after corroding in 1.1 m/s flowing water at 310 °C: (a) O 1s, (b) Fe 2p_{3/2}, and (c) Cr 2p_{3/2} region.

Based on the weight loss measurements, the variation of the average corrosion rates of SS310 and P91 steels with flow rate are shown in Figs. 4-17 and 4-18, respectively. Interestingly, the corrosion rates of SS310 slightly decreased with an increase in flow rate, suggesting that the FAC would not be a serious concern for the Cr-bearing steels in HTL conditions under continuous operation mode. Such trend of corrosion rates may be attributed to the localized nodular oxidation being suppressed in the flowing hot water as indicated in Figs. 4-4 and 4-12. Different from SS310, the corrosion rate of P91 steel noticeably increased with flow rate, suggesting that the chemical dissolution of Fe₃O₄ and iron-chromium spinel oxides formed on the steel would be enhanced with increasing flow rate, similar to those occur on low-alloyed steels at nuclear plants [320-322]. Note that further increasing flow rate from 0.6 to 1.1 m/s only resulted in a marginal increase in the corrosion rate, implying that the effect of flow rate on the corrosion of P91 would be still limited under the HTL continuous mode. From industrial application, this finding suggested that it would be applicable to increase flow rate to achieve better homogeneity of the feeding slurry and mitigate clogging issues in HTL reactors as such an increase would not lead to severe corrosion damage.

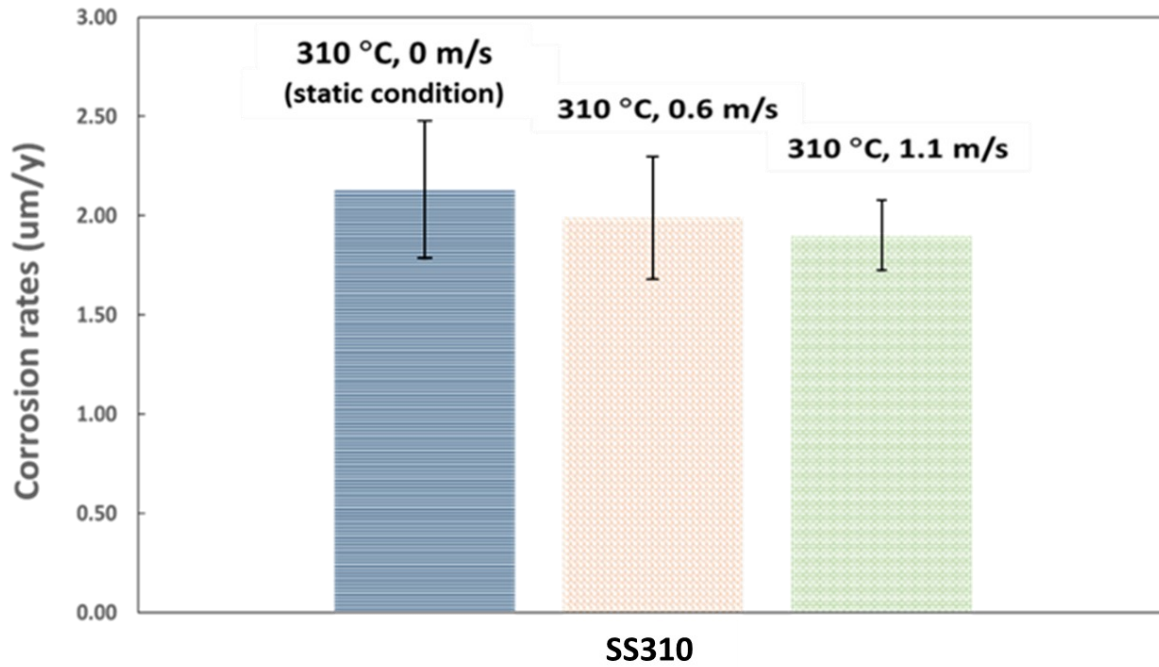


Fig. 4-17. Variation of the corrosion rates of SS310 steel with flow rate in HTL water at 310 °C.

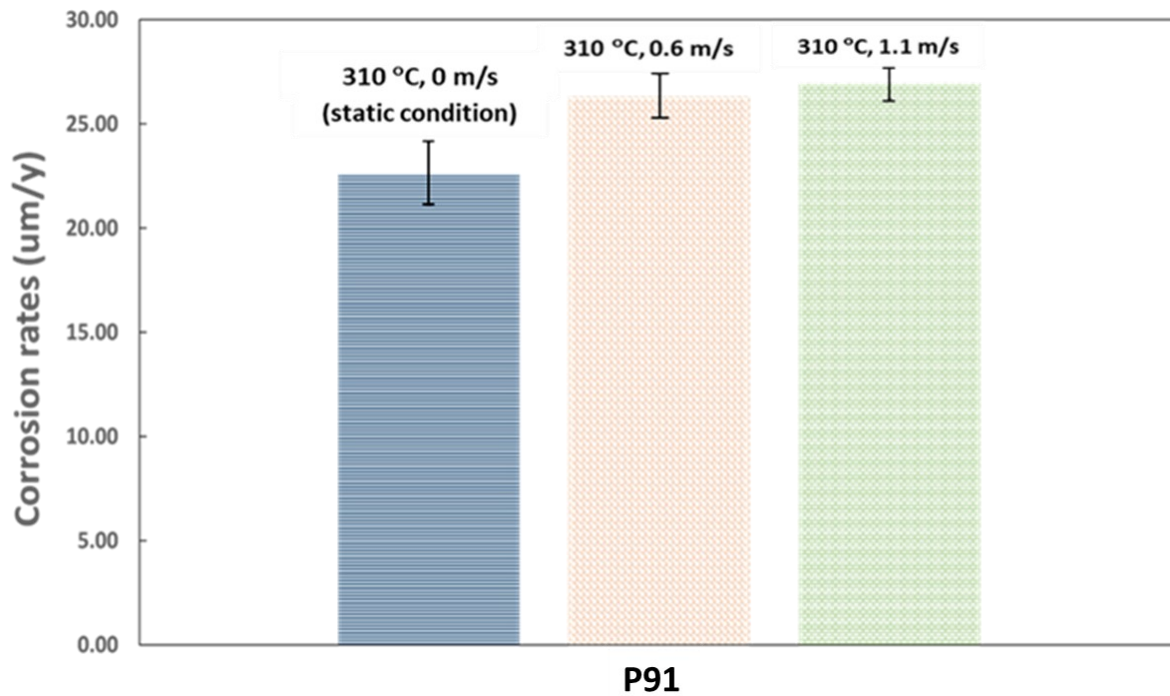


Fig. 4-18. Variation of corrosion rates of P91 steel with flow rate in HTL water at 310 °C.

4.3.3 Effect of operating pressure on corrosion

Fig. 4-19 shows the photographic images of SS310 and P91 coupons after high temperature loop tests in 310 °C water at different pressures. At 310 °C, increasing pressure from saturated vapor pressure (~9.8 MPa) to 25 MPa resulted in the presence of a slightly darker surface, implying the formation of thicker corrosion layers on the steels. For SS310, nodular oxidation or corrosion product deposition became less visible with increasing pressure. Compared to SS310, the surface of P91 steel was much darker at a specific HTL operating pressure.

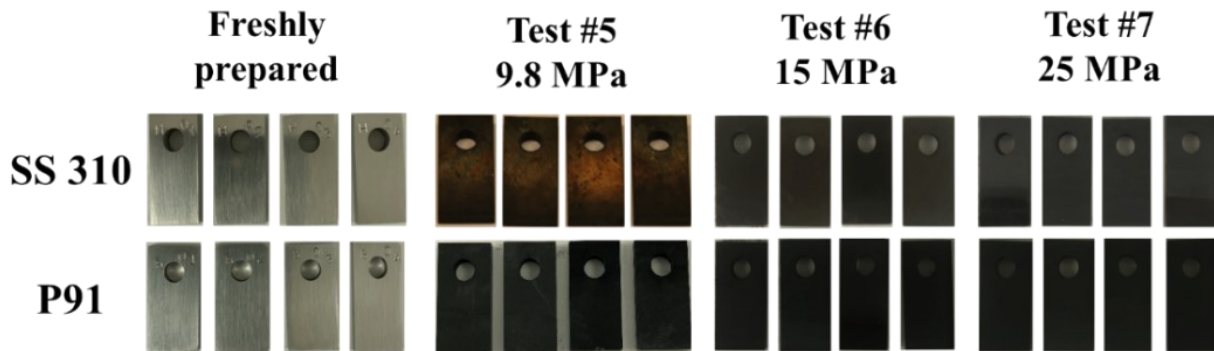


Fig. 4-19. Photographic images of SS310 and P91 steels (20 mm long \times 10 mm wide \times 2 mm thick) before and after the exposure to 310 °C hot water at the flow rate of 1.1 m/s and different HTL operating pressures.

The top-view SEM images of the two steels are shown in Fig. 4-20. As mentioned in previous sections, FIB cutting and subsequent high magnification cross-sectional TEM characterization were employed on SS310 while diamond saw cutting and cross-sectional SEM examination were conducted on P91 samples. The results are shown in Figs. 4-21 and 4-23, respectively. Compared with the results in Figs. 4-4 and 4-12, increasing operating pressure from 9.8 to 25 MPa at 310 °C led to the formation of smaller nodular oxides/deposit particles on SS310. For P91 steel, increasing pressure to 25 MPa caused the formation of relatively large oxide particles and loose oxide layer, with micro-cracks presented near the top oxide layer (see Fig. 4-21). Moreover, the outer oxides seemed to locally accumulate around the cracks. Compared to SS310, the variation of HTL operating pressure was likely to have a more remarkable influence on the corrosion of P91 steel in the hot HTL water.

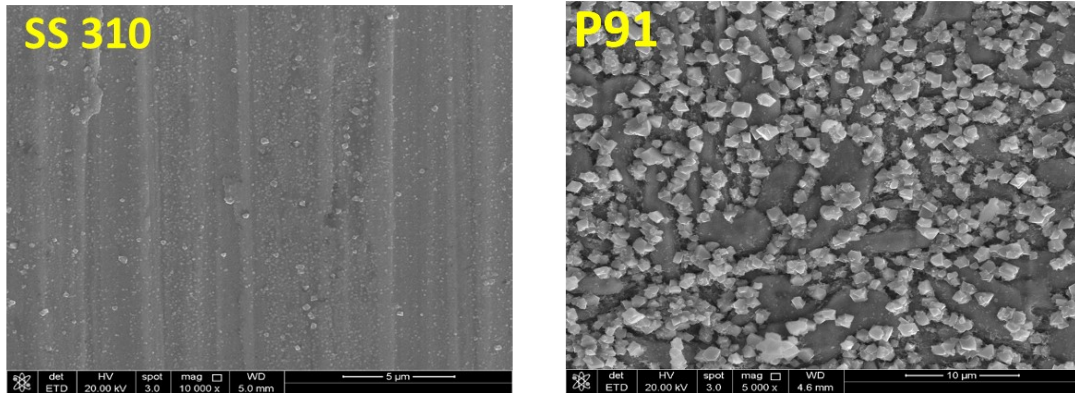


Fig. 4-20. Top-view SEM images of SS310 and P91 after the exposure to 310 °C loop water at the flow rate of 1.1 m/s and 25 MPa.

To explore the effect of pressure on chemistry of corrosion layer and particles, EDS elemental mapping and XRD spectrum were collected from P91 steel after corroding under the 25 MPa condition. Fig. 4-21 indicated the corrosion layer formed in the pressurized hot water was consist of two layer, outer porous Fe oxides and inner relative compact and uniform Fe/Cr oxides, similar to that grown in the flowing hot water at vapor pressure (9.8 MPa) (see Fig. 4-14). XRD results (see Fig. 4-22) showed that the corrosion layer was mainly composed of magnetite (Fe_3O_4) along with chromite ($\text{Fe}_{3-x}\text{Cr}_x\text{O}_4$). Compared to that formed at 9.8 MPa (see Fig. 4-15), increasing pressure likely led to the formed corrosion layer with a higher content of Fe_3O_4 .

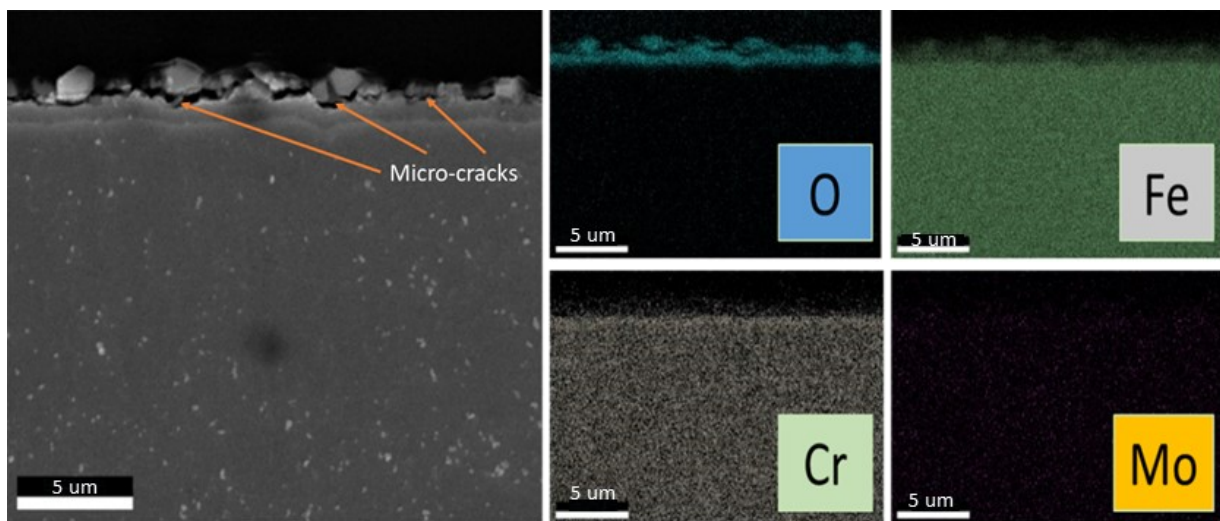


Fig. 4-21. Cross-sectional SEM image and corresponding EDS elemental mapping on P91 steel after the exposure to 310 °C water at the flow rate of 1.1 m/s and 25 MPa.

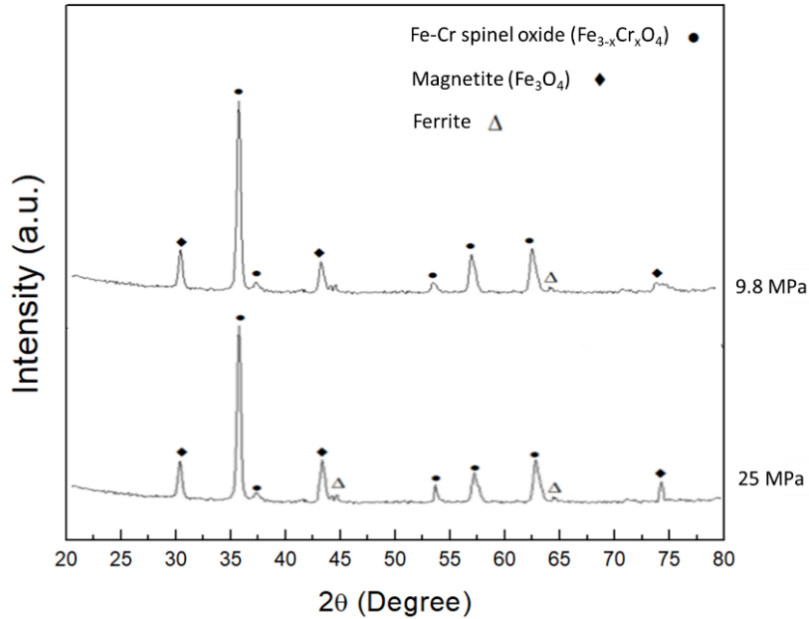


Fig. 4-22. Comparison of XRD spectrum collected on P91 steel samples after the exposures to 310 °C with flow rate of 1.1 m/s at different pressures.

High resolution TEM characterizations were conducted on the cross-sectional area of SS310 sample after corroding in 310 °C water with the flow rate of 1.1 m/s at 25 MPa, and the results are shown in Fig. 4-23. The formed oxide scale was consist of Cr-enriched oxides and alloying element Ni was accumulated at the oxide/metal interface, similar to that grown under 9.8 MPa conditions (see Figs. 4-6 and 4-15). Compared with those formed at 9.8 MPa, the oxide scale formed at 25 MPa became noticeably thicker (~110 nm). The collected XPS spectra with the depth profiling showed that Cr₂O₃ and Cr(OH)₃ were still the major composition of the oxide layer (see Fig. 4-24). The particles randomly distributed above the Cr-enriched oxide layer were iron oxides. It seemed that the increasing pressure might enhance the formation of Cr-enriched oxide layers, but did not affect the oxide chemistry.

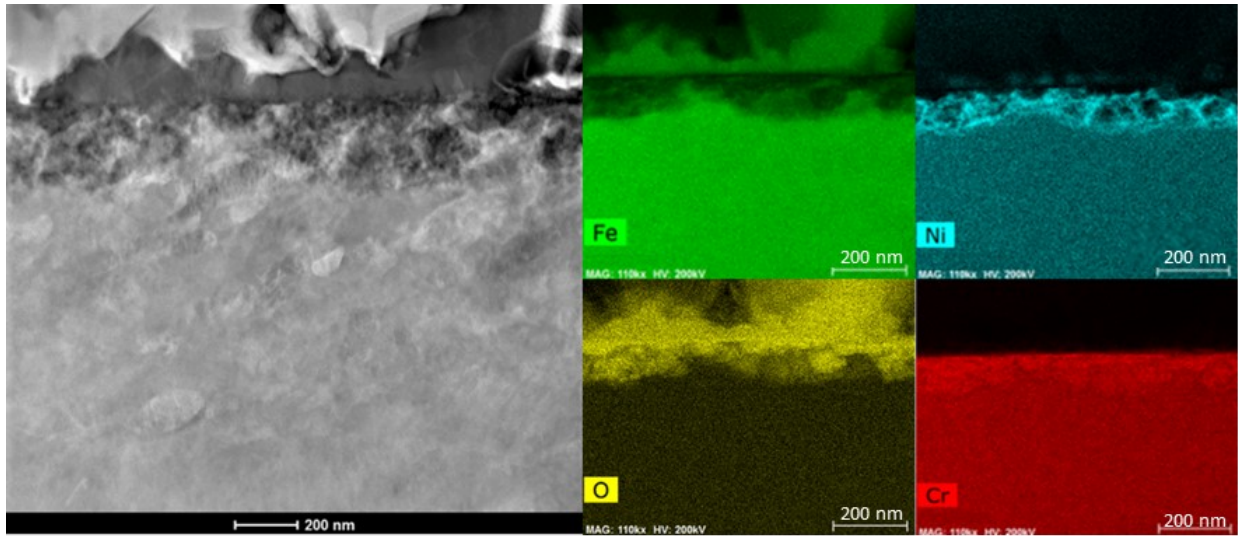


Fig. 4-23. TEM Cross-sectional images and corresponding EDS elemental mapping on SS310 after the exposure to 25 MPa water at 310 °C.

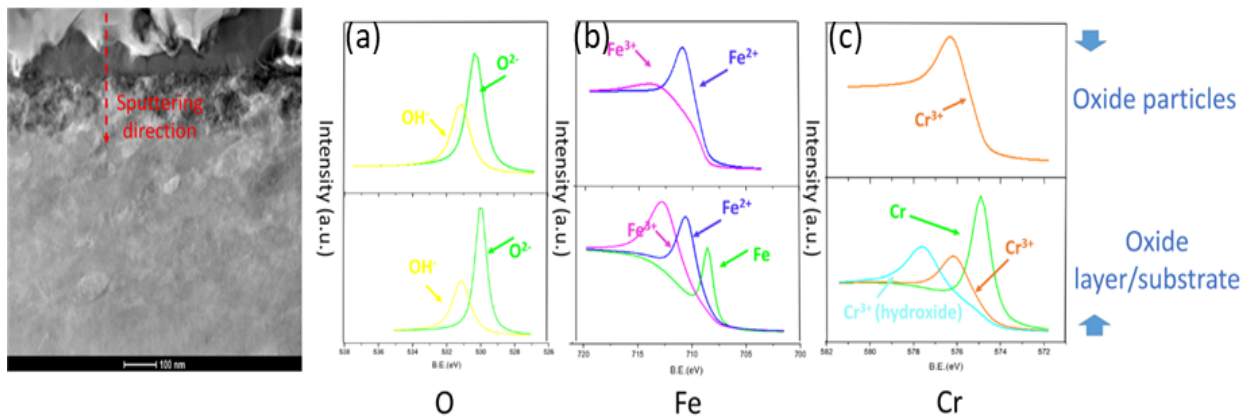


Fig. 4-24. XPS core level spectra collected on a SS310 sample after corroding under 25 MPa in 1.1 m/s flowing water at 310 °C: (a) O 1s, (b) Fe 2p_{3/2}, and (c) Cr 2p_{3/2} region.

Based on weight loss measurements, the change of the corrosion rates of SS310 and P91 steels with operating pressure are shown in Figs. 4-25 and 4-26, respectively. The corrosion rates of SS310 and P91 steels increased with pressure at 310 °C. Compared to that on SS310, the influence of pressure on P91 steel was more remarkable, implying the influence of operating pressure on the formation and/or chemical dissolution of Fe- and Cr-enriched oxides should be quite different. In addition, the change of the corrosion rates with operating pressure did not follow a linear

relationship. At pressure ≥ 15 MPa, further increasing pressure only led to a marginal increase in the corrosion rates of the two steels.

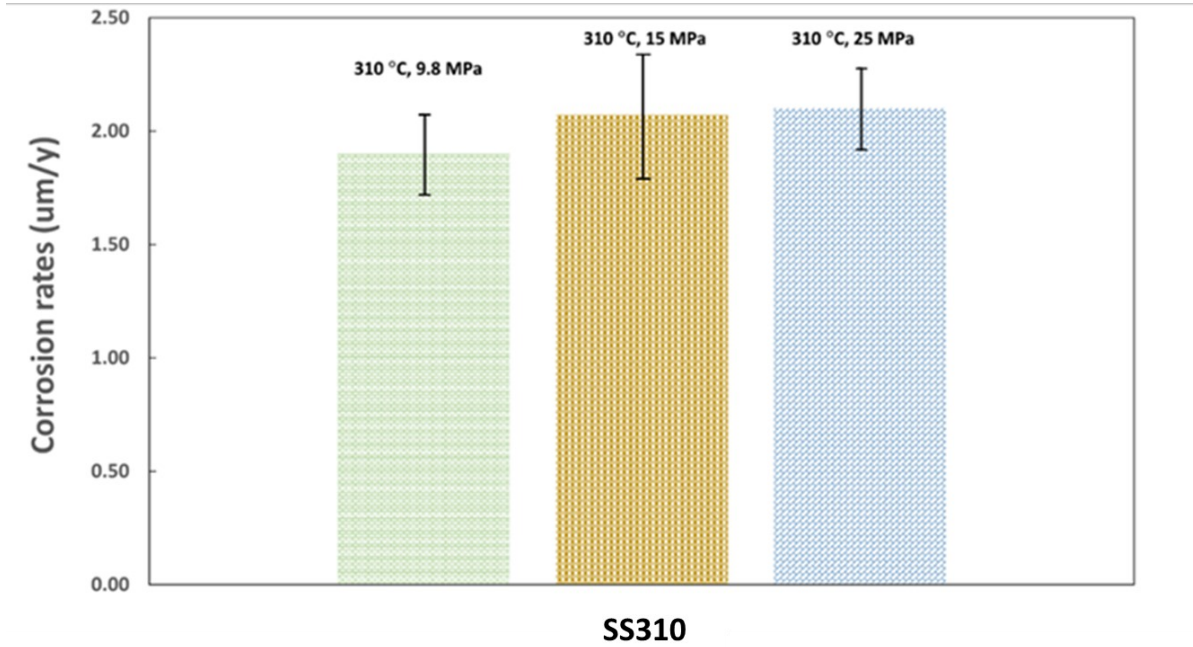


Fig. 4-25. Variation of the corrosion rates of SS310 with HTL operating pressure in 310 °C water with the flow rate of 1.1 m/s.

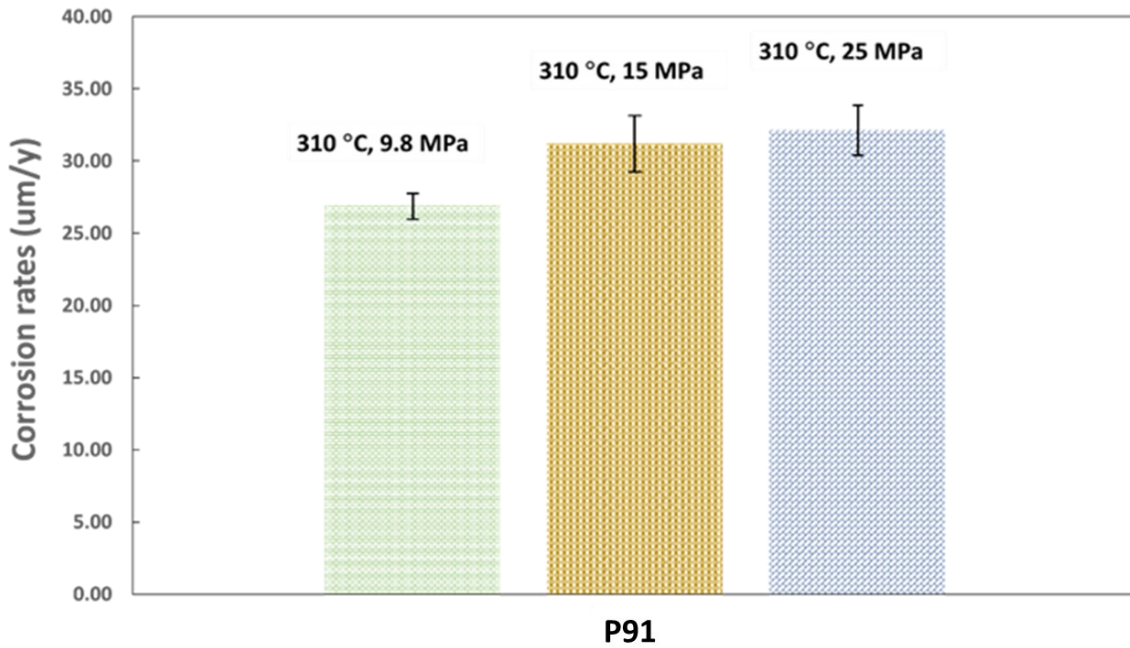


Fig. 4-26. Variation of the corrosion rates of P91 steel with HTL operating pressure in 310 °C water with the flow rate of 1.1 m/s.

4.4. Discussion

4.4.1. Influence of temperature on corrosion in HTL water

Thermodynamic calculations of several oxidation reactions were performed based on the database in HSC Chemistry software [336], and the results are present in Table 4-3. Within the two tested steels, the major alloying elements of Cr and Fe would experience general oxidation in HTL water at the temperature range of 250 - 365 °C. Compared to Fe, Cr should have higher affinity to the hot water for oxidation. Different from the two alloying elements, Ni element in SS310 exhibits positive oxide formation energy and thus would unlikely to involve in initial oxide formation stage. Therefore, depending on the Cr contents present in the two steels, the initially formed oxides on the steels should be composed of either Fe/Cr oxides or Cr-enriched oxides, as shown in Fig. 4-5 and 6, respectively. Based on the thermodynamic calculations, increasing temperature could enhance the initial oxidation rates of Fe and Cr, consistent with those shown in Figs. 4-4 and 4-5.

Table 4-3. The estimated Gibbs energy of major alloy elements formation of oxides present in the two steels at three HTL temperatures.

Possible Reactions of alloying elements with hot water	ΔG_T^θ (kJ/mol)	
	2 Cr (s) + 3 H ₂ O (l) = Cr ₂ O ₃ (s) + 3 H ₂ (g)	ΔG_{250}
ΔG_{310}		-394.981
ΔG_{365}		-403.106
2 Fe (s) + 3 H ₂ O (l) = Fe ₂ O ₃ (s) + 3 H ₂ (g)	ΔG_{250}	-72.436
	ΔG_{310}	-82.169
	ΔG_{365}	-90.255
3 Fe (s) + 4 H ₂ O (l) = Fe ₃ O ₄ (s) + 4 H ₂ (g)	ΔG_{250}	-125.992
	ΔG_{310}	-140.468
	ΔG_{365}	-152.672
<i>Ni</i> (s) + H ₂ O (l) = NiO (s) + H ₂ (g)	ΔG_{250}	11.936
	ΔG_{310}	8.819
	ΔG_{365}	6.267

After the formation of a thin oxide film on the steels, their corrosion rates would be dominated by the oxide growth and chemical dissolution processes. Several models, such as point defect model [337, 338, 339], solid-state diffusion model [340, 341] and dissolution-precipitation model [342], have been proposed to describe these processes in high temperature water [337, 338, 339, 343, 344]. For example, in solid-state diffusion model, it is proposed that corrosion would be controlled by solid state diffusion of cations along grain boundaries in the duplex oxide layers based on following hypotheses: (1) the oxidation of alloying elements occurred non-selectively; and (2) the composition of duplex oxide layers was controlled by the differences in the diffusion rates of major alloying elements [340, 345]. However, as described above, the oxidation of the alloying elements (Cr, Fe and Ni) exhibited selective behavior in the hot HTL water. Moreover, according to the observations in Figs. 4-6, 4-7 and 4-8, only a single Cr-enriched oxide layer instead of a duplex oxide layer was grown on SS310 after the exposure to hot HTL water. Thus, based on point defect model (PDM) and solid-state diffusion model [337, 338, 339, 343], the growth of Cr-enriched oxide layer on SS310 would likely to be determined by the outward diffusion of cations and/or inward diffusion of O^{2-} through the formed oxide film. Based on the estimations of the diffusion rates of Cr, Fe, and O within Cr_2O_3 matrix at the temperature range of 250 – 365 °C (see Table 4), the oxide growth on SS310 should be dominated by the inward diffusion of O^{2-} since its rate is much slower than those of Cr and Fe cations. Increasing temperature could result in remarkably increase in the diffusion rates of the ions, consequently leading to a higher general oxide formation rate. Note that the diffusion of cations (especially Fe ions) via interstitial and/or defective sites might also occur and be enhanced with higher temperature during the exposure to the hot water [344]. As implied in Table 4-4, the Fe cations could locally pass through the oxide layer and interact with water, resulting the formation of Fe-enriched nodular oxides. Considering the fact that the chemical dissolution of Cr-enriched oxides in high temperature water would occur concurrently and be enhanced with temperature [335, 346], increasing temperature would lead to a higher corrosion rate of the steels in the hot water as indicated in Fig. 4-9.

However, as shown in Fig. 4-9, further increasing temperature from 310 °C to 365 °C resulted in a decrease in the corrosion rate of SS310. Previous studies also found similar trend on SS 304 [141], proposed that at around 300 °C the corrosion scales would have transformed gradually from magnetite to chromite (with corrosion products phase structure change from octahedral to needle-shaped crystals). However, as shown in Figs. 4-7 and 4-8, the oxide layer grown on SS310 did not

change from magnetite to chromite and the proposed mechanisms are not suitable for Cr-bearing SS310. From another perspective, the existence of an inflection point at around 310 °C (the transition temperature) might be due to the change in water properties and corresponding oxidation and chemical dissolution at temperature close to 365 °C. Previous studies [347] found that chemical and electrochemical oxidation reaction could simultaneously occur on Cr-bearing steels at the temperature close to supercritical point (374 °C) or beyond, consequently resulting in a remarkable change in oxide growth pathways and chemical dissolution. As shown in Fig. 4-1, drop in the dissociation and dielectric constants of water at 365 °C (compared to that at 310 °C) would possibly mitigate the chemical dissolution of polar Cr-enriched oxides/hydroxides formed on SS310 and consequently suppress the outward diffusion of cations (especially Fe cations) [348]. Direct evidence is that Fe-enriched nodular oxides completely disappeared at 365 °C (see Fig. 4-6). Except for nodular oxidation, the suppressed dissolution could make the formed oxide layer less defective as shown in Fig. 4-6(c), thus leading to higher resistances to the electrochemical oxidation.

Due to its low bulk Cr content, the oxide layer formed on P91 steel at HTL operating temperatures should be composed of magnetite (Fe_3O_4) and chromite ($\text{Fe}_{3-x}\text{Cr}_x\text{O}_4$) as shown in Fig. 4-5, even though alloying element Cr has a higher affinity to oxygen than Fe (see Table 4-3). After the initial formation of Fe-enriched oxide layer, subsequent outward cation and inward oxygen diffusion within the layer could also occur. As indicated in Table 4-5, the diffusion rate of O anions in Fe_3O_4 is remarkably lower than that of Fe cations, suggesting that the inward diffusion of oxygen would still be the rate-limiting factor in Fe-enriched oxide growth. Note that the calculated diffusion rates are based on theoretical situation and may not representing actual diffusion rates during the reactions. However, the calculated value could be used for comparing in this study. Similar to those in Cr_2O_3 , diffusion rates of both cations and anions noticeably increase with temperature, especially at the range of 310 to 365 °C. However, as shown in Table 4-4 and 3-5, the diffusion rates of cations and anions in Fe_3O_4 are significantly higher than those in Cr_2O_3 at a HTL operating temperature, consequently leading to a much higher corrosion rate of the steel as shown in Figs. 4-9 and 4-10. Different from SS310, the corrosion rate of P91 steel continuously increases with increasing temperature from 250 to 365 °C. This might be due to the fact that the effect of temperature on the growth and chemical dissolution of oxides is more dominant on Fe-based

oxides when comparing to that of Cr₂O₃. Although the decreases in water density and dissociation constant at the temperature close to the supercritical point of water could retarded the dissolution of polar oxides, the lack of polarity between Fe-O bond comparing to Cr-O bond [349, 350] might offset such influence. Moreover, because of the higher temperature dependence of cation and anion diffusion within iron-enriched oxides, the increases in temperature would likely surpass the change of chemical dissolution introduced by the change of water properties.

Table 4-4. Estimated diffusion rates of Cr, Fe, Ni and O ions in Cr₂O₃ at HTL operating temperatures based on database in references [351-356].

Cations and Anions	Diffusion rates (cm ² /s)		
	250 °C	310 °C	365 °C
Cr	6.43E-37	4.84E-34	7.03E-32
Fe	9.53E-31	2.59E-28	1.75E-26
Ni	2.30E-27	3.45E-26	7.50E-23
O	1.16E-41	2.51E-37	4.55E-34

Table 4-5. Estimated diffusion rates of Fe and O ions in Fe₃O₄ at HTL operating temperatures based on database in references [357-359].

Cations and Anions	Diffusion rates (cm ² /s)		
	250 °C	310 °C	365 °C
O	6.00E-30	4.50E-29	8.36E-27
Fe	3.17E-22	2.96E-21	5.28E-19

4.4.2. Influence of flow rate on corrosion in HTL water

As shown above, the flow rate of HTL water in this study was in the range of 0-1.1 m/s. The flow states of HTL water on the steels in Tests #4 and 5 should be turbulent based on the following Reynolds number (Re) calculation equation [360-362]:

$$Re = \frac{Q * D_H}{v * A} \quad (4-4)$$

where Re is Reynolds number; D_H is the hydraulic diameter of the autoclave (m); Q is the volumetric flow rate (m^3/s); A is the autoclave cross-sectional area (m^2); ν is the kinematic viscosity of the fluid (m^2/s). At $310\text{ }^\circ\text{C}$, the kinematic viscosity of the water is equal to $1.19 \times 10^{-7} m^2/s$. The estimated Re was about 504,626 and 925,147 at the flow rates of 0.6 and 1.1 m/s, respectively. Thus, a thin fluid layer, consist of diffusion boundary, viscous and buffer sub-layers, might be established above the steels' surface, as schematically shown in Fig. 4-27.

As indicated in Figs. 4-12 to 4-15, increasing the flow rate in hot HTL water could noticeably enhance the chemical dissolution of outer Fe oxide layer grown on low-Cr P91 steel, but only have marginal effect on Cr-bearing SS310. This may be because the Fe oxides formed on the low-Cr steel would have a much higher chemical dissolution rate than the Cr-enriched oxides on 310 SS, especially in high temperature water [320-322, 363]. Moreover, increasing flow rate could affect the mass transfer process near the steel surfaces. According to previous studies [364-366], the mass flow of iron cations, J_{Fe} from steel surface to bulk fluid in a container could be governed by

$$J_{Fe} = Kc (C_m - C_b) \quad (4-5)$$

where Kc is the mass transfer coefficient, C_m is the concentration of iron at the metal surface, and C_b is the concentration of iron in the bulk fluid. Within the diffusion boundary layer (see Fig. 4-27), the mass flow rate might be controlled by [367, 368]

$$J_{Fe} = \frac{D}{L} (C_m - C_0) \quad (4-6)$$

where L is the distance from the base metal to the midpoint of boundary layer, D is the diffusion coefficient of iron, and C_0 is the iron concentration in the boundary layer. In the boundary region, the diffusion rates of cations/anions transfer would be low and independent on water flowing rate. Thus, under relative stable conditions, the mass transfer coefficient (K_c) could be derived to be

$$Kc = \frac{D}{L} \left(\frac{C_m - C_0}{C_m - C_b} \right) \quad (4-7)$$

Under static condition, the difference between C_b and C_0 should be negligible. With an increase in flow rate, the concentration of Fe cations in bulk fluid (C_b) could be down to near zero since the cations in water are continuously removed by the ion filter in the testing loop. This might lead to a remarkable increase in the mass transfer coefficient and consequently an enhanced corrosion rate of P91 steel. Furthermore, previous studies have also demonstrated the Cr-enriched oxide formed

on Cr-bearing steels would be stable, compact and protective in hot aqueous solutions at the temperature range of 250 - 370 °C [130, 343, 369, 370]. The solid solubility of Fe and Ni cations in Cr oxides is expected to be quite low [371, 372] and their outward diffusion rates should be significantly lower than those in Fe oxides as indicated in Table 4-4 and 3-5. The influence of flowing rate on Cr-enriched oxide would thus be much less noticeable than that on Fe oxide. In addition, as shown in Fig. 4-15, increasing flow rate is likely to suppress nodular oxidation of SS310. This might be due to the fact that the Fe cations, which diffuse through the surface oxide scale to the interface of oxide/water, would be readily removed by the flowing water and consequently have less chance for the nodular formation.

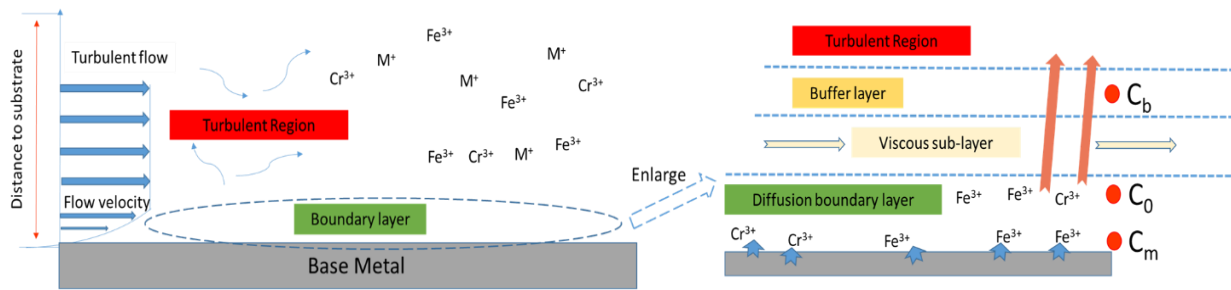


Fig. 4-27. Schematic of ion distribution and contents near a steel surface under flowing conditions in this study.

4.4.3. Influence of operating pressure on corrosion in HTL water

As shown in Fig. 4-23, increasing pressure from saturated vapor pressure (9.8 MPa) to 25 MPa could slightly increase the thickness of formed surface scale and reduce the formation of nodular oxides/deposit particles on SS310. Compared to SS310, the influence of pressure on P91 was more pronounced as micro-cracks were presented within the oxide scale and corrosion rates increased remarkably. The influence of pressure on corrosion would be associated with the change in water properties. Increasing pressure to 25 MPa could increase the ionic product and dielectric constant of water, favors the solubility and dissociation of ionic species [103]. For example, the solution conductivity was found to be increased by more than one order of magnitude with increasing pressure from 9.8 to 25 MPa at 310 °C [128, 315, 316]. These changes would lead to an increase of the dissolution of cations in the oxides into water and also possibly facilitate the adsorption of oxidizing species (H₂O, OH⁻, etc.) on the surface scales formed on the two steels [131, 314, 373],

consequently enhancing the chemical dissolution process of formed oxides and promoting the formation of cation vacancies near the oxide/solution interface. As shown in Fig. 4-23, the accumulation of Ni around grain boundaries within the oxide layer could be from the above effects.

Moreover, as shown above, the impact of pressure on SS310 was quite marginal, which might be due to the fact that the formation of relatively compact Cr-enriched layer could act as a barrier to well control the diffusion of cations and anions and then effectively limit the deleterious effect of increasing pressure. For P91 steel, the formed Fe-enriched layers were quite thick and fragile. Increasing pressure in the flowing water might not only enhance the oxidation and chemical dissolution, but also introduce additional stress to assist the formation of micro-cracks within the corrosion layer (see Figs. 4-20 and 4-21). The micro-cracks (marked in Fig. 4-21) might then act as short paths for the diffusion of HTL water into the oxide layer and further increase the chemical dissolution of the iron-based oxide layer.

4.5. Conclusions

This study investigated the influence of operating temperature, pressure and flow rate on the corrosion of P91 and SS310 under representative HTL conversion processes and the following conclusions are made:

- (1) At the HTL temperature range of 250-365 °C, increasing temperature enhanced the corrosion of P91 while there was a transition temperature (around 310 °C) above which the corrosion rate of SS310 decreased with temperature.
- (2) At 310 °C, increasing flow rate up to 1.1 m/s accelerated the corrosion of P91, but resulted in a decrease in the corrosion rate of SS310; the reason could be that increasing flow rate would enhance the chemical dissolution of Fe-based oxide on P91, but suppress local nodular oxidation on SS310.
- (3) At 310 °C, increasing pressure from saturated vapor pressure (9.8 MPa) to 25 MPa facilitated the oxide formation on both steels, and assisted the formation of micro-cracks on P91 steel, consequently resulting in enhanced corrosion rates of the steels. The effect of pressure on P91 was much more noticeable than that on SS310.
- (4) Under the HTL conditions, the corrosion layer formed on P91 was consist of magnetite (Fe_3O_4)

and chromite ($\text{Fe}_{3-x}\text{Cr}_x\text{O}_4$) while an inner compact Cr-enriched layer, mainly composed of Cr_2O_3 and $\text{Cr}(\text{OH})_3$, was grown on SS310. Except for general oxidation, Fe-enriched nodular oxides were formed on the steels, and the nodular oxidation of SS310 was likely suppressed with increasing temperature or flow rate.

Chapter 5. Impacts of Catalyst, Inorganic and Organic Corrodants on Corrosion under Batch-mode Catalytic Biomass Hydrothermal Liquefaction Conversion

In the previous chapter, corrosion rate results and characterization of oxide layers formed on SS310 and P91 steel were analyzed and the impact of HTL operating conditions was discussed in depth. In this chapter, these two steels were further examined in the real HTL operating conditions with existence of alkaline catalyst, inorganic corrodants and organic acid. I have carried out autoclave tests under different HTL conversion conditions and analyzed the impact of these corrodants on performance of SS310 and P91 steel. This study has found that the addition of alkaline catalyst and organic acid remarkably increases the corrosion rates of both steels and affected the chemistry and stability of formed oxide layers. The impact of inorganic corrodants is less severe, but these corrodants can diminish the integrity of formed oxide layers. This chapter serves to examine the corrosion of candidate steels in real HTL conversion environments and advance the mechanistic understanding of how steels corrode in these environments.

Abstract

Catalytic hydrothermal liquefaction (CHTL) is used to convert wet biomass for highly promising carbon conversion efficiency. This study investigated three major environmental factors, including catalyst, inorganic corrodants and organic acid on the corrosion of two candidate reactor steels (SS310 and P91) using autoclave methodology and advanced characterization techniques. The addition of 0.5M K_2CO_3 resulted in a remarkable increase in corrosion rates and significantly changed the corrosion layers formed. The acetic acid generated from CHTL also noticeably enhanced corrosion while the presence of Cl^- and S^{2-} only had marginable influence. SS310 exhibited much better performance than P91 under the CHTL conditions.

Keywords: Weight loss; Alkaline corrosion; High temperature corrosion; SEM; TEM, XRD.

5.1. Introduction

The rapid depletion in fossil fuel resources and the notorious environmental impacts induced by their combustion have introduced urgent demands on exploring clean, renewable and sustainable energy alternatives, such as hydro, solar, wind and biomass, to meet our increasing daily energy needs. Biomass, which is an abundant, sustainable and renewable resource derived from organic matters (wood chops, crop residues, organic municipal waste, energy crops, etc.), can be quickly transformed into marketable energy products via either biochemical or thermochemical pathways [9-13]. Among these developed biomass conversion technologies, hydrothermal liquefaction (HTL) is recognized as a cost-effective and environment friendly pathway to directly convert wet biomass and even industrial biowaste feedstocks (such as black liquor and hog fuel) into valuable bio-chemicals and bio-crude oils [91, 177, 374, 375]. During a HTL process, hot pressurized water is usually used as the conversion medium at the temperature range of 250 - 365 °C and pressure up to 25 MPa to facilitate the depolymerization of raw biomass materials while suppressing the repolymerization of produced fragmented species for the target of high carbon conversion efficiency [73-77]. The effects of water temperatures, pressures and flow rates on the corrosion of HTL reactor alloys have been well studied and reported in our recent publication [376].

Except for the hot pressurized water conversion medium, the introduction of homogenous catalyst into HTL processes is also a serious corrosion concern of the reactor alloys. Considerable studies have demonstrated that the addition of homogeneous alkaline catalysts (such as K_2CO_3 , Na_2CO_3 , NaOH, K_2CO_3 , KOH, LiOH, RbOH, or CsOH) into a HTL conversion process can effectively enhance the yield and quality of biocrude oil [76-89]. Among all the proposed catalysts, it is generally accepted that the addition of 0.5 - 1.0 M K_2CO_3 can lead to the most promising HTL conversion efficiency [90-94]. From the corrosion point of view, however, the introduction of K_2CO_3 catalyst would significantly change the pH value of the HTL biorefining environments, consequently introducing new challenge on the selection of appropriate reactor alloys. For example, Shao *et al.* reported that the surface scale formed on SS316LN was consist of Cr and Ni hydroxides instead of Cr_2O_3 and NiO after immersing in 1 M NaOH (pH ~13) at 300 °C for 720 hours [157]. Other studies found that the solubility of nickel oxides (NiO) in a 0.074 mmol/kg ammonium and 0.17 mmol/kg sodium hydroxide solution (pH = 10) was increased about twice with an increase in temperature from 200 °C to 315 °C [377]. These studies suggest that both solution pH and

temperature could significantly affect the corrosion of HTL reactor alloys during the conversion. But the related corrosion results are too limited to determine the corrosion modes and extents of Fe-based steels and Ni-based alloys in the catalytic HTL environments. Moreover, the pH value of HTL environments will vary with the conversion processes since the produced organic acids can directly interact with the alkaline catalyst applied. Based on pilot-scale operating results, the typical HTL processes are likely to be operated at the pH range of about 6 -12 [374, 375, 378-380]. Moreover, a number of investigations have shown that the physiochemical properties and yields of HTL products are coherently related to the chemical properties of biomass feedstocks applied [159, 381, 382]. Previous studies on different types of biomass feedstocks (such as lignocellulose, microalgae and biowaste) under typical HTL conditions found that the chemical compositions of biomass feedstocks, particularly the major components (including cellulose, hemicelluloses, lignin, lipids, proteins and hydrocarbons) presented, exhibited critical impacts on the variety and volatility of bio-products, the yield of biocrudes, and the concentration of corrodants released [383, 384]. For example, a previous study on the HTL conversion of miscanthus (lignocellulose), *spirulina platensis* (microalgae), and primary sewage sludge (residues) at 310 °C indicated that the application of miscanthus would lead to the highest biocrude yield (up to 69 wt.%), followed by the use of *spirulina platensis* and sewage sludge, respectively [385]. Note that the high yield of biocrude oil is usually accompanied by an increase in aqueous phase and oxygen and nitrogen contents, consequently requiring further upgrading treatments for final application [386, 387, 388]. Moreover, the heterogeneity in the same type of raw biomass feedstocks is also likely to be a key factor affecting the bio-crude yield. For instance, the application of high concentration of loosely packed celluloses could lead to an improved biocrude yield, but inevitably increase the contents of oxygen and moisture in bio-crude oil with poor oil quality and relatively low HHV [389, 390]. From the corrosion perspective, inorganic (such as Cl^- , S^{2-}) and organic corrodants (such as organic acids and sulfur-containing by-products) will be released from the feedstocks during the conversion, possibly enhancing the corrosion of the reactor alloys and even introducing severe structural integrity damage [159-164]. A number of studies have shown that both Cl^- and S^{2-} are notorious agents to facilitate pitting and stress corrosion cracking of Fe-based steels and Ni-based alloys in high temperature aqueous solutions [165-170]. Unfortunately, the contents of Cl^- and S^{2-} in typical industrial bio-wastes can be up to 15,000 and 13,200 ppm, respectively [391, 392]. Meanwhile, certain amounts (about in the range of 5 - 10 wt.%) of saturated short-chain organic

acids, such as formic, acetic and butyric acids, will also be generated during the HTL conversion [90, 91, 92, 94, 375, 393, 394]. For instance, about 7 wt.% acetic acid was found in the formed aqueous phase from the batch-mode HTL conversion of municipal sludge [395, 396]. The presence of these organic acids in the HTL hot water might accelerate the chemical dissolution of oxide scales formed on stainless steels at temperatures $> 120\text{ }^{\circ}\text{C}$ [91, 171-174]. It has also been found that the addition of acetic acid into water would increase concentration of protons in the pores and thus accelerate localized dissolution of oxide scales formed on steels [397]. According to our comprehensive literature review, little information is available to describe the influence of inorganic and organic corrodants released during the HTL conversion on the corrosion of HTL reactor alloys.

Despite that HTL conversion technology has been well established at laboratory and pilot scales, industrial-scale HTL plant has not yet been deployed worldwide because of economic concern and materials technology impediments (especially the potential corrosion damage of HTL reactor alloys). Therefore, this study aims at investigating the impacts of K_2CO_3 catalyst, inorganic corrodants, and organic acids on the corrosion modes and extents of two candidate HTL reactor steels (P91 and SS310). P91 steel is an extensively used low-alloyed ferritic-martensitic steel constructed as high temperature components at thermal power plants, and exhibit high resistance to stress corrosion cracking and desirable mechanical properties [203, 204]. SS310 is a Cr-bearing austenitic stainless steel and has promising corrosion performance even in high temperature supercritical water [304] or basic solution ($\text{pH} = 14$) at temperature $\leq 180\text{ }^{\circ}\text{C}$ [398]. Moreover, our recent study found that these two steels showed acceptable corrosion performance in flowing hot pressurized HTL water [376]. This study is expected to advance the mechanistic understanding of how the Fe-based steels with different Cr contents corrode under catalytic HTL conditions, and partially support the development of cost-effective materials technology solutions for the industrial-scale construction and continuing safe operation of HTL plants.

5.2. Experimental Procedure

5.2.1. Test Sample Preparation

Rectangular coupons with the dimensions of 20 mm long × 10 mm wide × 2 mm thick were made from commercial P91 cylinder and SS310 plate. The chemical compositions of two steels are listed in Table 5-1 based on the associated certificates delivered by corresponding suppliers. The detailed information about the fabrication history of the two steels can be found in the reference [376]. On each coupon, a small hole with 4 mm diameter was drilled at its top for hanging on a custom-made Alloy 625 sample holder. Before a corrosion test, the coupons were well grounded in flowing deionized water using SiC papers down to 600 grit to ensure the complete removal of potential contamination introduced during the coupon machining and achieve consistent surface finish as our previous study [376]. Following that, the coupons were cleaned with ethanol in an ultrasonic bath for 10 minutes, rinsed using flowing ultrapure water, and followed by drying with pressurized air. On each prepared coupon, a sample ID was assigned and marked on its top left corner for record. After the preparation, optical microscopy examinations were performed to ensure that the final surface finish of each coupon exactly meet standard high temperature corrosion testing requirements [399]. Before the exposure to a desired catalytic HTL environment, the freshly prepared coupons were carefully weighed using the Mettler Toledo microbalance with the resolution of 0.001 mg and their dimensions were measured using the digital caliper with the precision of 0.01 mm. To ensure the accuracy and precision of results reported in this study, four freshly prepared coupons of each steel were used in each autoclave corrosion test as described below.

Table 5-1. The chemical compositions of SS310 and P91 steels used in this study.

Steel Types	Alloying element contents (wt.%)							
	Cr	Ni	Mo	Fe	C	Si	N	Mn
P91	8.36	0.07	0.90	Bal.	0.11	0.33	n/a	0.47
SS310	24.20	21.80	n/a	Bal.	0.02	0.20	0.10	1.60

5.2.2. Autoclave testing methodology and procedure

Table 5-2 summarizes the corrosion tests performed to identify the influence of K_2CO_3 catalyst, inorganic corrodants, and organic acids on corrosion in a static Alloy C-276 autoclave at 310 °C based on the methodology described in ASTM G31 [251]. In Test #1, ultrapure water was used to simulate the non-catalytic HTL conversion condition for the comparison with the results obtained from catalytic HTL environments. In Tests #2-5, certain amounts of alkaline catalyst, inorganic and/or organic corrodants were added into the ultrapure water to clarify their effect on the corrosion under representative HTL conversion conditions (see Table. 4-2). As mentioned above, the addition of 0.5 - 1.0 M K_2CO_3 catalyst can achieve the desired HTL conversion efficiency. From the corrosion perspective, the addition of 0.5 M K_2CO_3 will increase the pH of the HTL conversion environment to about 12 at room temperature. Further increase in K_2CO_3 concentration to 1 M can make the HTL environment with the pH value of 12.2. In this study, 0.5 M K_2CO_3 was thus added to simulate the catalytic HTL conversion condition. Moreover, the water/biomass ratio during a HTL conversion is needed to be well controlled to maximize the conversion efficiency [400, 401]. Based on that, the ratio of water/biomass is determined to be 5/1 [385, 402], and 3500 ppm Cl^- and 2500 ppm S^{2-} was introduced in Tests #3-5 as the representative contents of inorganic corrodants released during the HTL conversion. Furthermore, short-chain organic acids would likely be generated during the typical HTL of bio-wastes and acetic acid was selected as the representative organic acid in this study based on former HTL conversion results [403, 404].

To avoid potential contamination from the autoclave wall alloy during Tests #1 - 5, a pre-oxidized Alloy 625 liner was used to accommodate the test solution and steel coupons in the autoclave as shown in Fig. 5-1. The freshly prepared testing coupons were loaded in a pre-oxidized sample holder made of Alloy 625 using pre-oxidized 20% Cr and 80% Ni Cr-Ni alloy wires to avoid potential galvanic effect between the holder and steel coupons. Note that both the liner and wire were pre-oxidized in an air furnace at 400 °C for ~ 12 hours. After loading the solution and samples into the liner, the autoclave was purged with N_2 gas for at least an hour to create a deaerated environment. After leak examination, the autoclave was heated up to 310 °C. Note that the heating rate was decreased from 6 to 3 °C/min to avoid overshooting when the temperature was approaching 310 °C. Once the temperature reached the target value, the time was recorded as starting point of each test. After the 240 hours' exposure to the designated HTL environment as

shown in Table 5-2, the autoclave was powered off and then cooled down in air. Finally, the tested coupons were carefully removed from the autoclave, rinsed using flowing ultrapure water, followed by drying with pressurized air. Note that each corroded steel coupon was re-weighed using the same microbalance mentioned above for subsequent corrosion rates evaluation.

Table 5-2. Tests conducted to investigate the effects of alkaline catalyst, inorganic corrodants, and organic acid on the corrosion of candidate reactor steels.

Candidate Materials	Test	Conditions
SS310, P91 steel	#1	In deaerated ultrapure water at 310 °C (Baseline)
	#2	In deaerated 0.5 M K ₂ CO ₃ at 310 °C for 10 days (influence of catalyst)
	#3	In deaerated 0.5 M K ₂ CO ₃ + 3500 ppm Cl ⁻ + 2500 ppm S ²⁻ at 310 °C for 10 days (influence of inorganic corrodants)
	#4	In deaerated 0.5 M K ₂ CO ₃ + 3500 ppm Cl ⁻ + 2500 ppm S ²⁻ + 5 wt.% acetic acid at 310 °C for 10 days (influence of organic acids)
	#5	In deaerated 0.5 M K ₂ CO ₃ + 3500 ppm Cl ⁻ + 2500 ppm S ²⁻ + 10 wt.% acetic acid at 310 °C for 10 days (influence of organic acid content related to Test #4)

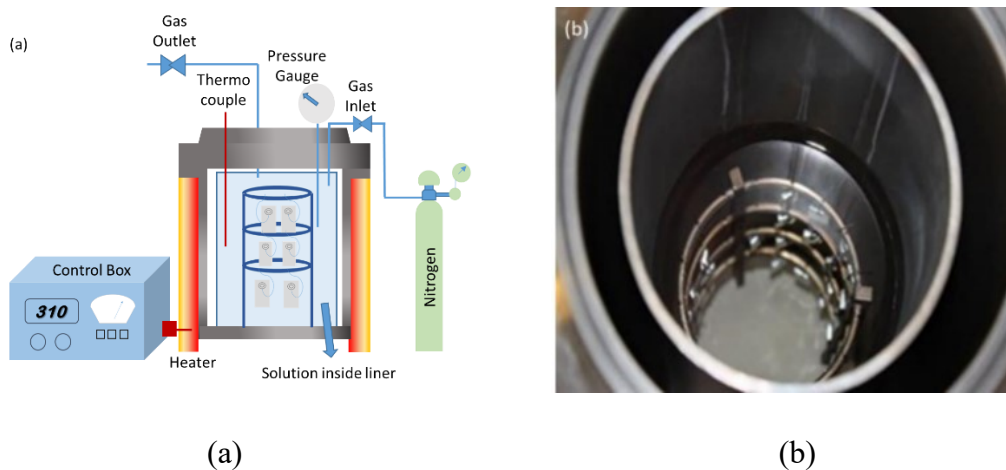


Fig. 5-1. (a) Schematic of autoclave setup used in this study, and (b) A top-view of Alloy C-276 autoclave with an Alloy 625 liner and sample holder used for the designed tests.

5.2.3. Corrosion rate assessment

For high-temperature aqueous corrosion testing, two techniques, including direct mass change and weight loss measurements, can be applied for the corrosion rate evaluation. In this study, the two methods were used to assess the corrosion rates of the steels in catalytic HTL environments for comparison. The direct mass change method was to measure the mass change of a steel coupon before and after an autoclave test directly. This method has been successfully and widely applied for assessing the corrosion rate of an alloy in high temperature systems in which the oxidation of the alloy was the dominant reaction occurred and the formed oxide layers were compact without excessive nodular oxidation and/or surface spallation [405, 406]. The corrosion rate ($\mu\text{m}/\text{year}$) of a steel coupon can thus be calculated by [225]:

$$\text{Corr. Rate} = \frac{\eta \cdot 8.76 \times 10^7 \cdot \Delta m}{dAt} \quad (5-1)$$

where Δm_1 (g) is the weight change of a coupon before and after a test; d (g/cm^3) denotes the steel density; η is the estimated molar mass ratio of consumed alloying elements to oxygen in formed corrosion products, and is about 2.3 for P91 steel and 2.2 for SS310 [230]; A (cm^2) is the measured surface area of a coupon; and t (h) denotes the testing duration. Note that the molar mass ratio used in the equation is based on the assumption that Cr_2O_3 and Fe_2O_3 are the major oxides formed on SS310 and P91, respectively. According to ASTM G16 [226], the average corrosion rate of each steel was obtained from four parallel coupons after corroding in a HTL environment.

Compared with the direct mass change, the weight loss measurement is more complicated and time-consuming as it involves two major steps. The first step is to completely remove the formed corrosion products based on ASTM-G1 standard [227]. Such descaling can be reached through immersing the corroded coupons in suitable solutions, which can effectively dissolve the formed corrosion products, but only has negligible effect on the steel substrates. In this study, the descaling of SS310 was firstly carried out in the solution A of 2 wt.% $\text{C}_6\text{H}_8\text{O}_7$ + 5 wt.% $(\text{NH}_4)_2\text{HC}_6\text{H}_5\text{O}_7$ + 0.5 wt.% $\text{C}_{10}\text{H}_{14}\text{N}_2\text{Na}_2\text{O}_8$ at 90 °C for 30 minutes, and subsequently in the solution B of 4 wt.% KMnO_4 + 5 wt.% NaOH at 90 °C for next 30 minutes, followed by ultrasonic ethanol cleaning for ~15 minutes. The coupons were then immersed in the solution A at 90 °C again for another 30 minutes' exposure and weighed. The above process was carried out repeatedly until the formed corrosion products were completely removed and the coupon mass remained constant as described

in the references [230, 231]. Different from SS310, the descaling of P91 steel was carried out by immersing corroded coupons in the solution of 500 ml HCl + 3.5 g (CH₂)₆N₄ + 500 ml H₂O at room temperature for 10 minutes. Both cotton swab and soft copper brush were applied for gently removing any remaining corrosion products after the immersion. The second step is to weigh the coupons and then calculate the mass difference before the corrosion test and after the descaling. The corrosion rate of a coupon (μm/year) could thus be estimated by [232]:

$$\text{Corr.Rate} = \frac{8.76 \times 10^7 \cdot \Delta m}{dAt} \quad (5-2)$$

where d (g/cm³) is the steel bulk density; A (cm²) is the surface area of a coupon during exposure; and t (h) denotes the testing time. Note that the average corrosion rate of a steel in a typical catalytic HTL environment was obtained from three parallel corroded coupons after the descaling process based on the requirements in ASTM G16 [226].

5.2.4. Corrosion products characterization

After each autoclave test, the coupon which has the direct mass change value closest to the average value in a given replicate set was chosen for subsequent characterization to explore the microstructure and chemical properties of corrosion layers formed. Preliminary surface morphology examination was carried out by taking optical images to quickly check whether noticeable change occurred in the surface morphology of coupons. Following that, the FEI Nova NanoSEM 650 scanning electron microscope (SEM) system with equipped Oxford energy dispersive X-ray spectroscopy (EDS) was employed at 20 keV to identify the corrosion modes (such as passivation, active corrosion, nodular oxidation and/or pitting) and characterize the corrosion layers' chemical properties. X-ray diffraction (XRD) technique with a Co K α X-ray source operated at 40 kV and 150 mA was used to determine the phase compositions of corrosion layers formed on P91. To further characterize the formed corrosion layers on P91, diamond saw cutting in low-rpm mode and SEM examinations were applied to obtain the cross-sectional view of corroded P91 steels. Different from P91, the corrosion layers grown on SS310 were found to be much thinner as shown in the later sections. FEI Helios NanoLab™ DualBeam™ Focus Ion Beam (FIB) microscope was thus employed to produce the SEM cross-sectional views of corroded SS310

samples and TEM samples. Note that a thin platinum (Pt) film was deposited on the corroded SS310 coupons in vacuum environment to protect the formed corrosion layers before the FIB operation. After the cross-sectional SEM examination, *in situ* lift-out technique was applied to generate thinner samples for subsequent TEM characterizations. A Tecnai Osiris™ scanning/transmission electron microscope (S/TEM) equipped with super X-field emission gun (FEG) and X-ray detection system (20 kV) was operated to obtain high-angle annular dark-field (HAADF) imaging, black field (BF) imaging, energy-dispersive X-ray spectroscopy (EDS) element mapping, and selected area diffraction (SAD) pattern of corroded SS310 cross-sectional samples.

5.3. Main Results

5.3.1. Effect of alkaline catalyst on corrosion

The photographic images of SS310 and P91 coupons before and after the exposure to ultrapure water and 0.5 M K_2CO_3 at 310 °C are shown in Fig. 5-2. Before the tests, the surfaces of newly prepared coupons were clean with shining metal luster. After the exposures, the coupon surfaces exhibited different appearances, indicating the formation of corrosion layers with different thickness as well as the localized deposition of corrosion products. As shown on Fig. 5-2, localized corrosion product deposition occurred on SS310 after the exposure to 310 °C water. Compared with that formed in the hot water, the introduction of 0.5M K_2CO_3 catalyst likely resulted in the formation of a much thicker corrosion layer on the steel. For P91 steel, the addition of the catalyst also led to the formation of a thicker surface layer than that formed in the hot water. In addition, no pit was found on the two steels after exposures.

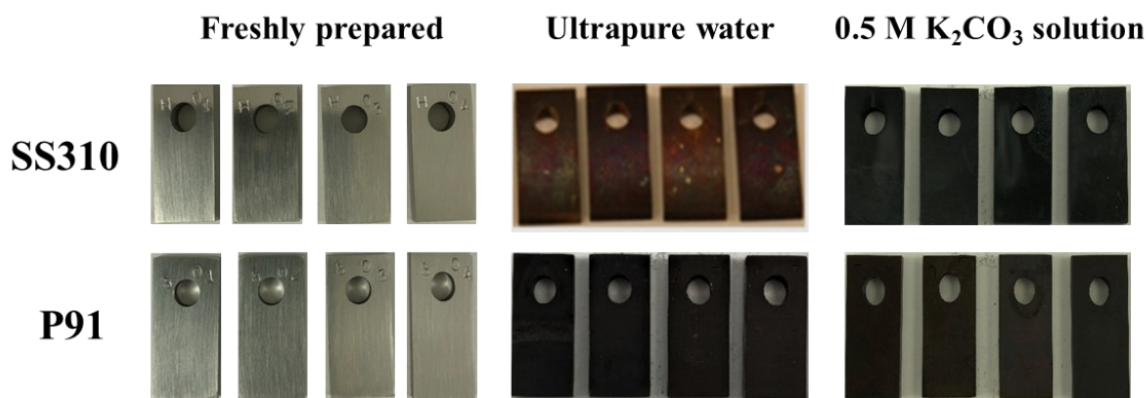
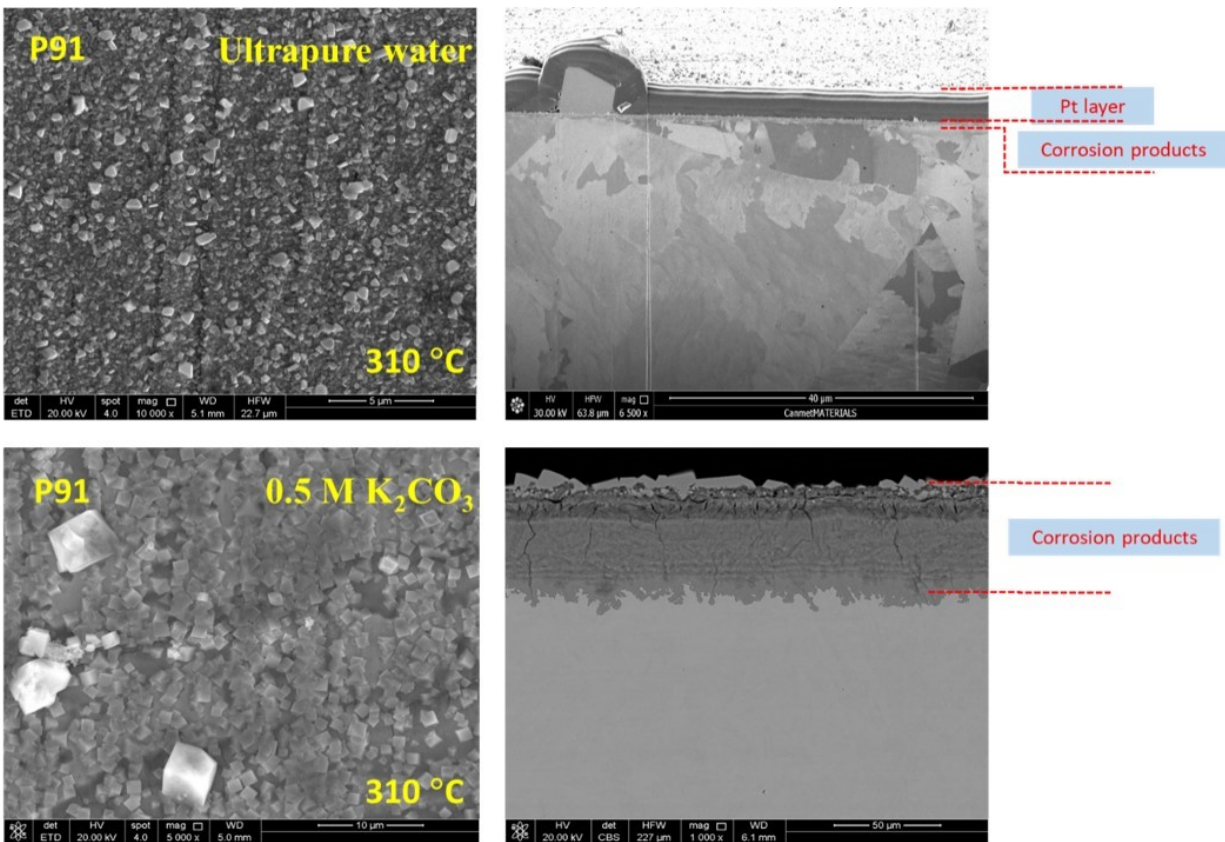


Fig. 5-2. Photographic images of SS310 and P91 steels before and after the exposure to ultrapure water and 0.5 M K₂CO₃ at 310 °C for 10 days, respectively.

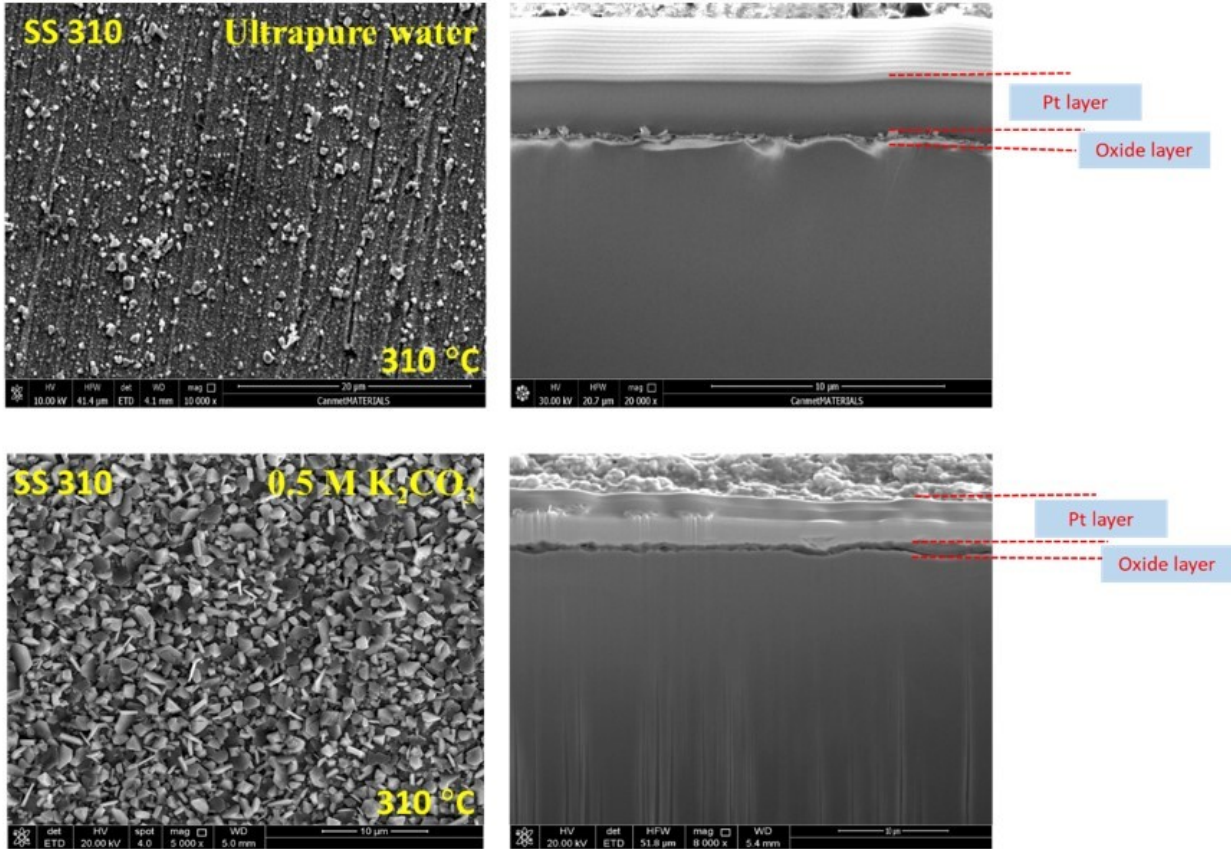
The SEM top and cross-sectional views of P91 and SS310 steels after the exposures to water and 0.5 M K₂CO₃ at 310 °C are shown in Fig. 5-3. Compared to the oxide scale formed on P91 steel in hot ultrapure water, the addition of 0.5 M K₂CO₃ catalyst led to the formation of a porous and less protective corrosion layer on the steel, which was likely composed of larger oxides and deposited corrosion particles. Localized dissolution and cracks were also present on the steel after the exposure to 0.5 M K₂CO₃ at 310 °C. As the corrosion layer formed in 0.5 M K₂CO₃ was quite thick, conventional diamond saw cutting method instead of FIB technique was employed to prepare the cross-sectional sample, and the corresponding SEM images further confirmed that the addition of K₂CO₃ catalyst significantly enhanced the corrosion of P91 under HTL conversion processes since the average thickness of corrosion layer formed on the steel was about 40 μm in 0.5 M K₂CO₃, more than ten time thicker of that grown in the ultrapure water at 310 °C. Moreover, the formed corrosion layer was likely double-layer structure consisted of outer porous and inner relatively compact layers. Furthermore, the micro-cracks formed in 0.5 M K₂CO₃ likely penetrated through the corrosion layer down to the steel substrate.

For SS310 steel, the formed surface scale in the hot ultrapure water was much thinner than that on P91 as the mechanically polishing lines were still clearly visible after the exposure to the hot water. Tiny nodular oxides and deposition particles were also found on SS310 after the exposure. As shown in Fig. 5-3(b), the addition of 0.5 M K₂CO₃ resulted in a remarkable change in the morphology of the surface scale grown on SS310 steel, and the formed layer was consist of relatively large flake-shaped oxide particles. The cross-sectional images of SS310 steel showed

that the average thickness of surface scale was also noticeably increased with the addition of 0.5 M K_2CO_3 . No crack was formed on the corroded SS310 after the exposure to water or 0.5 M K_2CO_3 . Both top and cross-sectional images indicated that the nodular oxidation of SS310 steel would likely be suppressed with the addition of the alkaline catalyst.



(a) Top and cross-sectional views of corroded P91 steel samples



(b) Top and cross-sectional views of corroded SS310 samples

Fig. 5-3. Top and cross-sectional SEM images of (a) P91 and (b) SS310 steels after the exposures to ultrapure water and 0.5 M K_2CO_3 at 310 °C for 10 days, respectively.

As mentioned above, XRD technique was used to characterize the phase compositions of the corrosion layers formed on P91, and the collected spectra are shown in Fig. 5-4. After the exposure to ultrapure water at 310 °C, formed oxide layer was likely consists of magnetite (Fe_3O_4) and Fe/Cr spinel oxides ($Fe_{3-x}Cr_xO_4$) according to references [407, 408]. Note that the peaks of ferrite phase were collected from the substrate. With the addition of 0.5 M K_2CO_3 , the phase composition of corrosion layer was still consisting of Fe_3O_4 and $Fe_{3-x}Cr_xO_4$ oxides. But the formed layer was much thicker than that grown in hot water, making the peaks of ferrite phase less visible. Not that there exists some uncertainty about the ferrite peak since the most intense peaks of it were not detected. Moreover, the peaks of iron hydroxide were not detected, different from those reported in previous studies [52, 155-158]. The above results imply that the addition of 0.5 M K_2CO_3 might

not affect the oxide formation and dissolutions pathways on the steel, but significantly enhance oxide growth and dissolution kinetics.

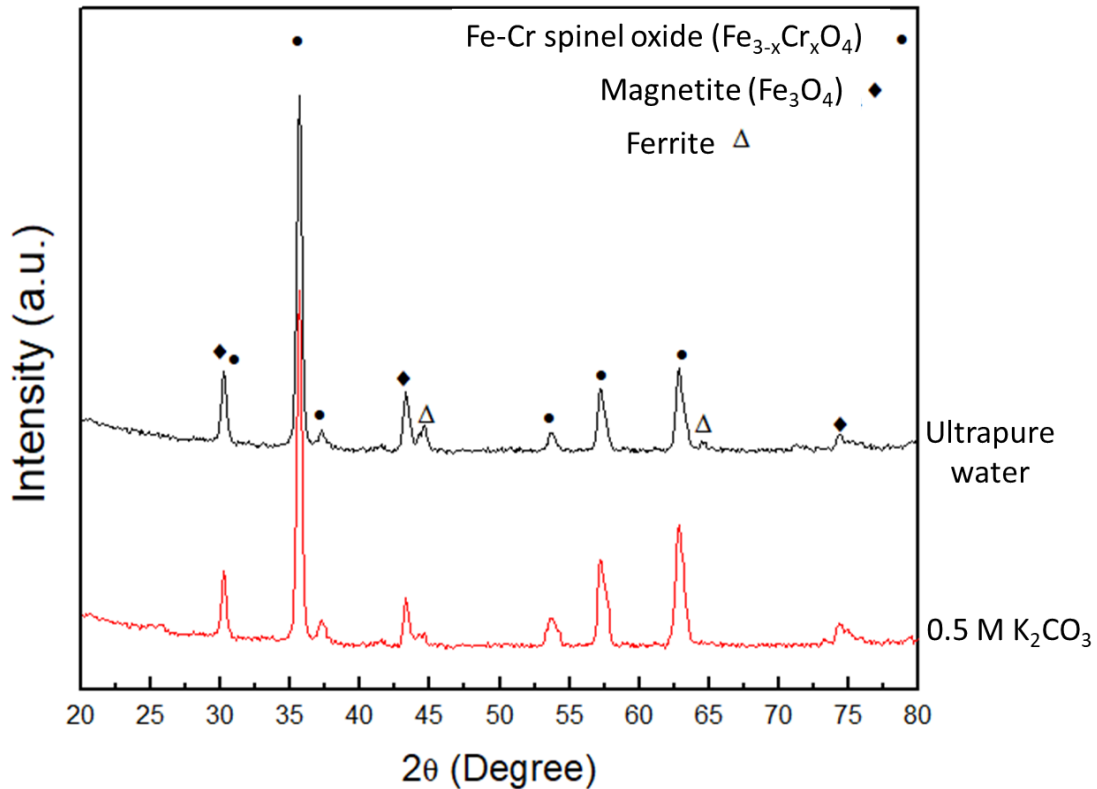


Fig. 5-4. XRD spectra collected on P91 steel samples after the exposures to ultrapure water and 0.5 M K_2CO_3 at 310 °C for 10 days, respectively.

To identify the chemical properties and structure of surface scales formed on SS310 after Tests #1 and 2, the cross-sectional TEM samples of the steel were prepared using FIB lift-out method, and then characterized using BF imaging, EDS mapping and SAD techniques as described above. The corresponding results are shown in Fig 5-5. After corroding in 310 °C water, both nodular oxides and corrosion product deposition particles, mainly composed of Fe and Ni oxides, were present on SS310. Below these randomly distributed particles, a thin and compact continuous Cr-enriched oxide layer was formed. At the interface of oxide layer/substrate, the accumulation of alloying element Ni was clearly visible. At 310 °C, the addition of 0.5 M K_2CO_3 catalyst led to the formation of a much thicker surface scale, which was three-layers structure, including outer porous Cr/Fe/Ni oxides, middle porous Cr-enriched oxide (with some Ni and Fe cations), and inner

compact and continuous Cr oxide layer. The outer porous layer might be formed from the deposition of corrosive ions in the testing solution during autoclave cooling-down. Otherwise, trace amounts of Fe/Ni cations should be also found within the inner Cr oxide. The average thickness of inner Cr oxide layer was about 750 nm, significantly higher than (40 nm) of the Cr-enriched oxide layer grown in the hot water. Below the interface of oxide layer/substrate, a thin Cr-depletion layer instead of Ni accumulation was presented, implying that the presence of 0.5 M K_2CO_3 might accelerate the outward diffusion of Cr from the substrate to the inner Cr oxide layer to maintain its integrity during the exposure. These results indicated that the addition of alkaline catalyst could remarkably enhance the corrosion of SS310 steel.

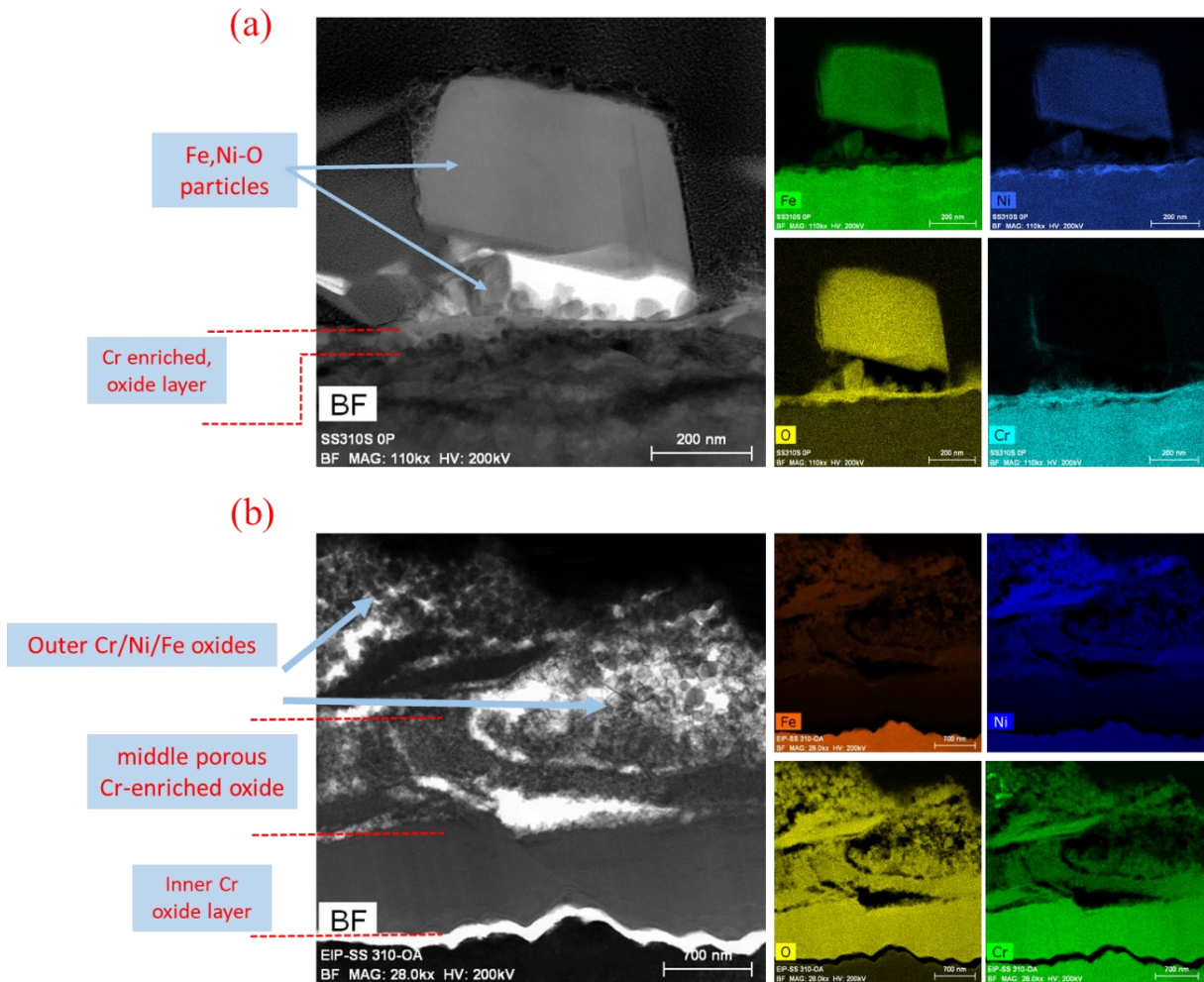
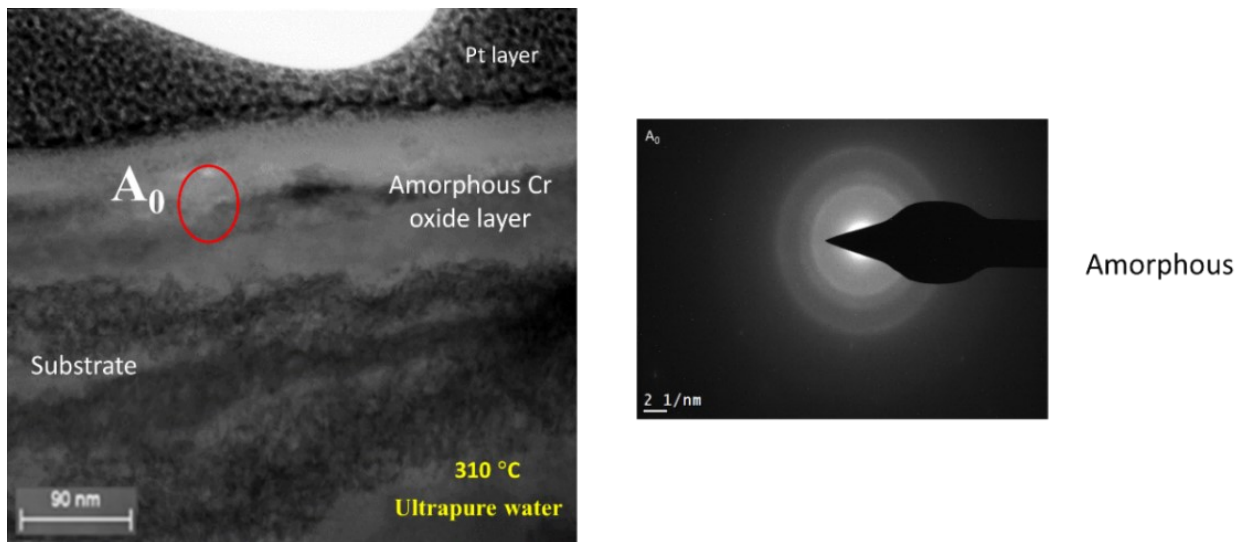
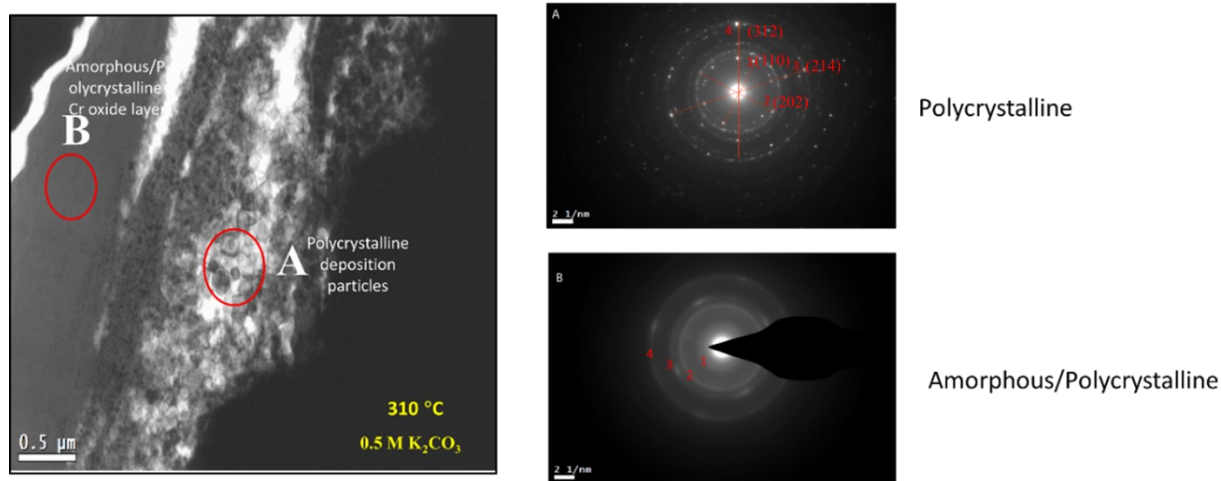


Fig. 5-5. Cross-sectional Black-field (BF) and corresponding EDS elemental mapping images of SS310 after exposed to (a) ultrapure water; and (b) 0.5 M K_2CO_3 at 310 °C for 10 days, respectively.

To further identify the microstructure of corrosion layer formed on SS310 in ultrapure water and 0.5 M K_2CO_3 at 310 °C respectively, BF image and corresponding diffraction patterns were collected on the cross-sectional TEM samples and the results are shown in Fig. 5-6. The collected SAD patterns showed that the inner continuous Cr-enriched oxide layer formed in the hot water has an almost amorphous structure. In 0.5 M K_2CO_3 , the formed outer porous Cr/Fe/Ni oxide layer (Area A) was consisting of nanocrystals. Based on the SAD pattern collected on area A, the interplanar distances were 2.48 Å, 2.04 Å and 1.47 Å respectively, which were corresponding with the (110), (202), and (214) plane with slight deviation due to the possible interaction between different crystals. Based on the observations in Figs. 5-5 and 5-6, it is likely that detected Fe cations could incorporate into the chromium and/or nickel oxides lattice instead of forming Fe oxides. The results further implied that the outer porous Cr/Fe/Ni oxide layer would be the corrosive deposition formed during the autoclave cooling-down as NiO nanocrystals were unlikely to be naturally grown on the steel during the HTL exposure based on thermodynamic calculations as shown in later discussion section. Similar to that formed in ultrapure water, the inner Cr oxide layer (Area B) was found to be amorphous/polycrystalline structure. It exhibited d-spacing values of 2.48 Å, 2.04 Å and 1.43 Å respectively, which were corresponding with the (110), (202), and (300) plane of Cr_2O_3 . Interestingly, the transformation of Cr oxide into hydroxide, which was predicted based on several former studies on austenitic stainless steels in basic solutions [409, 410], did not occur on SS310 when exposed to 0.5 M K_2CO_3 at 310 °C.



(a)



(b)

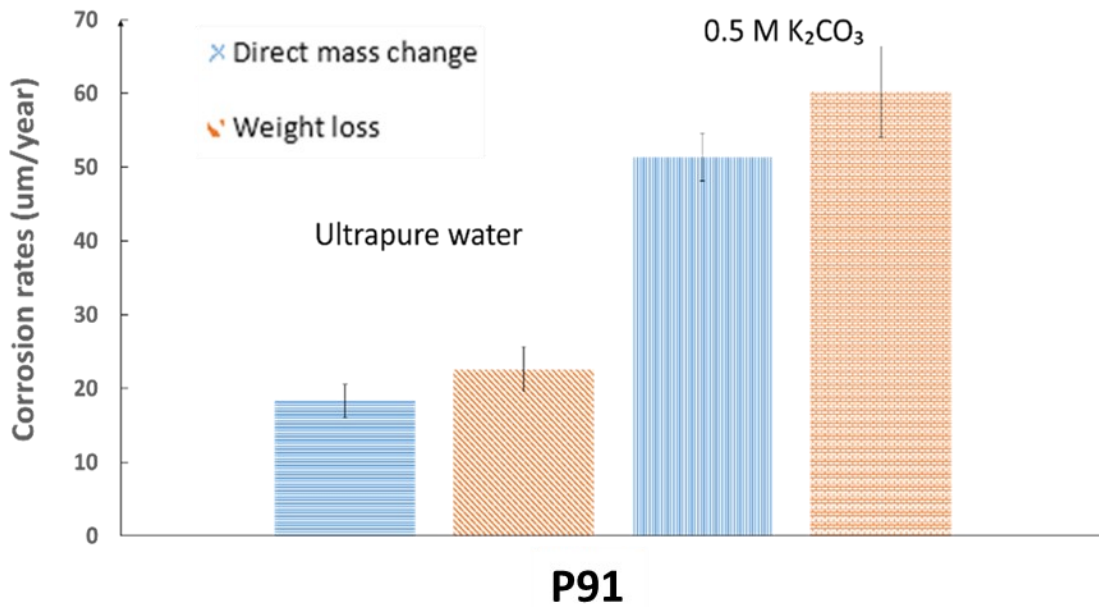
Fig. 5-6. BF image and corresponding selected area diffraction (SAD) patterns of cross-sectional SS310 samples after the exposure to 310 °C (a) ultrapure water and (b) 0.5 M K_2CO_3 for 10 days.

The average corrosion rates of the two steels were evaluated based on the Equations (5-1) and (5-2) as described in the Experimental section, and the results are shown in Fig. 5-7. Under the testing conditions, the corrosion rate of a steel obtained from direct mass change measurements was consistently lower than that from weight loss measurements because of following factors:

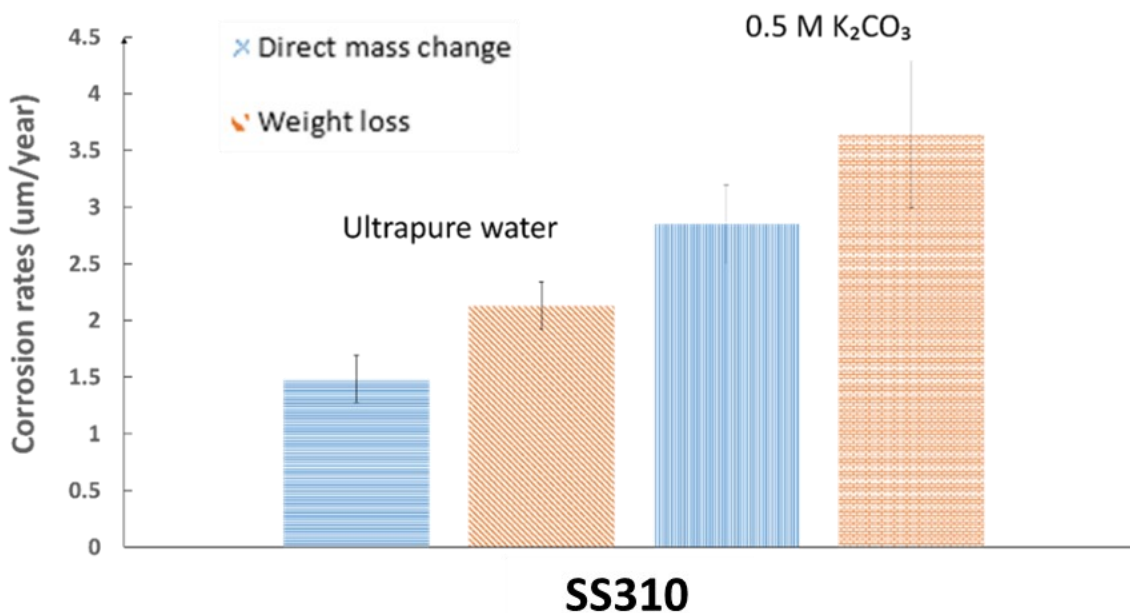
- (1) As shown in Figs. 5-3 and 5-5, localized nodular oxidation, corrosion product deposition and porous oxides formation occurred on the steels, introducing error on assessing the corrosion rates using the direct mass change measurements.
- (2) The molar mass ratio (η) used in Equation (5-1) may not be accurate enough for the assessment since the formed surface scales on both steels were not purely composed of Fe_2O_3 or Cr_2O_3 as indicated in Figs. 5-4 to 5-6.
- (3) The chemical dissolution rate of formed oxide scales in ultrapure water would be remarkably different from that in 0.5 M K_2CO_3 .

Therefore, weight loss instead of direct weight change measurement was seen as a more accurate approach on the corrosion rate assessments from the engineering application point of view. In this

study, the corrosion rates of the two steels was thus determined using the weight loss technique. As shown in Fig. 5-7, the average corrosion rates of SS310 and P91 steel increased with addition of K_2CO_3 catalyst at 310 °C. Compared to SS310, P91 steel experienced a more significant increase in the corrosion rate with the addition of 0.5 M K_2CO_3 , consistent with the cross-sectional SEM observations (Fig. 5-3). This could be mainly attributed to the difference between the corrosion layers formed on the two steels. As expected, the Cr oxides formed on SS310 would have much lower chemical dissolution rate than magnetite (Fe_3O_4) and Fe/Cr spinel oxides grown in P91 in 0.5 M K_2CO_3 at 310 °C. Moreover, the average corrosion rates of two steels in the catalytic HTL environment both fall under the corrosion allowance of 0.1 mm/year for a 20 years' life span [411, 412].



(a)



(b)

Fig. 5-7. Estimated average corrosion rates of (a) SS310 and (b) P91 steel in ultrapure water and 0.5 M K₂CO₃ at 310 °C for 10 days, respectively. Note that the corrosion rates presented here were assessed based on both direct mass change and weight loss measurements for comparison.

5.3.2. Influence of inorganic corrodants on corrosion

As mentioned in the introduction, aggressive inorganic corrodants (Cl⁻ and S²⁻) can be released during the HTL conversion of biomass feedstocks (particularly industrial bio-wastes) [391, 392]. In this study, 3,500 ppm Cl⁻ and 2,500 ppm S²⁻ was selected as the representatives of the inorganic corrodants based on the feeding ratio (5:1) of water/biomass to identify their influence on corrosion. The photographic images of SS310 and P91 coupons before and after Tests #2 and 3 in 0.5 M K₂CO₃ without and with 3,500 ppm Cl⁻ and 2,500 ppm S²⁻ are shown in Fig. 5-8. The presence of inorganic corrodants was unlikely to result in remarkable change of the surface appearances of the two steels. More importantly, pits were not found on the steels after the exposure to 0.5 M K₂CO₃ + 3,500 ppm Cl⁻ + 2,500 ppm S²⁻, suggesting that the concentrations of the inorganic corrodants would be not sufficient to trigger localized corrosion of the steels in the HTL environment at 310 °C.

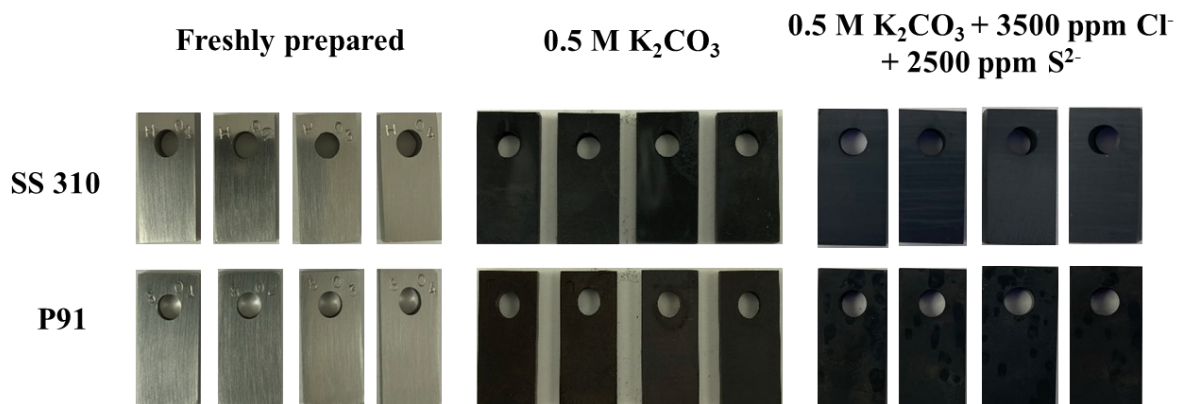


Fig. 5-8. Photographic images of SS310 and P91 steels before and after the exposures to 0.5 M K₂CO₃ and 0.5 M K₂CO₃ + 3,500 ppm Cl⁻ + 2,500 ppm S²⁻ at 310 °C, respectively.

The top and cross-sectional SEM views of P91 steel and SS310 after the exposure to 0.5 M K₂CO₃ + 3,500 ppm Cl⁻ + 2,500 ppm S²⁻ at 310 °C are shown in Fig. 5-9. For P91 steel, the introduction of inorganic corrodants was unlikely to initiate pitting, but reduced the thickness of outer layer. The average thickness of the formed corrosion layer was around 35 μm, thinner than that formed in 0.5 M K₂CO₃ at 310 °C. Compared with that in Fig 3, a slightly thinner outer layer and a thinner inner corrosion layer was formed with the presence of inorganic corrodants. After the exposure, micro-cracks were also present in the formed corrosion layer and almost penetrated down to the steel substrate. For SS310 steel, large flake-shaped oxide particles were also observed on the surface, similar to those formed in 0.5 M K₂CO₃. Cross-sectional examination revealed that the average total thickness of surface scale (~500 nm) was slightly increased with the presence of inorganic corrodants. Moreover, no pit was found on the steel. The results in Fig. 5-9 suggested that the presence of several thousand ppm of inorganic corrodants (S²⁻ and Cl⁻) might only have marginal effect on the general corrosion of the two steels under catalytic HTL conversion conditions.

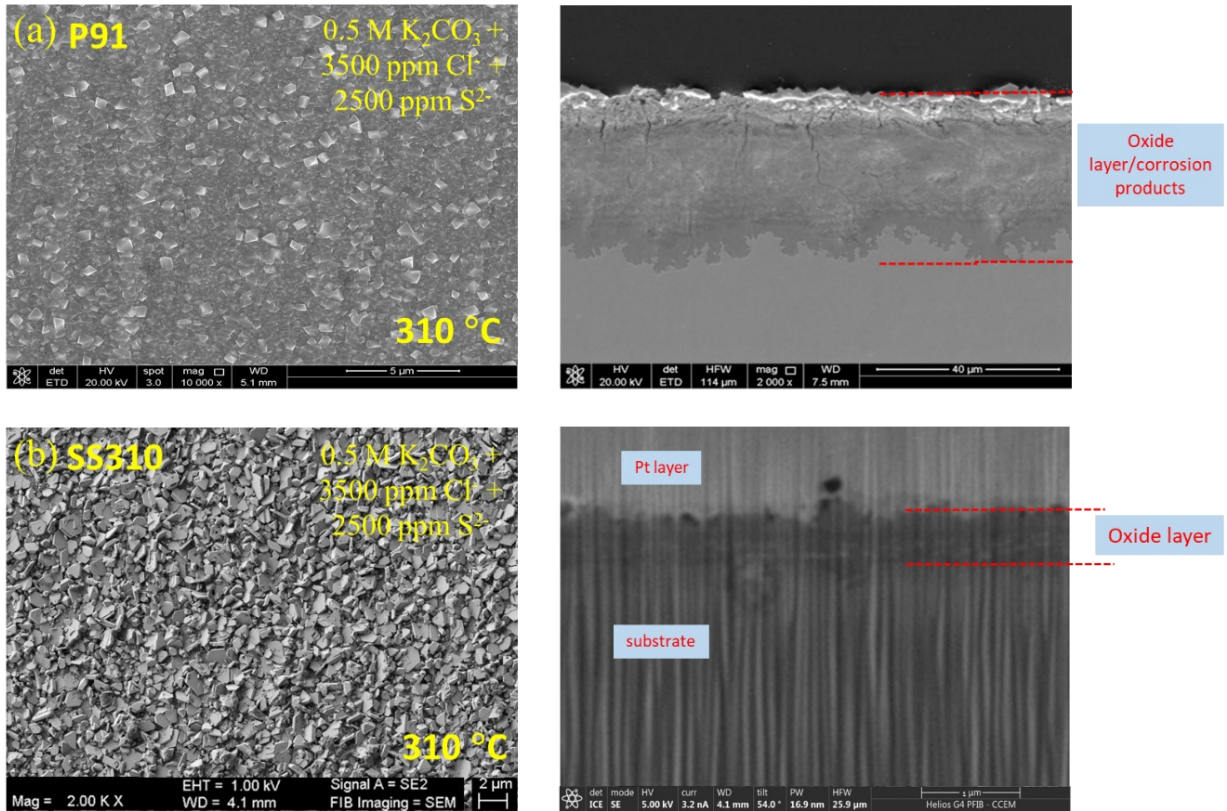


Fig. 5-9. Top and cross-sectional SEM images of (a) P91 and (b) SS310 steels after corroding in 0.5 M $K_2CO_3 + 3,500 \text{ ppm } Cl^- + 2,500 \text{ ppm } S^{2-}$ at 310 °C for 10 days, respectively.

XRD technique was also employed to characterize the corrosion layer formed on P91 after Test #3, and the collected spectrum is shown in Fig. 5-10. With the presence of Cl^- and S^{2-} , the formed layer was mainly composed of magnetite (Fe_3O_4) and Fe/Cr spinel oxides ($Fe_{3-x}Cr_xO_4$), similar to that grown in 0.5 M K_2CO_3 . Although the two strongest peaks of ferrite phase were not detected, its other peaks were found. This suggests that the corrosion layer formed on the steel might be thinner, consistent with the cross-sectional SEM observations (see Figs. 5-3 and 5-9).

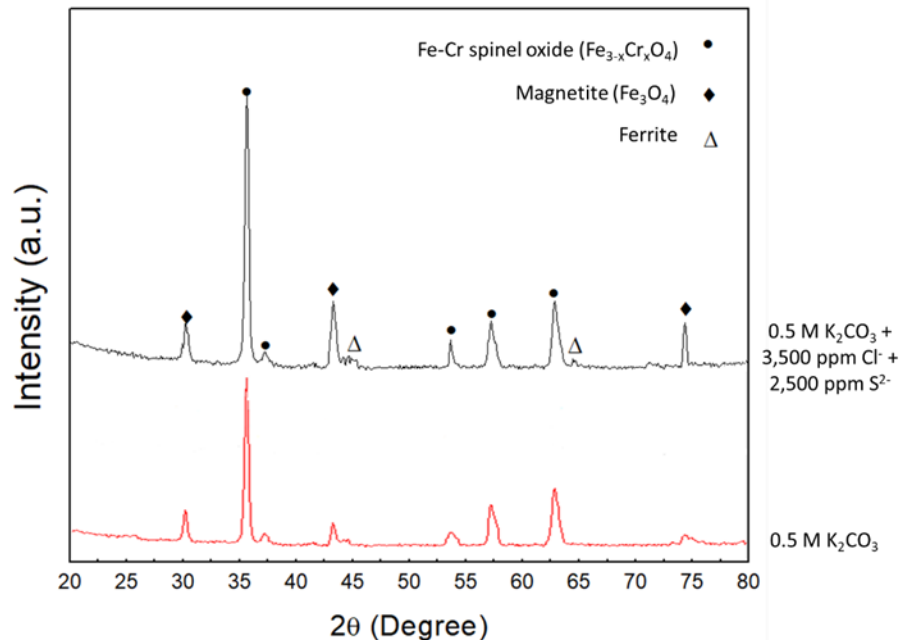


Fig. 5-10. XRD spectra collected on P91 steel samples after the exposures to 0.5 M K_2CO_3 and 0.5 M $K_2CO_3 + 3,500 \text{ ppm } Cl^- + 2,500 \text{ ppm } S^{2-}$ at 310 °C for 10 days, respectively.

To clarify the impacts of inorganic corrodants on the corrosion of SS310, cross-sectional TEM sample was prepared from the tested coupon using plasma-FIB lift-out technique, and the corresponding BF and EDS mapping results are shown in Fig. 5-11. It has been found that the formed corrosion layer was composed of three sub-layers: outer porous Cr/Ni/Fe oxide, middle porous Cr/Fe oxide, and inner relatively compact and continuous Cr-enriched oxide layers. As mentioned above, the outer porous Cr/Ni/Fe oxide layer might be the deposition layer formed during autoclave cooling-down. The morphology of outmost Cr/Fe/Ni layer was slightly different from that grown in 0.5 M K_2CO_3 (see Fig. 5-5). Interestingly, localized accumulation of Ni particles was present in the middle Cr/Fe oxide layer. More importantly, the addition of Cl^- and S^{2-} remarkably reduced the thickness of Cr-enriched oxide layer (about 70 nm) compared to that formed in 0.5 M K_2CO_3 , suggesting that the addition of Cl^- and S^{2-} could damage the integrity of Cr-oxide layer and then enhance its chemical dissolution. Within the inner Cr-enriched oxide layer, the random presence of Ni and Fe cations was observed, implying that the addition of Cl^- and S^{2-} might also facilitate the outward diffusion of Ni/Fe from the substrate through the Cr oxide layer. In addition, quantitative element analyses on several spots in the oxide layer indicated that little sulfur was present in the middle oxide layer, while chloride ions were not detected. Different from

that formed in water and 0.5 M K_2CO_3 , the thin Cr-depletion zone below the Cr-enriched oxide layer was not found.

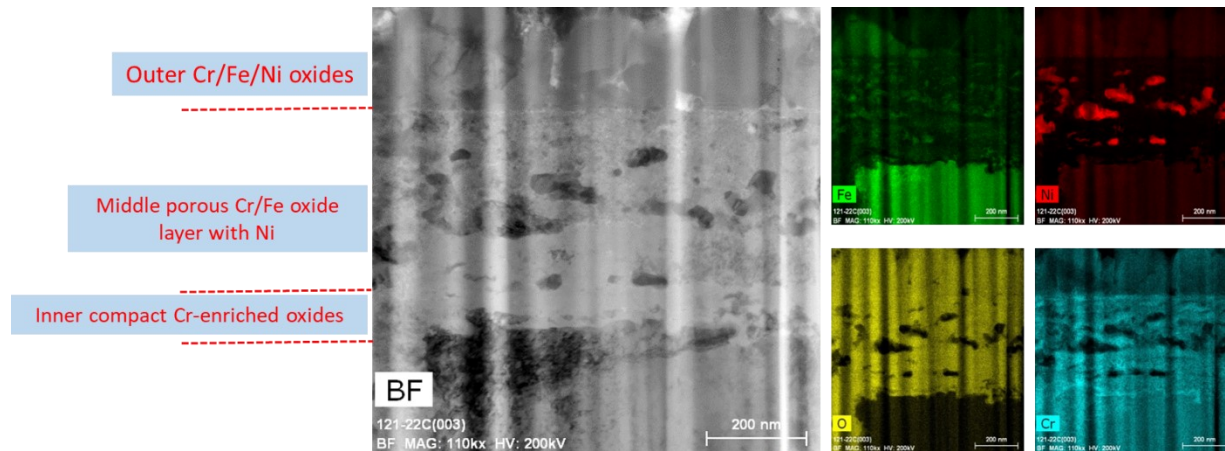
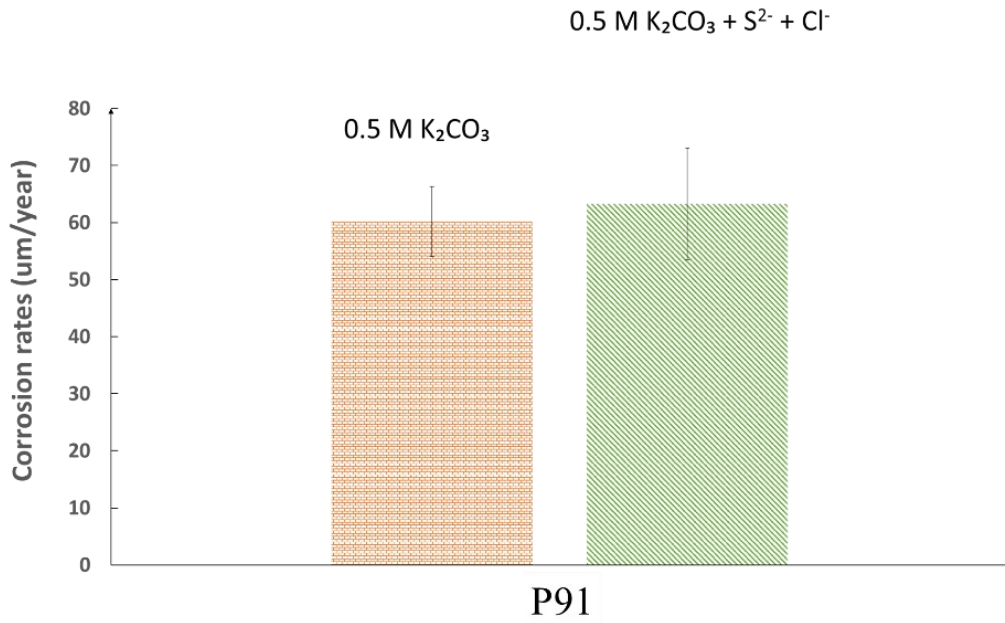
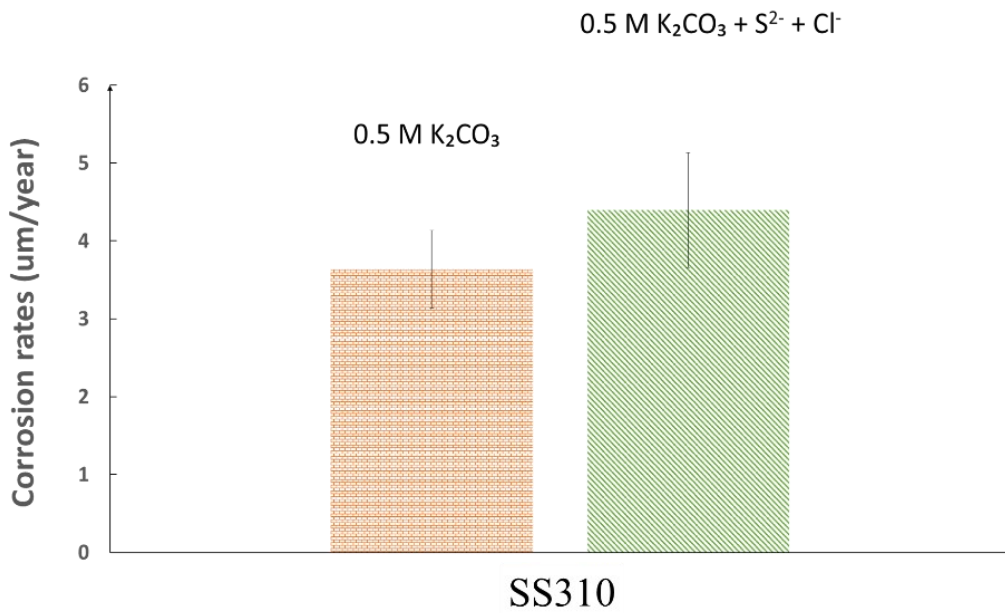


Fig. 5-11. Bright-field (BF) image and corresponding EDS elemental mapping images of SS310 after exposed to 0.5 M K_2CO_3 + 3,500 ppm Cl^- + 2,500 ppm S^{2-} at 310 °C for 10 days.

Based on weight loss measurements, the influence of inorganic corrodants on the average corrosion rates is shown in Fig. 5-12. The presence of inorganic corrodants in 0.5 M K_2CO_3 only resulted in a slight increase in the corrosion rates of the two steels. As shown in Figs. 5-9 and 5-11, such increase might be due to the fact that the inorganic corrodants released during the catalytic HTL conversion of industrial biowastes would likely promote the dissolution of formed oxides. Compared with P91, the impact of inorganic corrodants on the corrosion rate of SS310 was more noticeable, which could also be attributed to their influence on the stability and chemical dissolution of inner protective Cr-enriched oxide layer grown the steel. As the corrosion rates of the two steels were still less than the maximum allowable rate (0.1 mm/year) as mentioned above, the two steels should still be promising candidates for further evaluation in the solution with organic acids.



(a)



(b)

Fig. 5-12. Estimated average corrosion rates of (a) SS310 and (b) P91 steel in 0.5 M K₂CO₃ and 0.5 M K₂CO₃ + 3,500 ppm Cl⁻ + 2,500 ppm S²⁻ at 310 °C for 10 days, respectively.

5.3.3. Impact of organic acid on corrosion

As described above, about 5-10 wt.% saturated short-chain organic acids (formic, acetic and butyric acids etc.) will be produced as by-products during the HTL conversion of raw biomass feedstocks. In this study, acetic acid was selected as a representative agent for exploring the influence of organic acids on the corrosion of candidate reactor alloys. Fig. 5-13 shows the photographic images of SS310 and P91 samples before and after the exposure to catalytic solution with 5 wt.% acetic acid and 10 wt.% acetic acid (which reacted with catalyst during the tests) at 310 °C, respectively. After the exposures, the coupon surfaces became darker when comparing to those tested in 0.5 M K_2CO_3 + 3,500 ppm Cl^- + 2,500 ppm S^{2-} , implying that the presence of acetic acid might enhance the corrosion of the two steels. The formed corrosion products were possibly thicker, more fragile and looser compared to those formed in 0.5 M K_2CO_3 and 0.5 M K_2CO_3 + 3,500 ppm Cl^- + 2,500 ppm S^{2-} . Localized corrosion product deposition also occurred on the steels after the exposures. Increasing acetic acid content from 5 wt.% to 10 wt.% did not lead a noticeable change of surface appearance. In addition, the introduction of acetic acid did not result in the formation of pits on the steels.

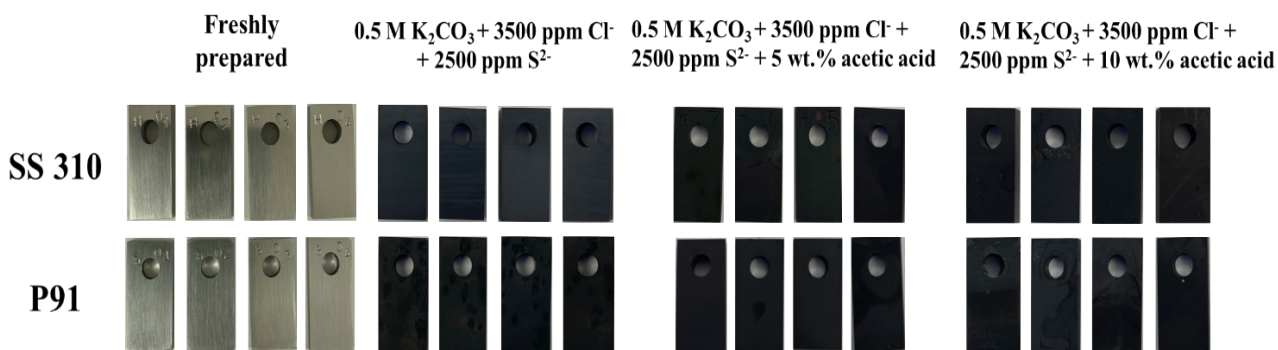
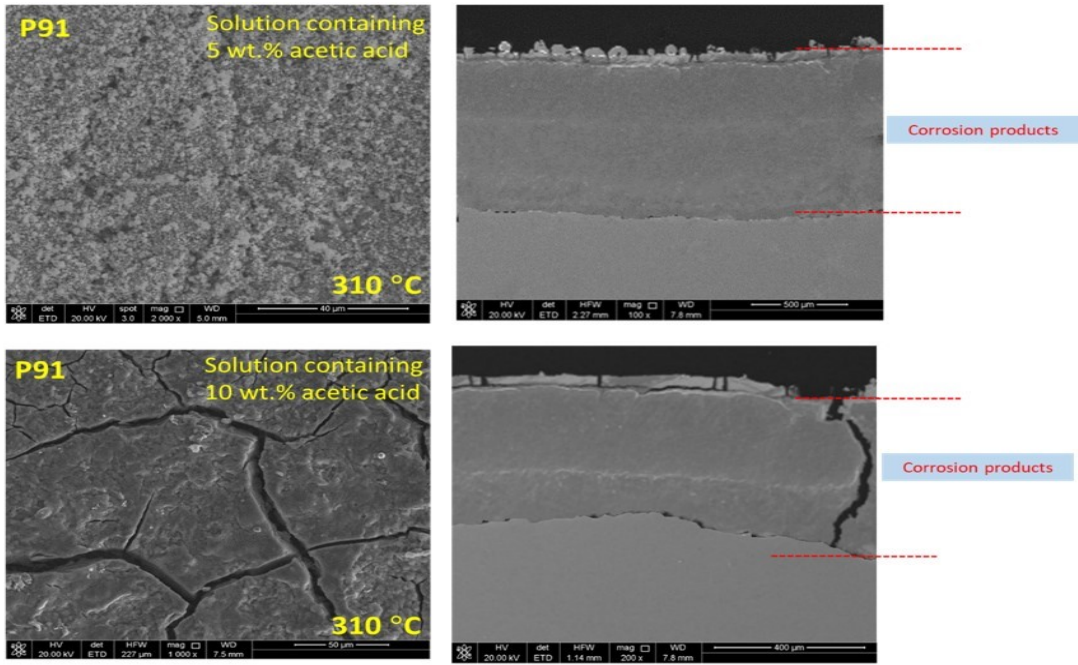


Fig. 5-13. Photographic images of SS310 and P91 steels before and after the exposure to 0.5 M K_2CO_3 + 3,500 ppm Cl^- + 2,500 ppm S^{2-} with and without the addition of acetic acid at 310 °C for 10 days, respectively.

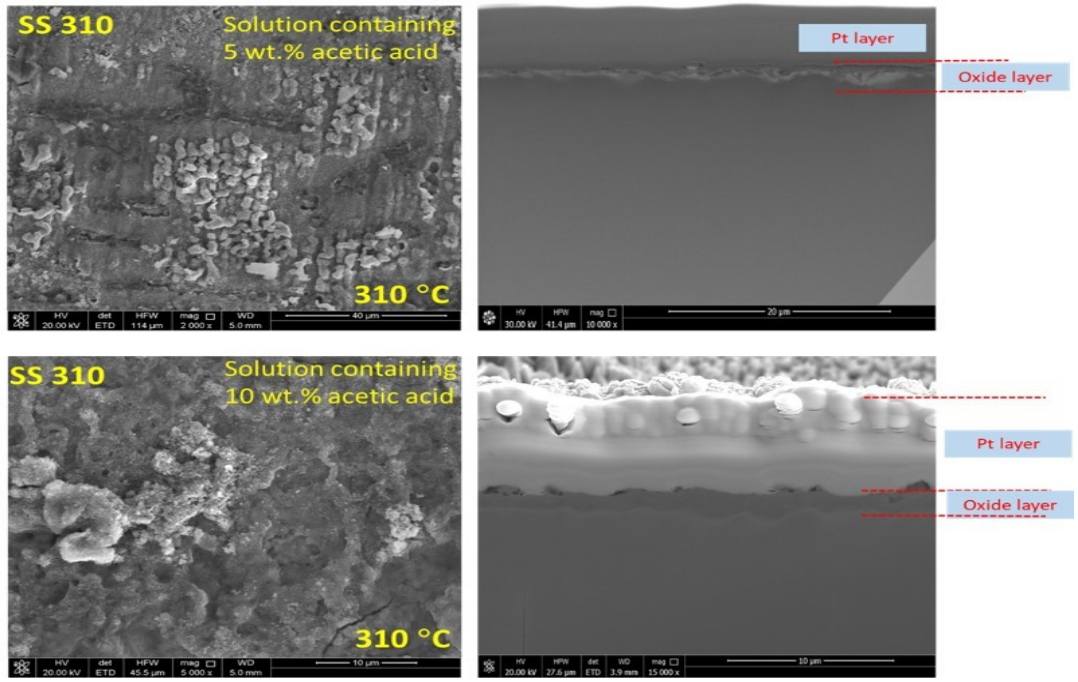
The top and cross-sectional SEM views of P91 and SS310 steels after the exposure to the two different conditions (5 wt.% and 10 wt.% acetic acid) are shown in Fig. 5-14. The introduction of acetic acid remarkably changed the surface morphology of two steels and resulted in the formation of thicker and porous corrosion layer and micro-cracks on the two steels. For P91 steel, the cross-sectional examinations using conventional diamond saw cutting method and SEM technique

confirmed that the introduction of acetic acid enhanced the steel corrosion since the average corrosion layer thickness were about eleven times thicker than that grown in 0.5 M K_2CO_3 + 3,500 ppm Cl^- + 2,500 ppm S^{2-} . In the solution with 10 wt.% acetic acid, the formed micro-cracks completely penetrated through the corrosion layer down to the substrate, making the corrosion layer much less protective to the metal. It is also worth noticing that increasing acetic acid concentration from 5 to 10 wt.% also led to a noticeable decrease in the total corrosion layer thickness, suggesting that the presence of acetic acid along with micro-cracks would also enhance the chemical dissolution of corrosion layers on the steel. Similar to those formed in 0.5 M K_2CO_3 and 0.5 M K_2CO_3 + 3,500 ppm Cl^- + 2,500 ppm S^{2-} , the corrosion layer grown in acetic acid-containing solution also had a double-layer structure consist of outer thin and porous and inner thick and relatively compact layers, and the presence of acetic acid apparently increased the inner layer thickness (see Fig. 5-9(a) and Fig. 5-14(a)).

For SS310 steel, the addition of acetic acid also led to a significant change of the formed corrosion layer. Localized accumulation of irregular particles was observed. Below them, the formed oxide was quite porous as considerable number of holes and micro-cracks were formed. Moreover, increasing acetic acid content from 5 to 10 wt.% seems to facilitate the localization dissolution and the formation microcracks within oxide layers. As shown in Fig. 5-14(b), the average thickness of the corrosion layer apparently increased with the addition of acetic acid. However, further increasing acid content from 5 to 10 wt.% only had a marginal effect on the corrosion layer thickness. Thus, it was more likely that the presence of acetic acid might locally damage the integrity of surface oxide scale and consequently enhance the corrosion of SS310 in the catalytic HTL environments.



(a) Top and cross-sectional views of corroded P91 steel samples



(b) Top and cross-sectional views of corroded SS310 samples

Fig. 5-14. Top and cross-sectional SEM images of (a) P91 and (b) SS310 steels after corroding in 0.5 M K_2CO_3 + 3,500 ppm Cl^- + 2,500 ppm S^{2-} containing 5 wt.% and 10 wt.% acetic acid at 310 °C for 10 days, respectively.

For P91 steel, XRD technique was used to characterize the phase compositions of the formed corrosion layer after the exposure to the solution with 10 wt.% organic acid, and the collected spectrum is presented in Fig. 5-15. When comparing different spectrum collected, the addition of 10 wt.% organic acid was unlikely to change the chemical composition of corrosion layers as the formed layer was still composed of magnetite (Fe_3O_4) and iron-chromium spinel oxides ($\text{Fe}_{3-x}\text{Cr}_x\text{O}_4$). Note that the most intense peaks of ferrite were not detected from the collected spectrum, which could be due to the fact that the corrosion layer formed was considerable thick as shown in Fig. 5-14 (a).

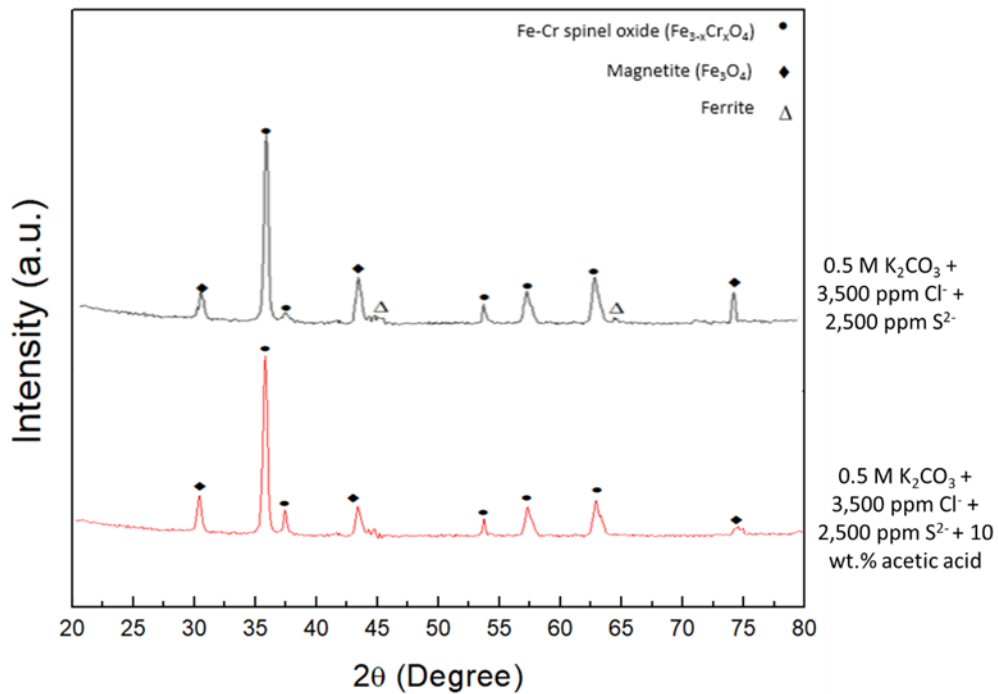


Fig. 5-15. XRD spectrum collected on P91 steel after the exposures to 0.5 M K_2CO_3 + 3500 ppm Cl^- + 2500 ppm S^{2-} with and without 10 wt.% acetic acid at 310 °C for 10 days.

To clarify the influence of acetic acid on the corrosion, cross-sectional SS310 sample was prepared from the tested coupon using FIB lift-out method, and the corresponding BF and EDS mapping results are shown in Fig. 5-16. The average thickness of corrosion layer which formed with the presence of 10 wt.% acetic acid was thicker (about 1500 nm) than those grown in the above solutions without acetic acid (see Figs. 5-5 and 5-11). Similar to that grown in 0.5 M K_2CO_3 +

3500 ppm Cl^- + 2500 ppm S^{2-} , the formed corrosion layer was also a three-layer structure, including outer porous Cr/Ni/Fe oxide, middle porous Cr oxide, and inner relatively compact and thin Cr oxide layers. Localized accumulation of element Ni was also present in the middle Cr oxide layer. Different from that formed in 0.5 M K_2CO_3 + 3500 ppm Cl^- + 2500 ppm S^{2-} , Fe oxides were barely found in the middle porous layer, and the inner continuous Cr layer (~ 200 nm) was thicker but less compact comparing to that formed in 0.5 M K_2CO_3 + 3500 ppm Cl^- + 2500 ppm S^{2-} . Quantitative element analysis indicated that little sulfur was present in the middle porous Cr oxide layer.

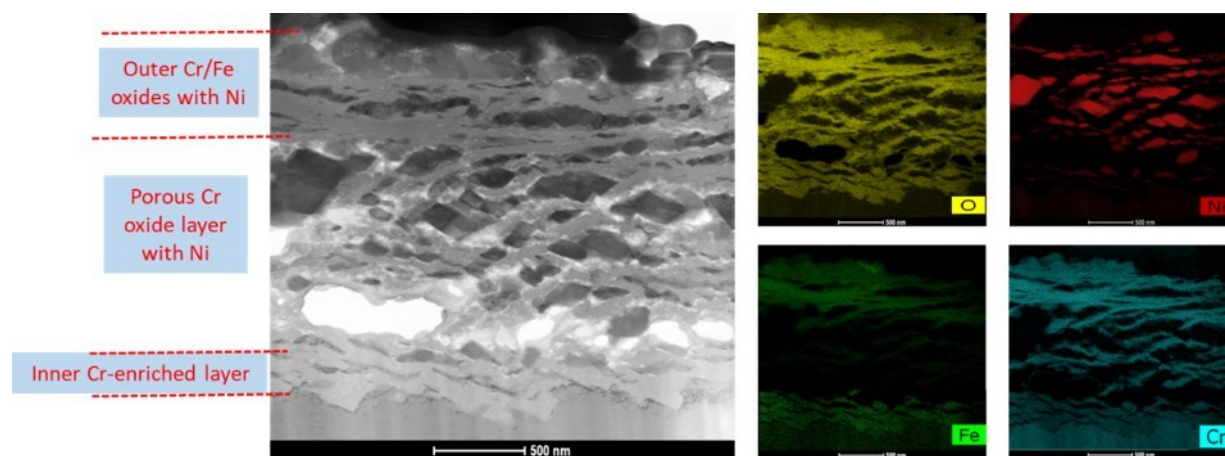
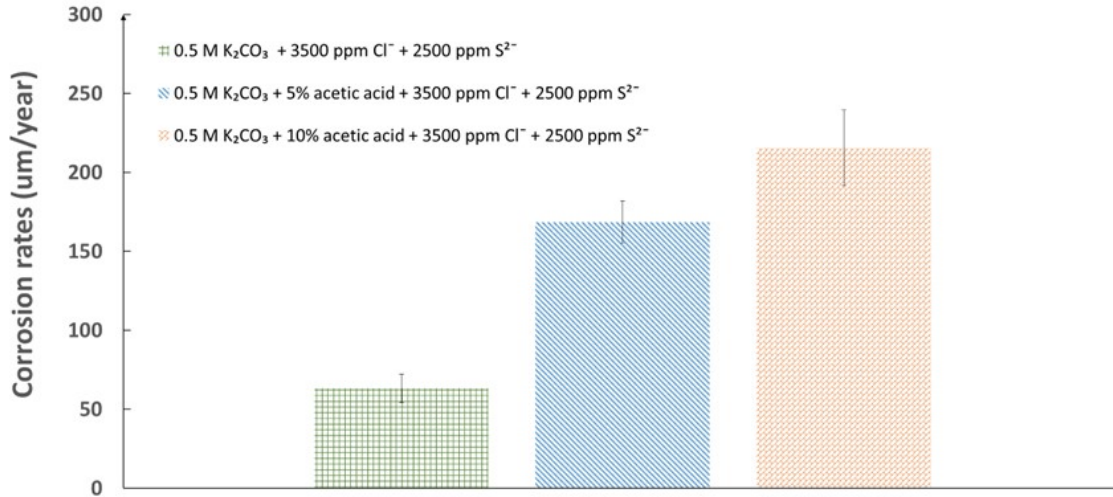


Fig. 5-16. HAADF and BF images with corresponding EDS elemental mapping images of SS310 after exposing to 0.5 M K_2CO_3 + 3,500 ppm Cl^- + 2,500 ppm S^{2-} + 10 wt.% acetic acid at 310 °C for 10 days.

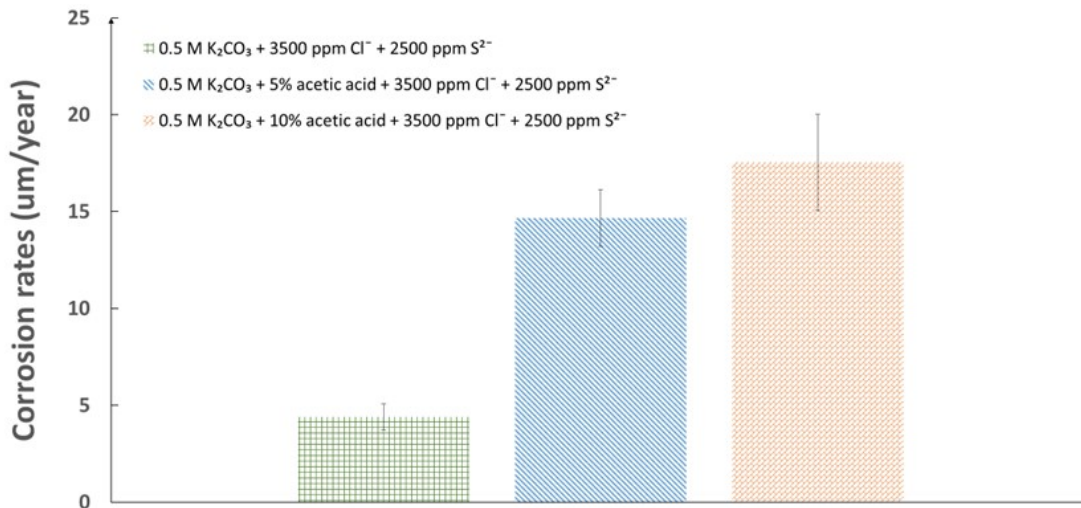
The effect of organic acid on the average corrosion rates of two steels are shown in Fig. 5-17. The addition of acetic acid led to a remarkable increase in the corrosion rates. For P91, it was likely that the introduction of acetic acid would promote the formation and chemical dissolution of Fe_3O_4 and $\text{Fe}_{3-x}\text{Cr}_x\text{O}_4$ on the steel. Further increasing the content of acetic acid to 10% might also facilitate the microcrack growth and consequently result in a higher corrosion rate. For SS310, as shown in Figs. 5-14 and 5-16, the presence of acetic acid could enhance the dissolution of Fe and Cr oxides, especially the inner compact Cr-enriched oxide layer, thus leading to the increase of the corrosion rate. Moreover, based on the abovementioned maximum allowable corrosion rate (0.1

mm/year) [411, 412], only SS310 exhibited promising potential for further validation testing on the construction of HTL conversion reactors.



P91

(a)



SS310

(b)

Fig. 5-17. Estimated average corrosion rates of (a) SS310 and (b) P91 steels in 0.5 M K₂CO₃ + 3,500 ppm Cl⁻ + 2,500 ppm S²⁻ with and without acetic acid at 310 °C for 10 days, respectively.

5.4. Discussion

As described above, hot pressurized water is used as the conversion medium during the thermochemical HTL conversion of different types of biomass feedstocks. Note that the ionization constant of ultrapure water is about $1 \times 10^{-11.4}$ at 310 °C, thus making the non-catalytic HTL conversion environment has an initial pH value of ~ 5.7 . The addition of homogeneous 0.5 M K_2CO_3 catalyst can increase the pH value of the biorefining environment from near neutral to ~ 11.2 at 310 °C. During the biomass conversion, the generated organic acids will react with the basic catalyst and consequently decrease the environmental pH. For instance, the generation of 5% and 10% acetic acid should result in the HTL environments with the pH of ~ 7.6 and ~ 5.4 at 310 °C, respectively.

During the non-catalytic and catalytic HTL conversions at 310 °C, the general oxidation of major alloying elements (Cr, Fe and Ni) present in the two candidate reactor steels could occur and thus cause the formation of different oxide films on the two tested steels. Based on thermodynamic calculations (see Table 5-3), the alloying element Ni in SS310 is unlikely to involve in the oxide formation due to the positive Gibbs formation energy. Thus, as shown in Fig. 5-5(a), the outer Fe/Ni oxide particle formed on the steels in non-catalytic HTL environment would be from the re-deposition of dissolved corrosive production in testing solution during the autoclave cooling-down process. Moreover, as reported in previous studies [335, 413], the chemical dissolution rate of Fe oxides grown on the two steels would be much higher than that of formed Cr-enriched oxides in the non-catalytic and catalytic HTL solutions. Therefore, Fe-based oxides (such as Fe_3O_4 and $Fe_{3-x}Cr_xO_4$) are expected to be grown on P91 due to the low bulk Cr content while Cr-enriched oxides be formed on Cr-bearing SS310 after the exposures to non-catalytic and catalytic HTL environments respectively, as shown in Figs. 5-4, 5-5 and 5-11.

Except for the oxides, the hydroxides of major alloying elements might also be formed on the steels through the direct reaction of alloying elements with OH^- anions or the transformation of oxides into hydroxides in the HTL environments with 0.5 M K_2CO_3 catalyst at 310 °C because of their negative Gibbs formation energy as predicted in Table 5-3. With the generation of organic acids during the biomass HTL conversion, the hydroxide formation is likely to be suppressed because of the decrease in the HTL environmental pH as implied in Table 5-3. For example, with the production of 5% acetic acid, the catalytic HTL environment pH should be reduced to ~ 7.6 at

310 °C, and the estimated Gibbs free energy of direct or indirect hydroxide formation could be close to 0 kJ/mol when counting the anion concentration. However, as shown in Figs. 5-4 and 5-10, considerable amounts of Fe and/or Cr hydroxides were not found within the corrosion layers on the tested steels even after the 10 days' exposure to 0.5 M K₂CO₃ solution at 310 °C (see Figs. 5-4 and 5-5). This could be attributed to the much higher chemical dissolution rates of Fe/Cr hydroxides compared to their oxides in the hot catalytic solutions [335, 414, 415, 416, 417, 418]. In the catalytic HTL environments, both iron oxide and hydroxide are likely to experience following hydrolysis reactions to form dissoluble Fe(OH)₄⁻ through [419, 420]:



Former study indicated that the dissolution rate of Fe(OH)₃ in a basic solution (pH~9) was higher than that of Fe₂O₃ [418]. In the catalytic HTL environments, the transformation of the protective Cr₂O₃ and Cr(OH)₃ on SS310 into dissoluble Cr(OH)₄⁻ could also occur via



Previous studies found that Cr(OH)₃ could completely dissolve through the reaction (5-6) while Cr₂O₃ only suffer partial dissolution in the basic solutions with pH of 10-14 at temperature < 288 °C [417, 421]. Therefore, the formed corrosion layers would still be Fe-based oxide on P91 and Cr-enriched oxide on SS310 even after 10 days' exposure to the catalytic HTL environments.

Table 5-3. Oxide and hydroxide formation reactions possibly occurred on the two steels in catalytic HTL environments and estimated Gibbs free energy at 310 °C.

Formation Types	Formation reactions possibly occurred in HTL environments	Estimated ΔG ₃₁₀ (kJ/mol)
Direct oxide formation	2 Cr + 3 H ₂ O = Cr ₂ O ₃ + 3 H ₂	-394.98
	3 Fe + 4 H ₂ O = Fe ₃ O ₄ + 4 H ₂	-140.47
	Ni + H ₂ O = NiO + H ₂	8.82
	Cr + 3 OH ⁻ = Cr(OH) ₃ + 3 e ⁻	-1.71 at pH=11.2

Direct hydroxide formation		~0 at pH=7.6
	$\text{Fe} + 3 \text{OH}^- = \text{Fe}(\text{OH})_3 + 3 \text{e}^-$	-1.29 at pH=11.2
		~0 at pH=7.6
	$\text{Ni} + 2 \text{OH}^- = \text{Ni}(\text{OH})_2 + 2 \text{e}^-$	-1.18 at pH=11.2
Indirect hydroxide formation		~0 at pH=7.6
	$\text{Cr}_2\text{O}_3 + 2 \text{OH}^- + 3 \text{H}_2\text{O} = 2 \text{Cr}(\text{OH})_4^-$	-0.10 at pH=11.2
		~0 at pH=7.6
	$\text{Fe}_3\text{O}_4 + 4 \text{OH}^- + 4 \text{H}_2\text{O} = 3 \text{Fe}(\text{OH})_4^- + \text{e}^-$	-0.25 at pH=11.2
	~0 at pH=7.6	

To further explore the stability of the formed oxides under the HTL conversion conditions, the Pourbaix diagrams of Cr-H₂O and Fe-H₂O at 310 °C were constructed based on the thermodynamic calculations of all the possible electrochemical reactions occur during the exposures, the available databases [158, 256, 265, 422], and HSC Chemistry software [336]. As marked in Figs. 5-18 and 5-19, the non-catalytic and homogenous catalytic HTL conversions are typically operating at the pH range of 5.7 ~ 11.2 at 310 °C. Note that with the production of considerable amounts of organic acids (such as 10% acetic acid and even more), the catalytic HTL environmental pH could be slightly less than the near neutral value. In the HTL water at 310 °C (pH= ~5.7), the alloying elements (Cr and Fe) are likely to experience passivation and form stable oxides on the two steels. Different from Cr₂O₃, part of formed Fe₃O₄ might dissolve into the hot water as predicted in Fig. 5-18. Thus, the two tested steels would mainly undergo passivation in the non-catalytic HTL environment before considerable organic acids released from raw biomass feedstocks, consistent with the observations in Figs. 5-3 and 5-5. As mentioned above, Fe₃O₄ should exhibit higher chemical dissolution rate than Cr₂O₃ in the hot pressurized HTL water [335, 413]. Moreover, the oxides formation rate of P91 would be much higher than that of SS310 since the migration rates of cations (Fe³⁺ and Cr³⁺) and anions (O²⁻) within Fe₃O₄ are expected to be remarkably higher than those in Cr₂O₃ at 310 °C based our formal calculation [376]. The above two factors could thus lead to a higher corrosion rate of P91 than SS310 in the non-catalytic HTL water at 310 °C, as shown in Fig. 5-7.

As discussed above, the addition of 0.5 M K_2CO_3 catalyst can increase the HTL environmental pH up to 11.2 at 310 °C. Based on the constructed Pourbaix diagrams, both Fe and Cr are supposed to suffer active corrosion instead of passivation in the catalytic HTL environments as only dissolvable hydroxides (such as $Fe(OH)_4^-$ or $Cr(OH)_4^-$) could be thermodynamically present at the pH of ~11.2. However, as shown in Figs. 5-3 and 5-5, the addition of 0.5 M K_2CO_3 resulted in the formation of much thicker corrosion layers on the two steels comparing to those grown in the hot pressurised HTL water, suggesting that the introduction of this homogenous catalyst could not only enhance the chemical dissolution of oxides and hydroxides as discussed above, but also accelerate the oxide growth under the HTL conversion. The influence of K_2CO_3 on the enhanced oxide formation might be attributed to following reasons. Firstly, the chemical dissolution of Fe and Cr oxides could be increased with the addition of 0.5 M K_2CO_3 , consequently making the Fe-based oxide layer formed on P91 or the Cr-enriched oxide layer on SS310 with more defects, which could facilitate the outward migration of cations and inward diffusion of oxygen anions for further oxide growth. Secondly, the high dissolution of Fe and/or Cr hydroxides would help the formation of micro-cracks and localized pores within the corrosion layers (see Figs. 5-3 and 5-5), which would then act as ‘windows’ for the diffusion of aggressive anions from the testing solution to the steel substrates for oxide formation. Thirdly, under the batch-mode catalytic HTL conversion, part of dissolvable cations (Fe^{3+} and Cr^{3+}) generated from the chemical dissolution reactions might remain around the corrosion layer on P91 or SS310, consequently suppressing the further dissolution of Fe and/or Cr oxides and supporting the formation of outer non-protective corrosion layers as shown in Figs. 5-3 and 5-5, respectively. In addition, as shown in Fig. 7, the influence of K_2CO_3 on the corrosion rate of SS310 steel was likely to be less effective compared to that on P91. This could be due to the difference of chemical stability between Fe and Cr oxide in the catalytic HTL environments. Due to the low dissolubility, the formed inner Cr-enriched oxide layer on SS310 could be an effective barrier to protect the substrate from the environmental attack.

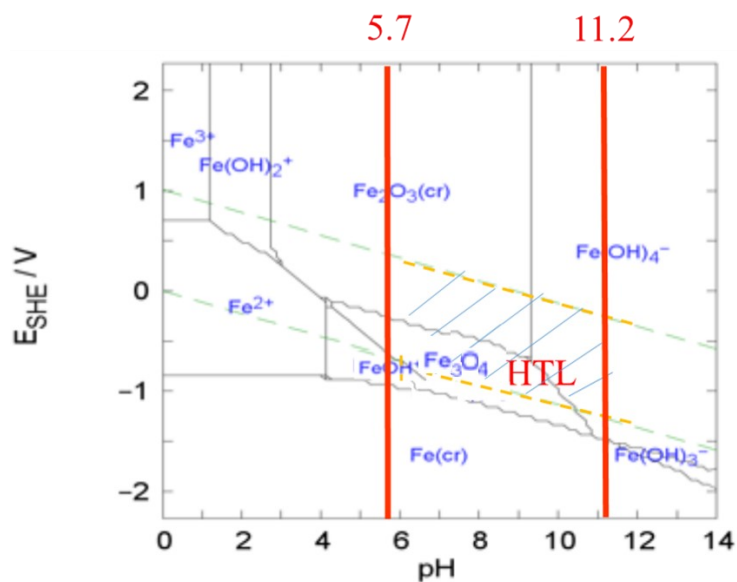


Fig. 5-18. Constructed Pourbaix diagram of Fe-H₂O system at 310 °C. Note that the diagram is also applicable for the 0.5 M K₂CO₃ solution with inorganic/organic corrodants.

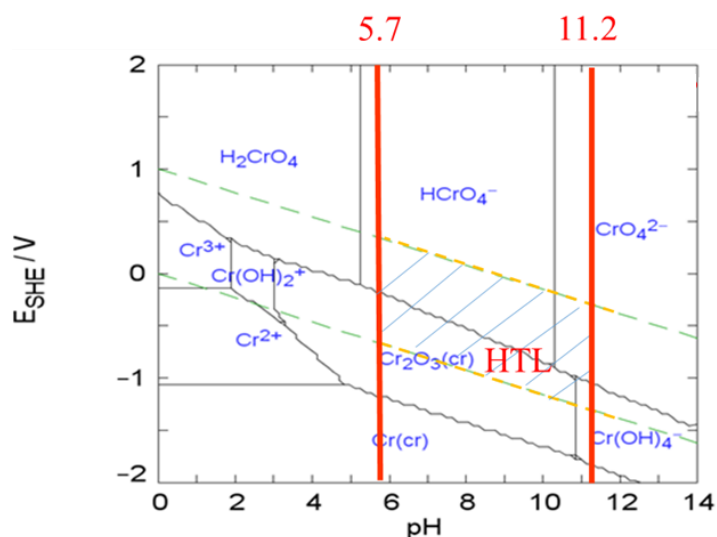


Fig. 5-19. Constructed Pourbaix diagram of Cr-H₂O system at 310 °C. Note that the diagram is also applicable for the 0.5 M K₂CO₃ solution with inorganic/organic corrodants.

Different from K₂CO₃ catalyst, the presence of trace amounts of inorganic corrodants (S²⁻ and Cl⁻) only led to a slight increase in the pH of the catalytic HTL environment due to the low concentration, even though its interaction with pressurized hot water is quite strong [423, 424]. However, as shown in Figs. 5-9 and 5-11, the addition of S²⁻ and Cl⁻ resulted in a noticeable change

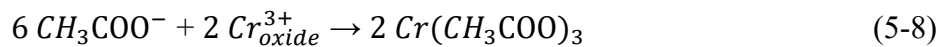
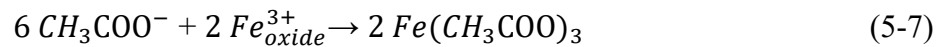
of corrosion layers formed on the two steels. Different from those found in previous studies [165-170], the introduction of S^{2-} and Cl^- in the catalytic HTL environment did not trigger localized corrosion (pitting), but actually affected the oxide formation and dissolution on the two steels. A number of studies have highlighted the effects of Cl^- and/or S^{2-} on pitting initiation and propagation on steels and alloys. Cl^- ions have been found to locally damage the integrity of passive oxide films as they can be adsorbed and accumulated at defects to replace O^{2-} in the oxides for the formation of highly soluble metal-anion complexes [425-430]. S^{2-} can interfere with formed oxide layer through incorporating sulfide ions on local defective sites to form metal-sulfide complexes (such as FeS and MnS) due to its high chemical affinity to the metal and consequently impair the oxide film integrity [192, 430-432]. In this study, the marginal effect of the inorganic corrodants on pitting under HTL condition might be ascribed to the following factors. The limited amounts of Cl^- and S^{2-} in the catalytic HTL solution might be insufficient to facilitate pitting. For instance, former studies suggested that the pitting of SS304L and SS316L would be more likely to occur in the solutions with Cl^- content higher than 0.5 wt.% [433-435]. Moreover, the high chemical dissolution rates of Fe and/or Cr oxides/hydroxides on the steels in the catalytic HTL solution might reduce the localized accumulation of Cl^- and S^{2-} , and consequently suppress pitting initiation and propagation.

As described above, the addition of Cl^- and S^{2-} caused a slight decrease in the thickness of the corrosion layer formed on P91 and the inner Cr-enriched layer grown on SS310, suggesting that the chemical dissolution of these defective oxides might be enhanced by replacing the O^{2-} in the oxides with the inorganic corrodants to form dissolvable complexes. For SS310 steel, the synergistic effect of K_2CO_3 catalyst and inorganic corrodants on enhanced oxide dissolution could also lead to the formation of porous middle Cr/Fe oxides layer and localized distribution of Ni particles (see Fig. 5-11). As implied in Table 5-3, the oxidation ability of alloying element Ni in SS310 should be much less than other two alloying elements (Cr and Fe). After a certain exposure time, the enhanced dissolution of Cr/Fe oxides by the basic catalyst and inorganic corrodants as well as high oxide formation rate in the catalytic HTL environment could cause the localized accumulation of Ni particles within the middle corrosion layer. Therefore, the above factors could consequently cause an increase in the corrosion rates of the two steels as shown in Fig. 5-12. Moreover, the inner Cr-enriched oxide layer formed on SS310 is the key barrier to protect the steel from catalytic HTL environmental attack. As shown in Fig. 5-11, its integrity was noticeably

affected with the addition of Cl^- and S^{2-} . This could make the inorganic corrodants with more noticeable impact on the corrosion of SS310 would than P91 as shown in Fig. 5-12.

Unlike K_2CO_3 catalyst and inorganic corrodants, the generation of acetic acid during the catalytic HTL conversion should decrease the environmental pH. At 310 °C, the pH of the catalytic HTL environments with 5 wt.% acetic acid was estimated to be about 7.6. Note that that the water ionization constant and the dissociation constant of carbonate in K_2CO_3 and conjugate base (acetate ion) in acetic acid should increase with temperature [436, 437]. For instance, the dissociation constant of acetic acid was estimated to be about $1.8 \times 10^{-2.6}$ at 310 °C, higher than that at room temperature. Based on the constructed Pourbaix diagrams (see Figs. 5-18 and 5-19), the addition of 5-10 wt.% acetic acid would create an HTL environment in which the two tested steels would experience passivation instead of active corrosion. As shown in the diagrams, stable oxides (Fe_3O_4 or Cr_2O_3) are predicted to be formed on the steels at 310 °C and the pH range of 4.7-10.4. However, as shown in Figs. 5-14 and 5-17, the presence of acetic acid in the catalytic HTL environment significantly enhanced the corrosion of the two steels, suggesting there is a puzzle about role of acetic acid on the corrosion during the catalytic HTL conversion.

In the catalytic HTL conversion environment, the influence of acetic acid on the corrosion may follow two different routes, depending on the content of acetic acid produced. It is estimated that the addition of ~ 8.5 wt.% acetic acid could completely interact with 0.5 M K_2CO_3 solution to generate a near neutral condition at 310 °C. Thus, the first route is that the addition of acetic acid (< 8.5 wt.%) would reduce the environmental pH and produce acetate ions (CH_3COO^-), which might react with cations in the oxides formed on the steels for the formation of dissolvable metal acetate via



This could enhance the chemical dissolution of formed oxides on the steels. Once the generated acetic acid content is more than 8.5 wt.%, which was calculated to be the threshold amount for catalyst to be completely reacted at 310 °C, the second route, i.e., the direct interaction of the acid with oxides, might also occur



Previous studies on stainless steels (such as SS304 and SS430) in acetic acid at temperature up to 118 °C indicated that the presence of acetic acid in the solution was expected to enhance chemical dissolution rates of oxides and subsequently make the oxide layer more defective [438, 439]. For SS310, as shown on Fig. 5-16, the addition of 10 wt.% acetic acid clearly led to the formed inner Cr-enriched oxide layer with more defects and also resulted in the formation of a thicker and more porous Cr/Fe oxide middle layer, which might be attributed to the effects of above reactions (7) - (10). Due to the reactions (7) and (9), it could be expected that the corrosion layer formed on P91 would be also porous and quite defective. As mentioned above, the mitigation of cations and anions with the oxide layers should be remarkably increased with an increase in the defect density in the layers. Moreover, as shown in Fig. 5-14, the presence of acetic acid in the catalytic HTL environment also resulted in the formation of cracks and pores on the steels (see Figs. 5-14 and 5-16), which would act as “windows” to facilitate the diffusion of testing solution to the substrates for further growth of oxides with less protectiveness. In general, the generation of acetic acid during the catalytic HTL conversion is likely to not only accelerate the chemical dissolution of corrosion layers, but also enhance their growth.

5.5. Conclusions

This study investigated the influence of major environmental factors, including alkaline catalyst (K_2CO_3), inorganic corrodants (S^{2-} and Cl^-), and organic acid (acetic acid), on the corrosion of P91 and SS310 during biomass HTL conversion at 310 °C, and the following conclusions are made:

- (1) The addition of homogeneous 0.5 M K_2CO_3 catalyst alone into the HTL environment significantly changed the corrosion layers formed on the tested steels, and led to remarkable increase in their corrosion rates. In the catalytic HTL environments, the corrosion layer grown on P91 was double-layer structure and mainly composed of Fe_3O_4 and $\text{Fe}_{3-x}\text{Cr}_x\text{O}_4$, while the layer formed on SS310 was three-layer structure and with a much thicker inner Cr-enriched oxide layer compared to that formed in non-catalytic HTL environment.

- (2) The existence of limited amount of inorganic corrodants (Cl^- and S^{2-}) during the catalytic HTL conversion did not trigger pitting. But their presence caused a decrease in the thickness of total corrosion layer formed on P91 and inner Cr-enriched layer on SS310, and led to a slight increase in the corrosion rates of the steels.
- (3) With generation of acetic acid under the catalytic HTL conversion, the corrosion rates of the steel were noticeably increased. The introduction of acetic acid resulted in the formation of thicker corrosion layer along with micro-cracks on P91 steel, and made the layer formed on SS310 much porous (especially the inner Cr-enriched oxide layer).
- (4) Increasing Cr content in Fe-based steels improved their resistance to HTL environmental attack. Due to the formation of inner Cr-enriched oxide layer, Cr-bearing SS310 exhibited promising potential for the construction of catalytic HTL reactors.

Chapter 6. Roles of Major Alloying Elements in Steels and Alloys on Corrosion under Biomass Hydrothermal Liquefaction (HTL) Conversion

In the previous chapter, two candidate steels were studied under different HTL conversion conditions and their corrosion performance has been assessed. In this chapter, I carried out autoclave tests on 5 candidate materials under three representative HTL conversion conditions to further understand the effect of major alloying elements on corrosion. It has been found that the performance of Fe-based steels was largely determined by their Cr content in substrate, and the effects of Ni and Mo are different among medium Cr content steels (~16 wt.%) and high Cr content steels (> 20 wt.%). Comparably, the effects of Ni and Mo are distinct in Ni-based alloys in which Mo only affects the corrosion layer chemistry and performance of alloys when Cr content is above a critical value. This chapter serves to further advance the mechanistic understanding of how each major alloying element participates in the corrosion and affects the oxide layer formation, to support the innovation of novel alloys that can specifically serve under catalytic HTL conversion conditions.

Abstract

Hydrothermal liquefaction (HTL) is one the most promising thermochemical technologies to convert wet biomass and biowaste streams to marketable bioenergy products. Significant knowledge gaps exist on the selection of suitable alloys for the construction of HTL reactor due to the existence of potential corrosion damage. This study investigated the roles of alloying elements (Cr, Fe, Ni and Mo) on corrosion in representative HTL environments through theoretical calculations, high temperature autoclave tests on five different alloys, and post characterizations of the formed corrosion products using XRD/SEM/FIB/TEM techniques. The alloying elements are theoretically predicted to experience general oxidation in non-catalytic HTL environment, but may suffer active corrosion under catalytic HTL condition at the temperature range of 250 - 365 °C. In Fe-based steels and Ni-based alloys, Cr acts as the dominant element for their corrosion performance under the HTL conditions. The Cr content in Fe-based steels is required to be > 16% for satisfactory corrosion resistance at 310 °C. In the alloys with ~ 16 % Cr, increasing Ni to replace Fe facilitates the formation of a more protective surface scale. In the alloys with > 20 %

Cr, increasing Mo leads to a remarkable improvement in corrosion performance. For Ni-base alloys, there is likely a critical Cr content above which the effect of Mo becomes noticeable.

Keywords: Biomass hydrothermal liquefaction, Alloying elements, Thermodynamic calculation, High temperature corrosion, XRD, TEM

6.1. Introduction

Biomass is the world's fourth largest energy source and a promising energy feedstock because of its unique characteristics: renewable, environmentally friendly, and strongly beneficial to economic growth. Available biomass resources include wood, agricultural, industrial and municipal waste streams, as well as microalgae. However, without the deployment of innovative thermochemical conversion techniques (such as hydrothermal liquefaction (HTL) and gasification), these raw biomaterials could not be cost-effectively and efficiently converted into marketable bioenergy and biochemical products in a timely fashion [9-13]. Over the past few decades, intensive investigations have been carried out to optimize HTL processes, and it has been generally concluded that the HTL conversion of wet feedstocks can be successfully achieved in hot pressurized water at the temperature range of 250 - 365 °C and pressure up to 25 MPa [73-77]. Moreover, catalysts and biomass feedstock categories are also recognized as the two major factors affecting carbon conversion efficiency and the properties of final bio-products [76-89]. For instance, a number of studies reveal that the addition of 0.5 - 1.0 M K_2CO_3 into the hot water medium leads to the desired conversion outputs [90-94]. Furthermore, the effect of alkaline catalysts on biocrude oil yield coherently depends on the lignin content in the biomass feedstocks [12, 440, 441].

The HTL technology is conceptually simple and robust for a wide range of wet feedstocks (especially industrial and municipal biowastes), and more economically favorable compared to other thermochemical conversion pathways. Despite these promising advantages, the industrial-scale commercialization of HTL has not yet been achieved due to the relatively high capital investment and significant materials knowledge gaps on the construction of critical components (particularly conversion reactors and high-pressure feeding pumps). As describe above, the

reactors are required to resist hot pressurized water attack at the pH range of 5.7 - 11.2, thus raising the challenge of selecting suitable alloys for cost-effective construction and long-term safe operation. Previous studies found that increasing pH only from 10 to 12 could result in a remarkable increase in the corrosion rates of austenitic stainless steels since the formed protective surface oxide scales on the steels would be transformed into dissolvable hydroxides in high temperature basic solutions [52, 155-158]. Moreover, certain amounts of inorganic and organic corrodants (such as Cl^- , S^{2-} , lactic acid and acetic acid) will be released during the conversion of wet biomass or biowaste feedstocks. From corrosion perspective, their presence may affect the corrosion mode and kinetics of reactor alloys [374-380]. For instance, our recent study indicated that the presence of acetic acid in catalytic HTL environment could lead to a remarkable increase in the corrosion rates of Fe-based steels [442].

Based on the knowledge and experience accumulated at existing high temperature aqueous systems [230, 299, 300, 301, 302, 304], several types of commercial steels and alloys, including ferritic-martensitic (F/M) steels, austenitic stainless steels, Ni-based alloys, and even Zr alloys, have the potential for the construction of HTL reactors from the materials engineering and corrosion science points of view. Both laboratory and field studies indicate that Zr alloys exhibit excellent corrosion resistance to several harsh aqueous environments at temperature $< 400\text{ }^\circ\text{C}$, where even Alloy C-276 and Alloy 22 cannot successfully survive [443-445]. However, their application for the construction of HTL reactors is limited due to the high cost of alloy. F/M steels (such as P91 and P92) are widely used as boiler tubes at temperature $\leq 620\text{ }^\circ\text{C}$ due to their high resistance to stress corrosion cracking (SCC) and excellent thermal properties, such as high resistance to thermal fatigue and creep [202, 441, 446]. Several 300-series austenitic stainless steels, including 304, 316L, 310 and 347, can be used at temperature $\leq 675\text{ }^\circ\text{C}$ with minimum carbides formation and satisfactory mechanical strength [447, 448]. Previous investigations found that the corrosion resistance of these austenitic stainless steels in high temperature neutral aqueous solutions ($\text{pH} \approx 7$) would rely on the bulk Cr content in the steels [133, 266, 449, 450]. Increasing Cr content higher than 16 wt.% is likely to result in satisfactory corrosion performance [451-454]. In basic solutions, however, the steels with Cr content even up to 18 wt.% do not exhibit acceptable corrosion resistance at temperature $< 200\text{ }^\circ\text{C}$ [455-457]. Moreover, because of the potential pitting and SCC risks, caution needs to be taken if using the steels in high temperature environments with

the presence of Cl^- and/or S^{2-} [458, 459]. On the contrary, the addition of alloying element Mo into the steels may improve their performance in high temperature aggressive aqueous environments because the presence of Mo can suppress the dissolution of the formed Cr oxides, thus enhance their resistance to pitting [211-213]. For instance, the addition of 6 wt.% Mo into Fe-22Cr steel resulted in a promising performance in the environments with 9,000 – 70,000 ppm Cl^- ions [460]. Ni-based alloys, such as Alloy C-276 and Alloy 625, are highly recommended for their applications in high temperature corrosive environments [214, 461, 462]. Alloy C-276 with 16 wt.% Mo is one of the most well-established alloys with many successful application cases in high temperature environments [214, 215]. For example, the alloy only exhibited marginal weight change when exposed to supercritical water with 0.5 M NaOH at 400 °C and 25 MPa for 50 hours [215]. Alloy 625 is another well-recognized high-temperature alloy used in harsh environments [216-220], e.g., it only experiences a corrosion rate of 4.4 $\mu\text{m}/\text{year}$ in 527.5 °C water after 200 hours [220].

Unfortunately, few efforts have been taken to investigate the corrosion performance of the F/M steels, austenitic stainless steels and Ni-based alloys under the HTL conversion conditions. Therefore, to fill the knowledge gaps, this study conducted thermodynamic simulation to predict whether major alloying elements (Cr, Mo, Fe and Ni) in the alloys experience active corrosion or passivation in the typical HTL processes. Meanwhile, the corrosion kinetics of P91, SS316L, SS310, Alloy C-276 and Alloy 625 were investigated in a static autoclave under simulated catalytic HTL operating conditions, followed by detailed microscopic examinations of the formed corrosion products. It is anticipated to advance the mechanistic understanding of the roles of major alloying elements (Cr, Mo and Ni) on corrosion in HTL biorefining environments and partially support the development of applicable materials technology solutions for the construction of industrial HTL plants.

6.2. Thermodynamic simulation

Pourbaix diagrams, originally developed by Marcel Pourbaix, describe the stable species or phases of an alloying element in aqueous solution as a function of potential and pH. According to our literature review, most previous studies were carried out in aqueous solution at temperatures < 100 °C [463-465]. Recently, several studies constructed the diagrams to reflect high temperature

aqueous and supercritical water environments [258, 265, 466]. However, the results are insufficient to predict the performance of major alloying elements (Cr, Fe, Ni and Mo) under the specific HTL conditions. Therefore, this study intended to develop the diagrams that could depict whether a major alloying element experiences active corrosion or passivation in the HTL environments based on available public thermodynamic database and commercial Medusa software.

In a Pourbaix diagram, the standard Nernst equation of an electrochemical reaction ($aA + mH^+ + ne^- = bB + cH_2O$) is expressed as:

$$E_T = E_T^\theta - 2.303 * \frac{mRT}{nF} * pH - 2.303 * \frac{RT}{nF} * \lg\left(\frac{a_B^b}{a_A^a}\right) \quad (6-1)$$

where E_T^θ and E_T stand for the standard electrochemical potential and electrochemical potential at temperature T , respectively; R is the gas constant; a_A or a_B is the overall activity of species A or B, respectively. In the equation, the concentrations of dissolved ions are assumed to be 10^{-6} mol/L based on the previous studies [255, 257, 258].

The thermodynamic properties of aqueous species can be found in the literatures or public databanks [158, 256, 265, 422] while the activities of solid are generally assumed to be unity, and activities of aqueous species are calculated in this study. At a designed HTL operating temperature, the standard electrochemical potential (E_T^θ) of the reaction ($aA + mH^+ + ne^- = bB + cH_2O$) can be estimated by:

$$E_T^\theta = -\frac{\Delta G_T^\theta}{nF} \quad (6-2)$$

where ΔG_T^θ is the Gibbs free energy of the reaction at the designated temperature (J), F is the Faraday constant (96485 C/mol), and the number of electrons transferred in the reaction (mol). The Gibbs free energy can be calculated by:

$$\Delta G_T^\theta = \Delta G_{298}^\theta - (T - 298)S_{298}^\theta + \int_{298}^T C_p dT - T \int_{298}^T C_p \frac{dT}{T} + \int_{P_v}^P V dP \quad (6-3)$$

where ΔG_{298}^θ stands for Gibbs free energy of formation of the species at room temperature; S_{298}^θ stands for entropy at room temperature, C_p stands for heat capacity for the specie; $\int_{P_v}^P V dP$ stands for the pressure term and is assumed to be 0 in this study. To calculate the Gibbs free energy for

the construction of high temperature Pourbaix diagrams of a major alloying element (Cr, Ni, Fe or Mo), following assumptions have been made:

- (1) Under HTL conversion conditions, the effect of pressure on the thermodynamic properties of an aqueous specie or solid would be neglected as the properties should be much more sensitive to temperature instead of pressure.
- (2) The thermodynamic properties of solid species were directly borrowed from existing public databases [467].
- (3) For ions and some complex aqueous species, the Gibbs free energies of formation were estimated based on some existing Pourbaix diagrams and/or the results described in previous studies [255, 256, 259-263], since the changes of their entropy and/or heat capacity were not available readily.
- (4) Due to the lack of experimental data, the activity coefficient of a solid or aqueous species at high temperature was assumed to be unity, similar to those done in former studies [257, 264, 265]. In Pourbaix diagrams, the reaction solution can be treated as an ideal dilute solution with limited concentration of cations and anions, making the activity of a solute or solid very close to its concentration in solution.

Once the Gibbs free energy was calculated, the Medusa software was then employed for the construction of the Pourbaix diagrams. Note that the software has an internal algorithm that can execute Nernst equation calculations based on the obtained thermodynamic properties of each species for the construction of Pourbaix diagrams [468].

6.3. Experimental testing procedure

6.3.1. Preparation of testing samples

Rectangular alloy coupons with the dimensions of 20 mm long × 10 mm wide × 2 mm thick were machined from commercial ferrite/martensitic steel (P91) cylinder, austenitic stainless steels (SS310 and SS316L) and Ni-based alloys (Alloy C-276 and 625) plates, respectively. Their normalized bulk chemical compositions are listed in Table 6-1 based on the Mill Test Certificate provided by different suppliers. The fabrication history of P91 and SS310 can be found in the reference [376]. SS316L plate was made through annealing at 1038 °C, followed by quenching in

water. Alloy C-276 and 625 plates were made through solution annealing at 1148 °C and 1038 °C, respectively, and then quenched in water. A hole with the radius of 2 mm was made near the top of each coupon for subsequently hanging on a custom-made Alloy 625 holder during each autoclave corrosion test. Before a corrosion test, each sample including its four edges was carefully polished with a series of SiC papers from 120 to 600 grit in deionized water to remove all the potential contaminants and defects which might be introduced during the machining processes. Following that, the samples were cleaned in an ultrasonic bath with ethanol for 10 minutes, washed with flowing ultrapure water, and finally dried with pressurized air. After that, optical inspections were carried out to determine whether the prepared samples met the high temperature autoclave corrosion testing standard [399]. For each sample, an ID was assigned and marked on its upper-left corner to ensure its correct identification after the exposure to an HTL environment. Before a corrosion test, all the freshly prepared samples were weighed with a microbalance with the resolution of 1 µg and measured using a digital caliper with the precision of 0.001 cm. Four prepared samples of a test alloy were applied in each designed autoclave corrosion test to improve the precision and accuracy of the obtained results.

Table 6-1. Normalized bulk chemical composition of steels and alloys used in this study.

Alloy Types	Chemical Composition (wt.%)							
	Cr	Ni	Mn	C	Mo	Si	N	Fe
P91	8.36	0.07	0.47	0.11	0.90	0.33	/	Bal.
SS316L	16.60	10.00	1.20	0.02	2.00	0.30	0.10	Bal.
SS310	24.20	21.80	1.60	0.02	/	0.20	0.10	Bal.
Alloy C-276	15.90	58.80	0.40	0.01	15.50	0.02	/	5.70
Alloy 625	22.40	64.00	0.01	0.01	8.79	0.10	/	0.56

6.3.2. Autoclave testing methodology and procedure

Table 6-2 shows the autoclave test matrix for the tests performed for identifying the impacts of three major alloying elements (Cr, Mo and Ni) on corrosion under non-catalytic and catalytic HTL conversion conditions. Note that in Test #3, the addition of inorganic corrodants (Cl⁻ and S²⁻) and

organic acid (acetic acid) into 0.5 M K_2CO_3 was done to simulate the HTL conversion of industrial biowastes in which certain amounts of corrosive compounds will be released based on pilot-scale tests [159-164, 395, 396].

As shown in Fig. 6-1, all the tests were conducted in an Alloy C-276 autoclave with a pre-oxidized Alloy 625 liner to mitigate the influence of autoclave wall alloy based on the methodology described in ASTM G31 [251]. Note that Alloy 625 liner was pre-oxidized in an air furnace at 400 °C for 24 hours and used for accommodating testing solution and samples. For each autoclave test, the freshly prepared samples were loaded on the Alloy 625 holder using 20% Cr and 80% Ni Cr-Ni alloy wires, which were also pre-oxidized in the furnace at 400 °C for 24 hours to avoid the galvanic effect between the testing samples and the holder. The autoclave was then sealed and purged with pure N_2 for at least an hour to produce a deaerated environment, followed by leaking test under high pressure N_2 condition. The autoclave was then powered on to reach the target temperature. Once the temperature reached 310 °C, the time was recorded as starting point and all the three tests proceeded for 10 days. When the exposure duration was reached, the autoclave heater was powered off and naturally cooled down in air. At room temperature, the alloy samples were removed from autoclave, cleaned with distilled water, dried with pressurized air, and finally reweighed using the microbalance as stated above.

Table 6-2. Test matrix conducted to identify the impacts of alloying elements under simulated non-catalytic and catalytic HTL conversion conditions.

Test #	Testing Conditions
#1	in static Alloy C-276 autoclave with an Alloy 625 liner containing deaerated ultrapure water at 310 °C for 10 days
#2	in static Alloy C-276 autoclave with an Alloy 625 liner containing deaerated 0.5 M K_2CO_3 at 310 °C for 10 days
#3	in static Alloy C-276 autoclave with an Alloy 625 liner containing deaerated 0.5 M K_2CO_3 + 3500 ppm Cl^- + 2500 ppm S^{2-} + 5 wt.% acetic acid at 310 °C for 10 days

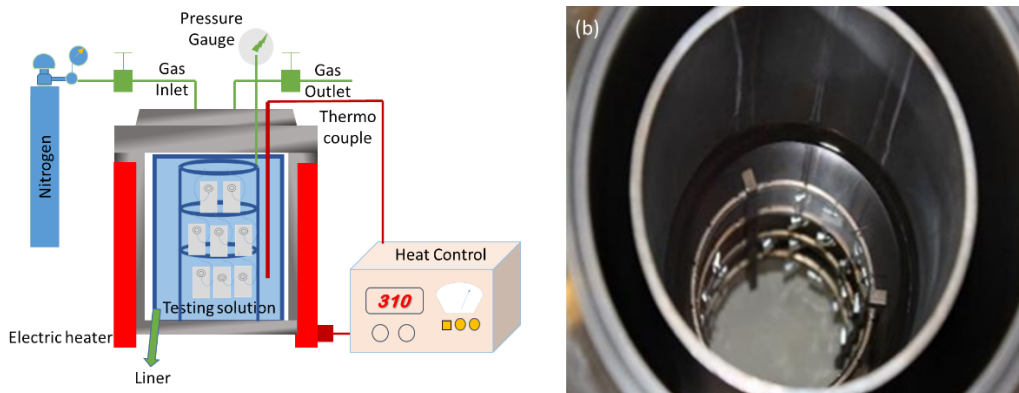


Fig. 6-1. (a) Schematic of the static autoclave setup used in this study; (b) Top-view photograph of the Alloy C-276 autoclave with an Alloy 625 liner, testing samples and sample holder.

6.3.3. Corrosion rate assessment

Two different methods can be used to evaluate the corrosion rates of alloys in high temperature aqueous solutions, including direct mass change measurement (i.e., measuring mass difference of a sample before and after an exposure), and indirect weight loss measurement which involves: (1) completely removing the formed corrosion products on a sample and (2) measuring the mass change of the sample before the test and after the descaling. Our previous studies have demonstrated that the indirect weight loss measurement is a more accurate method to assess corrosion rates compared to direct mass change technique since considerable chemical dissolution and localized breakdown of the formed corrosion layers will occur during the exposures to HTL environments [376]. In this study, the weight loss measurement was thus applied for corrosion rate assessment. Based on ASTM-G1 standard [228, 252], the descaling process is required to be done in suitable solution that only has negligible influence on the base metal, but can effectively and completely dissolve the formed corrosion products. In this study, the descaling of the corrosion products formed on SS310, SS316L, Alloy C-276, and Alloy 625 was successfully achieved via the following key steps:

- (1) Immersing the corroded samples in the solution A of 2 wt.% citric acid + 5 wt.% dibasic ammonium citrate + 0.5wt.% disodium EDTA at 90 °C for 30 minutes;
- (2) Submerging the samples in the solution B of 4 wt.% or 6 wt.% potassium permanganate + 5 wt.% caustic soda at 90 °C for 30 minutes, followed by cleaning in ethanol ultrasonic bath for

10 minutes. 4 wt.% potassium permanganate was used for the corroded stainless steels while 6 wt.% potassium permanganate was used for Ni-based alloys;

- (3) Dipping the samples in the solution A again at 90 °C for 30 minutes and weighing the samples after rinsing with water and drying with pressurized air;
- (4) Repeating the processes (1)-(3) until the weight of each sample reached a constant value as described in the reference [230].

Due to the nature of the formed corrosion products, the descaling of corroded P91 samples was done through immersing them in the solution of 500 ml HCl + 3.5 g + 500 ml H₂O at room temperature for 10 minutes, followed by gently removing the remaining corrosion products using cotton swabs and soft copper brush.

The average corrosion rate of a sample (µm/year) was then calculated by [232]:

$$Corr.Rate = \frac{8.76 \times 10^7 \bullet \Delta m}{dAt} \quad (6-4)$$

where $\Delta m(g)$ is the measured mass loss of a sampled before an exposure and after the descaling, $d(g/cm^3)$ is the alloy density, $A(cm^2)$ is surface area of the coupon, and $t(h)$ is the exposure duration. Based on ASTM-G16 standard [226], the average corrosion rate of an alloy was obtained from three parallel corroded samples of an alloy in this study.

6.3.4. Corrosion product characterization

After an autoclave test, primary optical checks on the surface morphology of corroded samples were performed to initially evaluate corrosion modes and extents of corrosion of the tested steels and alloys. Following that, the sample, which had the direct mass change value closest to the average value in a given replicated set, was used for more detailed microscopy characterizations. The corrosion layers formed on the alloys were examined using a FEI Nova NanoSEM 650 scanning electron microscope (SEM) system operated at 20 KeV and equipped with an Oxford energy dispersive X-ray spectroscopy (EDS) system to identify their chemistry and the related corrosion modes (such as active corrosion, general oxidation, nodular oxidation, and/or pitting, etc.). Since the corrosion layers grown on P91 samples were quite thick, the phase compositions of the layers were determined using X-ray diffraction (XRD) technique with a Co K α X-ray source

operated at 40 kV and 150 mA. For the thin corrosion layers formed on SS310, SS316L, Alloy C-276 and Alloy 625, a FEI Helios NanoLab™ DualBeam™ Focus Ion Beam (FIB) microscope was employed to produce cross-sectional SEM views of the layers and substrates. Before FIB operation, a thin Pt layer was deposited on the selected samples in vacuum to protect them from unexpected cutting damages. After the FIB cutting, the cross-sectional samples were also thinned using in-situ life-out technique for subsequent TEM examinations, including black field (BF) imaging, elemental mapping and corresponding EDS analyses. These characterizations were carried out using Tecnai Osiris™ scanning/transmission electron microscope (S/TEM) equipped with super X-field emission gun (FEG) and X-ray detection system operated at 200 kV.

6.4. Results and Discussion

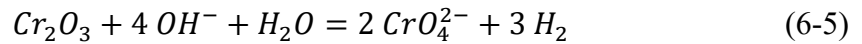
6.4.1. Pourbaix diagrams of major alloying elements under catalytic HTL conversion conditions

As mentioned above, the HTL conversion processes are usually operated at the pH range of 5.7 - 11.2 and the temperature range of 250 - 365 °C, depending on the properties of raw biomass feedstocks and the chemistry of catalysts applied [91, 93, 94]. Note that the ionization constant of ultrapure water is about $1 \times 10^{-11.20}$ at 250 °C, $1 \times 10^{-11.40}$ at 310 °C and $1 \times 10^{-11.98}$ at 365 °C, consequently making the non-catalytic HTL conversion environment to have the initial pH of about 5.6, 5.7, and 5.9 at 250, 310 and 365 °C, respectively. Note that the ionization constant of ultrapure water increases with temperature, i.e., from 1×10^{-14} at 25 °C to $1 \times 10^{-11.20}$ at 250 °C. At temperature > 260 °C, however, the ionization constant of subcritical water will decrease with a further increase in temperature close to the supercritical point (374.3 °C) because of the distortions of hydrogen-bond networks [152, 469]. Based on the above information and methodology, the related Pourbaix diagrams of the four alloying elements were thus constructed, and are shown in Fig. 6-2. The following general observations could be made:

- (1) At temperature ≤ 310 °C, iron might experience oxidization at the pH range of 6.3 - 10.2 or suffer active corrosion at a higher pH value. Interestingly, the alloying element would mainly undergo general oxidation at the pH range of 6.5 - 12.0 at 365 °C. This could be because the Gibbs free energy of oxide formation increases with an increase in temperature. The formed

oxides could be composed of Fe_3O_4 and Fe_2O_3 , depending on exposure time. The transition of iron oxides into dissolvable ferric hydroxide complexes ($\text{Fe}(\text{OH})_4^-$) could also occur at $\text{pH} > 9$.

- (2) At temperature ≤ 310 °C, Cr would also undergo either general oxidation or active corrosion, depending on the pH value of conversion environments. For instance, dissolvable chromium hydroxide complexes could be present at 250 °C and $\text{pH} > 9.3$. At 365 °C, general oxidation would be the dominant reaction on Cr. The formed oxide is likely to be Cr_2O_3 . Depending on temperature, pH and exposure time, the transition of Cr and the formed oxide Cr_2O_3 into dissolvable $\text{Cr}(\text{OH})_4^-$ and CrO_4^{2-} could occur through following reactions:



- (3) At 250 °C, Ni would be oxidized at $\text{pH} < 10.80$ or suffer active corrosion to form dissolvable $\text{Ni}(\text{OH})_3^-$ via the following reaction:

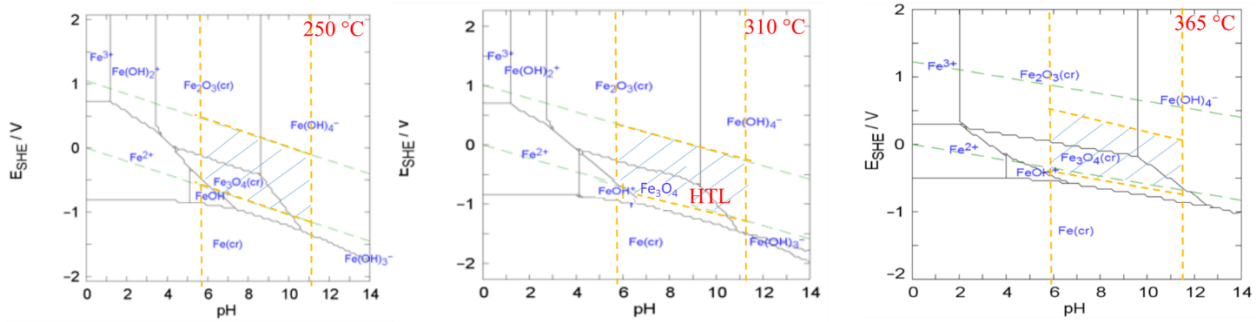


Different from Fe and Cr, Ni would mainly be subjected to general oxidation in the HTL environments at temperature ≥ 310 °C. Depending on environmental pH and time length of service, the chemical dissolution of Ni oxides into $\text{Ni}(\text{OH})_3^-$ could also occur via the reaction (6-7).

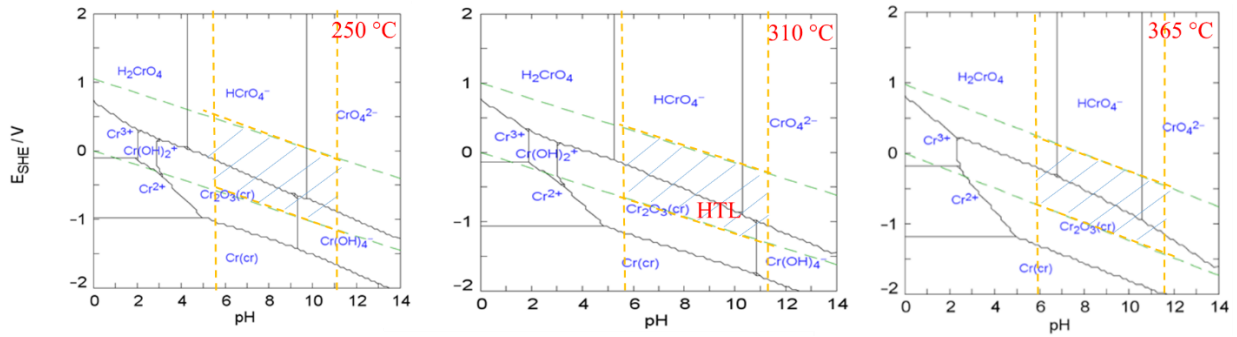
- (4) Similar to Fe and Cr, Mo would likely experience passivation or active corrosion to form MoO_4^{2-} at temperature ≤ 310 °C, depending on environmental pH. For example, active corrosion could occur and MoO_4^{2-} might be present in the 250 °C environment with $\text{pH} > 8.9$. Moreover, increasing temperature would result in an expansion of the passivation region to a higher pH region. At 365 °C, Mo would mainly go through general oxidation to form stable MoO_2 under the HTL conditions.

In general, the four alloying elements are likely to experience general oxidation or active corrosion in the HTL conversion environments at temperature ≤ 310 °C. Further increasing temperature would help the formation of thermodynamically stable oxides on them, because of the gradual shift of passivation region to wider pH range and negative electrochemical potential. Depending on pH

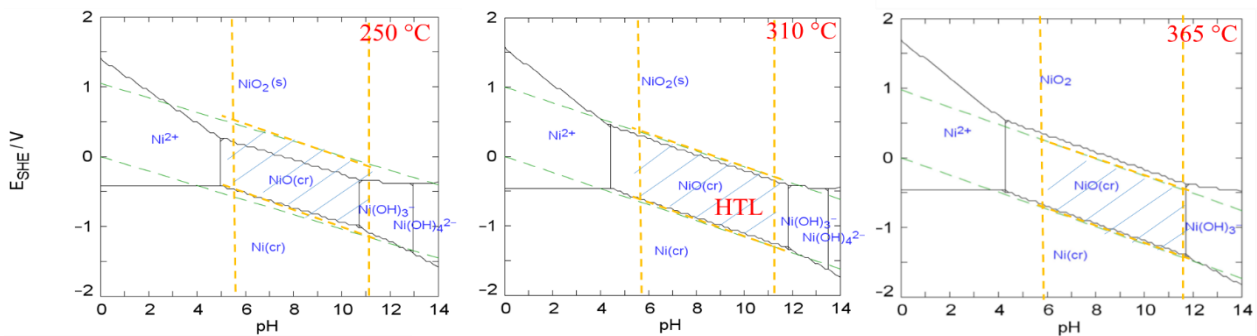
and exposure time, the transition of the protective oxides into dissolvable hydroxide compounds/complexes is expected to occur as described above.



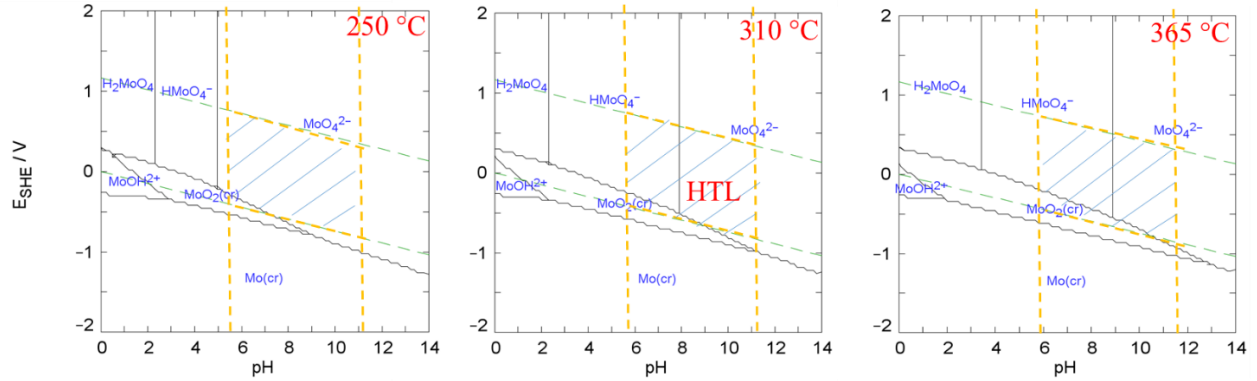
(a) Pourbaix diagrams of Fe-H₂O system at different HTL operating temperatures



(b) Pourbaix diagrams of Cr-H₂O system at different HTL operating temperatures



(c) Pourbaix diagrams of Ni-H₂O system at different HTL operating temperatures



(d) Pourbaix diagrams of Mo-H₂O system at different HTL operating temperatures

Fig. 6-2. Established Pourbaix diagrams of major alloying elements and H₂O system at the temperature range of 250 - 365 °C, constructed by extrapolating thermodynamic properties of compounds that retrieved from databases [255, 256, 258-265, 466].

6.4.2. Influence of major alloying elements on corrosion processes under the HTL conversion

6.4.2.1. Effects of alloying elements on corrosion kinetics

In the HTL environments, the corrosion kinetics of candidate reactor alloys are determined by the chemistry and structure of the formed surface scales as indicated in our pervious study [442]. Based on the predictions in Fig. 6-2, four major alloying elements (Fe, Cr, Ni and Mo) in the Fe-based steels and Ni-based alloys would either experience passivation to form protective oxides, or active corrosion to generate dissolvable complexes, depending on applied HTL conversion mode (non-catalytic or catalytic), the amounts of organic acids generated, and other key operating parameters (such as temperature, pressure and flowing rate). Thus, the corrosion kinetics of the five candidate alloys were investigated under three typical HTL conversion conditions, including ultrapure water (i.e., non-catalytic HTL, pH = 5.7 at 310 °C), 0.5 M K₂CO₃ (simulating homogenous catalytic HTL, pH = 11.2 at 310 °C), and 0.5 M K₂CO₃ + 3500 ppm Cl⁻ + 2500 ppm S²⁻ + 5 wt.% acetic acid (representing homogenous catalytic HTL with the production of inorganic and organic corrodants, pH= 7.6 at 310 °C).

The photographic images of the alloys before and after the exposures at 310 °C for 10 days are shown in Fig. 6-3. Before the corrosion tests, the surfaces of all the freshly prepared coupons were neat with shining metal luster. However, after the exposures to the HTL conversion environments,

the alloy exhibited distinct difference in appearance, especially for SS310, SS316L, Alloy 625 and C-276, implying the formation of different corrosion layers. After being corroded in the non-catalytic HTL environment (Test #1), P91 samples showed the darkest surface, while the surface of corroded SS310 and SS316L were light brownish along with several localized depositions. Compared with the above Fe-based steels, the two Ni-based alloys (Alloy C-276 and Alloy 625) presented lighter yellowish surface without localized deposition, suggesting the formation of relatively thinner corrosion layers. After the exposure to the catalytic HTL environment (Test #2), all the Fe-based steels with different Cr contents exhibited dark grey, indicating the formation of thicker corrosion layers comparing to those grown in the non-catalytic HTL environment. Different to the steels, the two Ni-based alloys only exhibited light grey. After Test #3 (catalytic HTL with presence of inorganic and organic corrodants), all the tested alloys showed darker surface and the surface of the two Ni-based alloys were still lighter than those of the Fe-based steels. In addition, the presence of inorganic corrodants (Cl^- and S^{2-}) in the catalytic HTL environment was unlikely to trigger pitting on all the five alloys.

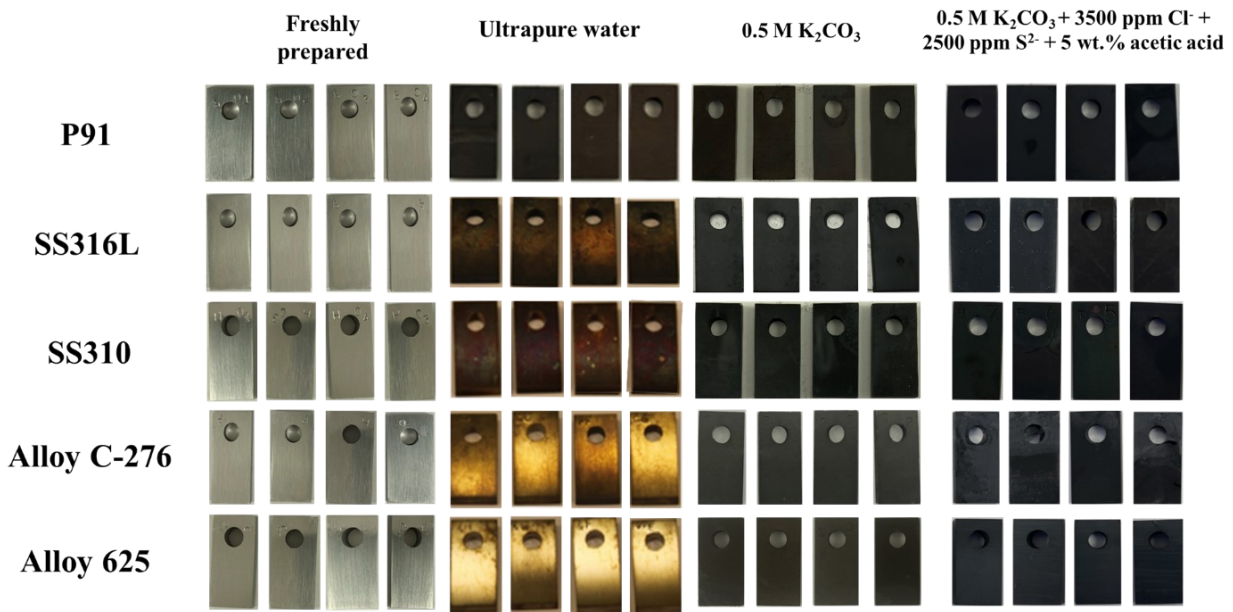


Fig. 6-3. Photographic images of five candidate alloys before and after the exposures to three HTL conversion environments at 310 °C for 10 days, respectively.

After the 10 days' exposure to a typical HTL conversion environment, the average corrosion rate of each alloy was estimated based on the weight loss measurement and equation (6-4) as described

in the Section 6.3.3, and all the obtained results are presented in Fig. 6-4. The following observations and discussions are made:

- (1) All of the tested alloys suffered the highest corrosion damage in the catalytic HTL environment with inorganic corrodants (Cl^- and S^{2-}) and 5% acetic acid ($\text{pH}=7.6$), while exhibit the lowest corrosion rates in the non-catalytic HTL environment ($\text{pH}=5.7$) at $310\text{ }^\circ\text{C}$. Based on the above thermodynamic predications, the major alloying elements (Fe, Cr, Ni and/or Mo) in these alloys would experience passivation instead of active corrosion in the non-catalytic HTL environment (see Fig. 6-2). Thus, it could be expected that the alloys would exhibit satisfactory performance under such a HTL conversion condition. During catalytic HTL conversion, however, the higher corrosion rates of the alloys did not occur in the catalytic environment ($\text{pH}=11.2$) even though the alloying elements of Fe, Cr and Mo would experience active corrosion as predicted in Fig. 6-2. As mentioned above, adding inorganic and organic corrodants could change the pH of catalytic HTL environment down to about 7.6 because of the reaction of acetic acid with OH^- and the interaction of S^{2-} with the pressurized hot water, the four alloying elements were predicted to form stable oxides as shown in Fig 2. The above findings suggested that the inorganic and organic corrodants released during the catalytic HTL conversion could significantly decrease the integrity of corrosion layers formed on the alloys and/or remarkably enhance the chemical dissolution of the layers. Therefore, both the environment pH and the generated corrodants during the conversion should be the two key factors affecting the corrosion kinetics of candidate reactor alloys.
- (2) For Fe-based steels, increasing Cr and/or Ni content resulted in a remarkable decrease in their corrosion rates, particularly in the catalytic HTL environment with inorganic and organic corrodants (Cl^- , S^{2-} and acetic acids). In the non-catalytic HTL environment, thermodynamic calculation indicated that element Ni would not involve the surface oxide formation because of the positive Gibbs free energy of the reaction ($\text{Ni} + \text{H}_2\text{O} = \text{NiO} + \text{H}_2$) [376]. Thus, the improved corrosion resistance in the non-catalytic HTL environment would be mainly attributed to the Cr content that was present in the steels. As shown in the following characterization section, increasing Cr content could lead to the transition of Fe-enriched oxides to Cr-enriched oxides formed on the Fe-based steels. In the catalytic HTL

environments, increasing Cr content could also result in an enhanced corrosion resistance as the Cr-enriched oxides would be expected to have higher chemical stability than Fe-based oxides based on former studies [376, 470, 471]. But the role of element Ni on the formed surface scales is still a puzzle. As predicted in Fig. 6-2, stable NiO could be formed at the pH range of 6-12 at 310 °C. Detailed information about the influence of Ni is further explored in the next section. In addition, although it is generally accepted that the chemical compositions of Fe-based steels, instead of their crystallographic phases, are more critical to their corrosion performance in various high temperature aggressive environments [472, 473, 474, 475], the effect of crystalline structure still needs to be considered under non-catalytic and catalytic HTL conversion conditions. As mentioned above, P91 is a ferrite-martensite steel with body-centered cubic/tetragonal crystalline structure while SS310 and SS316L are austenitic stainless steels with face-centered cubic crystal structure containing austenite stabilizers (Mn and Ni). Previous studies found that in comparison with austenite phase, ferrite-martensite interfaces would have lower carbon dissolution and affordably provide pathways for voids/microcracks propagation along the boundaries, possibly leading to Cr depletion and thus enhancing corrosion [473, 476, 477]. Moreover, most of the alloying elements in P91 tend to participate in martensite phase instead of ferrite [478, 479], which could create “galvanic couple” between the two phases and consequently make the steel more prone to environmental attack compared to the two austenitic stainless steels.

- (3) For the alloys with medium Cr content (around 16%), it was likely that increasing Mo and/or Ni contents resulted in a remarkable increase in their resistance to the non-catalytic and catalytic HTL environments. Previous studies proposed that the addition of Mo might help the formation of a protective Cr-enriched oxide film through the dissolution of Mo^{6+} ions in the oxyhydroxide network [123], or aid the formation of $\text{MoO}(\text{OH})_2$ or MoO_4^{2-} to suppress localized damage of the oxide layer [124-126]. Mo has also been found to facilitate the growth of finer lamellar microstructure of the alloys, consequently increasing their corrosion resistance [480, 481]. Our most recent study in hot dilute acidic pre-hydrolysis environment found that increasing Mo content could help the formation of a compact and protective Mo oxide layer to resist environmental attack at elevated temperatures [482]. As predicted in Fig. 6-2(d), Mo can be oxidized to form stable oxide in the HTL environments. Thus, the above factors making the corrosion resistance of alloys increase with an increase in Mo content in

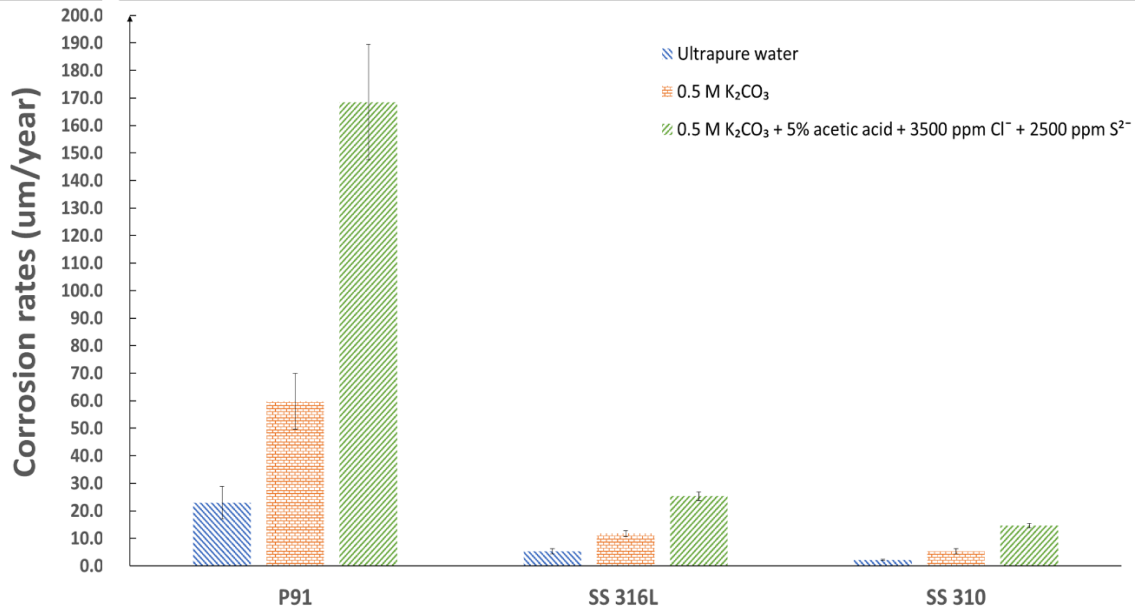
the HTL environments. For Ni element, the role in corrosion process in the HTL environments is unclear, as stated above. A previous study on Fe-based and Ni-based alloys in 0.5 M NaOH at temperature up to 400 °C found that Alloy C-276 showed lower corrosion rate than SS316, likely because of its higher Ni and Mo contents [215]. Also, it has been found that increasing Ni and Mo contents could reduce corrosion rates and SCC susceptibility in alkaline solution as well [215]. In the next section, the role of Ni in the corrosion layer formed on Alloy C276 is presented. In addition, although both SS316L and alloy C-276 have austenitic structures, Alloy C-276 has two unique phases (γ' and γ'') which are formed during precipitation hardening and has high dissolubility of alloying elements (e.g. Cr, Mo, Nb) in the matrix, thus improving its resistance to high temperature systems [483-486]. However, several studies on austenitic alloys (such as SS316L, SS310, Fe-17Cr-9Ni steel, and Alloy 625) have shown that influence of crystalline structure on corrosion should be much less noticeable than the effect of chemical compositions [487- 489].

- (4) For the alloys with high Cr content ($> 22\%$), increasing Mo and/or Ni led to certain improvement of their corrosion resistance, particularly in the catalytic HTL environment with Cl^- , S^{2-} and acetic acid (see Fig. 6-4(c)). Similar to the above, the influence of Mo in the alloys on corrosion could be through improving microstructure, enhancing the stability of Cr-enriched oxide, and/or directly forming protective Mo oxide layer. For Ni content, a previous study (carried out in 6.7 mol/L KOH at temperature < 180 °C) found that the corrosion rate of SS310 was remarkably higher than that of Alloy 690 because of slightly higher Cr content, suggesting that increasing Ni content in alloys might improve corrosion resistance [398]. In this study, the influence of Ni in Ni-based alloys on corrosion in the catalytic HTL environments was also examined using SEM/TEM techniques and is presented in the next section.
- (5) As shown in Fig. 6-4, overall ranking in terms of increasing corrosion resistance in the non-catalytic and catalytic HTL environments is:

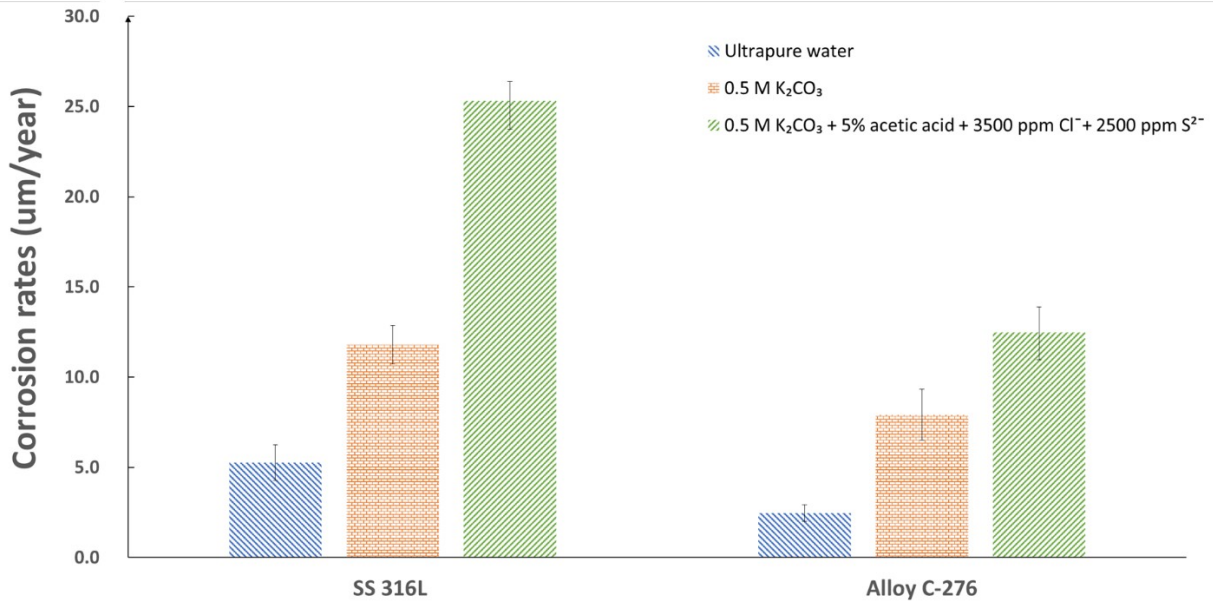
$$\text{P91} \ll \text{SS316L} < \text{SS310} < \text{Alloy C-276} < \text{Alloy 625}.$$

Note that Alloy C-276 showed slightly higher corrosion rates than SS310 in catalytic HTL environment without corrodants. It is worth noting that although no guideline is available at present to define the maximum corrosion rate allowance of the HTL conversion reactor

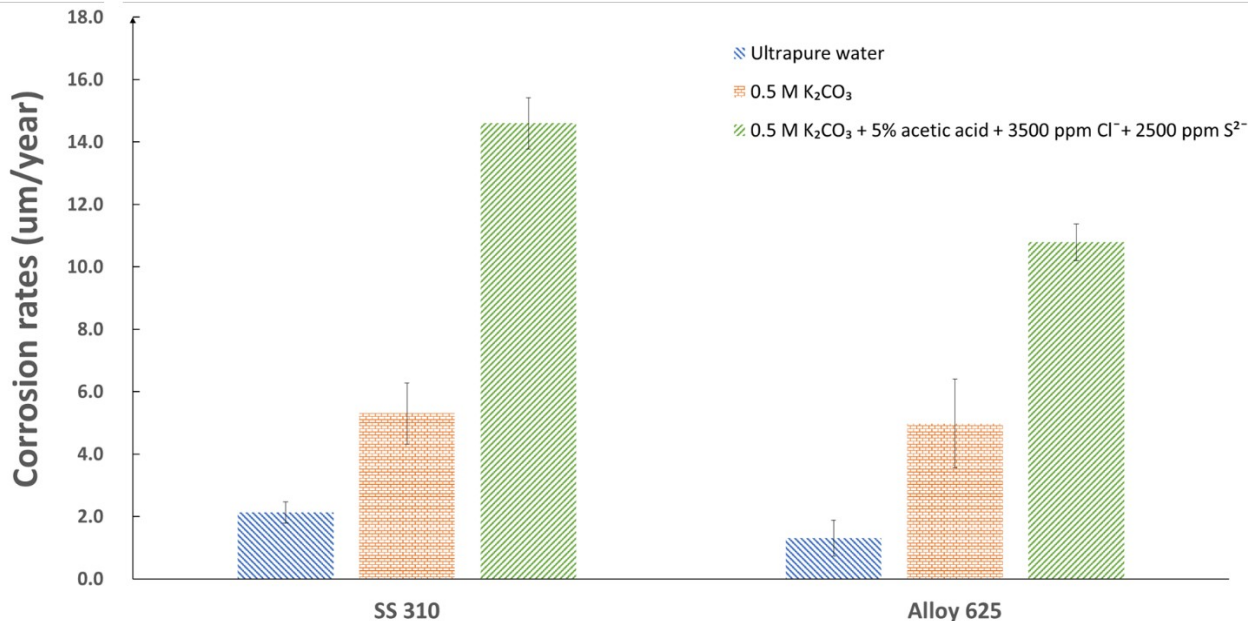
alloys, one can assume that the rate limit should be less than 0.1 mm/year based on the existing operating experience and knowledge at paper and mill plants [411, 412]. Therefore, the tested alloys except P91 exhibited promising corrosion performance for further stress corrosion cracking evaluations and pilot-scale validation tests.



(a) The average corrosion rates of Fe-based steels with different Cr and Ni contents



(b) The average corrosion rates of alloys with medium Cr content (~ 16 wt.%) but different Mo and Ni concentrations



(c) The average corrosion rates of alloys with high Cr content (> 22 wt.%) but different Mo and Ni concentrations

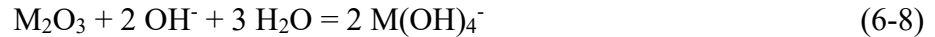
Fig. 6-4. Comparison of the average corrosion rates of Fe-based steels and Ni-based alloys with different alloying element contents in non-catalytic and catalytic HTL environments at 310 °C.

6.4.3. Influence of alloying elements on the corrosion layers formed in HTL environments

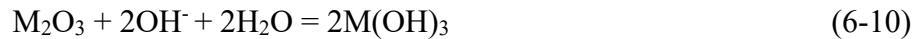
6.4.3.1. Roles of Cr and Ni in corrosion layers grown on Fe-based steels

Fig. 6-5 shows the SEM top-views of three Fe-based steels after the exposures to the HTL environments at 310 °C, respectively. In the non-catalytic HTL environment, the steel experienced general oxidation, consistent with the theoretical predictions in Fig. 6-2. Besides that, localized nodular oxidation and corrosion particles deposition also occurred on them. Note that the deposition of dissolved corrosion particles likely occurred during the autoclave cooling-down as described in our previous study [376]. More importantly, increasing Cr and/or Ni contents in the steels seemed to lead to the formation of thinner surface scales with much smaller size of oxide particles. As shown in the figures, the oxide layers formed on SS316L and SS310 were much thinner than that formed on P91 since the grinding lines were still clearly visible on the two austenitic steels even after the 10 days' exposure into the hot water at 310 °C.

In the catalytic environment, the steels not only experienced oxidation, but also suffered noticeable chemical dissolution of the formed oxides, particularly the oxides grown on P91 steel with the lowest Cr content. Localized enhanced oxide dissolution also occurred on P91 steel. As predicted in Fig. 6-2, stable Fe and Cr oxides could not be formed in the catalytic HTL environment with pH = 11.2 and thus, would dissolve into the solution at a higher rate than those in the non-catalytic environments through the following hydrolysis reaction [490]:



where M represents the alloying element Fe or Cr. Note that except for oxide, thermodynamic calculations also suggested that hydroxides could possibly be formed on the steels via following two different routes:



Previous studies found that both Fe and Cr hydroxides would experience higher dissolution in basic solutions (pH ~ 9) at temperature > 100 °C comparing to their oxides [418, 491]. In addition, increasing Cr and/or Ni contents possibly led to the transformation of oxide shape from irregular and very fine lumps into flakes. Deposited particles were also present on the corroded steels.

As implied in the figure, the addition of inorganic and organic corrodants (S^{2-} , Cl^- and acetic acid) into the catalytic environment might result in a remarkable enhancement in the chemical dissolution of oxides and hydroxides formed on the steels although the addition of acetic acid and S^{2-} made the environmental pH drop to ~ 7.6 because of the following two different reactions:



The above observations were different from the predictions in Fig. 6-2, in which stable Cr/Fe oxide could be thermodynamically formed at the pH range of 7 - 8 and 310 °C. More severely, the introduction of these corrodants caused local damage of the oxide integrity and consequently led to the formation of micro-cracks and holes, which were particularly noticeable on the two austenitic steels (SS316L and SS310). Besides that, localized accumulation of organic compounds on the three steels were also found. A number of studies have shown that both Cl^- and S^{2-} anions

could interact with the cations (Fe^{3+} or Cr^{3+}) in the oxides to form dissolvable complexes due to their high affinity to the cations [192, 430, 431, 432]. Moreover, CH_3COO^- ions produced from the reaction (6-11) could also interact with metal cations (M^{n+}) in the oxide to form dissolvable metal acetate based on previous studies [492]:



The above factors could make the steels suffer the severest damage among all the testing conditions, as shown in Figs. 6-4 and 6-5.

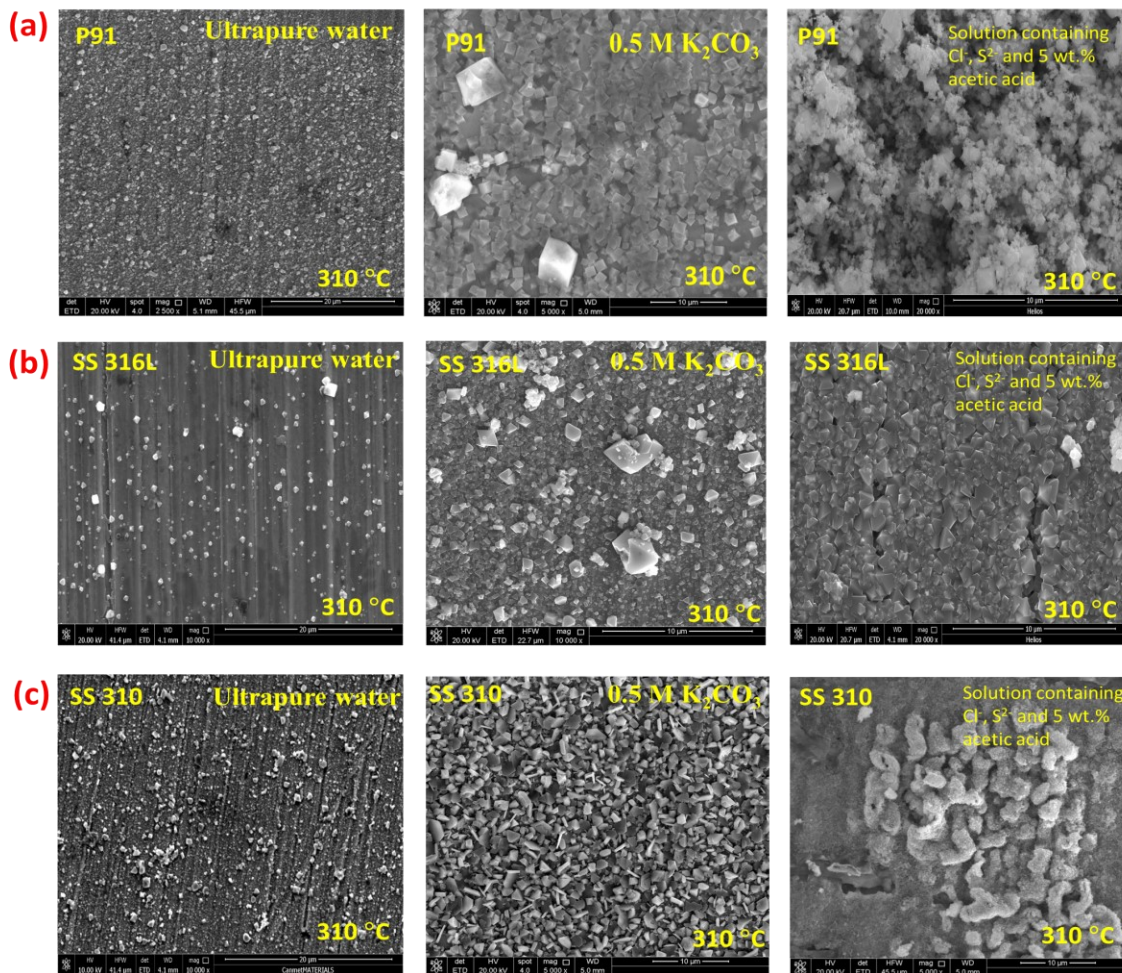


Fig. 6-5. SEM top-views of (a) P91, (b) SS16L and (c) SS16 samples after corroding in non-catalytic and catalytic HTL environments 310 °C.

Since the corrosion layers formed on P91 samples were quite thick, XRD characterizations were used for their phase composition characterizations, and the results are shown in Fig. 6-6. After the exposures to the non-catalytic and catalytic HTL environments, the formed corrosion layers were mainly consisting of Fe_3O_4 and $\text{Fe}_{3-x}\text{Cr}_x\text{O}_4$ compounds. The introduction of 0.5 M K_2CO_3 catalyst and/or the addition of the corrodants (Cl^- , S^{2-} and acetic acid) unlikely affected the phase composition of the layers. For the samples corroded in the catalytic HTL environments, the disappearance of ferrite peaks implied the formation of thicker layers than that formed in the non-catalytic HTL solution. More importantly, the results clearly indicated that protective Cr-enriched oxides and hydroxide could not be grown on the Fe-based steels with Cr content $< 9\%$ in the HTL environments, even though their formation would be thermodynamically feasible as predicted in Fig. 6-2, i.e. negative Gibbs free energy of oxidation reactions.

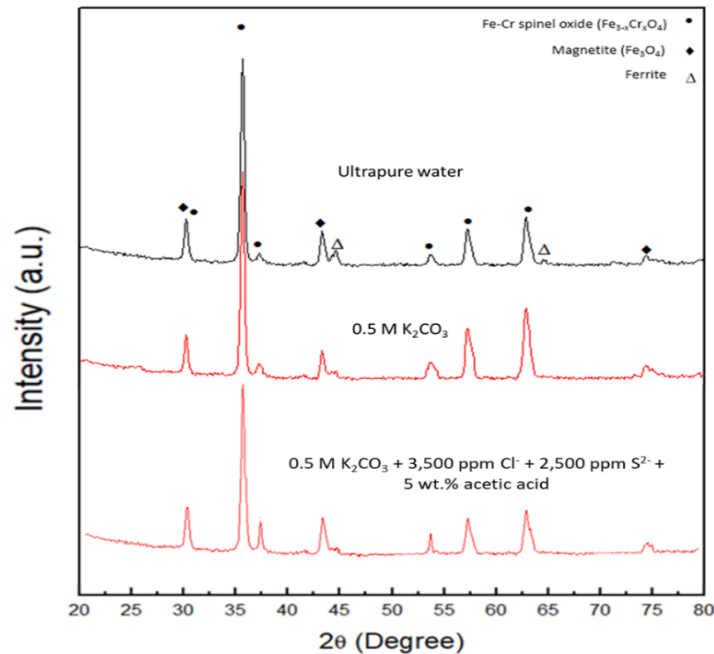


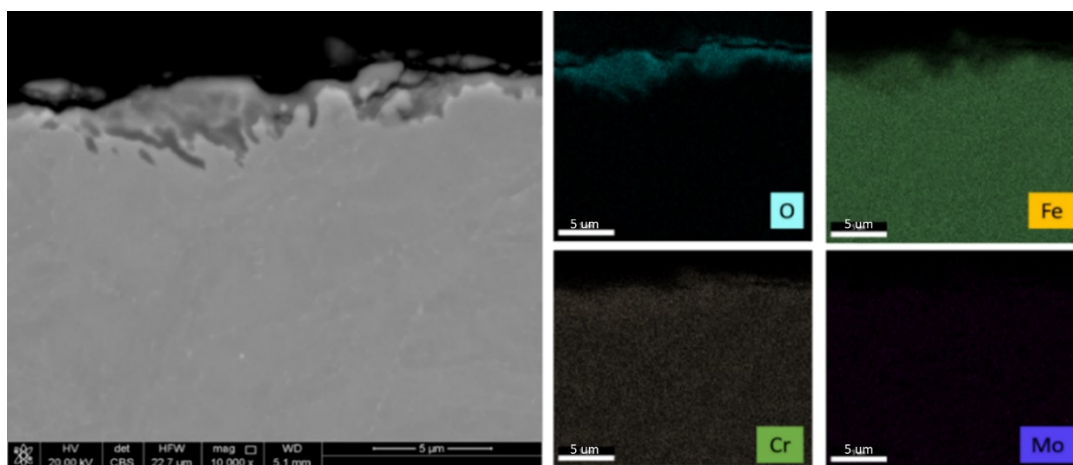
Fig. 6-6. XRD spectra collected on P91 samples after corroding in non-catalytic and catalytic HTL environments at 310 °C, respectively.

To further examine the microstructure and chemistry of the oxides formed on corroded P91 steels, cross-sectional samples were produced using diamond saw cutting technique, and the corresponding SEM/EDS elemental mapping results are shown in Fig. 6-7. Note that because of the thickness difference of the corrosion layers formed in different HTL environments, the SEM

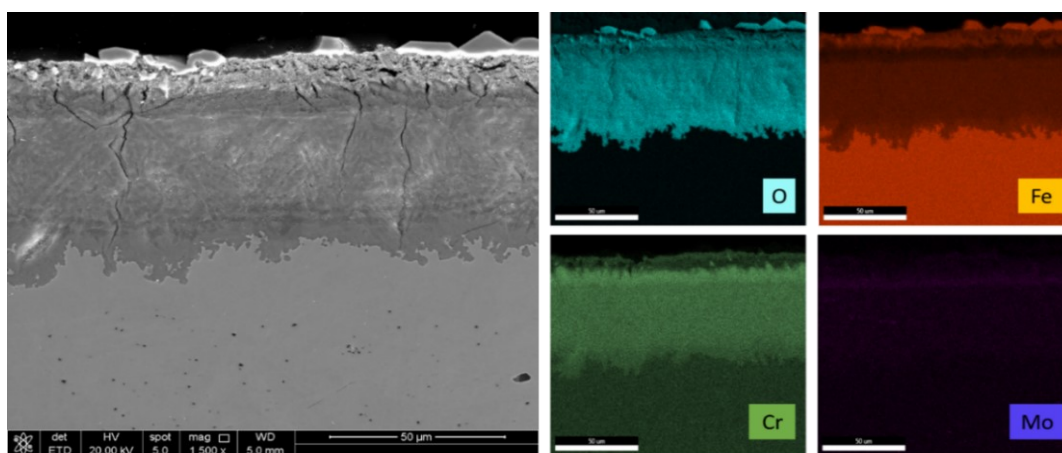
images were provided here with different resolution scales for clearer presentation. The thickness of corrosion layer was dramatically increased with the introduction of 0.5 M K_2CO_3 catalyst, and further thickened with the addition of the corrodants into the catalytic HTL environment. Except for the thickness, the microstructure and chemistry of the layers were also found to vary with the testing environmental chemistry:

- (1) In the non-catalytic HTL environment, the formed corrosion layer was a single-layer structure and mainly composed of Fe and O along with some Cr cations, consistent with the XRD results. Deposition particles were randomly distributed above the layer.
- (2) In the catalytic HTL environment, the layer was a three-layers structure, including outer porous Fe-enriched oxides with Cr cations, middle Cr-enriched oxide with Fe and trace amount of Mo cations, and finally the inner Fe-enriched oxides with Cr and limited amount of Mo cations. At the interface of middle and inner layers, the accumulation of Mo was observed. As the bulk content of Mo in the steel is only about 0.9 wt%, the accumulation of Mo suggests that the formed corrosion layer would be poorly protective to prevent the outward diffusion of Mo from the substrate. Moreover, combined with the result in Fig. 6-6, the total amount of Mo cations in the corrosion layer would be expected to be small. In addition, micro-cracks and holes were formed within the corrosion layer.
- (3) In the catalytic HTL environment containing inorganic corrodants and acetic acid, the formed layer was a two-layer structure, including a very thin outer layer composed of Fe and O, and a quite thick inner layer consisted of Fe/Cr oxides as well as trace amount of S. Moreover, the small cracks were surprisingly present at the interface of corrosion layer and substrate after exposure. The formation of these cracks might be due to the internal stress enhanced with the formation of thick corrosion layer, or the poor adhesion of corrosion layer with the substrate.

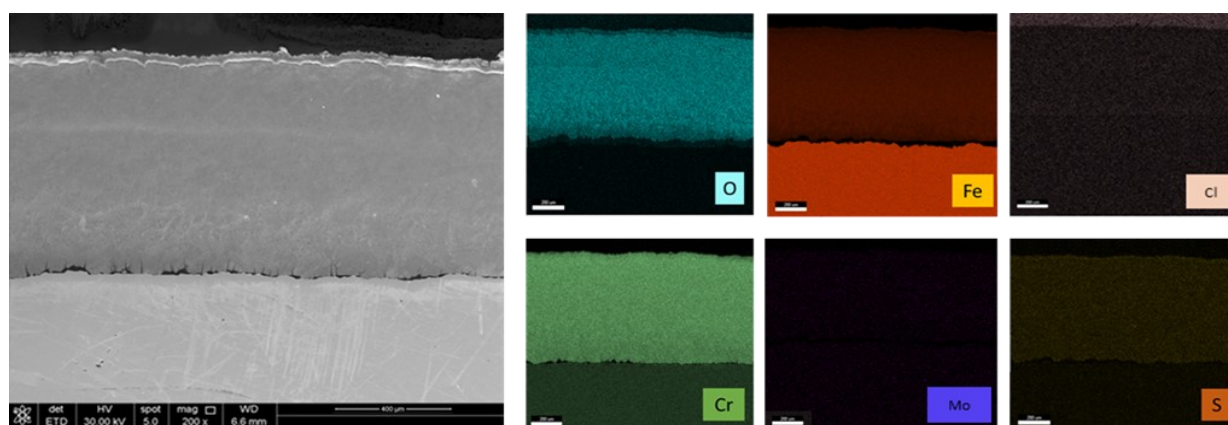
The above observations generally agree with the corrosion rate results shown in Fig. 6-4(a). The introduction of catalysts and/or corrodants apparently changed the oxide formation/growth processes and led to the formation of microcracks which could act as “windows” for the inward diffusion of corrosive anions during the exposures.



(a) in non-catalytic HTL environment



(b) in catalytic HTL environment



(c) in catalytic HTL environment with 3500 ppm Cl^- , 2500 ppm S^{2-} and 5 wt.% acetic acid

Fig. 6-7. SEM cross-sectional images and corresponding EDS elemental mappings of P91 samples after corroding in different HTL environments at 310 °C.

Different from P91 steel, the corrosion layers formed on SS310 and SS316L were expected to be thinner due to their higher Cr and/or Ni contents. FIB and TEM techniques were thus applied for the cross-sectional characterizations, and the results are shown in Fig. 6-8. Following major findings are obtained:

- (1) In the non-catalytic HTL environment, the surface scales formed on both SS316L and SS310 were only a single-layer structure composed of Cr-enriched oxide with limited amount of Fe cations. The thicknesses of the layers on the steels were around 40-50 nm, suggesting that increasing Cr content in the steels from 16% to 24% would only have marginal influence on the formation of Cr oxide. Above the Cr oxide layer, deposition particles and local nodular oxides, which were mainly composed of Fe oxides, were present on SS316L, instead of Fe/Ni oxides on SS310. At the interface between oxide layer and substrate, the accumulation of Ni was found. As mentioned above, Ni would be thermodynamically unfavorable to form oxides and the mitigation of Ni within the Cr oxide would be slow based on previous studies [356, 493], consequently leading to the Ni accumulation at the interface. Based on the results in Figs. 6-4, 6-7 and 6-8, it could be generally concluded that increasing Cr content in Fe-based steels would lead to the transformation of Fe-enriched oxide to Cr-enriched oxide, and a protective and compact Cr-enriched oxide layer could be formed on the steels with Cr content > 16 wt.% in the non-catalytic HTL environment. Note that the chemical dissolution of Cr oxide would be much less than that of Fe oxide in high temperature aqueous solutions based on previous studies [335, 413].
- (2) After the exposure to the catalytic HTL environment, the scale formed on SS316L became a double-layer structure, which consisted of thin outer Fe/Ni oxides (about 100 nm thick) and inner Cr-enriched oxides with Fe/Ni cations (around 350 nm thick). Different from SS316L, the scale grown on Cr-bearing SS310 was composed of outer porous Fe/Cr/Ni oxides and a more compact and thicker Cr-enriched oxide (about 750 nm) with trace amounts of Fe/Ni cations. Moreover, the accumulation of Ni cations was observed at the interface of oxide and substrate only on SS316L. Based on the results in Figs. 6-4 and 6-8, it was likely that increasing Cr content in the austenitic stainless steels could enhance the formation of an inner protective Cr-enriched oxide layer. The results also implied that increasing the content of Fe/Ni cations in the Cr-enriched oxides might result in a high chemical dissolution of the

oxides in the catalytic HTL environment. Otherwise, the accumulation of Ni layer would occur on SS310 with higher Ni content (21.8 wt.%), instead of on SS316L. As indicated in Fig. 6-8, increasing Ni content in the steels was unlikely to lead to an improved corrosion resistance as the inner Cr-enriched oxide layer would be the key barrier to resist the attack from the hot catalytic HTL environment. In addition, it is unclear about the difference of outer oxide layers formed on the two steels as the layer might be formed during the exposure and/or the deposition of corrosive particles during autoclave cooling-down. One possible reason is that Cr/Fe/Ni oxides might have lower dissolution rates than Fe/Ni oxides in the catalytic environment at 310 °C based on the former studies [215, 417, 494-497]. In general, based on the results in Figs. 6-4, 6-7 and 6-8, the Fe-based steel with Cr content > 16 wt.% could have acceptable corrosion performance due to the formation of inner Cr-enriched oxide layer in the catalytic HTL environment.

- (3) As shown in Fig. 6-8(c), the addition of 3500 ppm Cl⁻, 2500 ppm S²⁻ and 5 wt.% acetic acid into the catalytic HTL environment resulted in a remarkable change of the oxide scales formed on the two steels, which were more porous comparing to those formed in the non-catalytic and catalytic HTL environments. The scale formed on SS316L was a single Cr/Fe/Ni oxide layer with the average thickness of ~ 400 nm. Localized accumulation of Ni cations was found near the interface of the oxide/substrate. Different from SS316L, an inner Cr-enriched oxide layer (about 550 nm thick) with Ni/Fe cation was grown on SS310, suggesting that increasing Cr content up to 24 wt.% could improve the formation of protective Cr oxides even in the catalytic HTL conversion of biowastes. Previous studies found that there would be a critical Cr content (about 20%) in Fe-based steels, above which a protective Cr-enriched oxide layer could form in high temperature systems [498, 499, 500]. Compared with that formed in the above catalytic HTL environment, the enhanced contents of Fe and Ni cations in the layer implied that the chemical dissolution of Cr oxides would be accelerated with the addition of Cl⁻, S²⁻ and acetic acid, consequently leading to the high outward diffusion rates of Fe and Ni cations within the layer. Besides that, the outer layer formed on SS310 still consisted of Cr/Ni/Fe oxides, but was more porous, thinner and less content of Fe cations, implying that the addition of Cl⁻, S²⁻ and acetic acid could lead to a higher dissolution rate of Cr/Fe/Ni oxides in the catalytic HTL environment. In addition, based on the results in Figs. 6-4 and 6-8, increasing Ni content in the steels led to the

formation of more Ni oxides, but unlikely result in a remarkable improvement of corrosion resistance as the inner Cr-enriched oxide layer would still be the critical protective barrier in the environment.

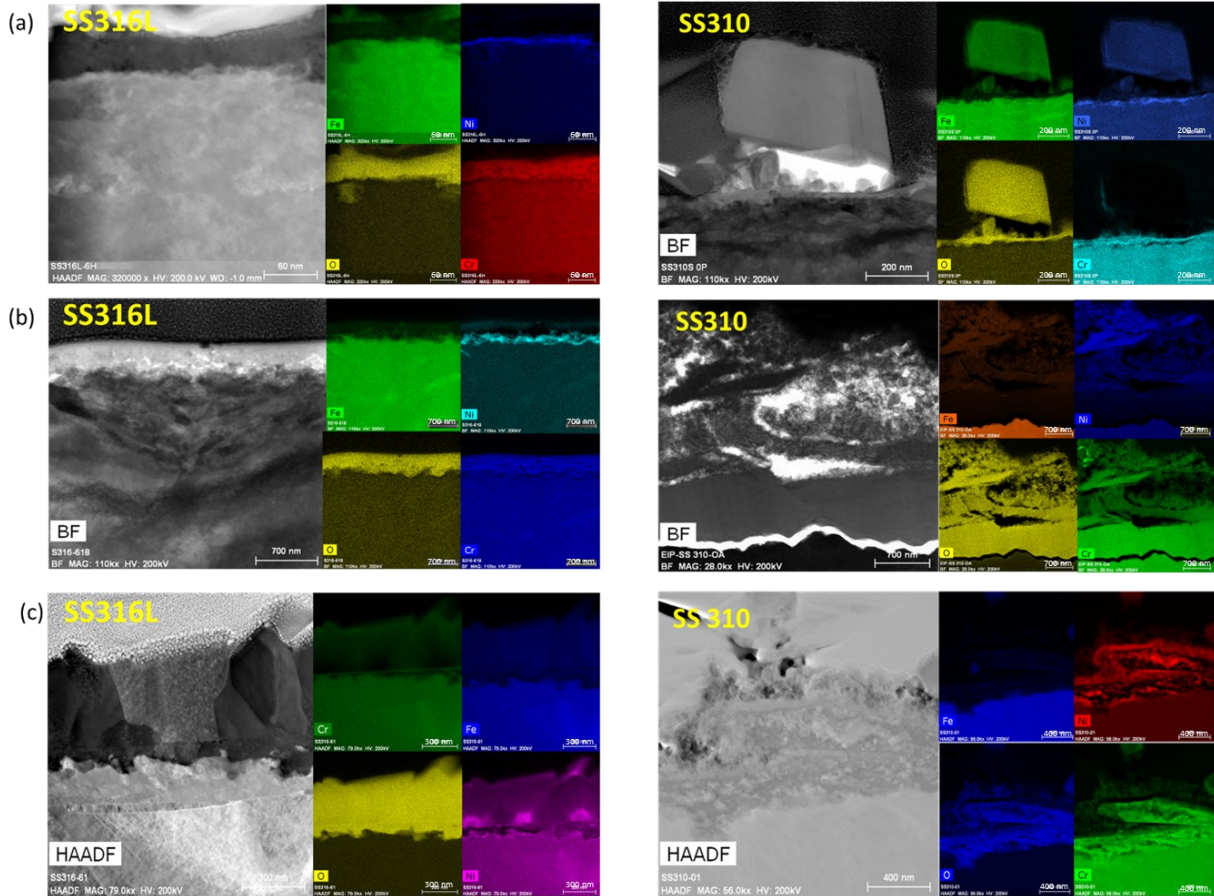


Fig. 6-8. TEM Black-field (BF) and HAADF images with corresponding EDS elemental mapping collected on SS316L and SS310 samples after the exposures to (a) ultrapure water; (b) 0.5 M K_2CO_3 ; and (c) 0.5 M K_2CO_3 + 3500 ppm Cl^- + 2500 ppm S^{2-} + 5 wt.% acetic acid at 310 °C for 10 days, respectively.

6.4.3.2. Roles of Ni and Mo in corrosion layers formed on the alloys with medium Cr content

To explore the roles of Ni and Mo in the alloys with medium Cr content (~ 16 wt.%), the corrosion performance of Alloy C-276 was investigated in the non-catalytic and catalytic HTL environments,

and the SEM top-view and FIB/TEM cross-section examinations of Alloy C-276 samples results after the exposures are shown in Figs. 6-9. and 6-10, respectively. Compared with SS316L, the following observations are made:

- (1) In the non-catalytic HTL environment, Alloy C-276 experienced general oxidation accompanied with local nodular oxidation and corrosive particles deposition, similar to those formed on SS316L. The TEM cross-sectional examinations further revealed that the surface scale grown on Alloy C-276 was a two-layer structure, including outer Ni-enriched oxides (~60 nm thick) and inner Cr-enriched oxides with Ni cations and a trace amount of Fe cations (~50 nm). The formation of outer Ni-enriched layer on the alloy was noticeably different from that of SS316L, indicating that increasing Ni content could promote the formation of outer Ni-enriched oxide and/or hydroxide layer. As mentioned above, the formation of NiO in the non-catalytic HTL environment should be thermodynamically unfavorable. However, the formation of Ni(OH)₂ might be possible due to the negative Gibbs formation energy (~ -2.04 KJ/mol) of the reaction (Ni+2H₂O=Ni(OH)₂+H₂) in 310 °C water. Previous studies also found that the Ni(OH)₂ layer was formed above a Cr-enriched oxide layer on Alloy 600 in pressurized water reactor environments at the temperature range of 325 - 350 °C [501, 502, 503]. In addition, the role of Mo is another concern. The EDS elemental mapping results (see Fig. 6-10) suggested that Mo unlikely contributed to the formation of oxide layer as only trace amount of Mo cations was present at the interface of oxide/substrate. Based on the results in Figs. 6-4 and 6-10, it thus could be concluded that increasing Ni content in the alloys with medium Cr content could cause the formation of an outer Ni-enriched hydroxide layer, which might provide protection to the underlying Cr-enriched oxide layer in the non-catalytic HTL environment.
- (2) In the catalytic HTL environment, Alloy C-276 also experienced general oxidation as well as nodular oxidation. Compared with SS316L, the nodular oxides formed on Alloy C-276 were smaller, and the surface oxide scale seemed to be thinner since the grinding lines were still observable on Alloy C-276 but disappeared on SS316L. TEM cross-sectional characterization results indicated that different from the corrosion product (double-layer structure) formed on SS316L, the layer grown on Alloy C-276 was a single Cr-enriched oxide layer (~ 400 nm thick) with Ni cations in which the Ni²⁺ ions were mainly distributed

close to the interface of oxide/substrate. Another noticeable difference was that the amount of Fe cations in the layer on Alloy C-276 was noticeably less than that in the oxides on SS316L, suggesting the formation of a better layer with less unstable cations on Alloy C-276 with low Fe content. Moreover, as predicted in Fig. 6-2, both stable NiO and dissolvable iron hydroxide complexes could be formed in the environment. Increasing Ni to replace Fe in this type of alloy could also lead to lower chemical dissolution rates of the formed oxides in the environment. In addition, Mo cations were barely found in oxide layers formed on Alloy C-276, indicating the negligible influence of Mo content on corrosion in the catalytic HTL solution.

- (3) In the catalytic HTL environment with inorganic corrodants and acetic acid, a thicker layer was grown on Alloy C-276 compared to those formed in the above two HTL environments. The formed oxides were noticeably smaller than that grown on SS316L. More importantly, micro-cracks were not present on Alloy C-276, suggesting the much better integrity of the formed layer. TEM Cross-sectional and EDS mapping results showed that the formed oxide scale on Alloy C-276 was a single Cr-enriched oxides layer (~ 350 nm thick) with trace amounts of Ni and Fe cations. Different from SS316L, localized accumulation of Ni particles instead of Ni oxides was found within the formed oxide layer, which might be caused by high Ni content in the alloys and/or the difference among the formation and dissolution rates of Cr, Ni and Fe oxides in the environments. Moreover, nodular Cr-rich oxides were present above the oxide layer, possibly due to the fact that Cr cations have higher outward diffusion than that of Ni and Fe in the Cr-enriched oxide layer. Furthermore, few Mo cations were detected within the oxide layer, suggesting the marginal role of Mo in providing the corrosion resistance of alloys in the catalytic HTL conversion of biowastes. Therefore, increasing Ni concentration to partially replace Fe in the alloys would support the formation of a Cr-enriched oxide layer and consequently result in a better corrosion resistance.

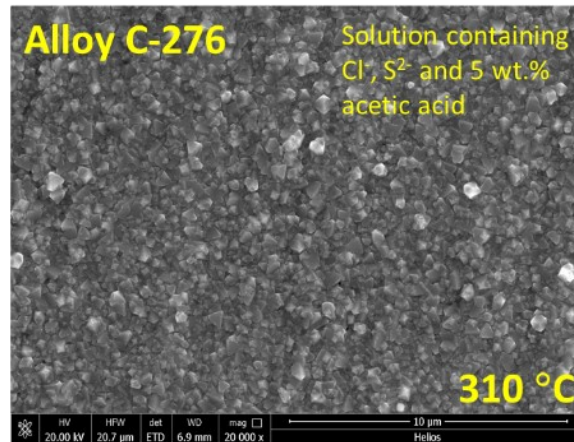
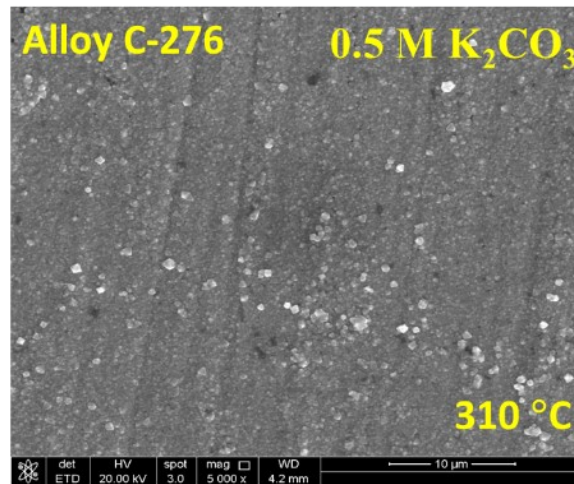


Fig. 6-9. SEM top-view images of Alloy C-276 after corroding in ultrapure water, 0.5 M K₂CO₃, and 0.5 M K₂CO₃ + 3500 ppm Cl⁻ + 2500 ppm S²⁻ + 5 wt.% acetic acid at 310 °C for 10 days, respectively.

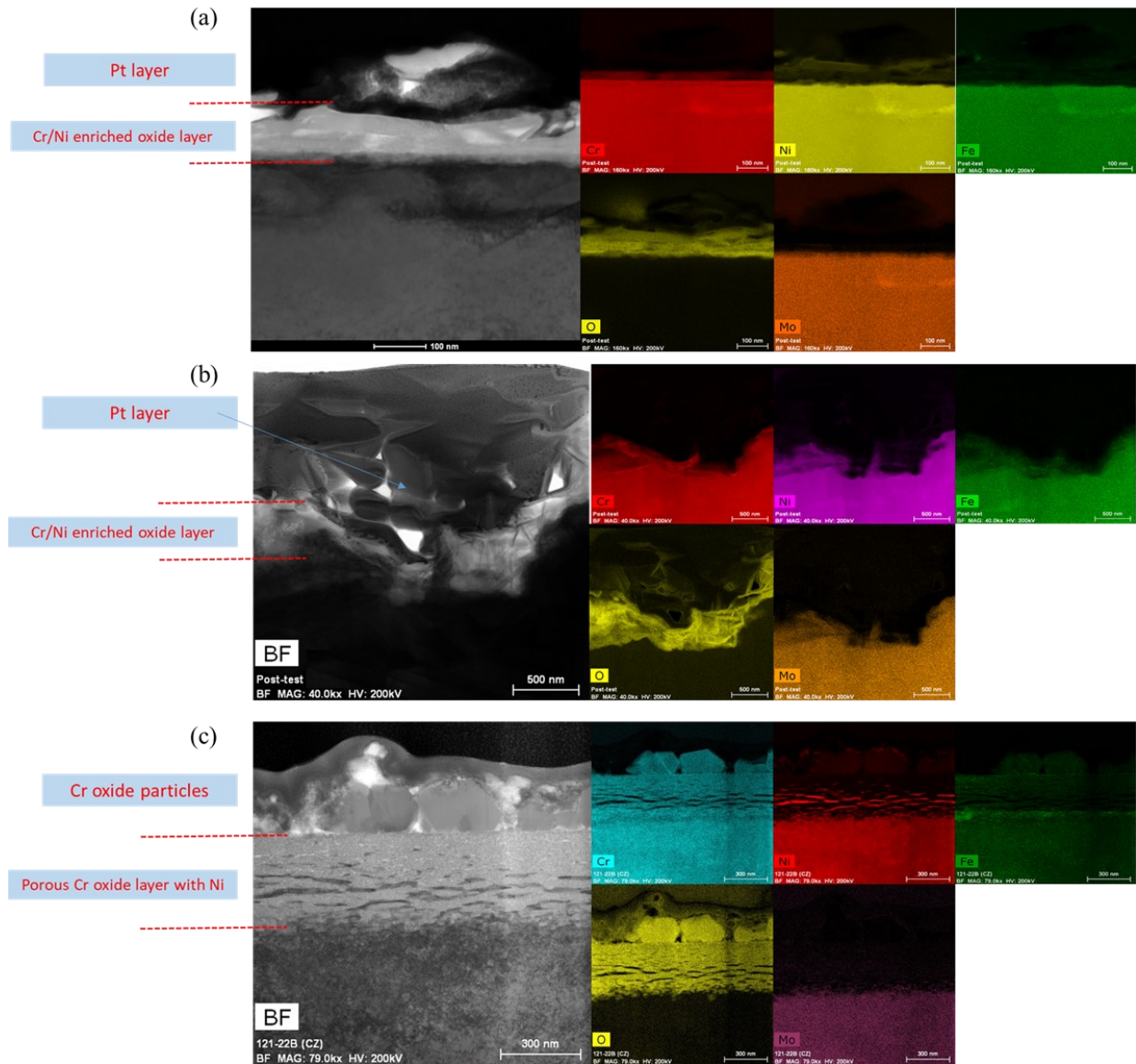


Fig. 6-10. Bright-field (BF) images and corresponding EDS elemental mapping on Alloy C-276 after exposing in (a) ultrapure water; (b) 0.5 M K_2CO_3 ; and (c) 0.5 M K_2CO_3 + 3500 ppm Cl^- + 2500 ppm S^{2-} + 5 wt.% acetic acid at 310 °C for 10 days, respectively.

6.4.3.3. Roles of Ni and Mo in corrosion layers formed on high Cr content alloys

As described above, SEM/FIB and TEM techniques were also applied for examining the corroded Alloy 625 samples after the exposures, followed by the comparison with corroded SS310 samples to explore the roles of Ni and Mo in the corrosion process of high Cr content alloys in the HTL

environments. Based on the images shown in Figs. 6-5, 6-8, 6-11 and 6-12, the following results are obtained:

- (1) In the non-catalytic HTL environment, a very thin and compact oxide layer was formed on the two alloys. Compared with SS310, less nodular oxides and deposit particles were present on Alloy 625. TEM cross-sectional characterizations indicated the single oxide layer formed on Alloy 625 was Cr-enriched with Ni and Mo cations, above which the nodular oxide was composed of Cr/Ni/Mo oxide. The average thickness of Cr-enriched oxide layer was around 75 nm, slightly thicker than that on SS310. Different from SS310, the accumulation of Ni at the oxide/substrate interface was not found on Alloy 625 with much higher Ni content (64 wt.%), implying that the outward diffusion of Ni cations in the Cr-enriched oxide layer grown on Alloy 625 could be higher than that in the oxide layer on SS310. The results in Figs. 6-4, 6-11 and 6-12 suggested that increasing Ni and Mo concentrations in Cr-bearing alloys could improve their resistance to the non-catalytic HTL environment. One possible explanation is that increasing Ni content to replace Fe would likely reduce chemical dissolution of the formed oxides. Another possible reason is that the presence of Mo cations might improve the stability of the formed Cr-rich oxide film as mentioned in Section 6.4.2.1.
- (2) After being corroded in the catalytic HTL environment, Alloy 625 had very fine needle-shaped oxide particles grown on it, while larger flake-shaped particles were present on SS310. TEM cross-section characterizations showed the scale formed on Alloy 625 was a triple-layer structure, including outer porous Cr/Mo oxides/oxide particles (~ 50 nm thick), middle Cr/Mo oxides (~ 310 nm thick), and inner Cr-enriched oxides (~240 nm thick on average), significantly different from that on SS310. Based on the results in Figs. 6-4, 6-8 and 6-12, it was likely that increasing Mo content in Cr-bearing alloys would lead to the formation of a protective Cr/Mo layer and consequently mitigate corrosion damage in the catalytic HTL environment. As predicted in Fig. 6-2, Mo oxides could be formed in this environment at 310 °C. Thus, the above results further suggested that the Cr/Mo oxides would be more stable than Fe/Cr/Ni oxides since the middle Cr/Mo oxide layer was compact and continuous instead of being porous. The SAD patterns (see Fig. 6-13) collected on the middle and inner oxide layers showed that the two layers were of polycrystalline/amorphous structure. In addition, although Alloy 625 had much higher Ni content than SS310, the

absence of considerable Ni cations in the surface scale was observed. This may be due to the fact that: (1) the formed middle Cr/Mo and inner Cr-rich oxide layers could efficiently hinder the outward diffusion of Ni cations and consequently make them accumulating at the interface of oxide/substrate; and/or (2) Ni oxide would have higher chemical dissolution rate than Cr and Mo oxides, making most of the formed Ni cations (small and even trace amount) directly dissolve into the solution during the exposure. Thus, increasing Ni to replace Fe in high Cr content alloys might improve corrosion resistance, but could be less remarkable than that induced by the addition of Mo.

- (3) In the catalytic HTL environment with Cl^- , S^{2-} and acetic acid, localized dissolution and/or spalling of formed oxides on Alloy 625 was observed, but it was much less severe than that occur on SS310. Different from SS310, localized accumulation of organic compounds was not found on Alloy 625, implying the former oxide layer would have lower chemical affinity to the organic matter. TEM cross-sectional examinations revealed that the scale formed on Alloy 625 was only a single Cr oxide layer (about 200 nm thick) with trace amounts of Mo and Ni cations, significantly different from the corrosion layer grown on SS310 (see Fig. 6-8). The morphology of the interface of oxide/solution suggested that the scale on Alloy 625 would experience considerable chemical dissolution during the exposure. Compared to the oxide formed in 0.5 M K_2CO_3 , it was very likely that the presence of Cl^- , S^{2-} and acetic acid could enhance the chemical dissolution of Mo cations and consequently damage the integrity of Cr/Mo oxide layer, which might be due to the high affinity of these corrodants to Mo cation to form dissolvable complexes based on previous investigations [504-506]. Based on the results in Figs. 6-4, 6-8 and 6-12, increasing Mo and Ni concentrations to replace Fe in high Cr content alloys could probably reduce the chemical dissolution of the formed oxides and lead to the formation of a more compact and protective Cr-rich oxide layer with much less defects and voids.

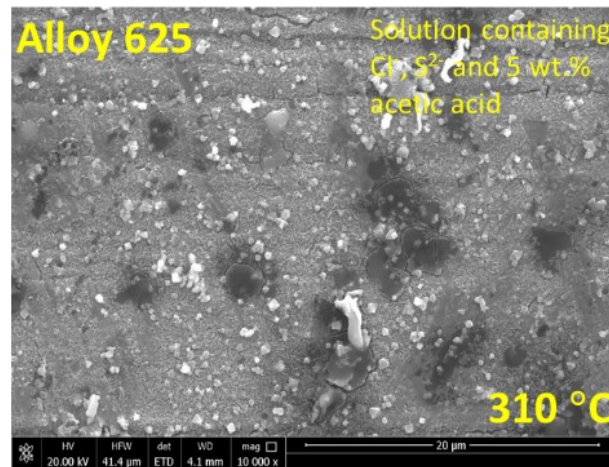
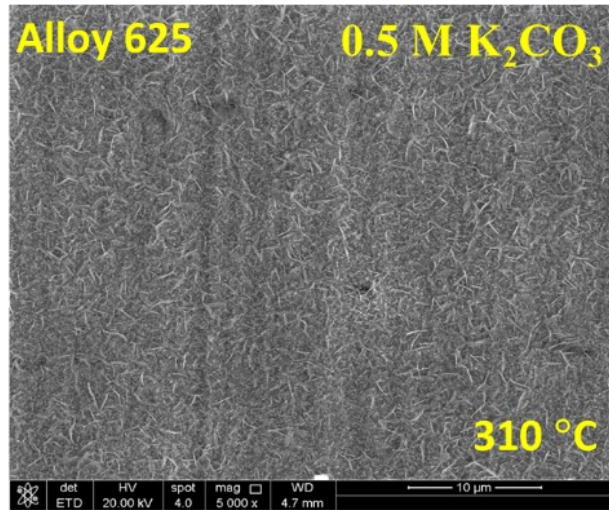
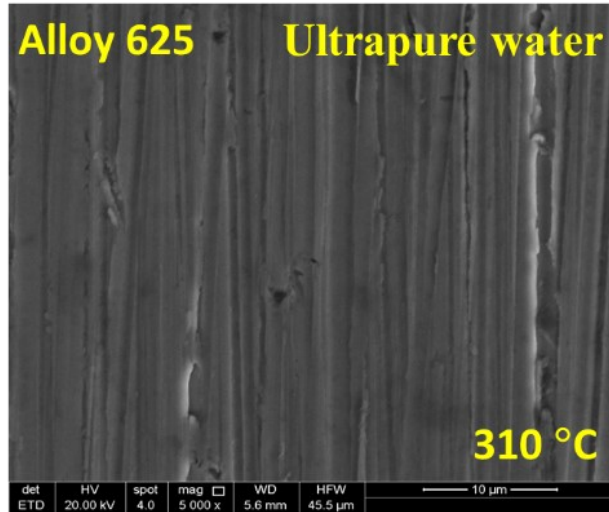


Fig. 6-11. SEM top-view images of Alloy 625 after corroding in ultrapure water, 0.5 M K₂CO₃, and 0.5 M K₂CO₃ + 3500 ppm Cl⁻ + 2500 ppm S²⁻ + 5 wt.% acetic acid at 310 °C for 10 days, respectively.

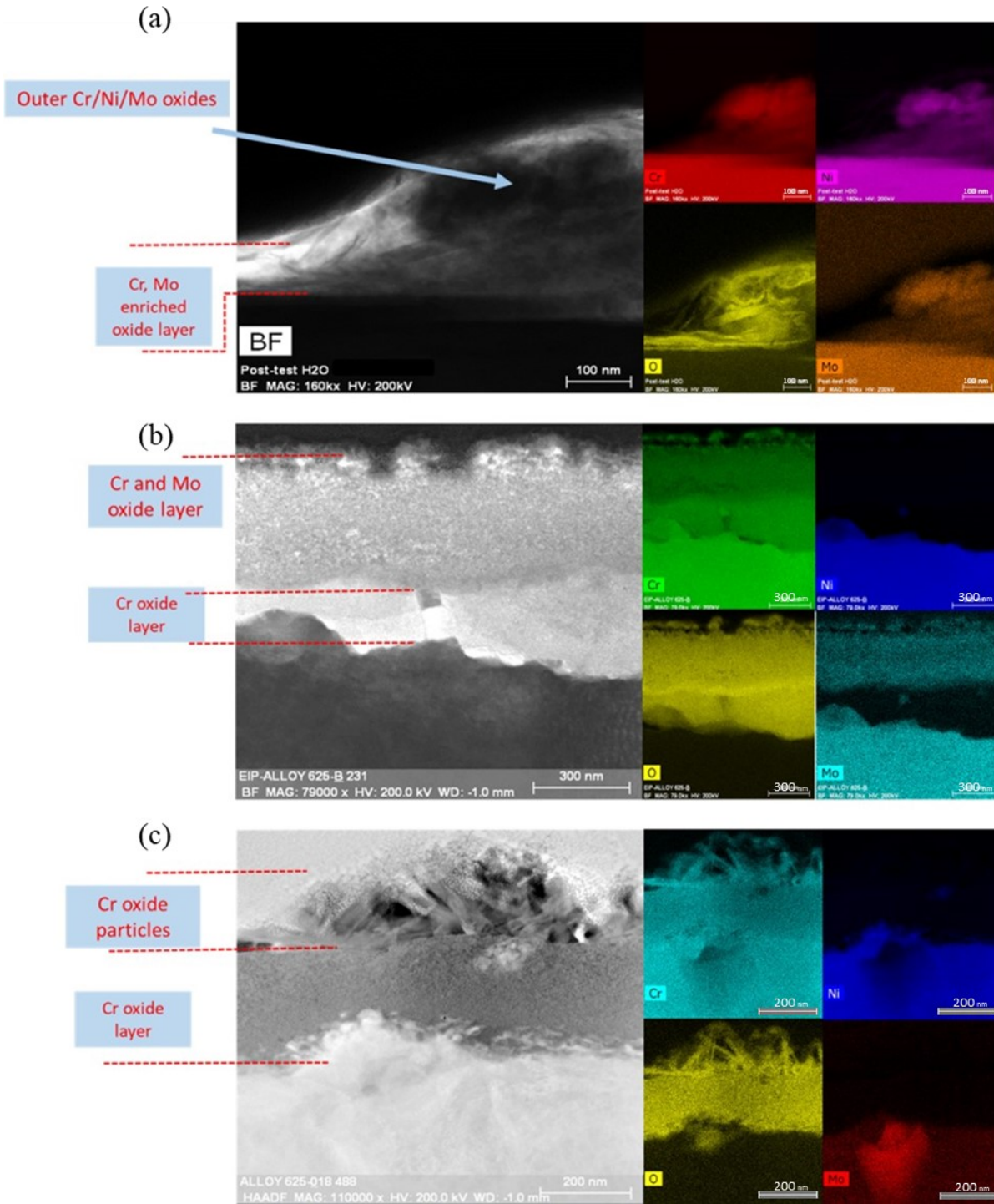


Fig. 6-12. Black-field (BF) and HADDF images with corresponding EDS elemental mappings on Alloy 625 after exposing in (a) ultrapure water; (b) 0.5 M K_2CO_3 ; and (c) 0.5 M K_2CO_3 + 3500 ppm Cl^- + 2500 ppm S^{2-} + 5 wt.% acetic acid at 310 °C for 10 days, respectively.

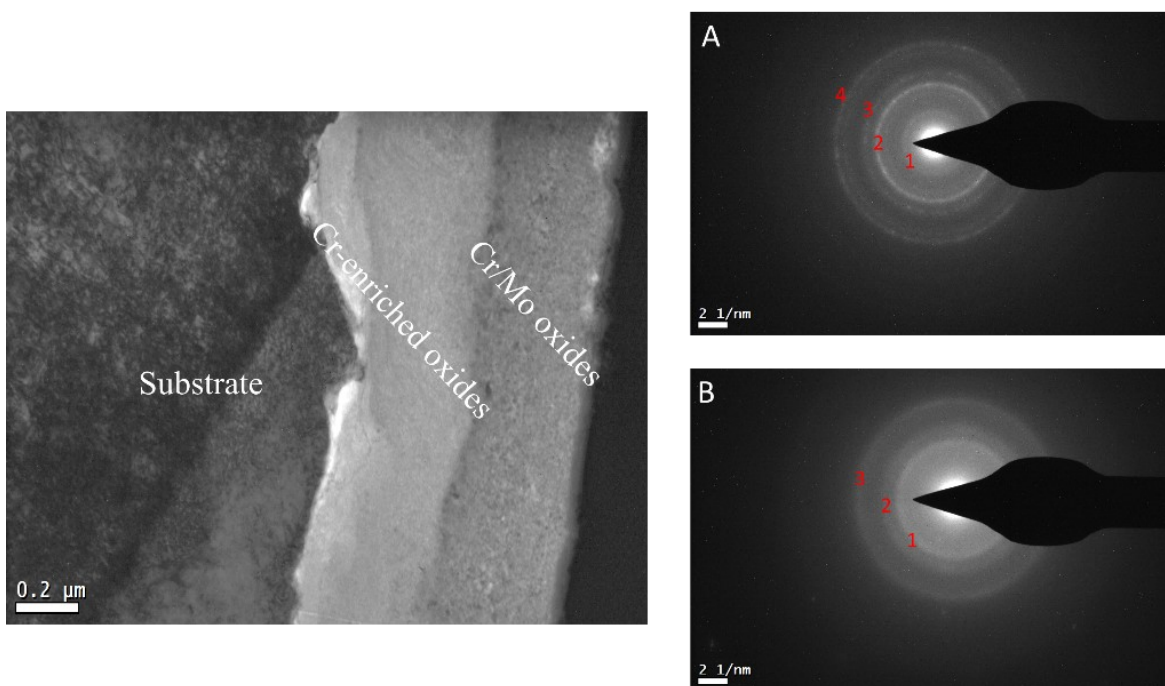


Fig. 6-13. BF image of Alloy 625 exposed in 0.5 M K_2CO_3 solution and selected area diffraction (SAD) obtained from different oxide layers.

6.4.3.4. Role of Mo in Ni-based alloys

As stated above, Ni-based alloys are important candidates for the construction of HTL reactors. The results in Figs. 6-4, 6-10 and 6-12 suggested that the influence of Mo on corrosion would be coherently related to Cr content that was present in the alloys, practically in the catalytic HTL environments. After the exposure to the catalytic HTL environment without inorganic and organic corrodants, a Cr/Mo oxide layer was formed on Alloy 625 instead of on Alloy C-276 even though Alloy C-276 had much higher bulk Mo content. One possible explanation is that the alloy with higher Cr concentration would form a more compact Cr-enriched oxide layer with less defects, which could be further improved with the addition of Mo cations. In the non-catalytic HTL environment, the formation of an outer $Ni(OH)_2$ layer on Alloy C-276 suggested that the Cr oxide layer on Alloy 625 would be much more protective and compact than that grown on Alloy C-276. Moreover, a previous study proposed that the presence of Mo cations in Cr_2O_3 would reduce cation vacancies within the layer grown on Ni-based alloys during high temperature oxidation [279]. Due to the existence of higher Cr content in Alloy 625, Mo cations produced at the interface of

oxide/substrate would likely be trapped within the Cr oxides to improve their integrity instead of diffusing through them and then directly dissolving into the catalytic HTL solution. With the addition of inorganic corrodants and organic acid to the solution, the presence of Mo cations was not found on the layers formed on the two alloys, suggesting that Cr would be the dominant alloying element on their corrosion. In general, there is likely a critical Cr content above which the improvement effect of Mo on corrosion became noticeable under the HTL conversion conditions.

6.5. Conclusions

This study investigated the roles of major alloying elements (Cr, Ni, Mo, and Fe) in corrosion process under typical HTL conversion conditions via thermodynamic calculation and high temperature corrosion testing. The following conclusions can be made:

- (1) High temperature Pourbaix diagrams of alloying elements have been constructed. At temperatures ≤ 310 °C, Cr, Ni and Mo would experience passivation in non-catalytic HTL environment, but suffer active corrosion under catalytic HTL conditions. Increasing temperature could expand their passivation region. Different from them, Fe would likely experience general oxidation or active corrosion, depending on HTL temperature and pH value.
- (2) Under the HTL conditions, the corrosion resistances of five candidate alloys with different alloying element contents have been ranked as follows:

$$P91 \ll SS316L < SS310 < \text{Alloy C-276} < \text{Alloy 625}$$

Their corrosion rates increase with the addition of catalyst, Cl^- , S^{2-} and acetic acid into the HTL solution.

- (3) For Fe-based steels, the Cr content should be above 16% in order to form protective surface scale and consequently achieve acceptable corrosion performance. Increasing Ni content in the steel unlikely leads to remarkable improvement of their corrosion resistance.
- (4) For the alloys with medium Cr content (~ 16 wt.%) alloys, increasing Ni to replace Fe can facilitate the formation of more compact Cr-enriched oxide layer. Increasing Mo only has marginal effect on their corrosion resistance.
- (5) For Cr-bearing alloys (Cr content > 22 wt.%), increasing Mo content supports the formation of protective and compact oxide layer and consequently leads to a noticeable

- improvement on their performance. The improvement effect of Ni is much less than Mo.
- (6) For Ni-based alloys, there is a critical Cr content, above which increasing Mo content results in the formation of the more stable and compact surface scales.

Chapter 7. Stress Corrosion Cracking Susceptibility of Candidate Reactor Alloys under Catalytic Hydrothermal Liquefaction Conditions

Following the autoclave tests of candidate materials under representative HTL conversion conditions, SS310 and SS316L showed acceptable corrosion rates and thus will be further examined with external stress to evaluate their SCC susceptibility. I have carried out autoclave tests on samples under different strain levels (0.45 % / 0.55 % and 3.3 %, respectively) by using constant strain and U-bending methods. The results indicating that SCC was absent on both steels, while the corrosion of steels became more severe with the increased strain deformation. Several explanations were proposed that may lead to the absence of SCC and more investigations would be required to further assess the SCC susceptibility of candidate materials in representative HTL environments.

7.1. Introduction

Over the past decades, continuous growth in global population and economy prosperity along with serious environmental degradation have caused a significant increase in the demand of clean and renewable energy to meet our daily needs in a cost-acceptable manner [507, 508]. Among all the promising renewable energy resources, biomass materials, such as wood, agricultural or industrial wastes, and specially engineered microalgae, are seen as the greatest emerging candidates [509, 510]. However, the natural conversion of these biomass feedstocks into useable bioenergy production is really time-consuming. As alternative energy sources, they need to be quickly converted to value-added bio-oils and other bio-chemicals through either biochemical or thermochemical conversion pathways. In recent years, hydrothermal liquefaction (HTL) has been developed as an attractive method due to the following prominent advantages: (1) eliminating the costly dewatering and drying pre-treatment operations; (2) achieving high carbon efficiency to produce the oil yields with higher heating value (HHV) compared to pyrolysis oils; and (3) directly applying for the direct conversion of wet industrial by-products and municipal biowastes [73-77, 381, 382, 511]. As described in previous chapters, a typical HTL process uses hot pressurized water as the reaction medium with the addition of catalysts (such as K_2CO_3) to achieve the most optimum yields [76, 78- 80, 82, 83, 86-94]. Depending on the properties of biomass feedstocks,

certain amounts of inorganic and organic corrodants (such as Cl^- , S^{2-} , and organic acids) will be released during the conversion [159, 162-164]. For instance, the amounts of chloride and sulfide ions can be up to about 15,000 and 13,200 ppm during the HTL conversion of bio-wastes feedstocks (such as black liquor) [165-167].

Due to the high corrosivity of HTL environments, corrosion performance of candidate alloys of construction must be well addressed to avoid significant capital loss. However, very limited information is available to describe the corrosion of HTL conversion reactor alloys even though several pilot-scale plants are currently in operations around the world [512, 513]. In fact, understanding the corrosivity of HTL processes is a paramount for the cost-effective materials selection of the required conversion equipment and will likely be feedstock-specific given myriad of bio-products that can form during the conversion [389]. As shown in the former chapters, austenitic stainless steels of types 310 and 316L exhibit acceptable corrosion performance for the construction of HTL reactors as their corrosion rates are less than 254 $\mu\text{m}/\text{year}$ in the representative non-catalytic and catalytic HTL conversion environments. As mentioned before, the corrosion rate allowances of pressure vessels/reactors used in similar chemical plants are generally between 762-1270 $\mu\text{m}/\text{year}$ over the projected service interval of 20 years [514-519].

Other than general corrosion, the stress corrosion cracking (SCC) susceptibility of candidate reactor alloys is another serious concern since the conversion process is required to operate in high pressure environments (up to 25 MPa) to achieve desired carbon conversion efficiency, thus introducing high stress (such as hoop stress) on the reactor wall [176, 177]. Unfortunately, the SCC knowledge and experience accumulated at pulp mills and light water reactor (LWR) plants are insufficient to support the selection of appropriate HTL construction alloys [143, 520-522]. For example, the concentrations of Cl^- and S^{2-} ions which are the well-known notorious agents to facilitate stress corrosion cracking (SCC) are well controlled in light water reactor in which irradiation-assisted SCC is a major issue [523]. In fact, previous studies indicated that the SCC of austenitic stainless steels (such as SS304, 310 and 316L) could occur in aqueous solution with 0.4 wt.% Cl^- under the stress just below their yield strengths at temperature $> 70\text{ }^\circ\text{C}$ [178-183]. Other studies found that austenitic stainless steels experienced high intergranular cracking in aqueous solutions (especially in the presence of Cl^- ions) at temperature close to supercritical water point (374 $^\circ\text{C}$) [524-526]. Except for Cl^- , S^{2-} ions, even at ppb level, were also found to facilitate the

pitting and SCC of Cr-Fe-Ni alloys (such as Alloy 600 and 800) at temperature > 275 °C [527]. Moreover, the addition of S^{2-} into basic solutions possibly resulted in high SCC risk of austenitic stainless steels at elevated temperatures [184, 185]. Furthermore, as described above, the concentration of organic acids (such as acetic acid and butyric acid) produced during the HTL conversion can be up to 10 wt.% or even higher, depending on the chemistry of biomass feedstocks used [395, 396]. In the mixture of acetic acid (70 wt.%) and Cl^- ions (1500 ppm), intergranular cracking of SS316L occurred at 90 °C [528]. In general, the available information is insufficient to identify the SCC susceptibility of candidate reactor alloys under high temperature HTL conditions although the SCC risk may be considerably high based on the previous studies in various high temperature aqueous environments.

Therefore, this chapter investigates the SCC susceptibility of the candidate steels (SS316L and SS310) using two standard constant strain methods under simulated HTL conversion of waste biomass feedstocks. As mentioned above, the two Fe-based steels exhibited acceptable corrosion performance in the non-catalytic and catalytic HTL environments. This chapter is expected to advance the fundamental understanding of SCC cracking under HTL conditions and further support the development of material technology solutions for the cost-effective construction and long-term safe operation of industrial HTL plants.

7.2. Experimental

7.2.1. SCC testing specimen preparation

In this study, both uniaxial constant strain and U-bending testing techniques were adopted to evaluate the SCC susceptibility of SS316L and SS310 in simulated catalytic HTL environments based on ASTM G49 and G30-97 standards [529, 530]. For the uniaxial constant strain testing, cylindrical tensile specimens instead of rectangular tensile specimens were machined to avoid unwanted bending or torsional stresses applied on the testing samples. The specimens were made from commercial SS310 and SS316L plates, and their bulk compositions are listed in Table 7-1 based on the associated Mill Test Certificate (MTC) provided by suppliers. The fabrication history of the two steels can be found in Chapter 6. Note that all the specimens were machined with the tensile axis along the rolling direction of the plates, and their dimensions are schematically shown

in Fig. 7-1. Each specimen was threaded with round gauge sections on both ends for subsequently fitting into a custom-made loading frame as shown in Figs. 7-2 and 7-3. The specimens were well polished with SiC papers up to 600 grit in deionized water to completely remove possible contaminants and defects introduced during machining, washed with ethanol in an ultrasonic bath for at least 10 minutes, cleaned with ultrapure water, and finally dried using pressurized air. Note that the loading frame was made of Alloy 33 and the washers and nuts were fabricated with Alloy C-276, to ensure adequate stiffness and strength of loading frame during the tests. To avoid the galvanic effect between loading system and testing specimens, all the loading components (including nuts and washers) were pre-oxidized in an air furnace at 400 °C for 24 hours before a SCC test.

Table 7-1. The bulk chemical composition of tested austenitic stainless steels used in this study.

Steel Types	Chemical Composition (wt.%)							
	Cr	Ni	Mn	C	Mo	Si	N	Fe
SS310	24.20	21.80	1.60	0.02	/	0.20	0.10	Bal.
SS316L	16.60	10.00	1.20	0.02	2.00	0.30	0.10	Bal.

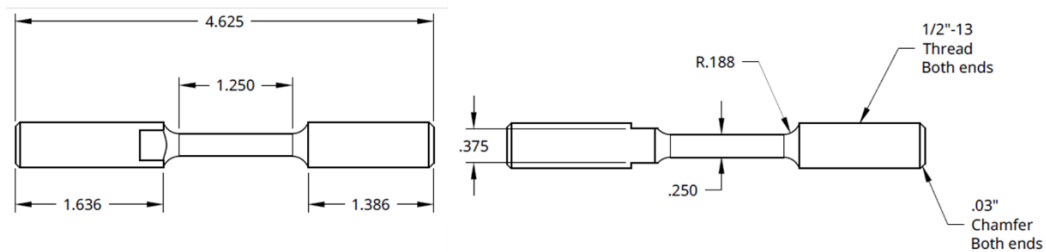


Fig. 7-1. Schematic of the dimensions of cylindrical tensile specimens used in this study (units in inch).

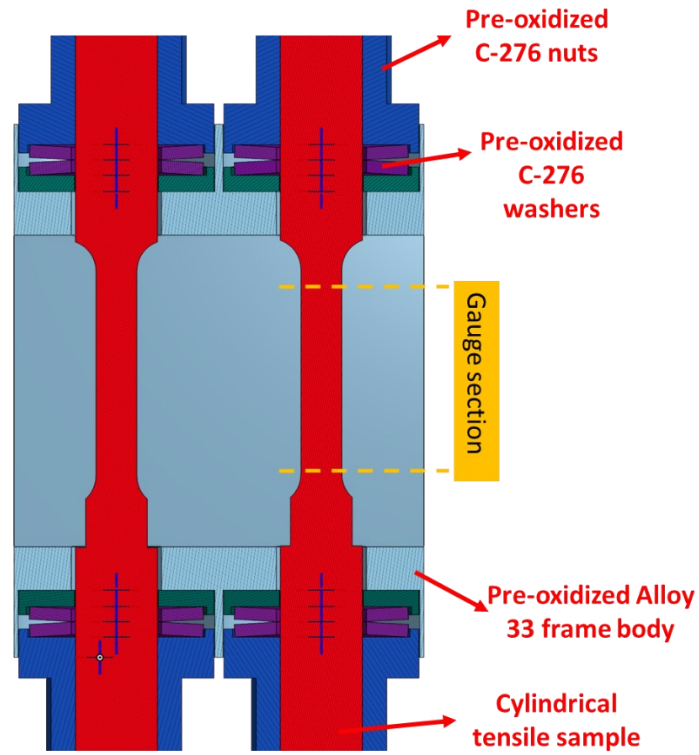


Fig. 7-2. Schematic of a custom-made loading frame used in this study.



Fig. 7-3. A photographic image of loading stressing frame and testing specimens before accommodating into a static autoclave.

The stress-strain curve of each steel was measured at both room temperature and 365 °C using commercial tensile testing equipment which consists of a loading rig, a heating oven (made of resistor elements and heat insulator), and the measuring and controlling sensors connecting to a remote computer. For the test, the prepared cylinder samples were used to ensure consistence with the SCC testing in an autoclave. During the mechanical testing, uniaxial loading was gradually applied and corresponding strain level was recorded using a digital extensometer attached to the gauge section of the sample. The maximum yield stress and corresponding strain level of each steel sample at 365 °C was determined based on the obtained stress-strain curve. The obtained strain level was then applied for loading the SCC cylinder samples at room temperature using the loading frame as shown in Figs. 7-2 and 7-3.

At room temperature, the desired strain deformation of a freshly prepared tensile specimen was reached by gradually fastening the moveable nut at one end of the frame (see Figs. 7-2 and 7-3). During the loading process, strain level was measured *in-situ* using a high-accuracy optical extensometer as shown in Fig. 7-4. To ensure the accuracy of measurement, before loading, a continuous layer of flat white paint was artificially applied on the whole gauge section of the specimen, accompanied with several patterned black spot painting at both ends of the gauge section (see targets #3 and #4 marked in Fig. 7-4). Before and during the loading, the optical extensometer was used to record the initial distance between two black spot patterns, and continuously measure the real-time distance change between the black spots to determine whether the required strain deformation was achieved. After that, the painted patterns were thoroughly cleaned using acetone and once done, the prepared tensile specimens were stored in a vacuum chamber for subsequent high temperature autoclave SCC testing.

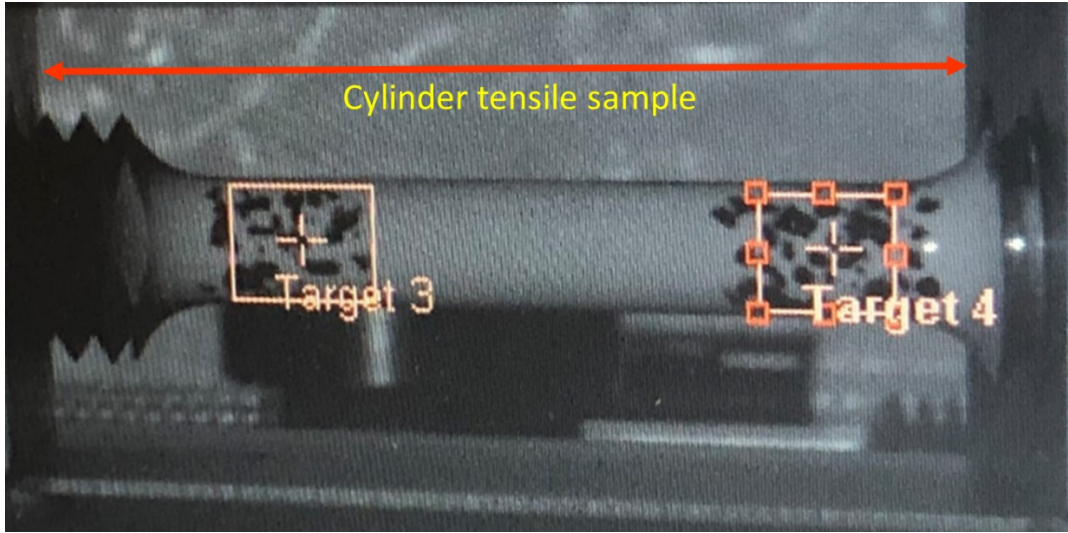


Fig. 7-4. A photographic image showing how to measure the applied strain level of a tensile specimen with application of an optical extensometer.

Different from uniaxial constant strain method, U-bending samples are usually applied for evaluating the SCC susceptibility of an alloy at high deformation levels. In this study, thin U-bending flat samples were also machined from the commercial plates listed in Table 7-1, and their dimensions are schematically shown in Fig. 7-5. Before the test, the U-bending samples were also well polished and cleaned, following the same preparation procedure applied on the cylinder tensile specimens. After that, the samples were strained using single-stage stressing method as described in ASTM G30-97 using a custom-made rig, as schematically shown in Fig. 7-6. Note that the Zr702 nuts, which were used to separate the rod and U-bending samples, were pre-oxidized in a furnace at 400 °C for 24 hours.



Fig. 7-5. The dimensions of a U-bending sample used in this study.

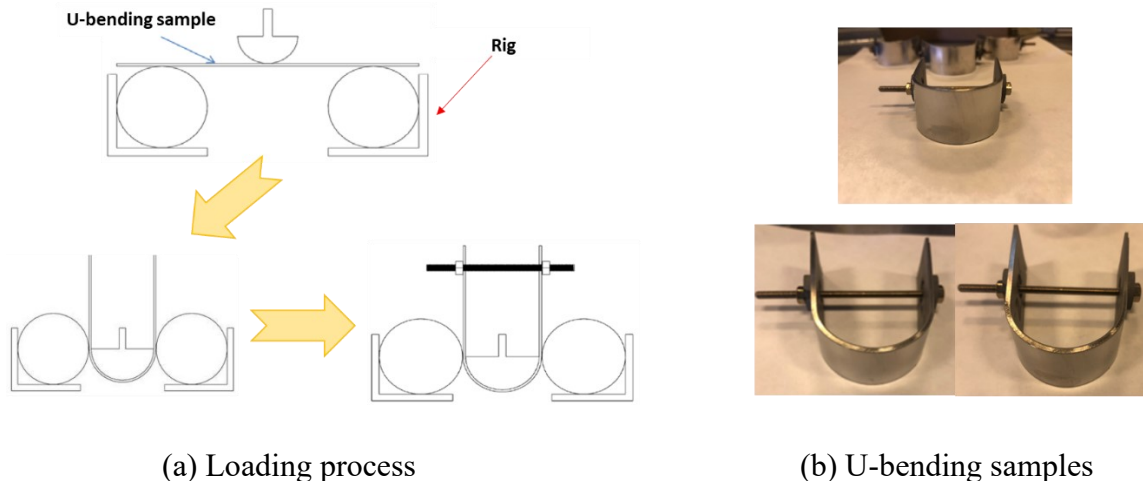


Fig. 7-6. Schematic of (a) loading process and (b) the photographic images of U-bending samples.

Since the thickness ($T = 1 \text{ mm}$) of a U-bending sample was much less than its radius of bending curvature ($R = 15 \text{ mm}$), the total strain (ϵ) on the outermost side of the bent sample is thus roughly estimated by [531]:

$$\epsilon = \frac{T}{2R} \quad (7-1)$$

In this study, the maximum applied strain on the tested samples was estimated to be $\sim 3.3\%$ at the center of the bent sample. Also, note that the outer surface of the sample was under tension while the inner surface was under compression state.

7.2.2. Autoclave test matrix and methodologies

Based on the high temperature testing methodology described in ASTM G31 [251], the SCC test was done in an 1 L Alloy 625 autoclave containing the solution of $0.5 \text{ M K}_2\text{CO}_3 + 3500 \text{ ppm Cl}^- + 2500 \text{ ppm S}^{2-} + 10 \text{ wt.}\% \text{ acetic acid}$ at $365 \text{ }^\circ\text{C}$. Note that the inorganic corrodants and acetic acid were added to simulate the corrosive agents released during the catalytic HTL conversion. After the testing solution and the strained cylindrical and U-bending samples were loaded, the autoclave was sealed and purged with Ar for about an hour to create a deaerated environment. Once leak test was completed, the autoclave was heated up to $365 \text{ }^\circ\text{C}$, but when the temperature was getting close

to the target temperature, the heating rate was slowed down to 3 °C/min to avoid temperature overshooting. The time when temperature just reached the target value was recorded as the starting time and test was to proceed for 5 days. The pressure and temperature were routinely monitored to avoid any unexpected leakage or thermal fluctuations during the test. Once the exposure duration was reached, the autoclave was powered off and cooled down in air. At room temperature, all the tested specimens were removed from the autoclave, rinsed with distilled water, and dried by pressurized air for subsequent microscopic characterizations.

7.2.3. Post-mortem characterization of tested samples

After the test, optical images were firstly taken to check the corroded specimens and compare with those without loading. After that, each specimen was carefully examined using a FEI Nova NanoSEM 650 scanning electron microscope (SEM) system at 20 keV to identify whether any surface cracks were formed. Once a surface crack was found, a FEI Helios NanoLab™ DualBeam™ Focus Ion Beam (FIB) microscope was employed to produce cross-sectional views of the crack from the top surface of corrosion products down to the substrate for determining whether a SCC crack was formed and which type of the crack (intergranular or transgranular) it was.

7.3. Main Results and Discussion

7.3.1. Microstructure and mechanical properties of tested steels

The microstructures of SS310 and SS316L used in this study are shown in Fig. 7-7. Their grain sizes were in the range of 30 - 50 μm and 20 - 40 μm, respectively. The secondary phases in the austenitic stainless steels, such as chromium carbides participate at grain boundaries during heat treatment, usually act as the crack initiation sites [532]. As shown there, no apparent carbide was found within the two steels, which could be due to the low carbon contents (<0.03 wt.%) in the steels [532, 533].

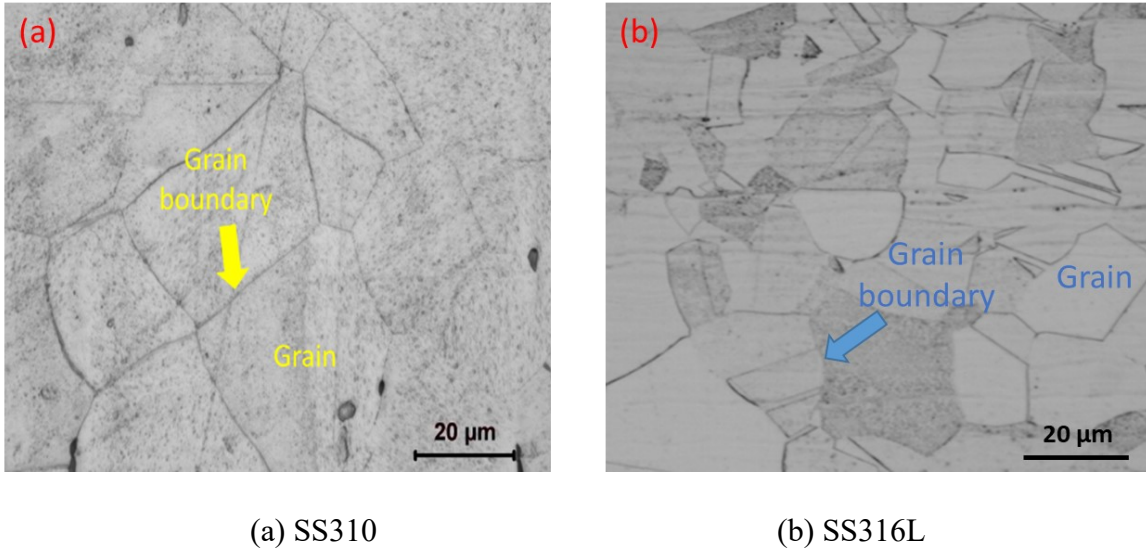
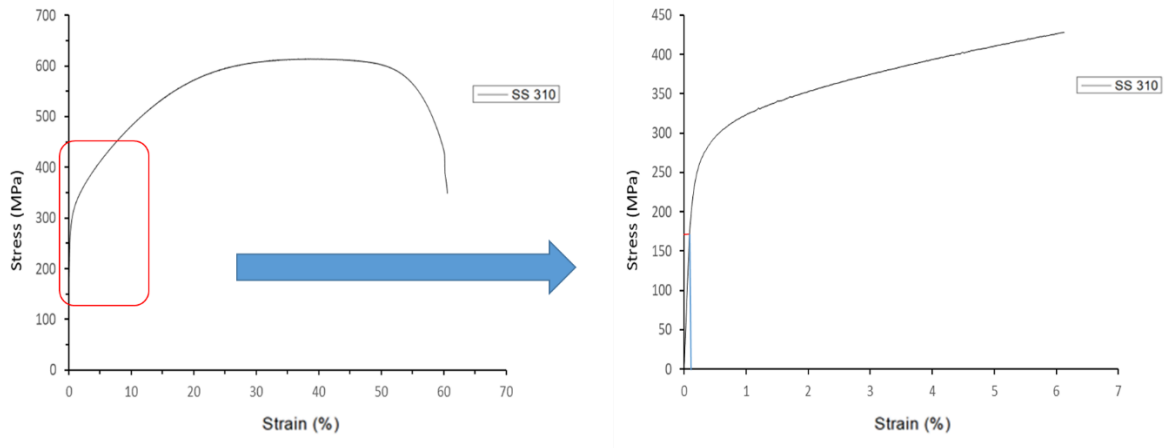


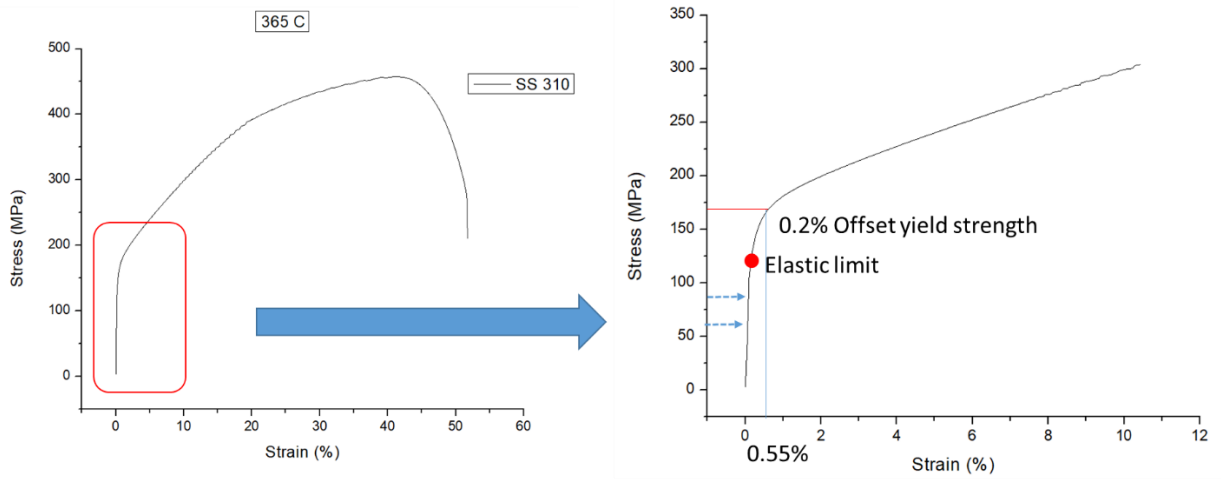
Fig. 7-7. Optical images of the microstructures of SS310 and SS316L steels used in this study.

As mentioned in Section 7.2.1, in order to determine the exact strain applied at 365 °C, mechanical tests on cylinder specimens were carried out and the obtained stress-strain curves are shown in Figs. 7-8 and 7-9. Increasing temperature led to a significant decrease in yield strength and ultimate tensile strength of each steel as expected. For instance, the ultimate tensile strength of SS310 decreased from 614 to 458 MPa with increasing temperature from room temperature to 365 °C.

At 365 °C, the 0.2% offset yield stress values of SS310 and SS316L were around 167 MPa and 174 MPa, respectively. The corresponding strains required to load on the cylindrical tensile specimens were about 0.55% on SS310 and 0.45% on SS316L at 365 °C, respectively. As mentioned above, the maximum stress strain applied on the U-bending samples was about 3.3%, which would be located in the plastic deformation region and the corresponding loadings at 365 °C were about 218 MPa on SS310 and 275 MPa on SS316L specimens, respectively.

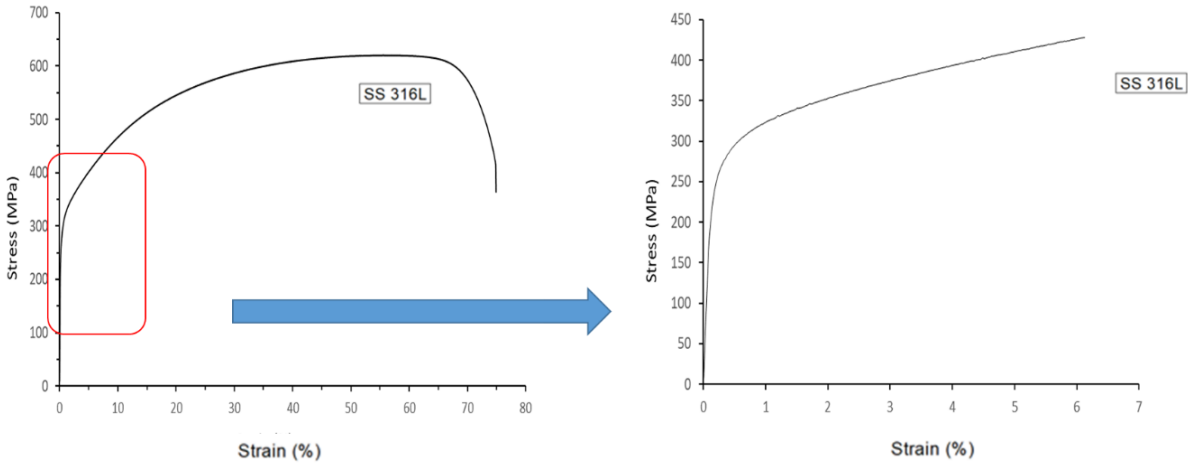


(a) at 25 °C

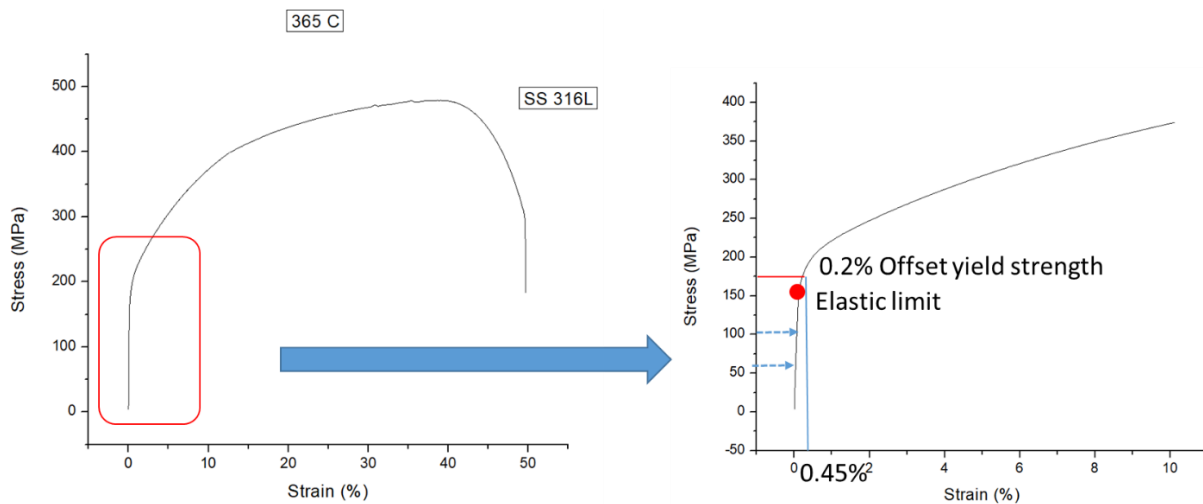


(b) at 365 °C

Fig. 7-8. Normalized stress-strain curves of SS310 at different temperatures.



(a) at 25 °C



(b) at 365 °C

Fig. 7-9. Normalized stress-strain curves of SS316L at different temperatures.

7.3.2. SCC susceptibility under simulated catalytic HTL conversion

After the SCC test in the simulated catalytic HTL environment, optical examinations were conducted on all the tested samples, and their photographic images are shown on Fig. 7-10. For each steel, its U-bending specimen exhibited much darker surface when compared with the cylindrical tensile specimens, implying that increasing loading would enhance the thickness of corrosion layers. No pitting/visible cracks were found on all the tested samples.



Fig. 7-10. Photographic images of U-bending and uniaxial tensile specimens after testing in 0.5 M K_2CO_3 + 3500 ppm Cl^- + 2500 ppm S^{2-} +10 wt.% acetic acid at 365 °C.

Subsequently, the high-resolution SEM top-view examinations were performed on the specimens, and the results are shown in Figs. 7-11 and 7-12, respectively. The following observations are made:

- (1) For each steel, increasing strain deformation resulted in the formation of a thicker corrosion layer. As shown in the figures, the mechanical polishing lines were still visible on the cylinder tensile specimens, but completely diminished on the U-bending samples. Moreover, the oxides formed on U-bending samples seemed to be finer than those grown on the cylindrical tensile specimens. The oxides formation energy on U-bending samples would be lower than that on the cylinder specimens, leading to the higher oxidation tendencies. Moreover, the oxidation enhanced with loading might be due to the reason that the oxides formed at defective/weak surface sites could be ruptured, consequently resulting in higher cation/anion diffusion at these spots based on previous studies [534, 535]. In addition, more deposit particles in larger size were likely present on the cylinder tensile samples compared to the U-bending samples, which might be attribute to the different physical and chemical affinity of oxides to dissolvable corrosion products during the autoclave cooling-down.

- (2) Microcracks were formed on all the tested specimens, and their density increased with increasing strain deformation. The cracks formed on the U-bending specimens were deeper and wider than those on the cylinder tensile samples. Compared to SS316L, the cracks formed on the U-bending SS310 specimen were considerably less. For the cylindrical tensile samples, no noticeable difference was found between the two steels. In addition, localized oxide spalling also occurred on all the tested samples, indicating that the formed oxide would be quite brittle.

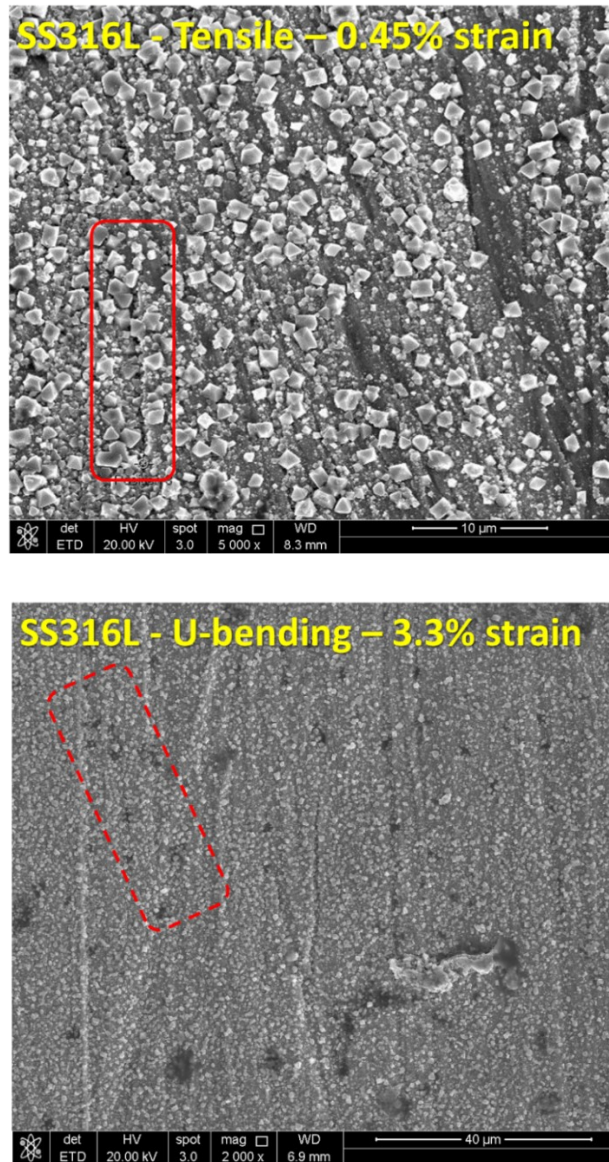


Fig. 7-11. SEM top-view images of SS316L after the exposure to 0.5 M K_2CO_3 + 3500 ppm Cl^- + 2500 ppm S^{2-} + 10 wt.% acetic acid under different strain loading levels at 365 °C.

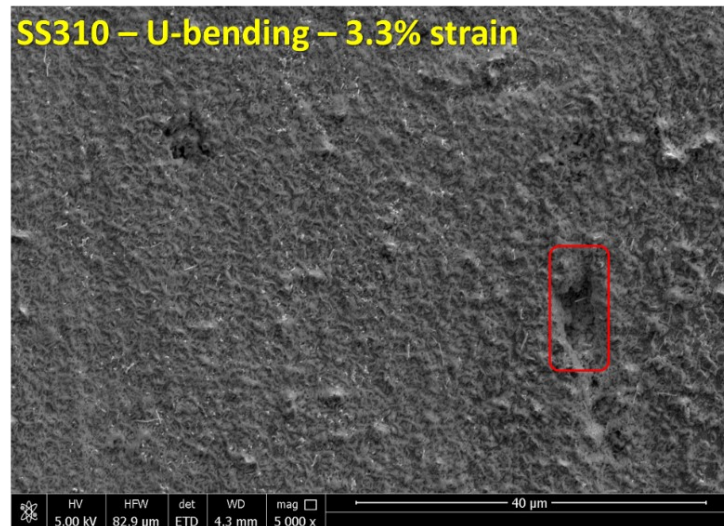
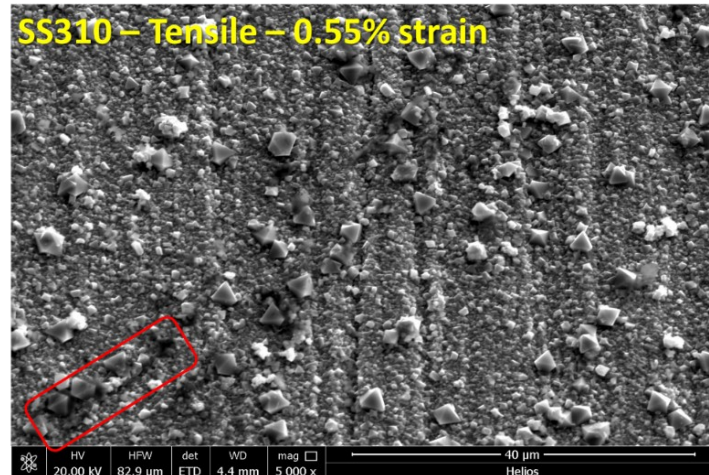


Fig. 7-12. SEM top-view images of SS310 after the exposure to 0.5 M K_2CO_3 + 3500 ppm Cl^- + 2500 ppm S^{2-} + 10 wt.% acetic acid under different strain loading levels at 365 °C.

To determine whether the formed microcracks were SCC cracks, FIB/SEM techniques were employed to produce the cross-sectional views of the tested samples, and the results are shown in Figs. 7-13 and 7-14. The cross-sectional results show that no cracks penetrated into the substrate, suggesting that SCC would unlikely occur on the two steels. As shown in the figure, remarkable lattice distortion and deformation occurred on the tested samples, particularly on the U-bending samples in which grain boundary sliding was observed. Moreover, SS310 seemed to be deformed to a higher degree comparing to the two cylinder tensile samples of the steels, particularly on the weak sites. These weak sites included localized inclusions and pits which caused stress

concentration and higher strain deformation as observed near the interface of oxide layer and substrate on SS310 cylinder tensile sample [535, 536].

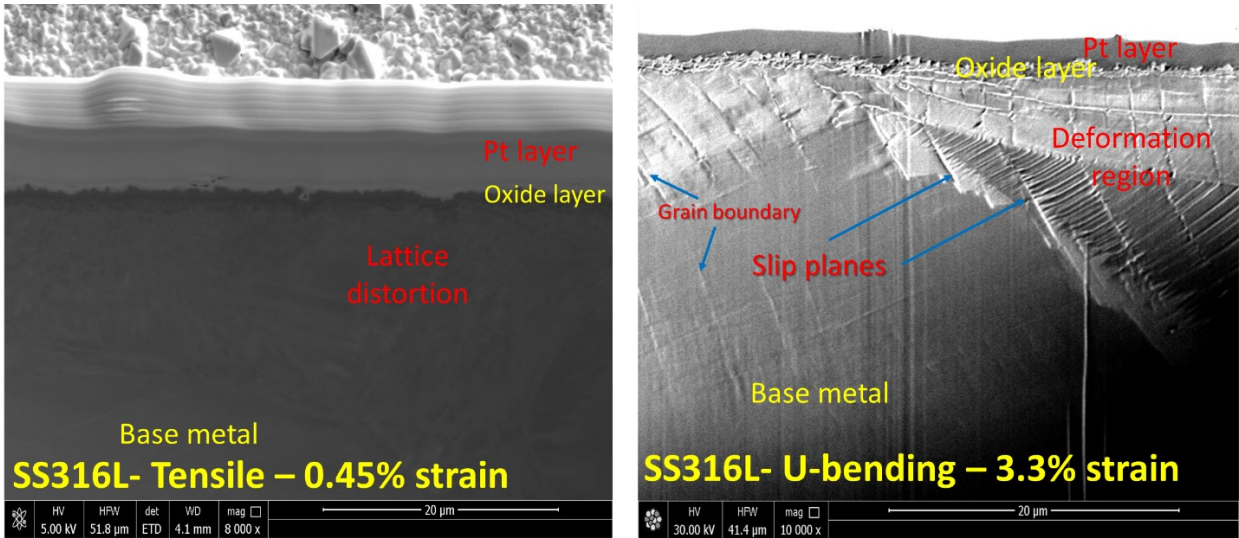


Fig. 7-13. Cross-sectional SEM images of SS316L samples after the autoclave exposure.

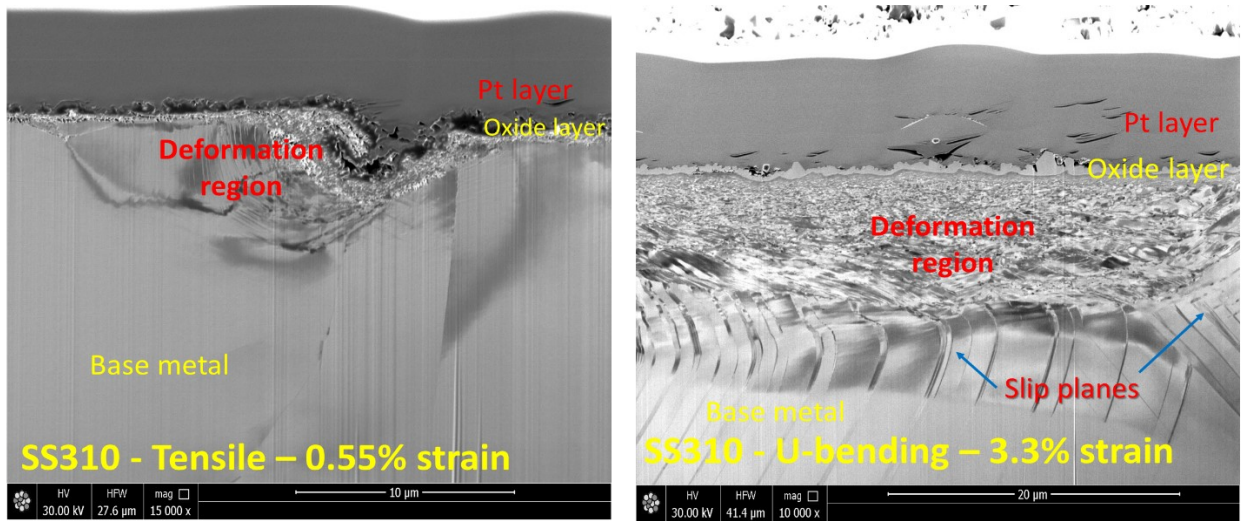


Fig. 7-14. Cross-sectional SEM images of SS310 samples after the autoclave exposure.

The results from this study indicated that the SCC risk of the two steels in the catalytic HTL environment would be relatively low. However, previous investigations showed that SCC actually

occurred on SS310 and SS316L in aqueous solutions with the presence of aggressive anions at temperature $> 288\text{ }^{\circ}\text{C}$ [459, 487, 532, 537-539]. It is generally concluded that the SCC of austenitic stainless steels in high temperature solutions could start at two susceptible sites, including pits and/or secondary phases. Pitting usually occurs when the localized accumulation of aggressive anions (Cl^- or S^{2-}) is sufficient to damage the integrity of a formed oxide scale [540, 541]. The pits would subsequently become the weak points with concentrated stress in the strained samples to facilitate SCC initiation and propagation [459, 542, 543]. Moreover, the secondary phases, including sigma phase in austenitic stainless steels and inclusions (such as MnS and MnO), may also be the susceptible sites for SCC initiation and propagation, since they could impair the corrosion resistance at grain boundaries via depleting key oxide-forming alloying elements (such as Cr) from surrounding regions and thus introducing defects/voids [532, 533, 544]. Similar to the pits, stress concentration is likely to occur at these spots to trigger SCC crack formation [545, 546]. Therefore, the absence of SCC in this study might be due to the following factors:

- (1) SCC incubation time. The SCC incubation time of the two steels in the catalytic HTL environment might be longer than expected. A previous SCC study found that the SCC cracks were formed in SS304 after the exposure to oxygenated water at $130\text{ }^{\circ}\text{C}$ for 100 hours, while for SS316L it occurred in $288\text{ }^{\circ}\text{C}$ water and over 360 hours [547, 548]. In this study, the 120 hours of exposure might be insufficient for SCC initiation.
- (2) The contents of inorganic corrodants and organic acids. The concentration of inorganic and organic corrodants in the HTL environments could be another major factor. As described before, the amounts of Cl^- and S^{2-} used in this study were only several thousand ppm. Previous studies in high temperature solutions found that there may exist a critical amount of Cl^- (0.5 wt.%), above which pitting would be more likely to occur on austenitic stainless steels [433, 434, 435]. Moreover, the negative impacts of Cl^- and S^{2-} on pitting might also be mitigated with the presence of K_2CO_3 as stated in Chapter 5. Furthermore, as indicated in Chapters 5 and 6, increasing the content of acetic acid in catalytic HTL environments could make the surface oxide scale formed on SS310 more porous. It is unclear whether the SCC risk of the two steels would still be low in the HTL environment with lower contents of organic acids. Previous studies found that thick and compact oxide layer formed on stainless steels in high temperature aqueous solutions might introduce internal stress and thus enhance the susceptibility of SCC cracking [549, 550]. With the presence of high content of acetic

acid, localized stress concentration is likely to be reduced because of the formation of relatively porous oxide layers. Further work is needed to explore the effect of organic acid.

- (3) The effect of temperature. As found in Chapter 4, there is a transition temperature at about 310 °C above which the corrosion rate of SS310 decreases with temperature. Increasing temperature from 310 to 365 °C can lead to a remarkable change of water properties and consequently suppress the chemical dissolution of the formed oxides, particularly at weak sites. This might reduce the chance of SCC crack initiation. Further study is required to evaluate this finding.
- (4) Materials Chemistry. Except for austenitic stainless steels, Ni-based alloys tested in Chapter 6 might be susceptible to SCC in the catalytic HTL environments based on previous studies [527]. The SCC susceptibility of Ni-based alloys (especially Alloy C-276) is required to be evaluated as this alloy is one of most promising candidates for construction.

7.4. Conclusions

This study investigated the SCC susceptibilities of SS316L and SS310 at different strain levels in the catalytic HTL environment (0.5 M K₂CO₃ + 3500 ppm Cl⁻ + 2500 ppm S²⁻ +10 wt.% acetic acid) at 365 °C. The following general conclusions are made:

- (1) Increasing strain deformation enhanced the corrosion of both austenitic stainless steels in the HTL environment.
- (2) Microcracks were formed within the corrosion layer grown on all the strained samples, and their density likely increased with an increase in strain level. For each steel, the cracks formed on U-bending specimens were deeper and wider comparing to those on the cylinder tensile sample. Moreover, SS310 seemed to be deformed to a higher degree on the cylinder sample comparing to SS316L, particularly on the local weak sites near the interface of oxide and substrate.
- (3) Cross-sectional examinations indicated that SCC were not present on all strained samples, suggesting a relatively low SCC risk. However, more investigations are still required to confirm the low SCC susceptibility in catalytic HTL conversion processes.

Chapter 8. Summary and Future Prospects

8.1. Summary

This study investigated the corrosion and stress corrosion cracking performances of Fe-based steels and Ni-based alloys in two unique biomass conversion environments to support the development of materials selection guidelines for the deployment of hot dilute acidic pre-hydrolysis and hydrothermal liquefaction technologies, and to advance the mechanistic understanding of how the steels and alloys corroded in hot dilute sulfuric acid and high temperature aqueous HTL environments with basic catalyst, inorganic and organic corrodants, and to identify the roles of major alloying elements (Cr, Ni, Fe, and Mo) for further development of cost-effective novel alloys for bioenergy industry. With the extensive and detailed theoretical analysis and laboratory tests, the following general conclusions are made:

1. In hot dilute acidic pre-hydrolysis environments, SS316L and DSS 2205 suffered active corrosion and their corrosion rates increased with temperature and time, while Alloy C-276 exhibited much better performance. Increasing Cr content in Fe-based steels mitigated corrosion damage, but could not provide adequate protection to the steels since the formed Cr oxide would be thermodynamically unstable and have higher dissolution rate in the biorefining environments. Different from Cr, increasing Mo content significantly improved corrosion resistance due to the formation of a continuous and protective Mo oxide layer, which could be stable and have acceptable dissolution rate under the pre-hydrolysis conditions. The inorganic and organic corrodants released during the conversion only had marginal effect on the corrosion of Alloy C-276, but noticeably exacerbated the localized corrosion of SS316L and DSS 2205.
2. High temperature high pressure water was used as conversion medium in the HTL conversion of wet biomass and biowaste feedstocks. Increasing temperature remarkably accelerated the corrosion of P91 steel with relatively low Cr content. For Cr-bearing SS310, there was a transition temperature (around 310 °C), above which the steel corrosion rate decreased with an increase in temperature close to supercritical point. Increasing flowing rate enhanced the corrosion of P91, but led to a moderate decrease in the corrosion rate of SS310 due to the suppressed localized nodular oxidation. Increasing pressure facilitated the oxidation of two tested steels, and had more noticeable impact on P91 than on SS310. In the

hot HTL water, the corrosion layer formed on P91 was mainly composed of Fe_3O_4 and $\text{Fe}_{3-x}\text{Cr}_x\text{O}_4$ compounds, while an inner compact and protective Cr-enriched layer could be found on SS310.

3. Basic catalyst, inorganic and organic corrodants are present in catalytic HTL conversion environments. This study found that the addition of basic catalyst significantly increased the corrosion of P91 steel and SS310 due to the accelerated chemical dissolution rates of the formed oxides in the catalytic environments. The corrosion layers formed on P91 steel and SS310 were much thicker than those formed in non-catalytic HTL environments. The presence of several thousand ppm of inorganic corrodants (Cl^- and S^{2-}) did not trigger pitting corrosion, but reduced oxide layers' thickness by facilitating their dissolution. The addition of acetic acid into the catalytic HTL environments notably accelerated the corrosion of both steels and resulted in the formation of micro-cracks and/or voids within the corrosion layers.
4. Thermodynamic calculations indicated that the four major alloying elements (Fe, Cr, Ni and Mo) would experience either passivation or active corrosion in the HTL conversion, depending on the environmental pH and temperatures. High temperature autoclave testing results showed that Cr played a vital role in Fe-based steels in the non-catalytic and catalytic HTL environments. Increasing Cr content in the steels resulted in a noticeable decrease in corrosion rate. In addition to Cr, increasing Mo content in the alloys also improved their corrosion performance. Increasing Ni content in the alloys would have negligible effect on corrosion in the non-catalytic HTL environment, but could lead to an improved performance in the catalytic HTL environments.
5. Stress corrosion cracking is a serious concern in the selection of suitable alloys for the construction and safe operation of HTL reactors. Both uniaxial constant strain and U-bending testing methodologies were applied for evaluating the SCC susceptibilities of SS316L and SS310 in the catalytic HTL environment with 3500 ppm Cl^- , 2500 ppm S^{2-} and 10 wt.% acetic acid at 365 °C. The preliminary results showed that increasing strain deformation could enhance the general corrosion of the steels, but the SCC risk of both steels was low, even under 3.3% deformation. These might be due to the insufficient incubation time and limited amounts of inorganic/organic corrodants. More assessments are still needed to confirm the above findings and determine the SCC risk of welded constructional alloys.

8.2. Future prospects

Although considerable efforts have been dedicated to this study, some materials knowledge gaps still exist on the cost-effective construction of the two biorefinery plants at industrial scale. Following studies were thus recommended for further clarifications and developments:

1. Further identify the SCC of candidate reactor alloys under catalytic HTL conditions.

As indicated in Chapter 5, increasing the content of acetic acid in catalytic HTL environments led to a remarkable increase in corrosion rate and the formation of localized holes and micro-cracks. It is thus necessary to determine whether SCC could occur in the catalytic HTL environments with more organic acids. Moreover, it is also important to identify the SCC risk of Ni-based alloys (such as Alloy C-276 and Alloy 625) as they exhibit better performance comparing to Fe-based steels in the catalytic HTL environments (see Chapter 6). Furthermore, the SCC susceptibility of welded steels and alloys is always a serious safety concern when constructing high temperature refining reactors. It is necessary to investigate the influence of welding techniques and processes on the SCC of selected constructional alloys under the catalytic HTL conditions.

2. Further explore corrosion mechanisms in biomass conversion environments using *in situ* high temperature electrochemical measurement techniques.

High temperature electrochemical techniques can be used to *in situ* detect the potential variations of steels and alloys with major operating parameters (temperature, pressure, catalyst and corrodants etc.) and constantly measure the corrosion resistance of corrosion layers formed in the biomass conversion environments. For example, open circuit potential and electrochemical impedance measurements on Cr and Mo electrodes in hot dilute pre-hydrolysis environments should be able to provide in-depth information about the formation and chemical dissolution processes of Cr and Mo oxides and further advance the mechanistic understanding. Due to limited time and the impact of pandemic on normal laboratory operation, the electrochemical investigations in the pre-hydrolysis and HTL environments have not yet been conducted in detail, even though preliminary preparations and tests were done.

3. Validate the developed materials technology solutions at pilot-scale HTL plants.

As mentioned in Chapter 4, the HTL processes can be operated either in batch or continuous mode. The chemistry in actual HTL environments could be more complicated than the simulated

environments used in Chapters 4-7. For example, an extensive variety of short-chain saturated acids (glycolic acid, levulinic acid, etc.) and long-chain polyunsaturated acids (linoleic acid, palmitoleic acid, etc.) might be produced when processing various lignocellulosic biomass and microalgae feedstocks, respectively. Moreover, the variation of temperature along the reactor can be expected during the continuous HTL operation. Thus, it is a “MUST” to validate whether the selected alloys still exhibit acceptable long-term anti-corrosion and anti-SCC performances at the pilot-scale continuous HTL plants.

4. Develop innovative coatings and/or novel alloys to mitigate corrosion damage under the biomass conversion conditions in a cost-effective fashion.

Based on the results in Chapters 3 and 6, the alloying elements Cr and Mo that present in alloys play the key roles during corrosion process in different biorefining environments. As mentioned before, high capital investment is an economic concern on the deployment of HTL technology at energy sectors. From the materials technology and corrosion points of view, the development of innovative protective coatings, which are composed of high Cr and/or Mo contents, on cheap low-Cr steel should be a practical way to effectively control corrosion damage in the biorefining processes. Lastly, with the increased demands on clean and renewable bioenergy products, cost-competitive novel alloys are urgently needed to meet the industrial needs.

Bibliography

1. Lamb, W.F., T. Wiedmann, J. Pongratz, R. Andrew, M. Crippa, J.G.J. Olivier, D. Wiedenhofer, G. Mattioli, A.A. Khourdajie, J. House, S. Pachauri, M. Figueroa, Y. Saheb, R. Slade, K. Hubacek, L. Sun, S.K. Ribeiro, S. Khennas, S. de la Rue du Can, L. Chapungu, S.J. Davis, I. Bashmakov, H. Dai, S. Dhakal, X. Tan, Y. Geng, B. Gu, and J. Minx, *A review of trends and drivers of greenhouse gas emissions by sector from 1990 to 2018*. Environmental Research Letters, 2021. **16**(7): p. 073005.
2. Gupta, S.K., A. Malik, and F. Bux, *Algal Biofuels: Recent Advances and Future Prospects*, 2017. p. 1-37. Springer International Publishing.
3. Wender, I., P.M. Yavorsky, S. Friedman, Y.C. Fu, H.R. Appell, and C. Pittsburgh Energy Research, *Converting organic wastes to oil: a replenishable energy source*, Report of investigations, Bureau of Mines, 1971. p. 1-20.
4. Carriquiry, M.A., X. Du, and G.R. Timilsina, *Second generation biofuels: Economics and policies*. Energy Policy, 2011. **39**(7): p. 4222-4234.
5. Balakrishna M., Ellen P., Thomas W., Teresa L., Marie S., Karl A., and Daniel H., *Quantitative Characterization of Aqueous Byproducts from Hydrothermal Liquefaction of Municipal Wastes, Food Industry Wastes, and Biomass Grown on Waste*, ACS Sustainable Chemistry & Engineering, 2017. **5**(3): p. 2205-2214.
6. Chunyan, T., J. Liu, and Y. Zhang, *Hydrothermal Liquefaction (HTL): A Promising Pathway for Biorefinery of Algae*. Algal Biofuels, 2017. p. 361-391.
7. Akizuki, M., T. Fujii, R. Hayashi, and Y. Oshima, *Effects of water on reactions for waste treatment, organic synthesis, and bio-refinery in sub- and supercritical water*. Journal of Bioscience and Bioengineering, 2014. **117**(1): p. 10-18.
8. Pierobon, S., X. Cheng, P. Graham, B. Nguyen, E. Karakolis, and D. Sinton, *Emerging microalgae technology: a review*. Sustainable Energy & Fuels, 2018. **2**(1): p. 13-38.
9. Cherubini, F., S. Bargigli, and S. Ulgiati, *Life cycle assessment (LCA) of waste management strategies: Landfilling, sorting plant and incineration*. Energy, 2009. **34**(12): p. 2116-2123.
10. Scarlat, N., J.-F. Dallemand, F. Monforti-Ferrario, and V. Nita, *The role of biomass and bioenergy in a future bioeconomy: Policies and facts*. Environmental Development, 2015. **15**: p. 3-34.

11. Lucia, L.A., D.S. Argyropoulos, L. Adamopoulos, and A.R. Gaspar, *Chemicals, Materials, and Energy from Biomass: A Review*, in *Materials, Chemicals, and Energy from Forest Biomass*. 2007, American Chemical Society. p. 2-30.
12. Elliott, D.C., P. Biller, A.B. Ross, A.J. Schmidt, and S.B. Jones, *Hydrothermal liquefaction of biomass: Developments from batch to continuous process*. *Bioresource Technology*, 2015. **178**: p. 147-156.
13. Dimitriadis, A. and S. Bezergianni, *Hydrothermal liquefaction of various biomass and waste feedstocks for biocrude production: A state of the art review*. *Renewable and Sustainable Energy Reviews*, 2017. **68**: p. 113-125.
14. Demichelis, F., M. Laghezza, M. Chiappero, and S. Fiore, *Technical, economic and environmental assesement of bioethanol biorefinery from waste biomass*. *Journal of Cleaner Production*, 2020. **277**: p. 124111.
15. Mohanty, S.K., S. Behera, M.R. Swain, and R.C. Ray, *Bioethanol production from mahula (*Madhuca latifolia L.*) flowers by solid-state fermentation*. *Applied Energy*, 2009. **86**(5): p. 640-644.
16. Butler, E., G. Devlin, D. Meier, and K. McDonnell, *A review of recent laboratory research and commercial developments in fast pyrolysis and upgrading*. *Renewable and Sustainable Energy Reviews*, 2011. **15**(8): p. 4171-4186.
17. Hroncová, E., J. Ladomerský, J. Valíček, and L. Dzurenda, *Combustion of biomass fuel and residues: emissions production perspective*. *Developments in Combustion Technology*, 2016. **1** : p. 1-32.
18. Sikarwar, V.S. and M. Zhao, *Biomass Gasification*, in *Encyclopedia of Sustainable Technologies*, M.A. Abraham, Editor. 2017, Elsevier: Oxford. p. 205-216.
19. Zhang, L., C. Xu, and P. Champagne, *Overview of recent advances in thermo-chemical conversion of biomass*. *Energy Conversion and Management*, 2010. **51**(5): p. 969-982.
20. Yaman, S., *Pyrolysis of biomass to produce fuels and chemical feedstocks*. *Energy Conversion and Management*, 2004. **45**(5): p. 651-671.
21. Chaiwong, K., T. Kiatsiriroat, N. Vorayos, and C. Thararax, *Study of bio-oil and bio-char production from algae by slow pyrolysis*. *Biomass and Bioenergy*, 2013. **56**: p. 600-606.

22. Lu, Q., Z.-x. Zhang, X. Wang, H.-q. Guo, M.-s. Cui, and Y.-p. Yang, *Catalytic Fast Pyrolysis of Biomass Impregnated with Potassium Phosphate in a Hydrogen Atmosphere for the Production of Phenol and Activated Carbon*. *Frontiers in Chemistry*, 2018. **6**: 32.
23. Bulushev, D.A. and J.R. Ross, *Catalysis for conversion of biomass to fuels via pyrolysis and gasification: a review*. *Catalysis Today*, 2011. **171**(1): p. 1-13.
24. Hassan, H., J. Lim, and B. Hameed, *Recent progress on biomass co-pyrolysis conversion into high-quality bio-oil*. *Bioresource Technology*, 2016. **221**: p. 645-655.
25. Shahbaz, M., S. yusup, A. Inayat, D.O. Patrick, and M. Ammar, *The influence of catalysts in biomass steam gasification and catalytic potential of coal bottom ash in biomass steam gasification: A review*. *Renewable and Sustainable Energy Reviews*, 2017. **73**: p. 468-476.
26. Rapagnà, S., N. Jand, and P.U. Foscolo, *Catalytic gasification of biomass to produce hydrogen rich gas*. *International Journal of Hydrogen Energy*, 1998. **23**(7): p. 551-557.
27. Kaur, R., P. Gera, M.K. Jha, and T. Bhaskar, *Chapter 8 - Thermochemical Route for Biohydrogen Production*, in *Biohydrogen (Second Edition)*, A. Pandey, et al., Editors. 2019, Elsevier. p. 187-218.
28. Shayan, E. and I. Mirzaee, *Hydrogen production from biomass gasification; a theoretical comparison of using different gasification agents*. *Energy Conversion and Management*, 2018. **159**: p. 30-41.
29. Ahmad, A.A., Zawawi N.A., Kasim F.H., Inayat A., and Khasri A., *Assessing the gasification performance of biomass: A review on biomass gasification process conditions, optimization and economic evaluation*. *Renewable and Sustainable Energy Reviews*, 2016. **53**: p. 1333-1347.
30. Udomsirichakorn, J. and P.A. Salam, *Review of hydrogen-enriched gas production from steam gasification of biomass: The prospect of CaO-based chemical looping gasification*. *Renewable and Sustainable Energy Reviews*, 2014. **30**: p. 565-579.
31. Amrullah, A. and Y. Matsumura, *Supercritical water gasification of sewage sludge in continuous reactor*. *Bioresour Technol*, 2018. **249**: p. 276-283.
32. Taherzadeh, M.J. and K. Karimi, *Pretreatment of Lignocellulosic Wastes to Improve Ethanol and Biogas Production: A Review*. *International Journal of Molecular Sciences*, 2008. **9**(9): p. 1621-1651.

33. Balan, V., B. Bals, S.P.S. Chundawat, D. Marshall, and B.E. Dale, *Lignocellulosic Biomass Pretreatment Using AFEX*, in *Biofuels: Methods and Protocols*, J.R. Mielenz, Editor. 2009, Humana Press: Totowa, NJ. p. 61-77.
34. Håkansson, H., U. Germgård, and D. Sens, *Influence of xylan on the degradability of laboratory kraft pulps from hardwood and reed canary grass in acid hydrolysis*. *Cellulose*, 2005. **12**(6): p. 621-628.
35. Vlasenko, E.Y., *Enzymatic hydrolysis of pretreated rice straw*. *Bioresource Technology*, 1997. **59**(2): p. 109 - 119.
36. Tsoutsos, T., D. Bethanis, and V. Gekas, *Simulation of fermentable sugar production from lignocellulosics to fuel ethanol*. 15th European Biomass Conference Proceedings. May 2007.
37. Binder, J.B. and R.T. Raines, *Fermentable sugars by chemical hydrolysis of biomass*. *Proceedings of the National Academy of Sciences*, 2010. **107**(10): p. 4516-4521.
38. Schenk, P.M., S.R. Thomas-Hall, E. Stephens, U.C. Marx, J.H. Mussgnug, C. Posten, O. Kruse, and B. Hankamer, *Second Generation Biofuels: High-Efficiency Microalgae for Biodiesel Production*. *BioEnergy Research*, 2008. **1**(1): p. 20-43.
39. Pan, X. and L. Shuai, *Saccharification of lignocellulosic biomass*. United States Patent US9187790B2. 2013.
40. Maurya, D.P., A. Singla, and S. Negi, *An overview of key pretreatment processes for biological conversion of lignocellulosic biomass to bioethanol*. *3 Biotech*, 2015. **5**(5): p. 597-609.
41. Amin, F.R., H. Khalid, H. Zhang, S.u. Rahman, R. Zhang, G. Liu, and C. Chen, *Pretreatment methods of lignocellulosic biomass for anaerobic digestion*. *AMB Express*, 2017. **7**: p. 72.
42. Wang, X., S. Leng, J. Bai, H. Zhou, X. Zhong, G. Zhuang, and J. Wang, *Role of pretreatment with acid and base on the distribution of the products obtained via lignocellulosic biomass pyrolysis*. *RSC Advances*, 2015. **5**(32): p. 24984-24989.
43. Jensen, J., J. Morinelly, A. Aglan, A. Mix, and D.R. Shonnard, *Kinetic characterization of biomass dilute sulfuric acid hydrolysis: Mixtures of hardwoods, softwood, and switchgrass*. *AIChE Journal*, 2008. **54**(6): p. 1637-1645.

44. T.-A. Hsu, C.E.W.E., *Handbook on Bioethanol Production and Utilization, Applied Energy Technology Series*. 1996, Taylor & Francis: Washington DC. p. 124-129.
45. D.R. Knappert, H.E.G., A.O. Converse, *Partial acid hydrolysis of poplar wood as a pretreatment for enzymatic hydrolysis*. *Biotechnol. Bioeng.*, **11**:3. 1981.
46. Lloyd, T.A. and C.E. Wyman, *Combined sugar yields for dilute sulfuric acid pretreatment of corn stover followed by enzymatic hydrolysis of the remaining solids*. *Bioresource Technology*, 2005. **96**(18): p. 1967-1977.
47. Wyman, C.E., B.E. Dale, R.T. Elander, M. Holtzapple, M.R. Ladisch, and Y.Y. Lee, *Comparative sugar recovery data from laboratory scale application of leading pretreatment technologies to corn stover*. *Bioresource Technology*, 2005. **96**(18): p. 2026-2032.
48. Martin, C., B. Alriksson, A. Sjöde, N.-O. Nilvebrant, and L.J. Jönsson, *Dilute sulfuric acid pretreatment of agricultural and agro-industrial residues for ethanol production*. *Applied Biochemistry and Biotechnology*, 2007. **137**(1): p. 339-352.
49. Mosier, N., C. Wyman, B. Dale, R. Elander, Y.Y. Lee, M. Holtzapple, and M. Ladisch, *Features of promising technologies for pretreatment of lignocellulosic biomass*. *Bioresource Technology*, 2005. **96**(6): p. 673-686.
50. Springer, E.L.H., John F., *Prehydrolysis of aspen wood with water and with dilute aqueous sulfuric acid*. **85**:15, 1982. p. 152-154.
51. Esteghlalian, A., A.G. Hashimoto, J.J. Fenske, and M.H. Penner, *Modeling and optimization of the dilute-sulfuric-acid pretreatment of corn stover, poplar and switchgrass*. *Bioresource Technology*, 1997. **59**(2): p. 129-136.
52. Dong, C., Y.X. Guan, X.Q. Cheng, F.H. Liu, Y. Li, A. Ren, and X. li, *Effects of pH values on the stress corrosion cracking of 304L stainless steel in high-temperature and high-pressure water*. *Beijing Keji Daxue Xuebao/Journal of University of Science and Technology Beijing*, 2010. **32**: p. 1569-1573.
53. Ricardo Soccol, C., V. Faraco, S. Karp, L.P.S. Vandenberghe, V. Thomaz-Soccol, A. Woiciechowski, and A. Pandey, *Chapter 5 - Lignocellulosic Bioethanol: Current Status and Future Perspectives*, in *Biofuels*, A. Pandey, et al., Editors. 2011, Academic Press: Amsterdam. p. 101-122.

54. Yang, T.C., J. Kumaran, S. Amartei, M. Maki, X. Li, F. Lu, and W. Qin, *Chapter 5 - Biofuels and Bioproducts Produced through Microbial Conversion of Biomass*, in *Bioenergy Research: Advances and Applications*, V.K. Gupta, et al., Editors. 2014, Elsevier: Amsterdam. p. 71-93.
55. Sarwar Jahan M., Mostafizur Rahman M., *Effect of pre-hydrolysis on the soda-anthraquinone pulping of corn stalks and Saccharum spontaneum (kash)*, *Carbohydrate Polymers*, 2012. **88**(2): p. 583-588.
56. Springer, E.L.H., John F., *Prehydrolysis of aspen wood with water and with dilute aqueous sulfuric acid*. . *Svensk papperstidning*, 1982. **85**(15): p. R152-R154.
57. Yang, B. and C.E. Wyman, *Pretreatment: the key to unlocking low-cost cellulosic ethanol*. *Biofuels, Bioproducts and Biorefining*, 2008. **2**(1): p. 26-40.
58. Yang, B. and C.E. Wyman, *Effect of xylan and lignin removal by batch and flowthrough pretreatment on the enzymatic digestibility of corn stover cellulose*. *Biotechnology and Bioengineering*, 2004. **86**(1): p. 88-98.
59. Redding, A.P., Z. Wang, D.R. Keshwani, and J.J. Cheng, *High temperature dilute acid pretreatment of coastal Bermuda grass for enzymatic hydrolysis*. *Bioresource Technology*, 2011. **102**(2): p. 1415-1424.
60. Hsu, T.-C., G.-L. Guo, W.-H. Chen, and W.-S. Hwang, *Effect of dilute acid pretreatment of rice straw on structural properties and enzymatic hydrolysis*. *Bioresource Technology*, 2010. **101**(13): p. 4907-4913.
61. Mussatto, S.I. and I.C. Roberto, *Acid hydrolysis and fermentation of brewer's spent grain to produce xylitol*. *Journal of the Science of Food and Agriculture*, 2005. **85**(14): p. 2453-2460.
62. Mussatto, S.I., M. Fernandes, A.M.F. Milagres, and I.C. Roberto, *Effect of hemicellulose and lignin on enzymatic hydrolysis of cellulose from brewer's spent grain*. *Enzyme and Microbial Technology*, 2008. **43**(2): p. 124-129.
63. Mussatto, S.I., L.M. Carneiro, J.P.A. Silva, I.C. Roberto, and J.A. Teixeira, *A study on chemical constituents and sugars extraction from spent coffee grounds*. *Carbohydrate Polymers*, 2011. **83**(2): p. 368-374.

64. Enslow, K.R. and A.T. Bell, *The kinetics of Bronsted acid-catalyzed hydrolysis of hemicellulose dissolved in 1-ethyl-3-methylimidazolium chloride*. RSC Advances, 2012. **2**(26): p. 10028-10036.
65. Mosier, N., R. Hendrickson, N. Ho, M. Sedlak, and M.R. Ladisch, *Optimization of pH controlled liquid hot water pretreatment of corn stover*. Bioresource Technology, 2005. **96**(18): p. 1986-1993.
66. Castellino, N., O. Elmino, and G. Rozera, *Experimental Research on Toxicity of Furfural*. Archives of Environmental Health: An International Journal, 1963. **7**(5): p. 574-582.
67. Bauer-Marinovic, M., F. Taugner, S. Florian, and H. Glatt, *Toxicity studies with 5-hydroxymethylfurfural and its metabolite 5-sulphoxymethylfurfural in wild-type mice and transgenic mice expressing human sulphotransferases 1A1 and 1A2*. Archives of Toxicology, 2012. **86**(5): p. 701-711.
68. Capuano, E. and V. Fogliano, *Acrylamide and 5-hydroxymethylfurfural (HMF): A review on metabolism, toxicity, occurrence in food and mitigation strategies*. LWT - Food Science and Technology, 2011. **44**(4): p. 793-810.
69. Sintamarean, I., I. Grigoras, C. Jensen, S. Toor, T. Pedersen, and L. Rosendahl, *Two-stage alkaline hydrothermal liquefaction of wood to biocrude in a continuous bench-scale system*. Biomass Conversion and Biorefinery, 2017. **7**.
70. Knežević, D., W. van Swaaij, and S. Kersten, *Hydrothermal Conversion Of Biomass. II. Conversion Of Wood, Pyrolysis Oil, And Glucose In Hot Compressed Water*. Industrial & Engineering Chemistry Research, 2010. **49**(1): p. 104-112.
71. Jindal, M.K. and M.K. Jha, *Hydrothermal liquefaction of wood: a critical review*. Reviews in Chemical Engineering, 2016. **32**(4): p. 459-488.
72. Lindemuth, T.E., *Carboxylolysis of Biomass*, in *Biomass Conversion Processes for Energy and Fuels*, S.S. Sofer and O.R. Zaborsky, Editors. 1981, Springer US: Boston, MA. p. 187-200.
73. Ruiz, H.A., R.M. Rodríguez-Jasso, B.D. Fernandes, A.A. Vicente, and J.A. Teixeira, *Hydrothermal processing, as an alternative for upgrading agriculture residues and marine biomass according to the biorefinery concept: A review*. Renewable and Sustainable Energy Reviews, 2013. **21**: p. 35-51.

74. Yu, G., S. Yano, H. Inoue, S. Inoue, T. Endo, and S. Sawayama, *Pretreatment of Rice Straw by a Hot-Compressed Water Process for Enzymatic Hydrolysis*. Applied Biochemistry and Biotechnology, 2010. **160**(2): p. 539-551.
75. Tekin, K., S. Karagöz, and S. Bektaş, *A review of hydrothermal biomass processing*. Renewable and Sustainable Energy Reviews, 2014. **40**: p. 673-687.
76. Hitzl, M., A. Corma, F. Pomares, and M. Renz, *The hydrothermal carbonization (HTC) plant as a decentral biorefinery for wet biomass*. Catalysis Today, 2015. **257**: p. 154-159.
77. Elliott, D.C., *Review of recent reports on process technology for thermochemical conversion of whole algae to liquid fuels*. Algal Research, 2016. **13**: p. 255-263.
78. Shakya, R., J. Whelen, S. Adhikari, R. Mahadevan, and S. Neupane, *Effect of temperature and Na₂CO₃ catalyst on hydrothermal liquefaction of algae*. Algal Research, 2015. **12**: p. 80-90.
79. Nazari, L., Z. Yuan, S. Souzanchi, M.B. Ray, and C.C. Xu, *Hydrothermal liquefaction of woody biomass in hot-compressed water: catalyst screening and comprehensive characterization of bio-crude oils*. Fuel, 2015. **162**: p. 74-83.
80. Minowa, T., F. Zhen, and T. Ogi, *Cellulose decomposition in hot-compressed water with alkali or nickel catalyst*. The Journal of supercritical fluids, 1998. **13**(1-3): p. 253-259.
81. Nagamori, M. and T. Funazukuri, *Glucose production by hydrolysis of starch under hydrothermal conditions*. Journal of Chemical Technology & Biotechnology: International Research in Process, Environmental & Clean Technology, 2004. **79**(3): p. 229-233.
82. Giaconia, A., G. Caputo, A. Ienna, D. Mazzei, B. Schiavo, O. Scialdone, and A. Galia, *Biorefinery process for hydrothermal liquefaction of microalgae powered by a concentrating solar plant: A conceptual study*. Applied Energy, 2017. **208**: p. 1139-1149.
83. Jazrawi, C., P. Biller, A.B. Ross, A. Montoya, T. Maschmeyer, and B.S. Haynes, *Pilot plant testing of continuous hydrothermal liquefaction of microalgae*. Algal Research, 2013. **2**(3): p. 268-277.
84. Thomsen, M.H., A. Thygesen, and A.B. Thomsen, *Hydrothermal treatment of wheat straw at pilot plant scale using a three-step reactor system aiming at high hemicellulose recovery, high cellulose digestibility and low lignin hydrolysis*. Bioresource Technology, 2008. **99**(10): p. 4221-4228.

85. Rossner, A. and C. Parra, *Pilot Plant Design and Operation Using a Hydrothermal Pretreatment: Bioenercel Experience*, in *Hydrothermal Processing in Biorefineries: Production of Bioethanol and High Added-Value Compounds of Second and Third Generation Biomass*, H.A. Ruiz, M. Hedegaard Thomsen, and H.L. Trajano, Editors. 2017, Springer International Publishing: Cham. p. 389-400.
86. Lemoine, F., I. Maupin, L. Lemée, J.M. Lavoie, J.L. Lemberton, Y. Pouilloux, and L. Pinard, *Alternative fuel production by catalytic hydroliquefaction of solid municipal wastes, primary sludges and microalgae*. *Bioresour Technol*, 2013. **142**: p. 1-8.
87. Zhang, L., C.C. Xu, and P. Champagne, *Energy recovery from secondary pulp/paper-mill sludge and sewage sludge with supercritical water treatment*. *Bioresour Technol*, 2010. **101**(8): p. 2713-21.
88. Murrieta, C.M., *Comparison of acidic and alkaline catalysts for preparation of fatty acid methyl esters from ovine muscle with emphasis on conjugated linoleic acid*. *Meat Science*, 2003. **65**(1): p. 523 - 529.
89. Tekin, K. and S. Karagöz, *Non-catalytic and catalytic hydrothermal liquefaction of biomass*. *Research on Chemical Intermediates*, 2013. **39**(2): p. 485-498.
90. Karagöz, S., T. Bhaskar, A. Muto, Y. Sakata, T. Oshiki, and T. Kishimoto, *Low-temperature catalytic hydrothermal treatment of wood biomass: analysis of liquid products*. *Chemical Engineering Journal*, 2005. **108**(1): p. 127-137.
91. Hammerschmidt, A., N. Boukis, E. Hauer, U. Galla, E. Dinjus, B. Hitzmann, T. Larsen, and S.D. Nygaard, *Catalytic conversion of waste biomass by hydrothermal treatment*. *Fuel*, 2011. **90**(2): p. 555-562.
92. Akhtar, J., S.K. Kuang, and N.S. Amin, *Liquefaction of empty palm fruit bunch (EPFB) in alkaline hot compressed water*. *Renewable Energy*, 2010. **35**(6): p. 1220-1227.
93. Zheng, J.-L., M.-Q. Zhu, and H.-t. Wu, *Alkaline hydrothermal liquefaction of swine carcasses to bio-oil*. *Waste Management*, 2015. **43**: p. 230-238.
94. Bhaskar, T., A. Sera, A. Muto, and Y. Sakata, *Hydrothermal upgrading of wood biomass: Influence of the addition of K₂CO₃ and cellulose/lignin ratio*. *Fuel*, 2008. **87**(10): p. 2236-2242.

95. Karagöz, S., T. Bhaskar, A. Muto, and Y. Sakata, *Hydrothermal upgrading of biomass: Effect of K₂CO₃ concentration and biomass/water ratio on products distribution*. Bioresource Technology, 2006. **97**(1): p. 90-98.
96. Hammerschmidt, A., N. Boukis, E. Hauer, U. Galla, E. Dinjus, B. Hitzmann, T. Larsen, and S. Nygaard, *Catalytic conversion of waste biomass by hydrothermal treatment*. Fuel, 2011. **90**: p. 555-562.
97. Electric, F., *Little Giant- Chemical Resistance Chart*. 2012. p. 11. <https://www.jaspereng.com/wp-content/uploads/2016/12/SiemensChemical-ResistanceChart.pdf>. Accessed on 24th August 2020.
98. Grubb, J.F., *Resistance of Stainless Alloys to Dilute Sulfuric Acid*, in *CORROSION 2011*. 2011, NACE International: Houston, Texas. p. 7.
99. Crook, P., *Corrosion of Nickel and Nickel-Base Alloys*, in *Corrosion: Materials*, S.D. Cramer and B.S. Covino, Jr., Editors. 2005, ASM International. p. 228-251.
100. International Nickel Co. Inc., *Corrosion Resistance of The Austenitic Chromium-Nickel Stainless Steels in Chemical Environments*. The International Nickel Company Inc. 1963. p. 1-19.
101. Nickel Institute, *Alloy Selection for Service in Sulphuric Acid - A Guide to the Use of Nickel-Containing Alloys (2nd Edition)*. ISBN: 978-1-5231-3101-3. Nickel Institute. 2019. p. 34-69.
102. Jian, Z., P. Ju, C. Wang, Y. Dun, X. Zhao, Y. Zuo, and Y. Tang, *Corrosion Behaviour of 316L Stainless Steel in Hot Dilute Sulphuric Acid Solution with Sulphate and NaCl*. Protection of Metals and Physical Chemistry of Surfaces, 2019. **55**(1): p. 148-156.
103. Kritzer, P., N. Boukis, and E. Dinjus, *Factors controlling corrosion in high-temperature aqueous solutions: a contribution to the dissociation and solubility data influencing corrosion processes*. The Journal of Supercritical Fluids, 1999. **15**(3): p. 205-227.
104. Marshall, W.L. and E.V. Jones, *Second Dissociation Constant of Sulfuric Acid from 25 to 350° Evaluated from Solubilities of Calcium Sulfate in Sulfuric Acid Solutions*^{1,2}. The Journal of Physical Chemistry, 1966. **70**(12): p. 4028-4040.
105. Saleh, S.B., J.P. Flensburg, T.K. Shoulaifar, Z. Sárossy, B.B. Hansen, H. Egsgaard, N. DeMartini, P.A. Jensen, P. Glarborg, and K. Dam-Johansen, *Release of Chlorine and*

- Sulfur during Biomass Torrefaction and Pyrolysis*. Energy & Fuels, 2014. **28**(6): p. 3738-3746.
106. Suriyati B.S., Julie Pauline F., Tooran K.S., Zsuzsa S., Brian B.H., Helge E., Nikolai De., Peter A.J., Peter G., and Kim D.J., *Release of Chlorine and Sulfur during Biomass Torrefaction and Pyrolysis*, Energy & Fuels, 2014. **28**(6): p. 3738-3746.
 107. NESCAUM, *Elemental Analysis of Wood Fuels*. 2013, New York State Energy Research and Development Authority.
 108. Li, K., Y. Zeng, and J.-L. Luo, *Condensed phase corrosion of P91 and DSS 2205 steels at advanced oxygen-fired pressurized fluidized bed combustion plants*. Materials and Corrosion. 2021. **72**: p. 757– 771.
 109. Gilbert, N., I. Hobbs, and J. Levine, *Hydrolysis of wood-using dilute sulfuric acid*. Industrial & Engineering Chemistry, 1952. **44**(7): p. 1712-1720.
 110. Kim, K.H., M.P. Tucker, and Q.A. Nguyen, *Effects of pressing lignocellulosic biomass on sugar yield in two-stage dilute-acid hydrolysis process*. Biotechnology Progress, 2002. **18**(3): p. 489-494.
 111. Kumar, S., P. Dheeran, S.P. Singh, I.M. Mishra, and D.K. Adhikari, *Kinetic studies of two-stage sulphuric acid hydrolysis of sugarcane bagasse*. Renewable Energy, 2015. **83**: p. 850-858.
 112. Yang, G., M. Jahan, L. Ahsan, L. Zheng, and Y. Ni, *Recovery of acetic acid from pre-hydrolysis liquor of hardwood kraft-based dissolving pulp production process by reactive extraction with triisooctylamine*. Bioresource Technology, 2013. **138**: p. 253-258.
 113. Rivas, S., C. Vila, V. Santos, and J.C. Parajó, *Furfural production from birch hemicelluloses by two-step processing: a potential technology for biorefineries*. Holzforschung, 2016. **70**(10): p. 901-910.
 114. Cutrim, F.M., E.C.S.S. Ramos, M.C.C. Abreu, A.S. Godinho, A.P. Maciel, C.J.S. Mendonça, and K.S.B. Cavalcante, *A Study of Chemical Composition and Enzymatic Hydrolysis of Solid Organic Waste from Agrosilvopastoral Systems*. Journal of the Brazilian Chemical Society, 2019. **30**: p. 1955-1963.
 115. Sunaba, T., Y. Tomoe, S. Hirano, D. Ito, and S. Okazaki, *Effect of acetic acid on corrosion behaviour of modified martensitic stainless steels in high temperature sour environments*. EUROCORR 2014 European Corrosion Congress Proceedings. 2014.

116. Chou, Y.L., J.W. Yeh, and H.C. Shih, *The effect of molybdenum on the corrosion behaviour of the high-entropy alloys Co_{1.5}CrFeNi_{1.5}Ti_{0.5}Mo_x in aqueous environments*. Corrosion Science, 2010. **52**(8): p. 2571-2581.
117. Gallo, G. and J. Edmondson, *The effect of molybdenum on stainless steels and naphthenic acid corrosion resistance*, in *CORROSION 2008*, 2008. NACE International: New Orleans, Louisiana. p. 13.
118. Sekine, I., T. Kawase, M. Kobayashi, and M. Yuasa, *The effects of chromium and molybdenum on the corrosion behaviour of ferritic stainless steels in boiling acetic acid solutions*. Corrosion Science, 1991. **32**(8): p. 815-825.
119. Mesquita, T.J., E. Chauveau, M. Mantel, N. Kinsman, and R.P. Nogueira, *Influence of Mo alloying on pitting corrosion of stainless steels used as concrete reinforcement*. Rem: Revista Escola de Minas, 2013. **66**: p. 173-178.
120. Wang, Z., F. Di-Franco, A. Seyeux, S. Zanna, V. Maurice, and P. Marcus, *Passivation-Induced Physicochemical Alterations of the Native Surface Oxide Film on 316L Austenitic Stainless Steel*. Journal of The Electrochemical Society, 2019. **166**(11): p. C3376-C3388.
121. Wu, X., H.M. Jing, Y. Zheng, Z.M. Yao, and W. Ke, *Resistance of Mo-bearing stainless steels and Mo-bearing stainless-steel coating to naphthenic acid corrosion and erosion–corrosion*. Corrosion Science, 2004. **46**: p. 1013-1032.
122. Vincent M., Hao P., Lorena H. Klein, Antoine S., Sandrine Z., Philippe M., *Effects of molybdenum on the composition and nanoscale morphology of passivated austenitic stainless steel surfaces*, Faraday Discuss., 2015. **18**: p. 151-170.
123. OGAWA, H., H. OMATA, I. ITOH, and H. OKADA, *Auger Electron Spectroscopic and Electrochemical Analysis of the Effect of Alloying Elements on the Passivation Behavior of Stainless Steels*. CORROSION, 1978. **34**(2): p. 52-60.
124. Hashimoto, K., K. Asami, A. Kawashima, H. Habazaki, and E. Akiyama, *The role of corrosion-resistant alloying elements in passivity*. Corrosion Science, 2007. **49**(1): p. 42-52.
125. Lynch, B., Z. Wang, L. Ma, E.-M. Paschalidou, F. Wiame, V. Maurice, and P. Marcus, *Passivation-Induced Cr and Mo Enrichments of 316L Stainless Steel Surfaces and Effects of Controlled Pre-Oxidation*. Journal of the Electrochemical Society, 2020. **167**: 141509.

126. Ha, H.-Y., T.-H. Lee, J.-H. Bae, and D.W. Chun, *Molybdenum Effects on Pitting Corrosion Resistance of FeCrMnMoNC Austenitic Stainless Steels*. Metals, 2018. **8**(8): p. 653.
127. Archer, D.G. and P. Wang, *The Dielectric Constant of Water and Debye-Hückel Limiting Law Slopes*. Journal of Physical and Chemical Reference Data, 1990. **19**(2): p. 371-411.
128. Guzonas, D., R. Novotny, S. Penttilä, A. Toivonen, and W. Zheng, *4 - Water chemistry*, in *Materials and Water Chemistry for Supercritical Water-cooled Reactors*, D. Guzonas, et al., Editors. 2018, Woodhead Publishing. p. 79-138.
129. Bandura, A. and S. Lvova, *The Ionization Constant of Water over Wide Ranges of Temperature and Density*. Journal of Physical and Chemical Reference Data, 2006. **35**: 15.
130. Duan, Z., F. Arjmand, L. Zhang, and H. Abe, *Investigation of the corrosion behavior of 304L and 316L stainless steels at high-temperature borated and lithiated water*. Journal of Nuclear Science and Technology, 2016. **53**(9): p. 1435-1446.
131. Kritzer, P., *Corrosion in high-temperature and supercritical water and aqueous solutions: a review*. The Journal of Supercritical Fluids, 2004. **29**(1): p. 1-29.
132. Faes, W., S. Lecompte, Z.Y. Ahmed, J.V. Bael, R. Salenbien, K. Verbeken, and M.D. Paepe, *Corrosion and corrosion prevention in heat exchangers*. Corrosion Reviews, 2019. **37**(2): p. 131-155.
133. Terachi, T., T. Yamada, T. Miyamoto, K. Arioka, and K. Fukuya, *Corrosion Behavior of Stainless Steels in Simulated PWR Primary Water—Effect of Chromium Content in Alloys and Dissolved Hydrogen*. Journal of Nuclear Science and Technology, 2008. **45**(10): p. 975-984.
134. Chen, K., W. Jiamei, D. du, X. Guo, L. Zhang, and P. Andresen, *Stress corrosion crack growth behavior of 310S stainless steel in supercritical water*. CORROSION, 2018. **74**(7): p.776-787.
135. Holcomb, G.R., C. Carney, and Ö.N. Doğan, *Oxidation of alloys for energy applications in supercritical CO₂ and H₂O*. Corrosion Science, 2016. **109**: p. 22-35.
136. Mahboubi, S., H. Zurob, G. Botton, and J. Kish, *Silicon Effects on the Wet Oxidation of Type 310 Stainless Steel*. Corrosion Science, 2018. **143**: p. 376-389.
137. Asteman, H., J.-E. Svensson, and L.-G. Johansson, *Oxidation of 310 steel in H₂O/O₂ mixtures at 600 °C: The effect of water-vapour-enhanced chromium evaporation*. Corrosion Science, 2002. **44**: p. 2635-2649.

138. Chen, H., R. Tang, C. Long, and G. Le, *Effect of exposure temperature on the corrosion behaviors of TP347H austenitic stainless steel in supercritical water*. Corrosion Science, 2019. **161**: p. 108188
139. Jansson, S., W. Hübner, G. Östberg, and M.d. Pourbaix, *Oxidation Resistance of Some Stainless Steels and Nickel-Based Alloys in High-Temperature Water and Steam*. British Corrosion Journal, 1969. **4**(1): p. 21-31.
140. Wang, K., J. Wang, and W. Hu, *Evaluation of temperature effect on the corrosion process of 304 stainless steel in high temperature water with electrochemical noise*. Materials & Design, 2015. **82**: p. 155-163.
141. Maekawa, T., M. Kagawa, and N. Nakajima, *Corrosion Behaviors of Stainless Steel in High-Temperature Water and Superheated Steam*. Transactions of the Japan Institute of Metals, 1968. **9**(2): p. 130-136.
142. Castello, D., T.H. Pedersen, and L.A. Rosendahl, *Continuous hydrothermal liquefaction of biomass: A critical review*. Energies, 2018. **11**(11): p. 3165.
143. Gordon, B., *Corrosion and Corrosion Control in Light Water Reactors*. JOM, 2013. **65**(8): p. 1043-1056.
144. Arcis, H., J.P. Ferguson, J.S. Cox, and P.R. Tremaine, *The Ionization Constant of Water at Elevated Temperatures and Pressures: New Data from Direct Conductivity Measurements and Revised Formulations from $T = 273\text{ K}$ to 674 K and $p = 0.1\text{ MPa}$ to 31 MPa* . Journal of Physical and Chemical Reference Data, 2020. **49**: p. 033103.
145. Hai-Fei, Z., H. Xie, Y. Xu, M. Song, J. Guo, and Y. Zhang, *The electrical conductivity of H_2O at $0.21\text{--}4.18\text{ GPa}$ and $20\text{--}350^\circ\text{C}$* . Chinese Science Bulletin, 1997. **42**: p. 969-976.
146. Nazari, L., S. Sarathy, D. Santoro, D. Ho, M.B. Ray, and C. Xu, *3 - Recent advances in energy recovery from wastewater sludge*, in *Direct Thermochemical Liquefaction for Energy Applications*, L. Rosendahl, Editor. 2018, Woodhead Publishing. p. 67-100.
147. Cheng, F., T. Le Doux, B. Treftz, S. Woolf, J. Yu, J. Miller, U. Jena, and C.E. Brewer, *Modification of a pilot-scale continuous flow reactor for hydrothermal liquefaction of wet biomass*. MethodsX, 2019. **6**: p. 2793-2806.
148. Anastasakis, K., P. Biller, R.B. Madsen, M. Glasius, and I. Johannsen, *Continuous Hydrothermal Liquefaction of Biomass in a Novel Pilot Plant with Heat Recovery and Hydraulic Oscillation*. Energies, 2018. **11**(10): p. 2695.

149. Ekambara, K., R.S. Sanders, K. Nandakumar, and J.H. Masliyah, *Hydrodynamic Simulation of Horizontal Slurry Pipeline Flow Using ANSYS-CFX*. Industrial & Engineering Chemistry Research, 2009. **48**(17): p. 8159-8171.
150. Gruar, R.I., C.J. Tighe, and J.A. Darr, *Scaling-up a Confined Jet Reactor for the Continuous Hydrothermal Manufacture of Nanomaterials*. Industrial & Engineering Chemistry Research, 2013. **52**(15): p. 5270-5281.
151. Trevin, S., *7 - Flow accelerated corrosion (FAC) in nuclear power plant components*, in *Nuclear Corrosion Science and Engineering*, D. Féron, Editor. 2012, Woodhead Publishing. p. 186-229.
152. Bandura, A.V. and S.N. Lvov, *The Ionization Constant of Water over Wide Ranges of Temperature and Density*. Journal of Physical and Chemical Reference Data, 2006. **35**(1): p. 15-30.
153. Wagner, W. and A. Pruß, *The IAPWS Formulation 1995 for the Thermodynamic Properties of Ordinary Water Substance for General and Scientific Use*. Journal of Physical and Chemical Reference Data, 2002. **31**(2): p. 387-535.
154. Peterson, A.A., F. Vogel, R.P. Lachance, M. Fröling, J.M.J. Antal, and J.W. Tester, *Thermochemical biofuel production in hydrothermal media: A review of sub- and supercritical water technologies*. Energy & Environmental Science, 2008. **1**(1): p. 32-65.
155. Trépanier, C. and A. Pelton, *Effect of temperature and ph on the corrosion resistance of passivated nitinol and stainless steel*. Medical Device Materials II - Proceedings of the Materials and Processes for Medical Devices Conference, 2004.
156. Kim, H., D.B. Mitton, and R.M. Latanision, *Effect of pH and Temperature on Corrosion of Nickel-Base Alloys in High Temperature and Pressure Aqueous Solutions*. Journal of The Electrochemical Society, 2010. **157**(5): p. C194-C199.
157. Shao, J.-M., C.-W. Du, X. Zhang, and L.-Y. Cui, *Effects of Lead on the Initial Corrosion Behavior of 316LN Stainless Steel in High-Temperature Alkaline Solution*. Acta Metallurgica Sinica (English Letters), 2019. **32**(1): p. 89-97.
158. You, H.-x., H.-b. Xu, Y. Zhang, S.-l. Zheng, and Y.-y. Gao, *Potential—pH diagrams of Cr-H₂O system at elevated temperatures*. Transactions of Nonferrous Metals Society of China, 2010. **20**(Supplement 1): p. s26-s31.

159. Brady, M.P., J.R. Keiser, D.N. Leonard, L. Whitmer, and J.K. Thomson, *Corrosion Considerations for Thermochemical Biomass Liquefaction Process Systems in Biofuel Production*. JOM - Journal of the Minerals, Metals and Materials Society, 2014. **66**: p. 2583-2592.
160. Brady, M.P., J.R. Keiser, D.N. Leonard, L. Whitmer, and J.K. Thomson, *Corrosion considerations for thermochemical biomass liquefaction process systems in biofuel production*. JOM. Journal of the Minerals, Metals & Materials Society, 2014: p. Medium: ED; Size: p. 2583-2592.
161. Duan, P. and P.E. Savage, *Hydrothermal liquefaction of a microalga with heterogeneous catalysts*. Industrial & Engineering Chemistry Research, 2010. **50**(1): p. 52-61.
162. Orebom, A., J.J. Verendel, and J.S.M. Samec, *High Yields of Bio Oils from Hydrothermal Processing of Thin Black Liquor without the Use of Catalysts or Capping Agents*. ACS Omega, 2018. **3**(6): p. 6757-6763.
163. Ong B., Walmsley T., Atkins M., Walmsley M., *A Kraft Mill-Integrated Hydrothermal Liquefaction Process for Liquid Fuel Co-Production*. Processes, 2020. **8**(10): 1216.
164. Ong, B.H.Y., T.G. Walmsley, M.J. Atkins, and M.R.W. Walmsley, *Hydrothermal liquefaction of Radiata Pine with Kraft black liquor for integrated biofuel production*. Journal of Cleaner Production, 2018. **199**: p. 737-750.
165. Xia, D.-H., Y. Behnamian, and J.-L. Luo, *Review—Factors Influencing Sulfur Induced Corrosion on the Secondary Side in Pressurized Water Reactors (PWRs)*. Journal of The Electrochemical Society, 2019. **166**(2): p. C49-C64.
166. Ahmed, S.R., *Influence of high temperature on corrosion behavior of 304 stainless steel in chloride solutions*. AIP Advances, 2016. **6**(11): p. 115301.
167. Klapper, H., J. Stevens, and G. Wiese, *Pitting Corrosion Resistance of CrMn Austenitic Stainless Steel in Simulated Drilling Conditions—Role of pH, Temperature, and Chloride Concentration*. Corrosion, 2013. **69**: p. 1095-1102.
168. Little, B.J., R.I. Ray, and R.K. Pope, *Relationship Between Corrosion and the Biological Sulfur Cycle: A Review*. Corrosion, 2000. **56**(4).
169. West, E.A., T. Nolan, D.S. Morton, G. Young, J.V. Mullen, G. Newsome, and C. Ehlert, *Effect of Sulfur on the SCC and Corrosion Fatigue Performance of Stainless Steel*,

- Conference on Contribution of Materials Investigations and Operating Experience to LWRs' Safety, Performance and Reliability, 2014. **46**(30).
170. Onaivi, D., T. Jibatswen, and O. Michael, *Effect of Chlorine and Sulphur on Stainless Steel (AISI 310) Due To High Temperature Corrosion*. American Journal of Engineering Research, 2016. **5**: p. 266-270.
 171. Cheng, X., X. Li, L. Yang, and C. Du, *Corrosion resistance of 316L stainless steel in acetic acid by EIS and Mott-Schottky*. Journal of Wuhan University of Technology-Mater. Sci. Ed., 2008. **23**(4): p. 574-578.
 172. Sekine, I., A. Masuko, and K. Senoo, *Corrosion Behavior of AISI 316 Stainless Steel in Formic and Acetic Acid Solutions*. CORROSION, 1987. **43**(9): p. 553-560.
 173. Invernizzi, A.J., E. Sivieri, and S.P. Trasatti, *Corrosion behaviour of Duplex stainless steels in organic acid aqueous solutions*. Materials Science and Engineering: A, 2008. **485**(1): p. 234-242.
 174. Scribner, L.A., *Corrosion by Organic Acids*, in *Corrosion: Environments and Industries*, S.D. Cramer and B.S. Covino, Jr., Editors. 2006, ASM International. p. 0.
 175. maroo, s., C. Palogi, M. Srinivasan, and S. Rangarajan, *Chemical dissolution of iron substituted chromium oxide by dissolved ozone*. Progress in Nuclear Energy, 2019. **120**.
 176. Lee, A., D. Lewis, T. Kalaitzidis, and P. Ashman, *Technical issues in the large-scale hydrothermal liquefaction of microalgal biomass to biocrude*. Current Opinion in Biotechnology, 2016. **38**: p. 85-89.
 177. Johannsen, I., B. Kilsgaard, V. Milkevych, and D. Moore, *Design, Modelling, and Experimental Validation of a Scalable Continuous-Flow Hydrothermal Liquefaction Pilot Plant*. Processes, 2021. **9**.
 178. Khalifeh, A.R., A. Dehghan Banaraki, H. Daneshmanesh, and M.H. Paydar, *Stress corrosion cracking of a circulation water heater tubesheet*. Engineering Failure Analysis, 2017. **78**: p. 55-66.
 179. Handbook, A., *Design Review for Failure Analysis and Prevention*. 2002.
 180. Scenini, F. and A. Sherry, *Stress Corrosion Cracking of Sensitized Type 304 Stainless Steel in High-Temperature Water with Anionic Impurities Contamination*. Corrosion, 2012. **68**(12): p. 1094-1107.

181. Khalifeh, A., *Stress Corrosion Cracking Behavior of Materials*. Engineering Failure Analysis, 2020: p. 55.
182. Abe, H. and Y. Watanabe, *Effect of Physical Property of Water on SCC Growth Rate of 316L Stainless Steels in High-Temperature Water*. Key Engineering Materials, 2007. **353-358**: p. 270-274.
183. Ru, X. and R. Staehle, *Historical experience providing bases for predicting corrosion and stress corrosion in emerging supercritical water nuclear technology: part 1*. Corrosion, 2013. **69**(3): p. 211-229.
184. Honda, M., Y. Kobayashi, and A. Tamada, *Stress Corrosion Cracking of Stainless Alloys in Alkaline Sulfide Solutions*. Corrosion, 1992. **48**(10): p. 822-829.
185. Charlton, R.S. and A. Wensley. *Environmentally Assisted Cracking in the Pulp and Paper Industry*. Corrosion 2002 Proceedings. paper No. 02131.
186. Feron, D. and R.W. Staehle, *Stress Corrosion Cracking of Nickel Based Alloys in Water-cooled Nuclear Reactors: The Coriou Effect*. 2016: Elsevier Science.
187. Boukis, N. and P. Kritzer, *Corrosion phenomena on alloy 625 in aqueous solutions containing hydrochloric acid and oxygen under subcritical and supercritical conditions*. 1997, United States: NACE International.
188. Alley, D. and S.A. Bradley. *Failure of UNS N10276 Reactor in Supercritical Water Service*. in *CORROSION 2003*. 2003.
189. Marrone, P.A., R.M. Latanision, B. Mitton, S.H. Zhang, M.S. Quintana, J.A. Cline, and N. Caputy. *Corrosion Mitigation in SCWO Systems for Hazardous Waste Disposal*. in *CORROSION 98*. 1998.
190. Toor, I.-u.-H., *Effect of Mn Content and Solution Annealing Temperature on the Corrosion Resistance of Stainless Steel Alloys*. Journal of Chemistry, 2014. **2014**: p. 951471.
191. Tanzi, M.C., S. Farè, and G. Candiani, *Chapter 4 - Biomaterials and Applications*, in *Foundations of Biomaterials Engineering*, M.C. Tanzi, S. Farè, and G. Candiani, Editors. 2019, Academic Press. p. 199-287.
192. Tang, J., X. Yang, Y. Wang, H. Wang, Y. Xiao, M. Apreutesei, Z. Nie, and B. Normand, *Corrosion behavior of 2205 duplex stainless steels in HCl solution containing Sulfide*. Metals, 2019. **9**(3): p. 294.

193. Kangas, P. and G.C. Chai. *Use of advanced austenitic and duplex stainless steels for applications in Oil & Gas and Process industry.* in *Advanced Materials Research*. 2013. Trans Tech Publ.
194. Aden, A., M. Ruth, K. Ibsen, J. Jechura, K. Neeves, J. Sheehan, B. Wallace, L. Montague, A. Slayton, and J. Lukas, *Lignocellulosic Biomass to Ethanol Process Design and Economics Utilizing Co-Current Dilute Acid Prehydrolysis and Enzymatic Hydrolysis for Corn Stover*. 2002. 154.
195. Bendall, K.C., *Duplex stainless steel in the pulp and paper industry*, *Anti-Corrosion Methods and Materials*, 1997. **44**(3): pp. 170-174.
196. Sanni, O., A.P.I. Popoola, and O.S.I. Fayomi, *Enhanced corrosion resistance of stainless steel type 316 in sulphuric acid solution using eco-friendly waste product*. *Results in Physics*, 2018. **9**: p. 225-230.
197. Loto, R.T., *Corrosion behaviour of S43035 ferritic stainless steel in hot sulphate/chloride solution*. *Journal of Materials Research and Technology*, 2018. **7**(3): p. 231 - 239.
198. I.N. Limited, *Corrosion Resistance of the Austenitic Chromium-nickel Stainless Steels in Chemical Environments*. 2001: International Nickel Limited. p. 2-15.
199. I.N. Limited, *The Corrosion Resistance of Nickel-containing Alloys in Sulfuric Acid and Related Compounds*. 1983: International Nickel Company, Incorporated. p. 1-8.
200. Wachowiak, D., *Duplex Stainless Steels, a Cost Effective Option for Biofuel Facilities*. Available on <https://www.rolledalloys.ca/shared/library/technical-papers/corrosive/Duplex-Stainless-Steels-A-Cost-Effective-Option-for-Biofuel-Facilities.pdf>. Accessed on June 11st 2020.
201. MacDonald, P.E., *Supercritical Water Reactor (SCWR)-Survey of Materials Research and Development Needs to Assess Viability*. 2003, Idaho National Laboratory (INL): Idaho. p. 26-32.
202. Skoumalová, Z., J. Burda, and E. Křečanová, *High Temperature Oxidation of 9-12% Cr Materials P91 and P92 in Supercritical Water*. *Key Engineering Materials*, 2015. **635**: p. 106-111.
203. Zeng, Y.G., D., *Corrosion Assessment of Candidate Materials for Fuel Cladding in Canadian SCWR* *JOM*, 2016. **68** (2), **475-479**.

204. Viswanathan, R.S., J.; Tanzosh, J. M. , *Boiler materials for ultra-supercritical coal power plants—Steamside oxidation*. 2006. **15 (3)**, 255-274.
205. Yonezawa, T., 7.10 - *Nickel-Based Alloys*, in *Comprehensive Nuclear Materials (Second Edition)*, R.J.M. Konings and R.E. Stoller, Editors. 2020, Elsevier: Oxford. p. 319-354.
206. Mehta, K.K., Mukhopadhyay, P., Mandal, R.K. et al. *Mechanical Properties Anisotropy of Cold-Rolled and Solution-Annealed Ni-Based Hastelloy C-276 Alloy*. Metall Mater Trans A, 2014. **45**: p. 3493–3504.
207. Hayes, J., J. Gray, A. Szmodis, and C. Orme, *Influence of chromium and molybdenum on the corrosion of nickel-based alloys*. Corrosion, 2006. **62(6)**: p. 491-500.
208. Asami, K., M. Naka, K. Hashimoto, and T. Masumoto, *Effect of Molybdenum on the Anodic Behavior of Amorphous Fe-Cr-Mo-B Alloys in Hydrochloric Acid*. Journal of The Electrochemical Society, 1980. **127(10)**: p. 2130.
209. Lloyd, A., J. Noël, N. McIntyre, and D. Shoesmith, *Cr, Mo and W alloying additions in Ni and their effect on passivity*. Electrochimica Acta, 2004. **49**: p. 3015-3027.
210. Lloyd, A.C., D. Shoesmith, N. McIntyre, and J.J. Noel, *Effects of Temperature and Potential on the Passive Corrosion Properties of Alloys C22 and C276*. Journal of The Electrochemical Society, 2003. **150**: p. B120-B130.
211. Reed, R.P., *Nitrogen in austenitic stainless steels*. JOM, 1989. **41(3)**: p. 16-21.
212. Pardo, A., M. Merino, A. Coy, F. Viejo, R. Arrabal, and E. Matykina, *Pitting corrosion behaviour of austenitic stainless steels – combining effects of Mn and Mo additions*. Corrosion Science - CORROS SCI, 2008. **50**: p. 1796-1806.
213. Muwila, A., *The effect of manganese, nitrogen and molybdenum on the corrosion resistance of a low nickel (< 2 wt%) austenitic stainless steel*. 2006. p. 36-46.
214. Zhang, Q., R. Tang, K. Yin, X. Luo, and L. Zhang, *Corrosion behavior of Hastelloy C-276 in supercritical water*. Corrosion Science - CORROS SCI, 2009. **51**: p. 2092-2097.
215. Fujisawa, R., M. Sakaiharu, Y. Kurata, and Y. Watanabe, *Corrosion behaviour of nickel base alloys and 316 stainless steel in supercritical water under alkaline conditions*. Corrosion engineering, science and technology, 2005. **40(3)**: p. 244-248.
216. Munir A., Fredrik S., Pär G. J., Christopher N. Hulme S., *Modelling of Strengthening Mechanisms in Wrought Nickel-Based 825 Alloy Subjected to Solution Annealing*, Metals, 2021. **11(5)**: 771.

217. Andresen, P.L. *SCC of Alloy 825, High Cr Alloy 800 and Other Interesting Alloys in High Temperature Water*. in *CORROSION 2013*. 2013.
218. Zhang, L., J. Wang, and F. Arjmand, *Electrochemical Behavior of Alloy 825 at High-Temperature Pressurized Water–Chloride Solutions (30°C to 280°C)*. *Corrosion*, 2018. **74**(11): p. 1245-1258.
219. Ziemniak, S.E. and M. Hanson, *Corrosion behavior of NiCrMo Alloy 625 in high temperature, hydrogenated water*. *Corrosion Science*, 2003. **45**(7): p. 1595-1618.
220. Rodriguez, D., A. Merwin, Z. Karmiol, and D. Chidambaram, *Surface chemistry and corrosion behavior of Inconel 625 and 718 in subcritical, supercritical, and ultrasupercritical water*. *Applied Surface Science*, 2017. **404**: p. 443-451.
221. Morinaga, M., *5 - Titanium Alloys*, in *A Quantum Approach to Alloy Design*, M. Morinaga, Editor. 2019, Elsevier. p. 77-94.
222. Vaughan, J. and A. Alfantazi, *Corrosion of titanium and its alloys in sulfuric acid in the presence of chlorides*. *Journal of the Electrochemical society*, 2005. **153**(1): p. B6.
223. Krishnan, R. and M.K. Asundi, *Zirconium alloys in nuclear technology*. *Proceedings of the Indian Academy of Sciences Section C: Engineering Sciences*, 1981. **4**(1): p. 41-56.
224. Knittel, D.R. and R.T. Webster, *Corrosion Resistance of Zirconium and Zirconium Alloys in Inorganic Acids and Alkalies*, E.W. Kleefisch, Editor. 1981, ASTM International: West Conshohocken, PA. p. 191-203.
225. ASTM, *Standard practice for laboratory immersion corrosion testing of metals*, in *American Society for Testing and Materials G31-72*. 2004, ASTM International p. 1-8.
226. ASTM, *Standard guide for applying statistics to analysis of corrosion data*, in *American Society for Testing and Materials, ASTM G16-95, Annual Book of ASTM Standards*. 1995, ASTM International. p. 1-13.
227. ASTM, *Standard Practice for Preparing, Cleaning, and Evaluating Corrosion Test Specimens* in *ASTM International Standard Practice G1-03*. 2017, ASTM International. p. 1-9.
228. Antunes, R.A. and M.d. Oliveira, *Corrosion in biomass combustion: A materials selection analysis and its interaction with corrosion mechanisms and mitigation strategies*. *Corrosion Science*. *Corrosion Science* 2013. **76**: p. 6-26.

229. Guzonas, D. and W. Cook, *Cycle chemistry and its effect on materials in a supercritical water-cooled reactor: A synthesis of current understanding*. Corrosion Science 2012. **65**: p. 48-66.
230. Yimin Z., J. Li, B.S. Amirkhiz, W. Zheng, M. Matchim, and M. Podlesny. *Corrosion and Stress Corrosion Cracking of UNS S31008 and UNS N08810 Alloys in Supercritical Water*. in *CORROSION 2015*. 2015. Dallas, Texas: NACE International.
231. Li, K., Y. Zeng, and J.-L. Luo, *Corrosion performance of candidate boiler tube alloys under advanced pressurized oxy-fuel combustion conditions*. Energy, 2021. **215**: p. 119-178.
232. Baboian, R., *Corrosion Tests and Standards: Application and Interpretation*. 1995: ASTM International.
233. Gustavsson, L., J. Holmberg, V. Dornburg, R. Sathre, T. Eggers, K. Mahapatra, and G. Marland, *Using biomass for climate change mitigation and oil use reduction*. Energy Policy, 2007. **35**(11): p. 5671-5691.
234. Kaygusuz, K., *Climate Change and Biomass Energy for Sustainability*. Energy Sources, Part B: Economics, Planning, and Policy, 2010. **5**(2): p. 133-146.
235. Balat, M. and G. Ayar, *Biomass Energy in the World, Use of Biomass and Potential Trends*. Energy Sources, 2005. **27**(10): p. 931-940.
236. Lee, R.A. and J.-M. Lavoie, *From first- to third-generation biofuels: Challenges of producing a commodity from a biomass of increasing complexity*. Animal Frontiers, 2013. **3**(2): p. 6-11.
237. Kang, Q., L. Appels, T. Tan, and R. Dewil, *Bioethanol from Lignocellulosic Biomass: Current Findings Determine Research Priorities*. The Scientific World Journal, 2014. **2014**: p. 13.
238. Zheng, J. and L. Rehmman, *Extrusion Pretreatment of Lignocellulosic Biomass: A Review*. International Journal of Molecular Sciences, 2014. **15**(10): p. 18967.
239. Limayem, A. and S.C. Ricke, *Lignocellulosic biomass for bioethanol production: Current perspectives, potential issues and future prospects*. Progress in Energy and Combustion Science, 2012. **38**(4): p. 449-467.

240. Otun Saha, A.S., Nikkon Sarker, Md. Ashfaque Rahman Siddiqui, Foysal Hossen, Sanjoy Kumar Mukharjee, *Biomass as a Renewable Resource for Energy and Chemical Products, Renewable Energy Research*. Renewable Energy Research, 2017. **2**(1): p. 6-11.
241. *Corrosion in the Pulp and Paper Industry*, in *Corrosion: Environments and Industries*, S.D. Cramer and B.S. Covino, Jr., Editors. 2006, ASM International. p. 8-14.
242. Castillo, A.P. and D.L. Caudill, *Monitoring the effect of pulp and paper mill process changes on the corrosion resistance of 316 and 316L austenitic stainless steels*. 1997: NACE International, Houston, TX (United States). p. 15, Paper 374.
243. Loto, R.T., *Effect of elevated temperature variations on the corrosion resistance of S31603 and SS2562 austenitic stainless steels in chloride-sulphate environments*. Journal of Materials Research and Technology, 2019. **8**(6): p. 5415-5421.
244. Loto, R., *Pitting corrosion evaluation of austenitic stainless steel type 304 in acid chloride media*. Journal of Materials and Environmental Science, 2013. **4**: p. 448-459.
245. TEAKLE, N.L. and S.D. TYERMAN, *Mechanisms of Cl⁻ transport contributing to salt tolerance*. Plant, Cell & Environment, 2010. **33**(4): p. 566-589.
246. *Sulfur amino acids of plants: An overview*. Methods in Enzymology, 1987. **143**: p. 419 - 426.
247. Bourzi, H., R. Oukhrib, B. El Ibrahim, H. Abou Oualid, Y. Abdellaoui, B. Balkard, S. El Issami, M. Hilali, L. Bazzi, and C. Len, *Furfural Analogs as Sustainable Corrosion Inhibitors-Predictive Efficiency Using DFT and Monte Carlo Simulations on the Cu(111), Fe(110), Al(111) and Sn(111) Surfaces in Acid Media*. Sustainability, 2020. **12**: p. 3304.
248. Finšgar, M. and J. Jackson, *Application of corrosion inhibitors for steels in acidic media for the oil and gas industry: A review*. Corrosion Science, 2014. **86**: p. 17-41.
249. Ali, S.A., A.M. El-Shareef, R.F. Al-Ghamdi, and M.T. Saeed, *The isoxazolidines: the effects of steric factor and hydrophobic chain length on the corrosion inhibition of mild steel in acidic medium*. Corrosion Science, 2005. **47**(11): p. 2659-2678.
250. Verma, C., L.O. Olasunkanmi, E.E. Ebenso, and M.A. Quraishi, *Substituents effect on corrosion inhibition performance of organic compounds in aggressive ionic solutions: A review*. Journal of Molecular Liquids, 2018. **251**: p. 100-118.
251. *Standard Practice for Laboratory Immersion Corrosion Testing of Metals*.

252. Guzonas, D.A. and W.G. Cook, *Cycle chemistry and its effect on materials in a supercritical water-cooled reactor: A synthesis of current understanding*. Corrosion Science. **65**: p. 48-66.
253. ASTM, *Standard Guide for Applying Statistics to Analysis of Corrosion Data*. 2019. p. 1-12.
254. Wensley, A. and H. Dykstra, *Materials for fabrication and repair of batch digesters*. TAPPI Engineering and Papermakers Conference. 1998. p. 1-14.
255. Beverskog, B. and I. Puigdomenech, *Revised pourbaix diagrams for iron at 25–300 °C*. Corrosion Science, 1996. **38**(12): p. 2121-2135.
256. Lemire, R.J., *Chemical thermodynamics of iron part 1*. Chemical Thermodynamics ed. J. Perrone. Vol. 13a. 2013, Canada OECD, TAB, NEA.
257. Pourbaix, M., *Atlas of Electrochemical Equilibria in Aqueous Solutions*. Pergamon Press, Oxford 1966.
258. Zhou, X., C. Liao, Y. Wang, and Y. Zhu, *Constructing the Pourbaix diagram of Fe-Cl-H₂O ternary system under supercritical water conditions*. Electrochimica Acta, 2021. **377**: p. 138075.
259. Qiu, L. and D.A. Guzonas, *Prediction of metal oxide stability in supercritical water reactors - Pourbaix versus Ellingham*. 2013: Canada. p. 12.
260. Cook, W.G. and R.P. Olive, *Pourbaix diagrams for the iron–water system extended to high-subcritical and low-supercritical conditions*. Corrosion Science, 2012. **55**: p. 326-331.
261. Beverskog, B. and I. Puigdomenech, *Revised Pourbaix diagrams for Copper at 5-150 C*. 1995: Sweden. p. 67.
262. Marshall, W.L. and E.U. Franck, *Ion product of water substance, 0–1000 °C, 1–10,000 bars New International Formulation and its background*. Journal of Physical and Chemical Reference Data, 1981. **10**(2): p. 295-304.
263. Segal, M.G. and W.J. Williams, *Kinetics of metal oxide dissolution. Oxidative dissolution of chromium(III) oxide by potassium permanganate*. Journal of the Chemical Society, Faraday Transactions 1: Physical Chemistry in Condensed Phases, 1986. **82**(10): p. 3245-3254.

264. Casey, W.H., *Oxidation-Reduction Reactions and Eh-pH (Pourbaix) Diagrams*, in *Encyclopedia of Geochemistry: A Comprehensive Reference Source on the Chemistry of the Earth*, W.M. White, Editor. 2017, Springer International Publishing: Cham. p. 1-6.
265. Cook, W.G. and R.P. Olive, *Pourbaix diagrams for the iron–water system extended to high-subcritical and low-supercritical conditions*. *Corrosion Science*, 2012. **55**(Supplement C): p. 326-331.
266. Sun, B., X. Zuo, X. Cheng, and X. Li, *The role of chromium content in the long-term atmospheric corrosion process*. *npj Materials Degradation*, 2020. **4**(1): p. 37.
267. Huizinga, S. and W.E. Liek, *Corrosion Behavior of 13% Chromium Steel in Acid Stimulations*. *Corrosion*, 1994. **50**(07).
268. Chermat-Aourasse, N. and R. Kesri, *Corrosion-Electrochemical behavior of 13% chromium (Cr) martensitic stainless steel in hydrochloric acid (HCl) solutions*. *Protection of Metals*, 2007. **43**(4): p. 344-352.
269. Li, X. and K. Ogle, *The Passivation of Ni-Cr-Mo Alloys: Time Resolved Enrichment and Dissolution of Cr and Mo during Passive-Active Cycles*. *Journal of The Electrochemical Society*, 2019. **166**(11): p. C3179-C3185.
270. Li, X., J. Han, P. Lu, J.E. Saal, G.B. Olson, G.S. Frankel, J.R. Scully, and K. Ogle, *Communication—Dissolution and Passivation of a Ni-Cr-Fe-Ru-Mo-W High Entropy Alloy by Elementally Resolved Electrochemistry*. *Journal of The Electrochemical Society*, 2020. **167**(6): p. 061505.
271. Reartes, G.B., P.J. Morando, M.A. Blesa, P.B. Hewlett, and E. Matijevic, *Reactivity of Chromium Oxide in Aqueous Solutions. 2. Acid Dissolution*. *Langmuir*, 1995. **11**(6): p. 2277-2284.
272. Jolivet, J.-P., C. Chanéac, and E. Tronc, *Iron oxide chemistry. From molecular clusters to extended solid networks*. *Chemical Communications*, 2004(5): p. 481-483.
273. Park, S.-A., S.-H. Lee, and J.-G. Kim, *Effect of chromium on the corrosion behavior of low alloy steel in sulfuric acid*. *Metals and Materials International*, 2012. **18**.
274. Salmimies, R., M. Mannila, J. Juha, and A. Häkkinen, *Acidic dissolution of magnetite: experimental study on the effects of acid concentration and temperature*. *Clays and clay minerals*, 2011. **59**(2): p. 136-146.

275. MacCarthy, J., A. Nosrati, W. Skinner, and J. Addai-Mensah, *Dissolution and rheological behaviour of hematite and quartz particles in aqueous media at pH 1*. Chemical Engineering Research and Design, 2014. **92**(11): p. 2509-2522.
276. Tang, J., X. Yang, Y. Wang, H. Wang, Y. Xiao, M. Apreutesei, Z. Nie, and B. Normand, *Corrosion Behavior of 2205 Duplex Stainless Steels in HCl Solution Containing Sulfide*. Metals, 2019. **9**: p. 294.
277. Liu, H., J. Sun, J. Qian, B. Wang, S. Shi, Y. Zhu, Y. Wang, A. Neville, and Y. Hua, *Revealing the temperature effects on the corrosion behaviour of 2205 duplex stainless steel from passivation to activation in a CO₂-containing geothermal environment*. Corrosion Science, 2021. **187**: p. 109495.
278. Peña-Bahamonde, J., C. Wu, S.K. Fanourakis, S.M. Louie, J. Bao, and D.F. Rodrigues, *Oxidation state of Mo affects dissolution and visible-light photocatalytic activity of MoO₃ nanostructures*. Journal of Catalysis, 2020. **381**: p. 508-519.
279. Park, S.-J., S.-M. Seo, Y.-S. Yoo, H.-W. Jeong, and H. Jang, *Effects of Cr, W, and Mo on the High Temperature Oxidation of Ni-Based Superalloys*. Materials (Basel, Switzerland), 2019. **12**(18): p. 2934.
280. Hillery, R., *The Oxidation of Chromium Diffusion Coatings on Molybdenum and on Iron-Nickel Alloys*. 1966: The University of Manchester (United Kingdom).
281. Ziemiak, S., L. Anovitz, R. Castelli, and W. Porter, *Thermodynamics of Cr₂O₃, FeCr₂O₄, ZnCr₂O₄, and CoCr₂O₄*. The Journal of Chemical Thermodynamics, 2007. **39**: p. 1474–1492.
282. Benny, S., R. Grau-Crespo, and N.H. de Leeuw, *A theoretical investigation of α -Fe₂O₃-Cr₂O₃ solid solutions*. Physical Chemistry Chemical Physics, 2009. **11**(5): p. 808-815.
283. Lindwall, G. and K. Frisk, *Assessment and Evaluation of Mobilities for Diffusion in the bcc Cr-Mo-Fe System*. Journal of Phase Equilibria and Diffusion, 2012. **33**(5): p. 375-389.
284. Gorichev, I.G. and N.A. Kipriyanov, *Regular Kinetic Features of the Dissolution of Metal Oxides in Acidic Media*. Russian Chemical Reviews, 1984. **53**(11): p. 1039-1061.
285. Salmimies, R., M. Mannila, J. Kallas, and A. Häkkinen, *Acidic Dissolution of Magnetite: Experimental Study on the Effects of Acid Concentration and Temperature*. Clays and Clay Minerals, 2011. **59**(2): p. 136-146.

286. Xia, D., S. Song, R. Zhu, Y. Behnamian, C. Shen, J. Wang, J. Luo, Y. Lu, and S. Klimas, *A mechanistic study on thiosulfate-enhanced passivity degradation of Alloy 800 in chloride solutions*. *Electrochimica Acta*, 2013. **111**: p. 510-525.
287. SZKLARSKA-SMIALOWSKA, Z., *Review of Literature on Pitting Corrosion Published Since 1960*. *CORROSION*, 1971. **27**(6): p. 223-233.
288. Widyanto, B., M. Wahyunda, and R. Suratman, *Study of Temperature and Chloride Concentration Effect on Pitting Corrosion of AISI 316L with Immersion Method*. 2017.
289. Loto, R.T., *Pitting corrosion evaluation of austenitic stainless steel type 304 in acid chloride media*. *J. Mater. Environ. Sci.*, 2013. **4**(4): p. 448-459.
290. Nguyen, T.H. and R. Foley, *On the mechanism of pitting of aluminum*. *Journal of the Electrochemical Society*, 1979. **126**(11): p. 1855.
291. MacDougall, B., D. Mitchell, and M. Graham, *Changes in Oxide Films on Nickel during Long-Term Passivation*. *Journal of the Electrochemical Society*, 1985. **132**(12): p. 2895.
292. Rostron, A., *The correlation between molecular structure and tendency to maintain or to destroy iron passivity in aqueous solution—II. Activation effectiveness of anions present together with a corrosion inhibitor and/or an oxidant*. *Corrosion Science*, 1979. **19**(5): p. 321-334.
293. Cohn, E.J., F.F. Heyroth, and M.F. Menkin, *The dissociation constant of acetic acid and the activity coefficients of the ions in certain acetate solutions*. *Journal of the American Chemical Society*, 1928. **50**(3): p. 696-714.
294. Levanov, A.V., O.Y. Isaikina, U.D. Gurbanova, and V.V. Lunin, *Dissociation Constants of Perchloric and Sulfuric Acids in Aqueous Solution*. *The Journal of Physical Chemistry B*, 2018. **122**(23): p. 6277-6286.
295. Yin, Z.F., Y.R. Feng, W.Z. Zhao, C.X. Yin, and W. Tian, *Pitting corrosion behaviour of 316L stainless steel in chloride solution with acetic acid and CO₂*. *Corrosion Engineering, Science and Technology*, 2011. **46**(1): p. 56-63.
296. Wennersten, R., Q. Sun, and H. Li, *The future potential for Carbon Capture and Storage in climate change mitigation - An overview from perspectives of technology, economy and risk*. *Journal of Cleaner Production*, 2015. **103**: p. 724-736.

297. Wang, S., S. Zhao, X. Cheng, L. Qian, B. Barati, X. Gong, B. Cao, and C. Yuan, *Study on two-step hydrothermal liquefaction of macroalgae for improving bio-oil*. *Bioresource Technology*, 2021. **319**: p. 124176.
298. Gollakota, A.R.K., N. Kishore, and S. Gu, *A review on hydrothermal liquefaction of biomass*. *Renewable and Sustainable Energy Reviews*, 2018. **81**: p. 1378-1392.
299. Peter Ford, F., B.M. Gordon, and R.M. Horn, *Corrosion in Boiling Water Reactors*, in *Corrosion: Environments and Industries*, S.D. Cramer and B.S. Covino, Jr., Editors. 2006, ASM International. p. 341-361.
300. Wang, P., S. Grdanovska, D.M. Bartels, and G.S. Was, *Corrosion behavior of ferritic FeCrAl alloys in simulated BWR normal water chemistry*. *Journal of Nuclear Materials*, 2020: p. 152744.
301. Kim, D., H.-G. Lee, J.Y. Park, J.-Y. Park, and W.-J. Kim, *Effect of dissolved hydrogen on the corrosion behavior of chemically vapor deposited SiC in a simulated pressurized water reactor environment*. *Corrosion Science*, 2015. **98**: p. 304-309.
302. Scott, P., *An overview of materials degradation by stress corrosion in PWRs*, in *EUROCORR 2004*. 2004: Nice, France. p. 1-18.
303. Lim, D.-S., S.-H. Jeon, B.J. Bae, J. Choi, K.M. Song, and D.H. Hur, *Effect of zinc addition scenarios on general corrosion of Alloy 690 in borated and lithiated water at 330 °C*. *Corrosion Science*, 2021. **189**: p. 109627.
304. Zeng, Y. and D. Guzonas, *Corrosion Assessment of Candidate Materials for Fuel Cladding in Canadian SCWR*. *JOM*, 2016. **68**(2): p. 475-479.
305. Cattant, F., D. Crusset, and D. Féron, *Corrosion issues in nuclear industry today*. *Materials Today*, 2008. **11**(10): p. 32-37.
306. Perrin, s., M. Dumerval, L. Marchetti, M. Sennour, F. Jomard, S. Vaubaillon, and Y. Wouters, *Influence of irradiation on stainless steel corrosion in PWR primary conditions*. *EPJ Web of Conferences*, 2016. **115**: p. 04006.
307. Sun, H., X. Wu, and E.-H. Han, *Effects of temperature on the oxide film properties of 304 stainless steel in high temperature lithium borate buffer solution*. *Corrosion Science*, 2009. **51**(12): p. 2840-2847.

308. Mahboubi, S., H.S. Zurob, G.A. Botton, and J.R. Kish, *Environment Effects on Chromia (Cr₂O₃) Scale Stability Formed on Type 310S Stainless Steel During Wet Oxidation*. Corrosion, 2020. **76**(7): p. 678-689.
309. Tan, J., Z. Zhang, H. Zheng, X. Wang, J. Gao, X. Wu, E.-H. Han, S. Yang, and P. Huang, *Corrosion fatigue model of austenitic stainless steels used in pressurized water reactor nuclear power plants*. Journal of Nuclear Materials, 2020. **541**: p. 152407.
310. Raiman, S.S., K.G. Field, R.B. Rebak, Y. Yamamoto, and K.A. Terrani, *Hydrothermal corrosion of 2nd generation FeCrAl alloys for accident tolerant fuel cladding*. Journal of Nuclear Materials, 2020. **536**: p. 152221.
311. Sáez-Maderuelo, A., D. Gómez-Briceño, and C. Maffiotte, *Influence of Changes in Pressure and Temperature of Supercritical Water on the Susceptibility to Stress Corrosion Cracking of 316L Austenitic Stainless Steel*. Journal of Nuclear Engineering and Radiation Science, 2016. **3**(1).
312. Watanabe, Y., H. Abe, and Y. Daigo. *Environmentally assisted cracking of sensitized stainless steel in supercritical water Effects of physical property of water*. in *GENES4/ANP2003: International conference on global environment and advanced nuclear power plants*. 2003. Japan: Atomic Energy Society of Japan.
313. Montgomery, M. and A. Karlsson, *Survey of oxidation in steamside conditions*. VGB KRAFTWERKSTECHNIK-ENGLISH EDITION-, 1995. **75**: p. 235-240.
314. Ootoguro, Y., M. Sakakibara, T. Saito, H. Ito, and Y. Inoue, *Oxidation Behavior of Austenitic Heat-resisting Steels in a High Temperature and High Pressure Steam Environment*. Transactions of the Iron and Steel Institute of Japan, 1988. **28**(9): p. 761-768.
315. Holzapfel, W.B., *Effect of Pressure and Temperature on the Conductivity and Ionic Dissociation of Water up to 100 kbar and 1000°C*. The Journal of Chemical Physics, 1969. **50**(10): p. 4424-4428.
316. Beccaria, A.M., G. Poggi, and G. Castello, *Influence of passive film composition and sea water pressure on resistance to localised corrosion of some stainless steels in sea water*. British Corrosion Journal, 1995. **30**(4): p. 283-287.
317. Wang, J., J. Wang, and E.-H. Han, *Influence of Conductivity on Corrosion Behavior of 304 Stainless Steel in High Temperature Aqueous Environment*. Journal of Materials Science & Technology, 2016. **32**(4): p. 333-340.

318. Abe, H. and Y. Watanabe, *Effect of Physical Property of Water on SCC Growth Rate of 316L Stainless Steels in High-Temperature Water*. Key Engineering Materials - KEY ENG MAT, 2007. **353-358**: p. 270-274.
319. Thomsen, L.B.S., P.N. Carvalho, J.S. Dos Passos, K. Anastasakis, K. Bester, and P. Biller, *Hydrothermal liquefaction of sewage sludge; energy considerations and fate of micropollutants during pilot scale processing*. Water Research, 2020. **183**: p. 116101.
320. Gordon, B., *Corrosion degradation of materials in nuclear power reactors—lessons learned and future challenges: Non-Environmentally Assisted Cracking Corrosion Concerns Affecting Life Extension of Light Water Reactors*. Corrosion -Houston Tx-, 2013. **69**: p. 1039.
321. Singh, J.L., U. Kumar, N. Kumawat, S. Kumar, V. Kain, S. Anantharaman, and A.K. Sinha, *Flow accelerated corrosion of carbon steel feeder pipes from pressurized heavy water reactors*. Journal of Nuclear Materials, 2012. **429**(1): p. 226-232.
322. Poulson, B., *Predicting and Preventing Flow Accelerated Corrosion in Nuclear Power Plant*. International Journal of Nuclear Energy, 2014. **2014**: p. 423295.
323. Lister, D.H., W. Cook, A. Feicht, M. Khatibi, L. Liu, K. Fujiwara, E. Kadoi, T. Ohira, H. Takiguchi, and S. Uchida. *A laboratory study of flow-accelerated corrosion in feedwater systems*. in *The 16th pacific basin nuclear conference Pacific partnership toward a sustainable nuclear future*. 2008. Japan: Atomic Energy Society of Japan.
324. Tomarov, G.V. and A.A. Shipkov, *Flow-Accelerated Corrosion Wear of Power-Generating Equipment: Investigations, Prediction, and Prevention: I. Flow-Accelerated Corrosion Processes and Regularities*. Thermal Engineering, 2018. **65**(8): p. 493-503.
325. Xie, Y. and J. Zhang, *Corrosion and deposition on the secondary circuit of steam generators*. Journal of Nuclear Science and Technology, 2016. **53**(10): p. 1455-1466.
326. Ziemniak, S.E. and M. Hanson, *Corrosion behavior of 304 stainless steel in high temperature, hydrogenated water*. Corrosion Science, 2002. **44**(10): p. 2209-2230.
327. Rodriguez, D., A. Merwin, and D. Chidambaram, *On the oxidation of stainless steel alloy 304 in subcritical and supercritical water*. Journal of Nuclear Materials, 2014. **452**(1): p. 440-445.

328. Brunner, G., *Chapter 12 - Corrosion in Hydrothermal and Supercritical Water*, in *Supercritical Fluid Science and Technology*, G. Brunner, Editor. 2014, Elsevier. p. 591-619.
329. Svishchev, I.M., R.A. Carvajal-Ortiz, K.I. Choudhry, and D.A. Guzonas, *Corrosion behavior of stainless steel 316 in sub- and supercritical aqueous environments: Effect of LiOH additions*. *Corrosion Science*, 2013. **72**: p. 20-25.
330. Mukahiwa, K., F. Scenini, M.G. Burke, N. Platts, D.R. Tice, and J.W. Stairmand, *Corrosion fatigue and microstructural characterisation of Type 316 austenitic stainless steels tested in PWR primary water*. *Corrosion Science*, 2018. **131**: p. 57-70.
331. Kritzer, P., N. Boukis, and E. Dinjus, *Review of the Corrosion of Nickel-Based Alloys and Stainless Steels in Strongly Oxidizing Pressurized High-Temperature Solutions at Subcritical and Supercritical Temperatures*. *CORROSION*, 2000. **56**(11): p. 1093-1104.
332. Tremaine, P.R. and J.C. LeBlanc, *The solubility of magnetite and the hydrolysis and oxidation of Fe²⁺ in water to 300°C*. *Journal of Solution Chemistry*, 1980. **9**(6): p. 415-442.
333. Bohnsack, G., *The Solubility of Magnetite in Water and in Aqueous Solutions of Acid and Alkali*. Hemisphere Publishing Corporation. 1987.
334. Ball, J.W. and D.K. Nordstrom, *Critical Evaluation and Selection of Standard State Thermodynamic Properties for Chromium Metal and Its Aqueous Ions, Hydrolysis Species, Oxides, and Hydroxides*. *Journal of Chemical & Engineering Data*, 1998. **43**(6): p. 895-918.
335. Rai, D., B.M. Sass, and D.A. Moore, *Chromium(III) hydrolysis constants and solubility of chromium(III) hydroxide*. *Inorganic Chemistry*, 1987. **26**(3): p. 345-349.
336. Guo, L., L. Li, Y. Guo, and T. Deng, *Progresses on Thermodynamic Databases*. IOP Conference Series: Materials Science and Engineering, 2018. **382**: p. 052018.
337. Li, Y., D. Macdonald, J. Yang, J. Qiu, and S. Wang, *Point defect model for the corrosion of steels in supercritical water: Part I, film growth kinetics*. *Corrosion Science*, 2019. **163**: p. 108280.
338. Macdonald, D., *The history of the Point Defect Model for the passive state: A brief review of film growth aspects*. *Electrochimica Acta*, 2011. **56**: p. 1761-1772.

339. Macdonald, D.D., *The Point Defect Model for the Passive State*. Journal of The Electrochemical Society, 1992. **139**(12): p. 3434-3449.
340. Sequeira, C.A.C., *Diffusion in Solid-State Systems*, in *High Temperature Corrosion*, C.A.C. Sequeira, Editor. 2019. p. 146-170.
341. Kuang, W., X. Wu, and E.-H. Han, *The oxidation behaviour of 304 stainless steel in oxygenated high temperature water*. Corrosion Science, 2010. **52**(12): p. 4081-4087.
342. Lister, D.H., R.D. Davidson, and E. McAlpine, *The mechanism and kinetics of corrosion product release from stainless steel in lithiated high temperature water*. Corrosion Science, 1987. **27**(2): p. 113-140.
343. Robertson, J., *The mechanism of high temperature aqueous corrosion of stainless steels*. Corrosion Science, 1991. **32**(4): p. 443-465.
344. Hallström, S., L. Höglund, and J. Ågren, *Modeling of iron diffusion in the iron oxides magnetite and hematite with variable stoichiometry*. Acta Materialia - ACTA MATER, 2011. **59**: p. 53-60.
345. Robertson, J., *Modelling of corrosion and corrosion release in PWR primary circuits*, in *5. International conference on water chemistry of nuclear reactor systems*. 1989, British Nuclear Energy Society: United Kingdom. p. 81-87.
346. Hiroishi, D., C. Matsuura, and K. Ishigure, *Hydrolysis of chromium (III) ion and solubility of chromium (III) oxide in high temperature water*. Mineral Mag, 1998. **62**: p. 626-627.
347. Guzonas, D. and W. Cook, *Cycle chemistry and its effect on materials in a supercritical water-cooled reactor: A synthesis of current understanding*. Corrosion Science, 2012. **65**: p. 48-66.
348. Sproul, G.D., *Evaluation of Electronegativity Scales*. ACS Omega, 2020. **5**(20): p. 11585-11594.
349. Liu, S., S. Wang, J. Guo, and Q. Guo, *Polarity and surface structural evolution of iron oxide films*. RSC Advances, 2012. **2**(26): p. 9938-9943.
350. Trivedi, V., *Chemical Bonding for JEE Main & Advanced, NEET 2nd Edition*. 2019: Disha Publication.
351. Young, D.J., *Chapter 6 - Alloy Oxidation II: Internal Oxidation*, in *High Temperature Oxidation and Corrosion of Metals (Second Edition)*, D.J. Young, Editor. 2016, Elsevier. p. 261-333.

352. Piehl, C., Z. Toekei, and H.J. Grabke, *Influence of chromium diffusion and different surface finishes on the oxidation behaviour of chromium steels*. Materials at High Temperatures, 2000. **17**(2): p. 243-246.
353. Saunders, S.R.J., M. Monteiro, and F. Rizzo, *The oxidation behaviour of metals and alloys at high temperatures in atmospheres containing water vapour: A review*. Progress in Materials Science, 2008. **53**(5): p. 775-837.
354. D.J. Young. *Appendix D - Self-Diffusion Coefficients, in High Temperature Oxidation and Corrosion of Metals (Second Edition)*, 2016. Elsevier. p. 719-720.
355. Lobnig, R.E., H.P. Schmidt, K. Hennesen, and H.J. Grabke, *Diffusion of cations in chromia layers grown on iron-base alloys*. Oxidation of Metals, 1992. **37**(1): p. 81-93.
356. Sabioni, A.C.S., A.M. Huntz, J.N.V. Souza, M.D. Martins, and F. Jomard, *Diffusion of nickel in single- and polycrystalline Cr₂O₃*. Philosophical Magazine, 2008. **88**(3): p. 391-405.
357. Millot, F. and N. Yan, *Diffusion of O₁₈ in Fe₃O₄: An experimental approach to study the behavior of minority defects in oxides*. Journal of Physics and Chemistry of Solids, 1997. **58**(1): p. 63-72.
358. Hallström, S., L. Höglund, and J. Ågren, *Modeling of iron diffusion in the iron oxides magnetite and hematite with variable stoichiometry*. Acta Materialia, 2011. **59**(1): p. 53-60.
359. Millot, F., J.-C. Lorin de la Grandmaison, B. Klossa, Y. Niu, and J. Tarento, *Oxygen self-diffusion in Fe₃O₄: An experimental example of interactions between defects*. Berichte Der Bunsen-Gesellschaft-Physical Chemistry Chemical Physics, 1997. **101**: p. 1351-1354.
360. Kawamura, T., H. Takami, and K. Kuwahara, *Computation of high Reynolds number flow around a circular cylinder with surface roughness*. Fluid Dynamics Research, 1986. **1**(2): p. 145-162.
361. Eckert, M., *Pipe flow: a gateway to turbulence*. Archive for History of Exact Sciences, 2021. **75**(3): p. 249-282.
362. Wharton, J.A. and R.J.K. Wood, *Influence of flow conditions on the corrosion of AISI 304L stainless steel*. Wear, 2004. **256**(5): p. 525-536.
363. Zhang, S., R. Shi, and Y. Tan, *Comparison of the Solubility of ZnFe₂O₄, Fe₃O₄ and Fe₂O₃ in High Temperature Water*. Journal of Solution Chemistry, 2018. **47**.

364. Zhou, Z., *Diffusion model and analysis of diffusion process at lagrangian method*. arXiv preprint arXiv:2010.02514, 2020.
365. Mittemeijer, E.J. and H.C.F. Rozendaal, *A rapid method for numerical solution of Fick's second law where the diffusion coefficient is concentration dependent*. Scripta Metallurgica, 1976. **10**(10): p. 941-943.
366. Wan, T. and S. Saito, *Flow-Accelerated Corrosion of Type 316L Stainless Steel Caused by Turbulent Lead–Bismuth Eutectic Flow*. Metals, 2018. **8**: p. 627.
367. Bhattacharyya, K. and M.S. Uddin, *Reactive Solute Diffusion in Boundary Layer Flow through a Porous Medium over a Permeable Flat Plate with Power-Law Variation in Surface Concentration*. Journal of Engineering, 2013. **2013**: p. 840596.
368. Doran, P.M., *Chapter 10 - Mass Transfer*, in *Bioprocess Engineering Principles (Second Edition)*, P.M. Doran, Editor. 2013, Academic Press: London. p. 379-444.
369. Stellwag, B., *The mechanism of oxide film formation on austenitic stainless steels in high temperature water*. Corrosion Science, 1998. **40**(2): p. 337-370.
370. Shen, Z., D. du, L. Zhang, and S. Lozano-Perez, *An insight into PWR primary water SCC mechanisms by comparing surface and crack oxidation*. Corrosion Science, 2018. **148**.
371. Ecer, G.M., R.B. Singh, and G.H. Meier, *The influence of superficially applied oxide powders on the high-temperature oxidation behavior of Cr₂O₃-forming alloys*. Oxidation of Metals, 1982. **18**(1): p. 55-81.
372. Sugimoto, K., M. Seto, S. Tanaka, and N. Hara, *Corrosion Resistance of Artificial Passivation Films of Fe₂O₃-Cr₂O₃- NiO Formed by Metalorganic Chemical Vapor Deposition (MOCVD)*. ChemInform, 1993. **24**.
373. Sanchez, R.G., X. Huang, and P. Liu, *Effect of Water Density/Pressure on the Corrosion Behavior of 304 and 310 Stainless Steels*. Oxidation of Metals, 2018. **89**(1): p. 165-182.
374. Zheng, J.L., M.Q. Zhu, and H.T. Wu, *Alkaline hydrothermal liquefaction of swine carcasses to bio-oil*. Waste Manag, 2015. **43**: p. 230-8.
375. Posmanik, R., C.M. Martinez, B. Cantero-Tubilla, D.A. Cantero, D.L. Sills, M.J. Cocero, and J.W. Tester, *Acid and Alkali Catalyzed Hydrothermal Liquefaction of Dairy Manure Digestate and Food Waste*. ACS Sustainable Chemistry & Engineering, 2018. **6**(2): p. 2724-2732.

376. Liu, M., Y. Zeng, and J.-L. Luo, *Influence of Major Operating Parameters (Temperature, Pressure, and Flow Rate) on the Corrosion of Candidate Alloys for the Construction of Hydrothermal Liquefaction Biorefining Reactors*. *Energy & Fuels*, 2022. **36**(6): p. 3134-3153.
377. Ziemniak, S.E. and M.A. Goyette, *Nickel(II) Oxide Solubility and Phase Stability in High Temperature Aqueous Solutions*. *Journal of Solution Chemistry*, 2004. **33**(9): p. 1135-1159.
378. Körner, P., D. Jung, and A. Kruse, *Influence of the pH Value on the Hydrothermal Degradation of Fructose*. *ChemistryOpen*, 2019. **8**(8): p. 1109.
379. Zhang, X., J. Scott, B.K. Sharma, and N. Rajagopalan, *Advanced treatment of hydrothermal liquefaction wastewater with nanofiltration to recover carboxylic acids*. *Environmental Science: Water Research & Technology*, 2018. **4**(4): p. 520-528.
380. Belkheiri, T., S.-I. Andersson, C. Mattsson, L. Olausson, H. Theliander, and L. Vamling, *Hydrothermal liquefaction of kraft lignin in sub-critical water: the influence of the sodium and potassium fraction*. *Biomass Conversion and Biorefinery*, 2018. **8**(3): p. 585-595.
381. Behrendt, F., Y. Neubauer, M. Oevermann, B. Wilmes, and N. Zobel, *Direct liquefaction of biomass*. *Chemical Engineering & Technology: Industrial Chemistry-Plant Equipment-Process Engineering-Biotechnology*, 2008. **31**(5): p. 667-677.
382. Toor, S.S., L. Rosendahl, and A. Rudolf, *Hydrothermal liquefaction of biomass: a review of subcritical water technologies*. *Energy*, 2011. **36**(5): p. 2328-2342.
383. Vardon, D.R., *Chemical properties of biocrude oil from the hydrothermal liquefaction of Spirulina algae, swine manure, and digested anaerobic sludge*. *Bioresource Technology*, 2011. **102**(17): p. 8295 - 8303.
384. Huang, H., X. Yuan, H. Zhu, H. Li, Y. Liu, X. Wang, and G. Zeng, *Comparative studies of thermochemical liquefaction characteristics of microalgae, lignocellulosic biomass and sewage sludge*. *Energy*, 2013. **56**(C): p. 52-60.
385. Madsen, R.B. and M. Glasius, *How Do Hydrothermal Liquefaction Conditions and Feedstock Type Influence Product Distribution and Elemental Composition?* *Industrial & Engineering Chemistry Research*, 2019. **58**(37): p. 17583-17600.
386. Xu, D., G. Lin, S. Guo, S. Wang, Y. Guo, and Z. Jing, *Catalytic hydrothermal liquefaction of algae and upgrading of biocrude: A critical review*. *Renewable and Sustainable Energy Reviews*, 2018. **97**: p. 103-118.

387. Kazemi Shariat Panahi, H., M. Tabatabaei, M. Aghbashlo, M. Dehghani, M. Rehan, and A.-S. Nizami, *Recent updates on the production and upgrading of bio-crude oil from microalgae*. Bioresource Technology Reports, 2019. **7**: p. 100216.
388. López Barreiro, D., B.R. Gómez, F. Ronsse, U. Hornung, A. Kruse, and W. Prins, *Heterogeneous catalytic upgrading of biocrude oil produced by hydrothermal liquefaction of microalgae: State of the art and own experiments*. Fuel Processing Technology, 2016. **148**: p. 117-127.
389. Akhtar, J. and N.A.S. Amin, *A review on process conditions for optimum bio-oil yield in hydrothermal liquefaction of biomass*. Renewable and Sustainable Energy Reviews, 2011. **15**(3): p. 1615-1624.
390. Kumar, M., A. Olajire Oyedun, and A. Kumar, *A review on the current status of various hydrothermal technologies on biomass feedstock*. Renewable and Sustainable Energy Reviews, 2018. **81**: p. 1742-1770.
391. Ryoji Ito, T.F., Jun Sadaki, Yoichiro Matsumoto and Ji-Whan Ahn, *Removal of Chloride in Bottom Ash from the Industrial and Municipal Solid Waste Incinerators* Int. J. Soc. Master. Eng. Resour. , 2006. **13**(2).
392. Dewil, R., J. Baeyens, J. Roels, B. Van, and D. Steene, *Evolution of the Total Sulphur Content in Full-Scale Wastewater Sludge Treatment*. Environmental Engineering Science - ENVIRON ENG SCI, 2009. **26**.
393. Song, C., H. Hu, S. Zhu, G. Wang, and G. Chen, *Nonisothermal Catalytic Liquefaction of Corn Stalk in Subcritical and Supercritical Water*. Energy & Fuels, 2004. **18**(1): p. 90-96.
394. Shen, Z., J. Zhou, X. Zhou, and Y. Zhang, *The production of acetic acid from microalgae under hydrothermal conditions*. Applied Energy, 2011. **88**(10): p. 3444-3447.
395. Albrecht, K.O., R.A. Dagle, D.T. Howe, J.A. Lopez-Ruiz, S.D. Davidson, B. Maddi, A.R. Cooper, and E.A. Panisko, *Final Report for the Project Characterization and Valorization of Aqueous Phases Derived from Liquefaction and Upgrading of Bio-Oils*. 2018, ; Pacific Northwest National Lab. (PNNL), Richland, WA (United States). p. Medium: ED; Size: 48 p.
396. Davidson, S.D., J.A. Lopez-Ruiz, Y. Zhu, A.R. Cooper, K.O. Albrecht, and R.A. Dagle, *Strategies To Valorize the Hydrothermal Liquefaction-Derived Aqueous Phase into Fuels and Chemicals*. ACS Sustainable Chemistry & Engineering, 2019. **7**(24): p. 19889-19901.

397. Otero, E., A. Pardo, M.V. Utrilla, F.J. Pérez, and C. Merino, *The corrosion behaviour of AISI 304L AND 316L stainless steels prepared by powder metallurgy in the presence of organic acids*. Corrosion Science, 1997. **39**(3): p. 453-463.
398. Gras, J.M. and P. Spiteri, *Corrosion of stainless steels and nickel-based alloys for alkaline water electrolysis*. International Journal of Hydrogen Energy, 1993. **18**(7): p. 561-566.
399. ASTM, *Standard Guide for Corrosion Tests in High Temperature or High Pressure Environment, or Both*. 2021, ASTM International. p. 1-8.
400. Bayat, H., M. Dehghanizadeh, J.M. Jarvis, C.E. Brewer, and U. Jena, *Hydrothermal Liquefaction of Food Waste: Effect of Process Parameters on Product Yields and Chemistry*. Frontiers in Sustainable Food Systems, 2021. **5**(160).
401. Jena, U., K.C. Das, and J.R. Kastner, *Effect of operating conditions of thermochemical liquefaction on biocrude production from Spirulina platensis*. Bioresource Technology, 2011. **102**(10): p. 6221-6229.
402. Valdez, P.J., M.C. Nelson, H.Y. Wang, X.N. Lin, and P.E. Savage, *Hydrothermal liquefaction of Nannochloropsis sp.: Systematic study of process variables and analysis of the product fractions*. Biomass and Bioenergy, 2012. **46**: p. 317-331.
403. Pipitone, G., G. Zoppi, S. Bocchini, A.M. Rizzo, D. Chiamonti, R. Pirone, and S. Bensaid, *Aqueous phase reforming of the residual waters derived from lignin-rich hydrothermal liquefaction: investigation of representative organic compounds and actual biorefinery streams*. Catalysis Today, 2020. **345**: p. 237-250.
404. Shimizu, N., B. Zeng, and K. Kushima, *Hydrothermal liquefaction of wood chips under supercritical and subcritical water reaction conditions*. SN Applied Sciences, 2021. **3**(5): p. 577.
405. Koszelow, D., M. Makowska, F. Marone, J. Karczewski, P. Jasiński, and S. Molin, *High temperature corrosion evaluation and lifetime prediction of porous Fe22Cr stainless steel in air in temperature range 700–900 °C*. Corrosion Science, 2021. **189**: p. 109589.
406. Huang, X., K. Xiao, X. Fang, Z. Xiong, L. Wei, P. Zhu, and X. Li, *Oxidation behavior of 316L austenitic stainless steel in high temperature air with long-term exposure*. Materials Research Express, 2020. **7**(6): p. 066517.
407. Restrepo, O., J. Montoya, and E. Chavarriaga, *Optical and Magnetical Properties of FeCr₂O₄ Nanopigments with Spinel Type Structure*. 2014. p. 39-45.

408. Lotfian, N., A. Noorbakhsh, S. Mirsattari, A. Saberi, and K.D. Mackenzie, *A comparison of the effect of nanostructured MgCr₂O₄ and FeCr₂O₄ additions on the microstructure and mechanical properties of direct-bonded magnesia-chrome refractories*. *Ceramics International*, 2019. **46**.
409. Davalos Monteiro, R., J. van de Wetering, B. Krawczyk, and D.L. Engelberg, *Corrosion Behaviour of Type 316L Stainless Steel in Hot Caustic Aqueous Environments*. *Metals and Materials International*, 2020. **26**(5): p. 630-640.
410. Leygraf, C., Wallinder, I.O., Tidblad, J. and Graedel, T., *The atmospheric corrosion chemistry of iron and low alloy steels*, *Atmospheric Corrosion*. 2016. p. 302-315.
411. Davies, M. and N.D. Institute, *Alloy Selection for Service in Caustic Soda: A Guide to the Use of Nickel-containing Alloys*. 2019: Nickel Institute.
412. Francis, R. and S. Clarke, *Corrosion in Caustic Soda in Mineral Processing Operations*. *Corrosion*, 2020. **76**(7): p. 707-715.
413. Jolivet, J.-P., C. Chanéac, and E. Tronc, *Iron Oxide Chemistry. From Molecular Clusters to Extended Solid Networks*. *Chemical communications (Cambridge, England)*, 2004. **35**: p. 481-7.
414. Palmer, D.A., P. Bénézech, and D. Wesolowski. *Solubility of Nickel Oxide and Hydroxide in Water*. 2005.
415. Papassiopi, N., K. Vaxevanidou, C. Christou, E. Karagianni, and G.S.E. Antipas, *Synthesis, characterization and stability of Cr(III) and Fe(III) hydroxides*. *Journal of Hazardous Materials*, 2014. **264**: p. 490-497.
416. Spiccia, L., *Solubility of chromium(III) hydroxides*. *Inorganic Chemistry*, 1988. **27**(2): p. 432-434.
417. Ziemniak, S.E., M.E. Jones, and K.E.S. Combs, *Solubility and Phase Behavior of Cr(III) Oxides in Alkaline Media at Elevated Temperatures*. *Journal of Solution Chemistry*, 1998. **27**(1): p. 33-66.
418. Liu, X. and F.J. Millero, *The solubility of iron hydroxide in sodium chloride solutions*. *Geochimica et Cosmochimica Acta*, 1999. **63**(19): p. 3487-3497.
419. Gayer, K.H. and L. Woontner, *The Solubility of Ferrous Hydroxide and Ferric Hydroxide in Acidic and Basic Media at 25°*. *The Journal of Physical Chemistry*, 1956. **60**(11): p. 1569-1571.

420. Menting, V.L., *Solubility studies of iron (III) oxides and hydroxides*. 1994.
421. Scholz, F. and H. Kahlert, *The calculation of the solubility of metal hydroxides, oxide-hydroxides, and oxides, and their visualisation in logarithmic diagrams*. ChemTexts, 2015. **1**(1): p. 7.
422. Parker, V.B., *Thermodynamic Properties of the Aqueous Ions(2+ and 3+) of Iron and the Key Compounds of Iron* ACS, 1995. **47**.
423. Azizi, M., P.F. Biard, A. Couvert, and M. Ben Amor, *Simulation of hydrogen sulphide absorption in alkaline solution using a packed column*. Environ Technol, 2014. **35**(21-24): p. 3105-15.
424. Pasternak, G., *Chapter 9 - Electrochemical approach for biogas upgrading*, in *Emerging Technologies and Biological Systems for Biogas Upgrading*, N. Aryal, et al., Editors. 2021, Academic Press. p. 223-254.
425. Wang, H., Y. Wu, X. Sun, J. Ling, and D. Zou, *Corrosion Resistance to Chloride of a Novel Stainless Steel: The Threshold Chloride Value and Effect of Surface State*. Materials (Basel, Switzerland), 2019. **12**(14): p. 2235.
426. Zhang, B., J. Wang, B. Wu, X.W. Guo, Y.J. Wang, D. Chen, Y.C. Zhang, K. Du, E.E. Oguzie, and X.L. Ma, *Unmasking chloride attack on the passive film of metals*. Nature communications, 2018. **9**(1): p. 2559-2559.
427. Khaksar, L. and J. Shirokoff, *Effect of Elemental Sulfur and Sulfide on the Corrosion Behavior of Cr-Mo Low Alloy Steel for Tubing and Tubular Components in Oil and Gas Industry*. Materials, 2017. **10**: p. 430.
428. Newman, R.C., H.S. Isaacs, and B. Alman, *Effects of Sulfur Compounds on the Pitting Behavior of Type 304 Stainless Steel in Near-Neutral Chloride Solutions*. Corrosion, 1982. **38**(5): p. 261-265.
429. Böhni, H., *Localized Corrosion of Passive Metals*, in *Uhlig's Corrosion Handbook*. 2011. p. 157-169.
430. Parangusan, H., J. Bhadra, and N. Al-Thani, *A review of passivity breakdown on metal surfaces: influence of chloride- and sulfide-ion concentrations, temperature, and pH*. Emergent Materials, 2021. **4**(5): p. 1187-1203.
431. Ke, R. and R. Alkire, *Initiation of Corrosion Pits at Inclusions on 304 Stainless Steel*. Journal of The Electrochemical Society, 1995. **142**(12): p. 4056-4062.

432. Macdougall, B., D.F. Mitchell, and M.J. Graham, *Changes in Oxide Films on Nickel during Long Term Passivation*. Journal of The Electrochemical Society, 1985. **132**: p. 2895-2898.
433. Asaduzzaman, M.D., M. Mohammad, and M.M. Islam, *Effects of concentration of sodium chloride solution on the pitting corrosion behavior of AISI 304L austenitic stainless steel*. Chemical Industry and Chemical Engineering Quarterly, 2011. **17**: p. 477-483.
434. Park, J.O., S. Matsch, and H. Böhni, *Effects of Temperature and Chloride Concentration on Pit Initiation and Early Pit Growth of Stainless Steel*. Journal of The Electrochemical Society, 2002. **149**(2): p. B34.
435. Widyanto, B., M. Wahyunda, and R. Suratman, *Study of Temperature and Chloride Concentration Effect on Pitting Corrosion of AISI 316L with Immersion Method*. 2017.
436. Bohloul, M.R., S.M. Peyghambarzadeh, A. Lee, and A. Vatani, *Experimental and analytical study of solubility of carbon dioxide in aqueous solutions of potassium carbonate*. International Journal of Greenhouse Gas Control, 2014. **29**: p. 169-175.
437. Lown, D.A. and H.R. Thirsk, *Effect of the solution vapour pressure on the temperature dependence of the dissociation constant of acetic acid in water*. Journal of the Chemical Society, Faraday Transactions 1: Physical Chemistry in Condensed Phases, 1972. **68**(0): p. 1982-1986.
438. Vashishtha, H., R. Taiwade, and S. Sharma, *Effect of acetic acid on corrosion behavior of AISI 201, 304 and 430 stainless steels*, 2017. **108**(5): p. 406-415.
439. Kahyarian, A., A. Schumaker, B. Brown, and S. Nesic, *Acidic corrosion of mild steel in the presence of acetic acid: Mechanism and prediction*. Electrochimica Acta, 2017. **258**: p. 639-652.
440. Feng, S., Z. Yuan, M. Leitch, and C.C. Xu, *Hydrothermal liquefaction of barks into bio-crude – Effects of species and ash content/composition*. Fuel, 2014. **116**: p. 214-220.
441. Hwang, H., J.H. Lee, I.-G. Choi, and J.W. Choi, *Comprehensive characterization of hydrothermal liquefaction products obtained from woody biomass under various alkali catalyst concentrations*. Environmental Technology, 2019. **40**(13): p. 1657-1667.
442. Liu, M., Y. Zeng, and J.-L. Luo, *Influence of Major Operating Parameters (Temperature, Pressure, and Flow Rate) on the Corrosion of Candidate Alloys for the Construction of Hydrothermal Liquefaction Biorefining Reactors*. Energy & Fuels, 2022. **36**(6): p. 3134-3153.

443. Ali, M. and A. Al-Beed. *Performance of selected materials in flue gas environment*. in *CORROSION* 98. 1998.
444. Franklin, D., *Performance of Zirconium Alloys in Light Water Reactors with a Review of Nodular Corrosion*. 2011. p. 17-36.
445. Steinbrück, M., *High-Temperature Oxidation of Zirconium Alloys in Various Atmospheres*. 2020.
446. Pandey, C., A. Giri, and M. Mahapatra, *Evolution of phases in P91 steel in various heat treatment conditions and their effect on microstructure stability and mechanical properties*. *Materials Science and Engineering A*, 2016. **664**: p. 58-74.
447. Desu, R.K., H. Nitin Krishnamurthy, A. Balu, A.K. Gupta, and S.K. Singh, *Mechanical properties of Austenitic Stainless Steel 304L and 316L at elevated temperatures*. *Journal of Materials Research and Technology*, 2016. **5**(1): p. 13-20.
448. Gardner, L., A. Insausti, K.T. Ng, and M. Ashraf, *Elevated temperature material properties of stainless steel alloys*. *Journal of Constructional Steel Research*, 2010. **66**(5): p. 634-647.
449. Adams, R., *A review of the stainless steel surface*. *Journal of Vacuum Science & Technology A: Vacuum, Surfaces, and Films*, 1983. **1**(1): p. 12-18.
450. Park, J.H. and Y. Kang, *Inclusions in stainless steels— a review*. *steel research international*, 2017. **88**(12): p. 1700130.
451. Kowaka, M., H. Nagano, K. Yoshikawa, M. Miura, and K. Ota, *Development of nuclear grade type 316 stainless steel for BWR pipings*. *Karyoku Genshiryoku Hatsuden*, 1981. **32**(12): p. 1303-1315.
452. Rao, T.V., R.W. Vook, and W. Meyer, *Characterization of 316 stainless steel surfaces used in BWR recirculation piping*. *Nuclear Engineering and Design*, 1987. **101**(2): p. 167-174.
453. Behnamian, Y., A. Mostafaei, A. Kohandehghan, B. Shalchi Amirkhiz, D. Serate, Y. Sun, S. Liu, E. Aghaie, Y. Zeng, M. Chmielus, W. Zheng, D. Guzonas, W. Chen, and J.-L. Luo, *A comparative study of oxide scales grown on stainless steel and nickel-based superalloys in ultra-high temperature supercritical water at 800 °C*. *Corrosion Science*, 2016. **106**.
454. Guo, S., D. Xu, N. Wei, Y. Wang, G. Chen, and S. Wang, *Oxidation Processes and Involved Chemical Reactions of Corrosion-Resistant Alloys in Supercritical Water*. *Industrial & Engineering Chemistry Research*, 2020. **59**(22): p. 10278-10288.

455. Freire, L., M.J. Carmezim, M.G.S. Ferreira, and M.F. Montemor, *The electrochemical behaviour of stainless steel AISI 304 in alkaline solutions with different pH in the presence of chlorides*. *Electrochimica Acta*, 2011. **56**(14): p. 5280-5289.
456. Fattah-alhosseini, A. and S. Vafaeian, *Passivation behavior of a ferritic stainless steel in concentrated alkaline solutions*. *Journal of Materials Research and Technology*, 2015. **4**(4): p. 423-428.
457. Leinonen, H., P. Pohjanne, T. Saukkonen, T. Schildt, J. Romu, and H. Hänninen. *Effect Of Selective Dissolution On Stress Corrosion Cracking Susceptibility Of Austenitic And Duplex Stainless Steels In Alkaline Solutions*. in *CORROSION 2011*. 2011.
458. Kanazawa, Y. and M. Tsubota, *Stress corrosion cracking of cold worked stainless steel in high temperature water*. 1994, United States: NACE International, Houston, TX (United States).
459. Du, D., K. Chen, H. Lu, L. Zhang, X. Shi, X. Xu, and P.L. Andresen, *Effects of chloride and oxygen on stress corrosion cracking of cold worked 316/316L austenitic stainless steel in high temperature water*. *Corrosion Science*, 2016. **110**: p. 134-142.
460. Phull, B.S., W.L. Mathay, and R. Ross. *Corrosion Resistance of Duplex and 4-6% Mo-Containing Stainless Steels in FGD Scrubber Absorber Slurry Environments*. in *Corrosion-national association of corrosion engineers annual conference*. 2000. NACE.
461. Zeng, Y., K. Li, R. Hughes, and J.-L. Luo, *Corrosion Mechanisms and Materials Selection for the Construction of Flue Gas Component in Advanced Heat and Power Systems*. *Industrial & Engineering Chemistry Research*, 2017. **56**(48): p. 14141-14154.
462. Cuevas-Arteaga, C., D. Verhelst, and A. Alfantazi, *Performance of alloy 625 under combustion gas environments: a review*. *ECS Transactions*, 2010. **28**(24): p. 61.
463. Ahmad, Z., *CHAPTER 2 - BASIC CONCEPTS IN CORROSION*, in *Principles of Corrosion Engineering and Corrosion Control*, Z. Ahmad, Editor. 2006, Butterworth-Heinemann: Oxford. p. 9-56.
464. Marimuthu, V., I. Dulac, and K. Kannoorpatti, *Significance of Pourbaix Diagrams to Study the Corrosion Behaviour of Hardfacing Alloys Based on Chromium Carbides at 298 K (25 °C)*. *Journal of Bio- and Tribo-Corrosion*, 2016. **2**(3): p. 17.
465. McCafferty, E., *Thermodynamics of Corrosion: Pourbaix Diagrams*, in *Introduction to Corrosion Science*. 2010, Springer New York: New York, NY. p. 95-117.

466. Beverskog, B. and I. Puigdomenech, *Revised pourbaix diagrams for chromium at 25–300 °C*. Corrosion Science, 1997. **39**(1): p. 43-57.
467. Perry, S.C., S.M. Gateman, L.I. Stephens, R. Lacasse, R. Schulz, and J. Mauzeroll, *Pourbaix Diagrams as a Simple Route to First Principles Corrosion Simulation*. Journal of The Electrochemical Society, 2019. **166**(11): p. C3186-C3192.
468. Puigdomenech I., *Medusa Software*. Accessed on May 20th, 2017.
469. Sahle, C.J., C. Sternemann, C. Schmidt, S. Lehtola, S. Jahn, L. Simonelli, S. Huotari, M. Hakala, T. Pylkkänen, A. Nyrow, K. Mende, M. Tolan, K. Hämäläinen, and M. Wilke, *Microscopic structure of water at elevated pressures and temperatures*. Proceedings of the National Academy of Sciences, 2013. **110**(16): p. 6301-6306.
470. Wang, L., A. Seyeux, and P. Marcus, *Thermal stability of the passive film formed on 316L stainless steel surface studied by ToF-SIMS*. Corrosion Science, 2020. **165**: p. 108395.
471. Fujiwara, K., K. Watanabe, M. Domae, and Y. Katsumura. *Stability Of Chromium Oxide Film Formed By Metal Organic Chemical Vapor Deposition In High Temperature Water Up To Supercritical Region*. in *CORROSION 2007*. 2007.
472. Shibaeva, T.V., V.K. Laurinavichyute, G.A. Tsirlina, A.M. Arsenkin, and K.V. Grigorovich, *The effect of microstructure and non-metallic inclusions on corrosion behavior of low carbon steel in chloride containing solutions*. Corrosion Science, 2014. **80**: p. 299-308.
473. Sarkar, P.P., P. Kumar, M.K. Manna, and P.C. Chakraborti, *Microstructural influence on the electrochemical corrosion behaviour of dual-phase steels in 3.5% NaCl solution*. Materials Letters, 2005. **59**(19): p. 2488-2491.
474. Jia, T., R. Ni, H. Wang, J. Shen, and Z. Wang, *Investigation on the Formation of Cr-Rich Precipitates at the Interphase Boundary in Type 430 Stainless Steel Based on Austenite–Ferrite Transformation Kinetics*. Metals, 2019. **9**(10): p. 1045.
475. Astafurov, S. and E. Astafurova, *Phase composition of austenitic stainless steels in additive manufacturing: A review*. Metals, 2021. **11**(7): p. 1052.
476. Das, D. and P.P. Chattopadhyay, *Influence of martensite morphology on the work-hardening behavior of high strength ferrite–martensite dual-phase steel*. Journal of Materials Science, 2009. **44**(11): p. 2957-2965.

477. Remmerswaal, T., *The influence of microstructure on the corrosion behaviour of ferritic-martensitic steel*. 2015.
478. Fernández, P., J. Lapeña, and F. Blazquez, *Corrosion of High Chromium Ferritic/Martensitic Steels in High Temperature Water. a Literature Review*. 2000. **31**(35).
479. Chen, H., Z. Lv, L. Lu, Y. Huang, and X. Li, *Correlation of micro-galvanic corrosion behavior with corrosion rate in the initial corrosion process of dual phase steel*. *Journal of Materials Research and Technology*, 2021. **15**: p. 3310-3320.
480. Zhang, B., Z. Jiang, H. Li, S. Zhang, H. Feng, and H. Li, *Precipitation behavior and phase transformation of hyper duplex stainless steel UNS S32707 at nose temperature*. *Materials Characterization*, 2017. **129**: p. 31-39.
481. Johnson, D.R., X.F. Chen, B.F. Oliver, R.D. Noebe, and J.D. Whittenberger, *Processing and mechanical properties of in-situ composites from the NiAlCr and the NiAl(Cr,Mo) eutectic systems*. *Intermetallics*, 1995. **3**(2): p. 99-113.
482. Minkang L., Yimin Z., Jing-Li L., *Corrosion Under Hot Dilute Acidic Pre-Hydrolysis Biorefining Process*. *Corrosion 2020 Proceedings*, 2020. 15438.
483. Cieslak, M., T. Headley, and A. Romig, *The welding metallurgy of HASTELLOY alloys C-4, C-22, and C-276*. *Metallurgical Transactions A*, 1986. **17**(11): p. 2035-2047.
484. Leonard, R., *Thermal stability of hastelloy alloy C-276*. *Corrosion*, 1969. **25**(5): p. 222-232.
485. Kesavan, D. and M. Kamaraj, *Influence of aging treatment on microstructure, wear and corrosion behavior of a nickel base hardfaced coating*. *Wear*, 2011. **272**(1): p. 7-17.
486. Ferreira, L., K. Graf, and A. Scheid, *Microstructure and properties of nickel-based C276 alloy coatings by PTA on AISI 316L and API 5L X70 steel substrates*. *Materials Research*, 2015. **18**: p. 212-221.
487. Was, G.S., S. Teyseyre, and J. McKinley. *Corrosion and Stress Corrosion Cracking of Iron and Nickel-base Austenitic Alloys in Supercritical Water*. in *CORROSION 2004*. 2004.
488. Was, G.S., S. Teyseyre, and Z. Jiao, *Corrosion of Austenitic Alloys in Supercritical Water*. *Corrosion*, 2006. **62**(11): p. 989-1005.
489. Shen, Z., D. Tweddle, H. Yu, G. He, A. Varambhia, P. Karamched, F. Hofmann, A.J. Wilkinson, M.P. Moody, L. Zhang, and S. Lozano-Perez, *Microstructural understanding*

- of the oxidation of an austenitic stainless steel in high-temperature steam through advanced characterization. Acta Materialia*, 2020. **194**: p. 321-336.
490. Johnson, J.R.T. and I. Panas, *Hydrolysis on Transition Metal Oxide Clusters and the Stabilities of M–O–M Bridges*. *Inorganic Chemistry*, 2000. **39**(15): p. 3192-3204.
491. Swaddle, T.W., J.H. Lipton, G. Guastalla, and P. Bayliss, *The Aqueous Chemistry of Chromium(III) above 100 °C: Hydrothermal Synthesis of Chromium Spinels*. *Canadian Journal of Chemistry*, 1971. **49**(14): p. 2433-2441.
492. Minkang Liu, Y.Z., Jing-Li Luo, *Impacts of Catalyst, Inorganic and Organic Corrodants on Corrosion under Batch-mode Catalytic Biomass Hydrothermal Liquefaction Conversion*, 2022. **204**(12): 110409.
493. Berthod, P. and L. Aranda, *Determination of Diffusion Coefficients Using Thermogravimetric Measurements during High Temperature Oxidation*. *Defect and Diffusion Forum*, 2012. **323-325**: p. 289-294.
494. Papassiopi, N., K. Vaxevanidou, C. Christou, E. Karagianni, and G.S. Antipas, *Synthesis, characterization and stability of Cr(III) and Fe(III) hydroxides*. *J Hazard Mater*, 2014. **264**: p. 490-7.
495. Liu, X. and F.J. Millero, *The solubility of iron hydroxide in sodium chloride solutions*. *Geochimica et Cosmochimica Acta*, 1999. **63**(19-20): p. 3487-3497.
496. Fujiwara, K., K. Watanabe, M. Domae, and Y. Katsumura. *Stability of chromium oxide film formed by metal organic chemical vapor deposition in high temperature water up to supercritical region*. in *CORROSION 2007*. 2007.
497. Fajardo, S., D.M. Bastidas, M. Criado, and J.M. Bastidas, *Electrochemical study on the corrosion behaviour of a new low-nickel stainless steel in carbonated alkaline solution in the presence of chlorides*. *Electrochimica Acta*, 2014. **129**: p. 160-170.
498. NiDI, *High-Temperature Characteristics of Stainless Steels* American Iron and Steel Institute
499. Hooshyar, H., *High Temperature Corrosion of Stainless Steels in Low Oxygen Activity Environments: The effect of H₂ and H₂O*. 2016: Chalmers Tekniska Hogskola (Sweden).
500. Tang, X., S. Wang, L. Qian, M. Ren, P. Sun, Y. Li, and J.Q. Yang, *Corrosion properties of candidate materials in supercritical water oxidation process*. *Journal of Advanced Oxidation Technologies*, 2016. **19**(1): p. 141-157.

501. Machet, A., A. Galtayries, S. Zanna, L. Klein, V. Maurice, P. Jolivet, M. Foucault, P. Combrade, P. Scott, and P. Marcus, *XPS and STM study of the growth and structure of passive films in high temperature water on a nickel-base alloy*. *Electrochimica Acta*, 2004. **49**(22): p. 3957-3964.
502. Kim, J.H. and I.S. Hwang, *Development of an in situ Raman spectroscopic system for surface oxide films on metals and alloys in high temperature water*. *Nuclear Engineering and Design*, 2005. **235**(9): p. 1029-1040.
503. Kim, J., K.J. Choi, C.B. Bahn, and J.H. Kim, *In situ Raman spectroscopic analysis of surface oxide films on Ni-base alloy/low alloy steel dissimilar metal weld interfaces in high-temperature water*. *Journal of Nuclear Materials*, 2014. **449**(1): p. 181-187.
504. Henderson, J.D., X. Li, F.P. Filice, D. Zagidulin, M.C. Biesinger, B. Kobe, D.W. Shoesmith, K. Ogle, and J.J. Noël, *Investigating the Role of Mo and Cr during the Activation and Passivation of Ni-Based Alloys in Acidic Chloride Solution*. *Journal of The Electrochemical Society*, 2021. **168**(2): p. 021509.
505. Misirlioglu, Z. and A. Aksüt, *Corrosion of Molybdenum in Aqueous Media*. *Corrosion*, 2002. **58**(11).
506. Henderson, J.D., X. Li, D.W. Shoesmith, J.J. Noël, and K. Ogle, *Molybdenum surface enrichment and release during transpassive dissolution of Ni-based alloys*. *Corrosion Science*, 2019. **147**: p. 32-40.
507. Perera, F., *Pollution from Fossil-Fuel Combustion is the Leading Environmental Threat to Global Pediatric Health and Equity: Solutions Exist*. *International journal of environmental research and public health*, 2017. **15**(1): p. 16.
508. Gielen, D., F. Boshell, D. Saygin, M.D. Bazilian, N. Wagner, and R. Gorini, *The role of renewable energy in the global energy transformation*. *Energy Strategy Reviews*, 2019. **24**: p. 38-50.
509. Elliott, D., D. Beckman, A. Bridgwater, J. Diebold, S. Gevert, and Y. Solantausta, *Developments in direct thermochemical liquefaction of biomass: 1983-1990*. *Energy & Fuels*, 1991. **5**(3): p. 399-410.
510. Tursi, A., *A review on biomass: importance, chemistry, classification, and conversion*. *Biofuel Research Journal*, 2019. **6**(2): p. 962-979.

511. Barreiro, D.L., W. Prins, F. Ronsse, and W. Brilman, *Hydrothermal liquefaction (HTL) of microalgae for biofuel production: state of the art review and future prospects*. Biomass and Bioenergy, 2013. **53**: p. 113-127.
512. Cabrini, M., S. Lorenzi, T. Pastore, S. Pellegrini, M. Burattini, and R. Miglio, *Study of the Corrosion Resistance of Austenitic Stainless Steels during Conversion of Waste to Biofuel*. Materials (Basel), 2017. **10**(3).
513. Brady, M.P., J. Keiser, D. Leonard, L. Whitmer, and J.K. Thomson, *Corrosion Considerations for Thermochemical Biomass Liquefaction Process Systems in Biofuel Production*. JOM, 2014. **66**: p. 2583-2592.
514. Schillmoller, C.M. and N.D. Institute, *Alloy Selection for Caustic Soda Service*. 1988: NiDI.
515. Davies, M., *Alloy selection for service in chlorine, hydrogen chloride and hydrochloric acid*, G. Moe, Editor. 2018, Nickel Institute.
516. Nordstrm, J. and B. Rung, *Digesters and pulp storage towers of duplex stainless steels saving weight and costs*. Avesta Corrosion Management, 1994. **3**: p. 1-6.
517. Wensley, A., *Experience with Duplex Stainless Steel Kraft Digesters*. 2004.
518. Wensley, A., M. Moskal, and W. Wilton. *Materials Selection For Kraft Batch Digesters*. in *Corrosion97*. 1997.
519. Wensley, A. *Corrosion of Carbon and Stainless Steels in Kraft Digesters*. in *CORROSION 2000*. 2000.
520. Alén, R., *Chapter 3A - Pulp Mills and Wood-Based Biorefineries*, in *Industrial Biorefineries & White Biotechnology*, A. Pandey, et al., Editors. 2015, Elsevier: Amsterdam. p. 91-126.
521. Singh, P.M., J. Mahmood, and P. Conde. *Stress corrosion cracking and corrosion susceptibility of duplex stainless steels in caustic solutions*. in *CORROSION 2005*. 2005.
522. Almebäck, J.L.H., A. Edberg, and R. Shah, *Corrosion in Pulp Mills: Material Selection for an Evaporation Plant*. 2020.
523. Bruemmer, S.M., E.P. Simonen, P.M. Scott, P.L. Andresen, G.S. Was, and J.L. Nelson, *Radiation-induced material changes and susceptibility to intergranular failure of light-water-reactor core internals*. Journal of Nuclear Materials, 1999. **274**(3): p. 299-314.
524. Andresen, P.L., *9 - Stress corrosion cracking (SCC) of austenitic stainless steels in high temperature light water reactor (LWR) environments*, in *Understanding and Mitigating*

- Ageing in Nuclear Power Plants*, P.G. Tipping, Editor. 2010, Woodhead Publishing. p. 236-307.
525. Hussain, M., I. Hussain, A. Hussain, and S. Kousar, *Failure Due to Cl-SCC of Austenitic Stainless Steels*. Journal of Materials Engineering and Performance, 2019.
526. Truman, J., *The influence of chloride content, pH and temperature of test solution on the occurrence of stress corrosion cracking with austenitic stainless steel*. Corrosion Science, 1977. **17**(9): p. 737-746.
527. M. Karaminezhaad-Ranjbar, J. Mankowski, D. D. Macdonald; *Pitting Corrosion of Inconel 600 in High Temperature Chloride Solution under Controlled Hydrodynamic Conditions*. Corrosion, 1985. **41**(4): p. 197–204.
528. Turnbull, A., S. Zhou, and A. Willetts. *Environment Assisted Cracking of 316L Stainless Steel in Acetic Acid Environments*. in *CORROSION 2002*. 2002.
529. ASTM, *Standard Practice for Preparation and Use of Direct Tension Stress-Corrosion Test Specimens*. 2019. p. 9.
530. ASTM, *Standard Practice for Making and Using U-Bend Stress-Corrosion Test Specimens*. 2022. p. 7.
531. Kim, H.-J., M.-G. Lee, S.-C. Yoon, F. Vucko, C.-w. Lee, D. Theiry, and S.-J. Kim, *Diffusible hydrogen behavior and delayed fracture of cold rolled martensitic steel in consideration of automotive manufacturing process and vehicle service environment*. Journal of Materials Research and Technology, 2020. **9**(6): p. 13483-13501.
532. Revie, R.W., *Uhlig's Corrosion Handbook*. 2005: Wiley.
533. Baker, M.A. and J.E. Castle, *The initiation of pitting corrosion of stainless steels at oxide inclusions*. Corrosion Science, 1992. **33**(8): p. 1295-1312.
534. Wu, X., L. Li, H. Li, B. Li, and Z. Ling, *Effect of strain level on corrosion of stainless steel bar*. Construction and Building Materials, 2018. **163**: p. 189-199.
535. Lv, J. and Z. Wang, *High-temperature oxidation inducing strain for the 2205 duplex stainless steels*. Materials Research Express, 2020. **7**(10): p. 106507.
536. Wu, G., *Effect of strain on general and localized corrosion behavior of steels*. 2019, Georgia Institute of Technology.

537. Kanzaki, M., K. Takeda, and T. Kudo, *Evaluation of SCC Crack Growth Behavior of Non-Sensitized Stainless Steels in High Temperature Water by SSRT*. Zairyo-to-kankyo, 2007. **56**: p. 259-264.
538. Kuniya, J., S. Kasahara, H. Anzai, and H. Fujimori, *Stress Corrosion Cracking Susceptibility of Various Solution Annealed Austenitic Stainless Steels in High Temperature Water*. Zairyo-to-kankyo, 2007. **56**: p. 22-28.
539. Huang, Y.-J., K. Kawakita, and A. Kimura, *Stress corrosion cracking susceptibility of 310S stainless steel in hydrogenated hot water*. Nuclear Materials and Energy, 2018. **15**: p. 103-109.
540. Refaey, S.A.M., F. Taha, and A.M.A. El-Malak, *Corrosion and inhibition of stainless steel pitting corrosion in alkaline medium and the effect of Cl^- and Br^- anions*. Applied Surface Science, 2005. **242**(1): p. 114-120.
541. Féron, D., B. Kursten, and F. Druyts, *Sulphur-Assisted Corrosion in Nuclear Disposal Systems. First edition*, 2020. CRC Press. p. 190.
542. Toppo, A., M.G. Pujar, N. Sreevidya, and J. Philip, *Pitting and stress corrosion cracking studies on AISI type 316N stainless steel weldments*. Defence Technology, 2018. **14**(3): p. 226-237.
543. Zhu, L.K., Y. Yan, L.J. Qiao, and A.A. Volinsky, *Stainless steel pitting and early-stage stress corrosion cracking under ultra-low elastic load*. Corrosion Science, 2013. **77**: p. 360-368.
544. Castle, J.E. and R. Ke, *Studies by auger spectroscopy of pit initiation at the site of inclusions in stainless steel*. Corrosion Science, 1990. **30**(4): p. 409-428.
545. Lee, D., Y. Huang, and J.D. Achenbach, *A comprehensive analysis of the growth rate of stress corrosion cracks*. Proceedings of the Royal Society A: Mathematical, Physical and Engineering Sciences, 2015. **471**(2178): p. 20140703.
546. Vasudevan, A.K. and K. Sadananda, *Role of Slip Mode on Stress Corrosion Cracking Behavior*. Metallurgical and Materials Transactions A, 2011. **42**(2): p. 405-414.
547. Mayuzumi, M., N. Ishiyama, Y. Mizutani, J.-i. Tani, and K. Kako, *Incubation Time of Stress Corrosion Cracking for Type 316L and Type 316 Stainless Steels by CBB Method in High Temperature Water*. Zairyo-to-kankyo, 2008. **57**: p. 230-234.

548. Sangeetha R., *A Review of Chloride Stress Corrosion Cracking Factors for Austenitic Stainless Steel*, 2022. AMPP Annual Conference. AMPP-2022-17524.
549. Hoffmeister, H. and O. Klein, *Modeling of SCC initiation and propagation mechanisms in BWR environments*. Nuclear Engineering and Design, 2011. **241**(12): p. 4893-4902.
550. Cui, T., Q. Xiong, J. Ma, K. Zhang, Z. Lu, J. Chen, Y. Jia, H. Zheng, S. Yang, Z. Zhong, S. Lozano-Perez, and T. Shoji, *Oxidation Resistance and Stress Corrosion Cracking Susceptibility of 308L and 309L Stainless Steel Cladding Layers in Simulated Pressurized Water Reactor Primary Water*. Corrosion, 2021. **77**(8): p. 878-895.